TECHNISCHE UNIVERSITÄT WIEN

HEPHY INSTITUT FÜR HOCHENERGIEPHYSIK

DISSERTATION

Radiation-Hard 4H Silicon Carbide Particle Detectors for High-Energy Physics and Medical Applications

Ausgeführt zum Zwecke der Erlangung des akademischen Grades eines Doktor der technischen Wissenschaften

unter der Leitung von

Associate Prof. DI Dr.techn. Albert Hirtl
E141 - Atominstitut

und

DI Dr.techn. Thomas Bergauer
ÖAW / HEPHY

ausgeführt am

Institut für Hochenergiephysik der Österreichischen Akademie der Wissenschaften

eingereicht an der

Technischen Unversität Wien

E130 - Fakultät für Physik

von

Andreas Gsponer

Wien, 2025

(Unterschrift Autor) (Unterschrift Betreuer)

Citius — Altius — Fortius — Communiter

Faster — Higher — Stronger — Together

OLYMPIC MOTTO

Kurzfassung

Zukünftige Teilchenphysikexperimente mit hoher Luminosität stellen extreme Anforderungen an Detektormaterialien hinsichtlich der Positions- und Zeitauflösung für Leptonen-Kollider sowie der Strahlenhärte für Hadronen-Kollider dar. Im Vergleich zum gängigen Silizium stellt das Wide-Bandgap Halbleitermaterial 4H-Siliziumkarbid (4H-SiC) eine Alternative mit überlegener Strahlenhärte dar, da es auch nach Bestrahlung mit hohen Fluenzen extrem geringe Leckströme aufweist. Durch jüngste Verbesserungen in der Materialqualität und Kosten, die auf Investitionen der Leistungselektronikindustrie zurückzuführen sind, sind großflächige 4H-SiC-Detektoren realisierbar geworden. Neben der Strahlenhärte von 4H-SiC sprechen auch die Unempfindlichkeit gegenüber sichtbarem Licht und die geringe Temperaturabhängigkeit dafür, dass das Material ein vielversprechender Kandidat für medizinische Anwendungen wie Strahlmonitore und Dosimetrie ist.

In dieser Dissertation werden 4H-SiC-Detektoren, die von IMB-CNM-CSIC (Barcelona) hergestellt wurden, mithilfe von Labormessungen, Simulationen und Bestrahlungsstudien untersucht.

Monte-Carlo-Simulationen wurden im Allpix^2 Framework durchgeführt, um die Zeitauflösungsgrenzen von 4H-SiC-Detektoren zu untersuchen. Dabei wurden der Beitrag des Jitters (Signal-zu-Rausch-Verhältnis) sowie die stochastischen Fluktuationen der Energiedeposition durch ionisierende Strahlung (Landau-Fluktuationen) berücksichtigt.

Der Hauptfokus dieser Dissertation liegt jedoch auf der experimentellen Charakterisierung von 4H-SiC-Detektoren. Zu diesem Zweck wurden drei neue Laboraufbauten in Betrieb genommen oder überholt. Hierzu zählen eine Probestation für Hochspannungen bis 3 kV, ein Vakuumaufbau für Alphaspektroskopie sowie ein UV-Laser-basiertes Setup für Transient-Current-Technique-(TCT)-Messungen. Mithilfe dieser Aufbauten wurden fundamentale Materialeigenschaften wie die Ladungsträgerdriftgeschwindigkeiten oder die Ionisationsenergie von 4H-SiC gemessen. Darüber hinaus werden Ergebnisse von Wafer-Level-Charakterisierungen von sechs Zoll großen 4H-SiC-Wafern vorgestellt, die von HEPHY entworfen und von CNM produziert wurden. Zusätzlich wurde eine neuartige Hochfrequenzauslesseelektronik mit einer Bandbreite von 6 GHz entwickelt, welche erstmals die experimentelle Messung des transienten Stroms des Ladungsträgerdrift in 4H-SiC-Detektoren mit einer Dicke von 50 µm ermöglichte.

Zwei Neutronenbestrahlungsstudien mit Fluenzwerten bis zu $1 \times 10^{16}\,/\mathrm{cm}^2$ und $1 \times 10^{18}\,/\mathrm{cm}^2$ 1 MeV-Neutronenäquivalent wurden durchgeführt, um die Strahlenhärte von 4H-SiC zu bewerten. Nach der Bestrahlung blieben die Leckströme mit Werten von unter einem $< 1\,\mathrm{pA}/\mathrm{mm}^2$ sehr niedrig und die Dotierungen der epitaktischen Schicht der Detektoren werden durch Defekte mit tiefen Energielevel kompensiert. Die Ladungssammel-Effizienz (CCE) wurde mithilfe von Alphateilchen, UV-Lasern und einem Protonenstrahl untersucht und zeigte einen Wert von bis zu 50 % bei einer Fluenz von 1×10^{15}. Es wurde beobachtet, dass die CCE mit der Quadratwurzel der Bias-Spannung wächst, was darauf hindeutet, dass donorartige Defekte eine effektive Raumladung einführen, welche das elektrische Feld verkleinert und die gesammelte Ladung reduziert.

Schließlich kamen 4H-SiC-Detektoren zur Messung neuartiger Extraktionsmethoden am Synchrotron des MedAustron Ionentherapiezentrums zum Einsatz. Diese zielen darauf ab, ultra-hohe Dosisraten zu liefern, die den sogenannten FLASH-Effekt auslösen können, welcher das therapeutische Fenster bei der Patientenbehandlung vergrössern kann. Mithilfe einer Ausleseelektronik mit einer Bandbreite von 20 MHz konnte die Extraktion im Synchrotron turn-by-turn gemessen werden. Dies lieferte wertvolle Einblicke, die zur Implementierung eines gepulsten Extraktionsschemas genutzt wurden, mit dem Ziel sichere FLASH-Strahlen für zukünftige präklinische Studien bereitstellen.

Abstract

Future high-luminosity colliders pose extreme challenges to semiconductor detector materials in terms of spatial and temporal resolution for lepton colliders and radiation hardness for hadron colliders. Compared to the ubiquitously used silicon, the wide bandgap semiconductor 4H silicon carbide (4H-SiC) exhibits superior resilience to radiation-induced damage with extremely low leakage currents even after irradiation to high fluences. With the recent improvements in material quality and cost, driven by the power electronics industry, large-scale 4H-SiC detectors have become feasible. Additionally, its insensitivity to visible light and low temperature dependency make it a compelling candidate for medical applications, such as beam monitoring and dosimetry.

In this thesis, 4H-SiC detectors, manufactured by IMB-CNM-CSIC (Barcelona), are investigated using laboratory characterization techniques, simulations, and irradiation studies.

Monte-Carlo simulations have been performed in the Allpix^2 framework to study the time resolution limits of 4H-SiC detectors, in terms of the contribution of the jitter (signal-to-noise ratio) and the stochastic fluctuations of energy deposition by ionizing radiation (Landau fluctuations). For low-gain avalanche diodes (LGADs), which rely on impact ionization to multiply charge carriers inside a detector, a time resolution of 22 ps for 50 µm thick SiC-LGADs has been found, which is a factor 1.4 better than that of silicon LGADs (30 ps). Additionally, Monte-Carlo simulations of the design of the RD50-SiC-LGAD, currently being manufactured, are presented.

The main focus of the thesis, however, is the experimental characterization. To this end, three new laboratory setups have either been commissioned or significantly improved. This includes a probe station capable of high voltages up to 3 kV, an alpha spectroscopy vacuum setup, and a UV-laser-based setup used for transient-current-technique (TCT) measurements. These setups have been used to measure the fundamental material properties, such as the ionization energy or the charge carrier drift velocities of 4H-SiC. Furthermore, results from wafer-level characterization of six-inch 4H-SiC wafers designed by HEPHY and produced by CNM are presented. Additionally, novel high-speed readout electronics with a bandwidth of 6 GHz have been developed, which allowed the transient current of charge carrier drift in 50 µm thin 4H-SiC detectors to be measured experimentally for the first time.

Two neutron irradiation studies, up to fluences of $1 \times 10^{16}\,/\mathrm{cm}^2$ and $1 \times 10^{18}\,/\mathrm{cm}^2$ 1 MeV neutron equivalent in silicon, have been undertaken to assess the radiation hardness of 4H-SiC. After irradiation, leakage currents remained very low ($< 1\,\mathrm{pA}/\mathrm{mm}^2$) and the dopants of the detectors' epitaxial layer are compensated by deep traps. The charge-collection efficiency (CCE) was studied using alpha particles, UV-lasers, and a proton beam, with an efficiency of up to 50 % at a fluence of $1 \times 10^{15}\ \mathrm{n_{eq.}}/\mathrm{cm}^2$. The CCE has been observed to grow with the square root of the bias voltage, indicating that deep donor-like traps introduce an effective space charge, which shrinks the electric field and reduces the collected charge. After irradiation, detectors can also be operated in forward bias. In this regime, anomalous observations of the CCE exceeding 100 % have been investigated and were attributed to the high injected charge densities in certain measurement modalities.

Finally, 4H-SiC detectors have been used to measure novel extraction techniques at the synchrotron of the MedAustron ion therapy center. These extraction methods aim at delivering ultra-high dose rates, capable of triggering the FLASH effect, which widens the therapeutic windows in patient treatment. With the 20 MHz bandwidth of the detector readout electronics, the extraction was able to be measured for each turn in the synchrotron, providing valuable insights which have been used to implement a pulsed extraction scheme that could provide safe FLASH beams for future pre-clinical studies.

Contents

1 Introduction

"New directions in science are launched by new tools much more often than by new concepts."
— Freeman Dyson

Semiconductor-based detectors have experienced a rapid adoption in particle physics, from single diodes in the 1960s to the current state of the art, with detectors covering hundreds of square meters [1]. Compared to other types of detectors (such as gas or crystal detectors), solid-state detectors offer unparalleled position resolution, scalability, and the possibility of integrated readout electronics.

With more ambitious particle physics experiments undertaken each year, the instrumentation demands of these experiments have grown accordingly. At the high-luminosity LHC [2], the extreme particle fluences and pile-up conditions translate into unprecedented demands in detector radiation hardness and timing resolution [3]. Envisioned future colliders, such as the Future Circular Collider in its hadron collider configuration (FCC-hh), are expected to push these requirements even further [4]. Additionally, future lepton colliders ("Higgs-factories") will require instrumentation with an extremely good spatial resolution and a small material budget [4]. Meeting these challenges will require significant advances in the sensor materials and readout electronics, which is the goal of the Detector R&D collaboration on solid-state detectors (DRD3) [5]. Figure 1.1.1 shows an overview of the technological readiness state of solid-state detectors (as of 2021). For many of the envisioned future collider experiments, the instrumentation needs are not yet met.

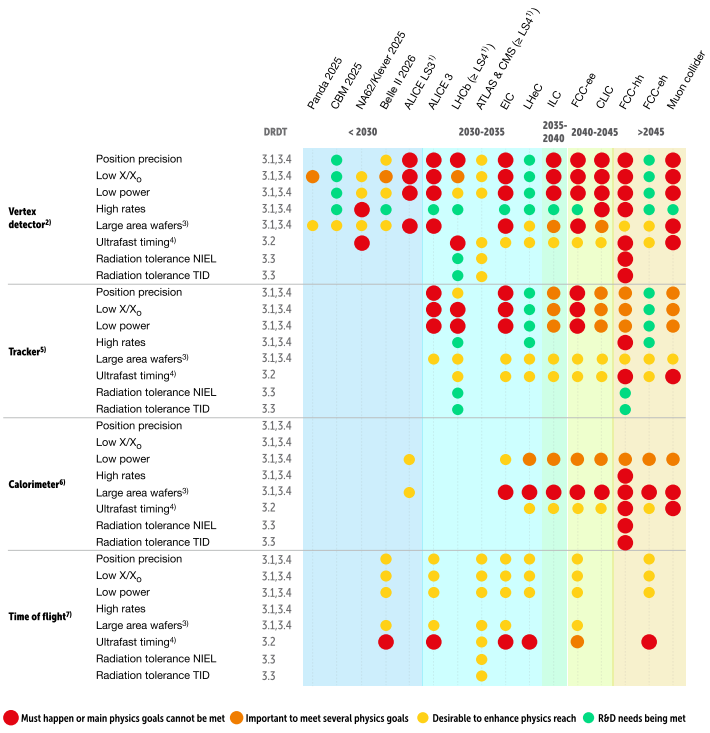

Figure 1.1.1: Detector Readiness Matrix identified in the ECFA Detector R&D Roadmap. Taken from [6].

For silicon detectors, the radiation hardness has been investigated in detail, and defect engineering recipes have been developed to cope with the increasing radiation hardness demands [7]. Additionally, new geometries and concepts (such as 3D-detectors [8], low-gain avalanche diodes [9], and resistive silicon detectors [10]) have enabled better timing and position resolution.

The search towards higher performance, however, includes not only new geometries but also detector materials other than silicon. Wide-bandgap semiconductors, such as silicon carbide (SiC) and diamond, offer material parameters (such as the drift velocity, breakdown electric field, and atomic displacement threshold) that surpass the performance of silicon. These materials are not new in the detector community [11]. Diamond detectors have matured as a technology and have found a niche in beam monitoring [12], but their deployment on larger scales and areas is still limited by cost. Silicon carbide (and specifically its 4H polytype) has been studied for detectors in high-energy physics for more than 20 years [13]. However, with the rapid development in material quality and decrease of cost due to the investment in the power electronics industry in 4H-SiC, the interest of the community in SiC detectors has been revitalized. Wafer sizes of 8 inches are now available in the industry, and the density of defects (such as micropipes or plane defects) has been reduced to reasonable levels [14].

Figure 1.1.2 shows a comparison between silicon and wide-bandgap semiconductors. 4H-SiC is a middle of the road between diamond (and its advantageous material properties) and silicon (with a wide variety of processing capabilities and a large industrial base).

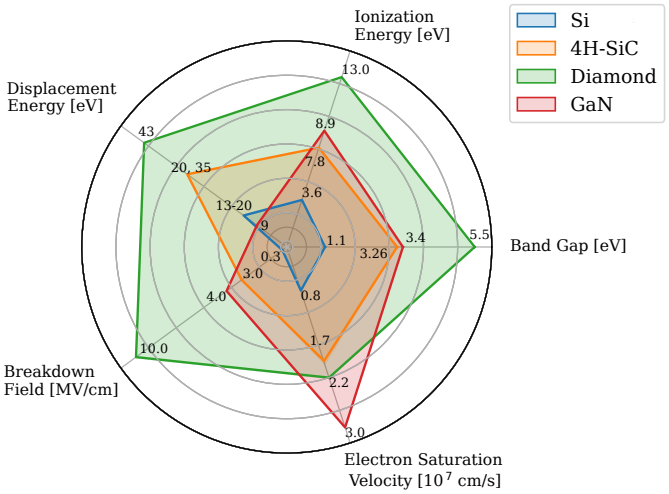

Figure 1.1.2: Material properties of silicon, 4H-SiC, diamond and gallium nitride [15].

Even though 4H-SiC is the most industrially mature wide bandgap semiconductor for particle detectors, some disadvantages compared to silicon remain: The ionization energy (energy required to produce an electron-hole pair) in 4H-SiC is twice as high as for silicon [16], and together with the epitaxial layer thickness that can be grown (and depleted) limited to values around 100 µm [17], only a relatively small amount of charge is available to be detected. This has driven a recent push in the community to develop 4H-SiC LGADs, which amplify charge using impact ionization [18, 19] and are envisioned to achieve a better timing resolution than Si-LGADs [20]. Compared to silicon, 4H-SiC does not suffer from an increase in leakage currents after irradiation [16], which allows for irradiated sensors to be operated in collider experiments without any cooling, reducing the power draw and mass budget significantly. Additionally, monolithic 4H-SiC sensors [21] could be operated even above room temperature, allowing for more efficient air cooling and a higher power budget in future lepton colliders such as the FCC-ee [22]. Furthermore, with the ability of 4H-SiC to operate at temperatures as high as 450 °C [23], SiC-based detectors have found applications in fusion diagnostics [24].

Studying 4H-SiC as a detector material for applications in high-energy physics has been the main focus of this thesis. Together with the Instituto de Microelectrónica de Barcelona (IMB-CNM-CSIC), the Institute of High Energy Physics (HEPHY) of the Austrian Academy of Sciences is developing 4H-SiC LGADs. This development is ongoing partially in the RD50-SiC-LGAD common project, where two runs of 4H-SiC PiN diodes on 6-inch wafers have been produced in the last two years. The detectors produced by CNM have been characterized thoroughly in this thesis, and their radiation hardness has been studied.

The material properties of 4H-SiC lend it not only to be used in high-energy physics, but also in medical applications, such as dosimetry [25]. 4H-SiC is insensitive to visible light, has very small leakage currents, and a lower temperature dependency than silicon [26]. HEPHY, together with MedAustron, is developing a SiC-based beam monitor [27] for ion therapy centers in the *HiBPM* (Hi-Precision Beam Position and Intensity Monitor for Accurate Cancer Treatment with Ions) FFG-Project. MedAustron is an ion therapy center in Wiener Neustadt, Austria, based on the CERN proton-ion medical machine study (PIMMS) [28]. The first patients have been treated in [29], and today proton, carbon (and soon helium [30]) beams are available. Figure 1.1.3 shows an overview of the MedAustron synchrotron. Four beamlines are available, with one irradiation room reserved for non-clinical research, which includes solid-state detectors. Proton-based ultra-high dose rate radiotherapy, which leverages the FLASH effect to achieve a wider therapeutic window [31], is currently under development at MedAustron [32, 33]. The very high dose rates and novel extraction mechanisms required for implementing FLASH-like beams make accurate dosimetry and analysis of the extraction time profile essential. To this end, 4H-SiC detectors were employed in this thesis to measure the extracted dose rate in FLASH conditions, capturing each revolution of the particles in the synchrotron [34].

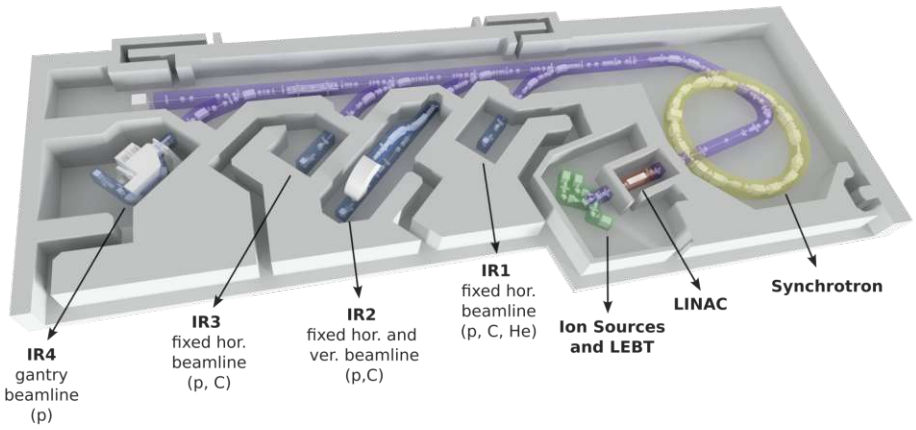

Figure 1.1.3: Floor plan of the MedAustron accelerator complex. Taken from [35].

Thesis Outline

Section 2 will first introduce the relevant theoretical background. This covers 4H-SiC as a material and the relevant semiconductor physics for PiN diodes and low-gain avalanche diodes (LGADs). The interaction of ionizing radiation with matter and its stochastic fluctuations are discussed in detail, together with radiation damage degrading the operation of solid-state detectors. The signal formation due to electron and hole drift is discussed and common detector geometries are introduced.

Fast readout electronics will be discussed in **Section 3**. While general circuit concepts are covered, a special focus is given to fast transimpedance amplifiers, which can directly measure the transient current of the charge carrier drift in a detector. Measurements of the frequency response for different amplifiers up to 10 GHz are presented, and the impact of parasitic impedances, such as the detector capacitance and bond wire inductance, are discussed.

Characterizing 4H-SiC requires not only readout electronics but also additional infrastructure, such as probe stations and setups with radioactive sources. This infrastructure has either been newly built or significantly improved and commissioned during the course of this thesis, as detailed in **Section 4**.

Section 5 presents studies of the performance of 4H-SiC detectors using Monte Carlo simulations. The Allpix^2 simulation framework is used to model the interaction of ionizing radiation and drift of charge carriers. Particular emphasis is placed on simulating time resolution, as the charge carrier drift velocities in 4H-SiC are nearly twice those in silicon, making it attractive for timing applications. The two main contributions to the timing resolution are studied: the effect of readout noise on the rising edge of the detector signal (jitter), and the effect of fluctuations in charge deposition (Landau fluctuations). A comparison between silicon, 4H-SiC, and other wide-bandgap materials is performed. For the first time, SiC-LGADs have been simulated in Allpix^2 , and the results are compared to TCAD simulations.

Section 6 will give an overview of the experimental measurements that have been carried out in this thesis. Silicon carbide devices from three productions of CNM are characterized electrically, in order to assess quantities such as the doping concentration and wafer yield. Two in-depth studies are then presented: The first aims at determining the ionization energy of 4H-SiC (where there have been significant disagreements in the literature) using alpha spectroscopy. The second employs very high bandwidth (6 GHz) detector readout electronics in order to study the transient current in 50 µm thin 4H-SiC diodes. With the extremely fast rise times achieved in this setup, the charge carrier drift in 4H-SiC detectors has been resolved for the first time, and electron and hole charge carrier velocities are extracted from the data.

The radiation hardness of 4H-SiC detectors is investigated through two neutron irradiation studies presented in **Section 7**. The first study used fluences between 5×10^{14} and 1×10^{16} $n_{eq.}/cm^2$, with a thorough characterization of electrical properties and charge collection efficiency in reverse and forward bias after irradiation. The second study focused on an extreme fluence of 1×10^{18} $n_{eq.}/cm^2$ (expected at future hadron colliders such as the FCC-hh).

Section 8 introduces a medical application of 4H-SiC detectors: monitoring beam intensity in ultra-high dose rate beams at the MedAustron ion therapy center. The motivation for higher dose rates and the FLASH effect are explained, and the dosimetric and clinical safety challenges are highlighted. Data is presented for different synchrotron extraction techniques used to implement pulsed beams that meet the FLASH dose rate threshold. Finally, **Section 9** summarizes the performed work and gives an outlook on currently ongoing activities.

2 Physical and Technological Background

2.1 Silicon Carbide

Silicon carbide (SiC) is a compound semiconductor consisting of silicon (Si) and carbon (C) in a 1:1 ratio. Before SiC was discovered in nature, it was synthesized in the laboratory, first being reported by Berzelius [36] in 1824. With its material properties becoming apparent (specifically the extreme hardness), SiC found its first applications in grinding and polishing, moving to the industrial scale with the introduction of the Acheson process [37] in 1892. Already early on, SiC gained attention not only for its hardness, but also for its electrical properties, for example with the discovery of electroluminescence in 1907 [38]. The first natural occurrence of SiC was only discovered in 1905 [39], more than 15 years after it had been synthesized on a large scale. This mineral, made of silicon carbide, has subsequently been named "Moissanite", in honor of its discoverer, Henri Moissan. While silicon carbide occurs only very rarely on Earth, it constitutes a significant fraction of interstellar dust particles, and thus plays an important role in astrophysics [40].

Silicon carbide can occur in different polytypes, with different stacking sequences of the silicon and carbon atoms in the crystal lattice. While more than 200 different known polytypes exist [14], the industry has converged on a few polytypes that have the most optimal material properties and are easiest to manufacture, depicted in Figure 2.1.1. Specifically, 4H-SiC, which has the highest electron drift velocity, has come to dominate the silicon carbide market [41].

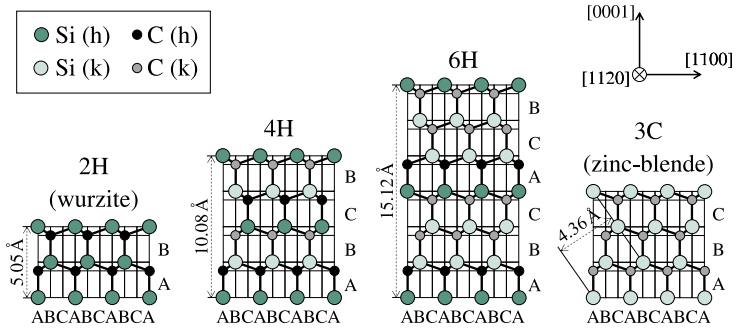

Figure 2.1.1: Common silicon carbide polytypes used in industry. 3C features a cubic lattice, while 2H/4H/6H are hexagonal. Taken from [42].

While the first detector prototypes using SiC were demonstrated already in the 1960s [43], the commercial industry (in particular for power electronics) only started adopting SiC during the 1990s, as material quality and prices progressed to reasonable standards [44]. Table 1.1 shows a comparison of SiC's material properties to silicon and other comparable semiconductors. Silicon carbide is a wide-bandgap (WBG) semiconductor, with a bandgap of 3.26 eV for the 4H polytype, which is significantly larger than silicon's bandgap of 1.12 eV. The large bandgap typically also coincides with other favorable material properties, such as high breakdown electric fields, high thermal conductivity, and high charge carrier velocities [44]. These favorable material properties lend silicon carbide (and other WBG materials) to be used heavily in power electronics applications, as well as in harsh environments (high temperature and high radiation). In power electronics, the high breakdown electric field allows for pro-

portionally thinner devices, which simultaneously decreases the on-state resistance and increases the switching frequencies that can be used, both enabling higher power efficiency and exceeding the performance of silicon [44]. Gallium nitride (GaN) and SiC, both wide-bandgap materials, have come to dominate the power electronics market over the last decade [41]. As GaN features some of the highest charge carrier saturation velocities, it excels in low- to medium-power applications, primarily in consumer electronics, as depicted in Figure 2.1.2. Silicon carbide, however, is typically used for high-power applications ($>$ 100 kW), where the highest switching voltages, and therefore its superior breakdown electric field, are required. Driven by the power electronic industry's large-scale adoption, SiC has become cheaper, higher quality, and is available as 6 or 8-inch wafers, which has renewed the interest of the particle physics community to use SiC for detectors.

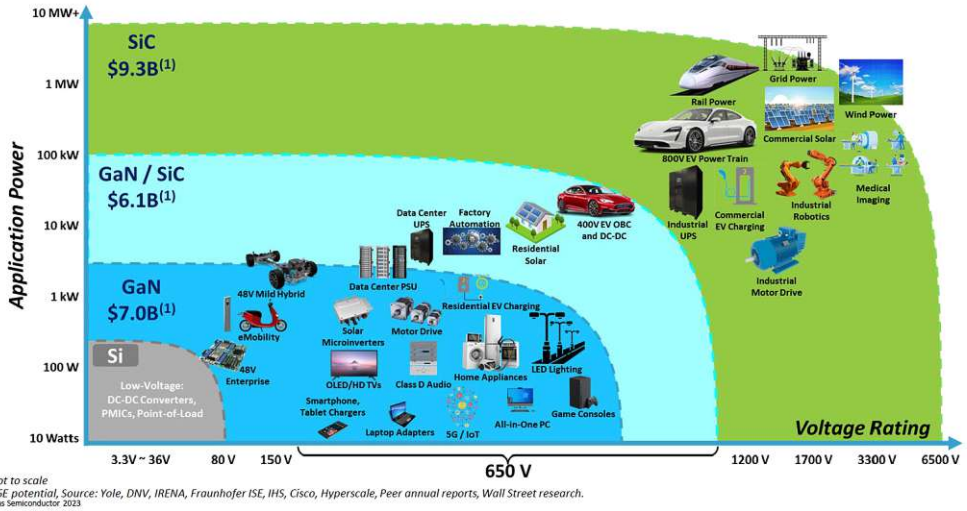

Figure 2.1.2: Overview of the power electronics market including Si, GaN, and SiC [45].

Property	4H-SiC	Silicon	Diamond	GaN
Crystal structure	Hexagonal	Cubic	Cubic	Hexagonal
Atomic Number	14/6	14	6	31 / 7
Bandgap (eV)	3.26	1.12	5.5	3.4
Relative Permittivity ϵ_r	10.3	11.9	5.7	9.6
e-h pair creation energy ϵ_i [eV]	7.83	3.62	$\sim$ 13	$\sim$ 8.9
Electron mobility [cm^2/Vs]	1100	1450	$\sim$1800	1000
Hole mobility [cm^2/Vs]	115	450	$\sim$1200	$\sim$30
Thermal conductivity [W/cm·K]	3-4	1.5	20	1.3-2.3
Breakdown field [MV/cm]	3-4	0.3	10	3.3
Electron saturation velocity [10^7 cm/s]	1.7	1.0	$\sim$2.6	2.5
Density [g/cm^3]	3.21	2.33	3.51	6.15
Thermal expansion [10^{-6}/K]	4.0	2.6	1.0	5.6
Radiation length [g^2/cm]	21.8	25.5	42.7	14.0
Operation temperature	up to 600 °C	up to 150 °C	up to 1000 °C	up to 600 °C

Table 1.1: Comparison of silicon and wide bandgap semiconductors relevant for particle detectors in high energy physics. The data has been taken from [14, 46, 47] and the radiation length has been calculated using Geant4 [48].

2.1.1 Growth and Processing

Contrary to silicon, silicon carbide (SiC) can not simply be grown from a melt, as the liquid phase of SiC only exists at very high temperatures and pressures [44]. Instead, it has to be grown on a seed crystal using techniques such as physical vapor transport (PVT) or chemical vapor deposition (CVD). In physical vapor transport [49], polycrystalline starting material (in this case silicon carbide powder) is vaporized at high temperatures (2500 °C) and low pressure (100 mbar), after which the vapor is transported via a carrier gas (typically argon) to a cooled seed crystal, where it condenses and grows the crystal. Growth rates using PVT are faster than using CVD, but still limited to below 1 mm h^{-1}. This means that growing

Figure 2.1.3: Left: silicon carbide boule grown using physical vapor transport [50]. Right: 4H-SiC wafer with a CVD-grown epitaxial layer ready for processing [51]. Note the transparency to optical light.

an entire SiC boule (see Figure 2.1.3) can take a significant amount of time (up to two weeks), which is a main cost-driver of SiC electronics [52]. After growing a SiC boule, it is sliced into individual wafers with a typical thickness of 350 µm. In order to encourage the growth of a specific polytype (such as 4H), the boule is cut slightly off-angle (4° for 4H-SiC) with respect to the crystal *c*-axis ([0001]), as depicted in Figure 2.1.4. With this off-axis cut, the top layer of the wafer presents "step edges" where the Si/C stacking layers end. These step edges present a nucleus for crystal growth, which ensures that the correct polytype is grown (together with precise control of the temperature and Si/C ratio) [42]. If a wafer is cut out of the boule without any off-axis angle, there are no step edges, and only very limited polytype control. While PVT can be used to grow large (centimeter-scale) crystals, the crystal quality is typically not good enough for electrical applications. Instead, an epitaxial layer is grown on top of the wafer in a second step, using chemical vapor deposition. In CVD, gases such as silane (SiH_4) and propane (C_3H_8) react chemically with the SiC wafer to grow additional crystal layers. The concentration of different elements (such as the Si/C ratio or dopants such as nitrogen) can be controlled precisely by adjusting gas flows [44]. Compared to PVT, the temperature is typically lower (1500 °C) and more uniform along

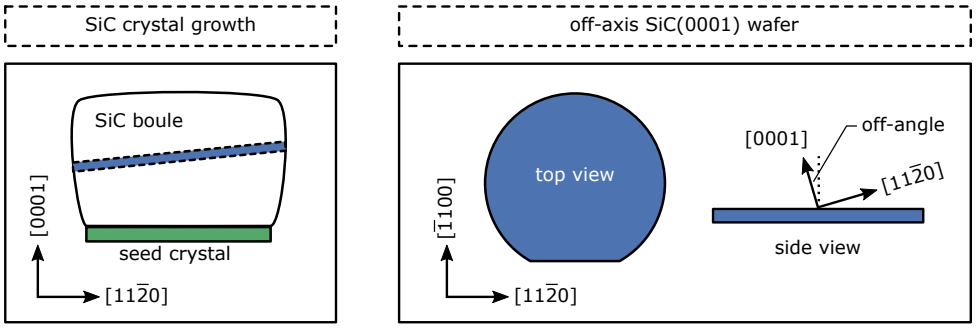

Figure 2.1.4: SiC boule and off-axis cut wafer. Taken from [42].

the wafer, leading to fewer thermally induced defects. While CVD growth yields the best crystal quality, the growth rate is also significantly lower than for PVT, at $5 - 20\,\mu m\,h^{-1}$ [53].

In order to obtain structured electrical devices, localized p and n dopants are added to create p-n junctions or other devices. In silicon devices, dopants are often introduced using diffusion, where the concentration gradient from a gas forces dopants into the silicon lattice. However, in SiC, the diffusion constant of dopants is extremely low, and would require very high temperatures in excess of 2000 °C (that would also introduce a large number of crystal defects) [44]. Therefore, doping of SiC devices after the epitaxial growth has to be performed using ion implantation, where dopants are ionized and accelerated to energy levels around 100 keV to 1 MeV and physically transported into the SiC crystal instead of relying on diffusion. After ion implantation, the SiC crystal has to be heated to temperatures as high as 1600 °C, in order for the dopants to find their way into the crystal lattice, a process referred to as *activation* of the dopants. This process also repairs crystal damage, which is why ion implantation is sometimes also performed at elevated temperatures ($\sim$ 600 °C), so that the crystal damage can be directly repaired, especially if high doping concentrations need to be obtained [44]. For deep implants ($> 1\,\mu m$), ion implantation energies in excess of 1 MeV are required. These high energies are above the typical working range for silicon-based devices and require special accelerators and hard masks [54].

As previously mentioned, a uniform doping of the epitaxially grown layers can be achieved by incorporating a dopant gas during the CVD growth. In typical power electronics applications, nitrogen-based n-doping with concentrations around 10^{15}-10^{16} cm^{-3} is used. If lower doping concentrations are required (for example, if large thicknesses are to be depleted for detectors in high energy physics), the intentionally added nitrogen can be reduced during the crystal growth. However, there are limitations on the lowest nitrogen concentrations that can be achieved in practice (due to contamination of the environment and source material). The minimum nitrogen doping that can be obtained commercially is on the order of $1 \times 10^{13}\,cm^{-3}$ [14].

Most metals on SiC work as Schottky contacts if they are deposited at temperatures below 700 °C [53]. However, if ohmic contacts with the lowest contact resistivities are required (such that the resistance of the contact is negligible compared to the device resistance), sintering is necessary to form materials with adequately low barrier heights. One popular choice of contact metal is nickel (Ni), which forms a silicide when sintered together with 4H-SiC at high temperatures. However, this process is not simple and research is still ongoing to improve it [44]. For example, as nickel forms silicides but not carbides, the silicon in SiC is consumed, but the carbon remains and has to be dealt with. One solution to this is to add titanium or tungsten (in a multi-metal stack), which form carbides that consume the excess carbon, while still keeping the barrier height sufficiently low.

2.2 Semiconductor Physics

2.2.1 Band-Model and Fermi Statistics

The periodic structure of a crystal forms a lattice, in which the discrete energy levels of electrons form continuous energy bands. At cryogenic temperatures, all electrons are bound to their atoms. However, for higher temperatures, electrons can be thermally excited to break free from their atoms, leaving behind a vacancy. After breaking away, the free electron can travel through the lattice and exist in the conduction band until it either recombines with an electron vacancy (hole) or leaves the lattice. The vacancies can also travel through the lattice, via a neighboring electron being absorbed into the vacancy, effectively moving the vacancy. For metals, these valence and conduction bands partially overlap, and charge carriers can freely move around. In semiconductors, there is a gap between both bands, the bandgap, as indicated in Figure 2.2.1. Depending on the size of the bandgap, semiconductors are classified as narrow-gap ($< 0.7\,eV$), conventional ($0.7 - 2.0\,eV$) or wide-bandgap ($> 2\,eV$) [53]. For band gaps above 3 eV, materials are typically referred to as insulators, as the distance between the valence

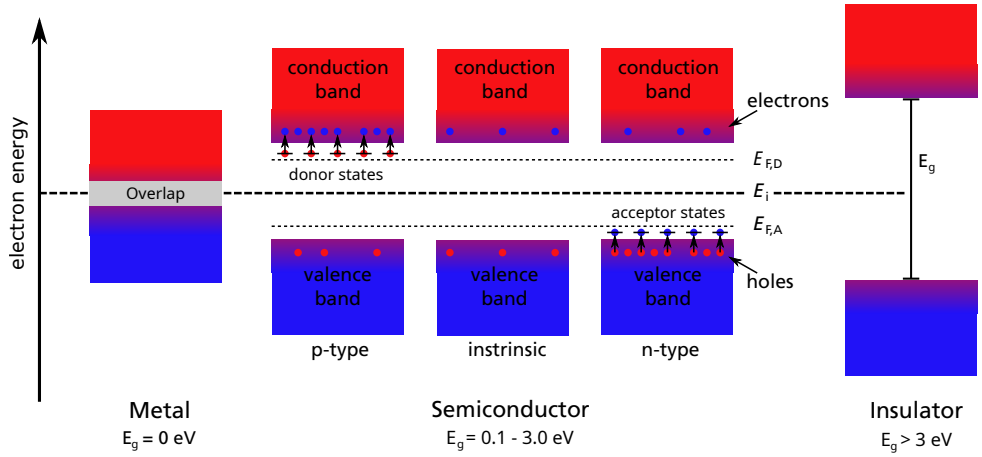

Figure 2.2.1: Bandgap for metals, semiconductors, and insulators. For semiconductors, the Fermi level is indicated in the case of intrinsic material and p- or n-doped material. Adapted from [55].

and conduction bands is so significant that no current can flow at room temperature. The probability of an electron (or hole) occupying a state in a band is given by the Fermi-Dirac statistics $F(E)$

$$F(E) = \frac{1}{1 + \exp\left(\frac{E - E_f}{k_b T}\right)}, \tag{2.2.1}$$

where E is the energy of the state, E_f the Fermi energy, k_b the Boltzmann constant and T the temperature. The Fermi energy is the energy level at which the probability of a state being occupied is 50 %. At temperatures above absolute zero, valence electrons can thermally obtain sufficient energy to overcome the bandgap and cross into the conduction band. This process not only generates a free electron but also leaves over a vacancy (hole) in the valence band, forming an electron-hole pair. The probability of this process is given by [56]

$$p(T) = CT^{3/2} \exp\left(-\frac{E_g}{2k_b T}\right), \tag{2.2.2}$$

where T is the temperature, E_g the bandgap of the material and C a material constant. For silicon ($E_g = 1.12\,\text{eV}$), this results in a significant amount of thermally generated charge carriers at room temperature, about $1 \times 10^{10}\,\text{cm}^{-3}$ [57]. It is immediately obvious that this intrinsic charge concentration is much larger than the charge generated by a minimum ionizing particle (see Section 2.4), so a method is required to reduce this concentration. Wide-bandgap materials (or insulators) have exponentially lower levels of intrinsic charge carriers and can be used directly to detect particles.

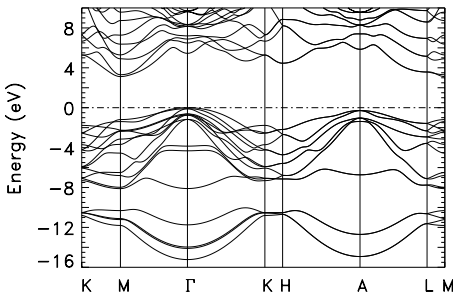

Figure 2.2.2: Band structure diagram for 4H-SiC obtained using numerical simulations. Taken from [58].

Figure 2.2.2 shows the band diagram for 4H-SiC. A bandgap is clearly visible in the band structure, with an energy difference of around 3.26 eV [14]. However, the maximum of the valence band and the minimum of the conduction band do not occur at the same wavevector k, which is referred to as an indirect bandgap. This implies that for an electron to transition from the valence to the conduction band, it needs an intermediate interaction (typically with a phonon) in order to change its wavevector while conserving momentum. Compared to direct bandgap semiconductors, the absorption of photons (light) is much smaller in indirect bandgap semiconductors, because even if a photon has an energy close to the bandgap, a phonon is required for the photon to be absorbed. Light absorption in indirect semiconductors typically depends strongly on the temperature, as the phonon concentration scales with temperature [57].

2.2.2 Doping and p-n Junctions

In intrinsic semiconductors, the number of holes and electrons balances out to be equal in thermal equilibrium. However, if impurities (small concentrations of foreign elements) are introduced that readily give away electrons or vacancies (holes), the prevalent concentration of charge carriers can be tipped in favor of one or the other. Group V elements (such as P, N or As) have one more electron than silicon and carbon (group IV), which they can give up (donate), creating n-doping (excess electrons). Group III elements (B, Al, Ga) instead have one less valence electron than silicon and carbon and readily accept an electron, thus creating p-doping.

If two regions with n- and p-doping are brought into contact (as depicted in Figure 2.2.3), the electrons (n) and holes (p) will recombine at the interface, until this zone is *depleted* and no charge carriers are present. By applying an external electric field, more p or n-type charge carriers can be pushed into this zone, effectively widening or narrowing the depletion zone. Even if no voltage is applied, the difference in Fermi levels (see Figure 2.2.1) results in a "built-in" voltage V_{bi} given by [59]

$$\mathrm{V_{bi}} = \frac{E_{F,A} - E_{F,D}}{q} = \frac{k_B T}{q} \ln\left(\frac{N_A}{N_D} n_i\right), \tag{2.2.3}$$

with N_A, N_D the acceptor/donor concentration and n_i the intrinsic charge carrier concentration.

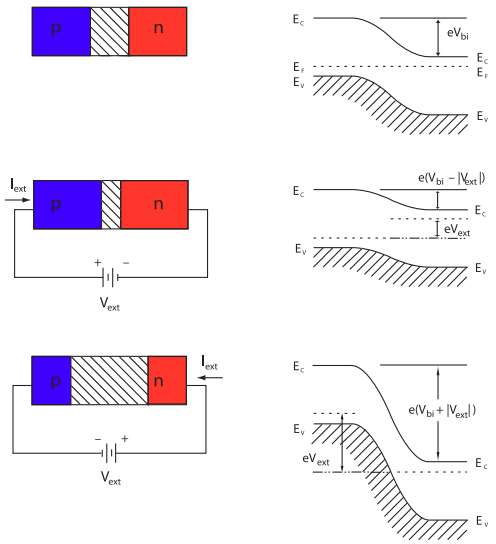

Figure 2.2.3: Working principle of a p-n junction. Adapted from [57].

Current-Voltage Characteristics

The large difference between charge carrier concentrations in the p and n regions results in a diffusion current (carriers diffusing from high to low concentrations), given by Fick's law [57]

$$\vec{\mathrm{I}}_{\mathrm{diff.}} = qD_n\vec{\nabla}\frac{\mathrm{d}\Delta n(\vec{x})}{\mathrm{d}\vec{x}} - qD_p\vec{\nabla}\frac{\mathrm{d}\Delta p(\vec{x})}{\mathrm{d}\vec{x}}\,, \tag{2.2.4}$$

where D_n, D_p are the respective diffusion constants and $n(\vec{x}), p(\vec{x})$ the electron and hole concentrations. The diffusion constants are related to the *charge carrier mobility* μ (which will be detailed in Section 2.2.4), as

$$D = \mu\frac{k_BT}{q}. \tag{2.2.5}$$

In equilibrium, the diffusion current is compensated by a drift current in the depletion zone such that

$$\vec{\mathrm{I}}_{\mathrm{drift}} = qn\mu_n\vec{E} + qp\mu_p\vec{E}, \quad \vec{\mathrm{I}}_{\mathrm{drift}} = -\vec{\mathrm{I}}_{\mathrm{diff.}} \tag{2.2.6}$$

If now an external bias voltage $\mathrm{V_{ext}}$ is applied, the Fermi level of the n and p-doped regions shifts, which will change the charge carrier populations n and p exponentially away from the equilibrium state [57]

$$n(\mathrm{V_{ext}}) = n_0e^{q(\mathrm{V_{bi}}-\mathrm{V_{ext}})/k_BT}\,, \tag{2.2.7}$$

$$p(\mathrm{V_{ext}}) = p_0e^{q(\mathrm{V_{bi}}-\mathrm{V_{ext}})/k_BT} \tag{2.2.8}$$

where n_0 and p_0 are the charge carrier concentrations in equilibrium ($\mathrm{V_{ext}} = 0$) at the boundaries of the n and p regions. Going into the depletion zone, the diffusing charge carriers have a chance to recombine (with a characteristic diffusion length $L_{n,p}$), yielding a difference between the edges of the depletion zone of

$$\Delta n(\mathrm{V_{ext}}, x) = n_0 + n_0\cdot e^{q(\mathrm{V_{bi}}-\mathrm{V_{ext}})/k_BT}\cdot e^{x/L_n}\,, \tag{2.2.9}$$

$$\Delta p(\mathrm{V_{ext}}, x) = p_0 + p_0\cdot e^{q(\mathrm{V_{bi}}-\mathrm{V_{ext}})/k_BT}\cdot e^{x/L_p}. \tag{2.2.10}$$

The diffusion current is then proportional to the gradient in charge carriers, according to Equation (2.2.4):

$$\mathrm{I}_n(\mathrm{V}) = qD_n\frac{\Delta n(0)}{L_n} = qD_n\frac{n_0}{L_n}\left(e^{\frac{q\mathrm{V}}{k_BT}} - 1\right)\,, \tag{2.2.11}$$

$$\mathrm{I}_p(\mathrm{V}) = qD_p\frac{\Delta p(0)}{L_n} = qD_p\frac{n_0}{L_p}\left(e^{\frac{q\mathrm{V}}{k_BT}} - 1\right) \tag{2.2.12}$$

$$\tag{2.2.13}$$

which corresponds to the well-known Shockley-diode equation [60], that can be written as

$$\mathrm{I}(\mathrm{V}) = I_s\left(e^{\frac{q\mathrm{V}}{k_BT}} - 1\right)\,, \tag{2.2.14}$$

with I_s the reverse saturation current, given by

$$\mathrm{I_s} = q\left(\frac{D_nn_0}{L_n} + \frac{D_pp_0}{L_p}\right). \tag{2.2.15}$$

Figure 2.2.4 shows the Shockley-diode equation as a function of voltage. In reverse bias (and at high voltages $\mathrm{V} \gg kT$), the current of a diode is constant, given simply by

$$\mathrm{I}(\mathrm{V}) = -\mathrm{I_s}. \tag{2.2.16}$$

However, in non-ideal semiconductors, there may be a thermal generation of charge carriers (due to defects, see Section 2.2.3), and the current can be significantly larger than I_s, scaling with the volume of the depletion zone.

In forward bias, the current will increase exponentially with the voltage. If there is a significant amount of recombination (such that the recombination length is shorter than the diffusion length), the charge carrier transport will be limited, which can be accounted for by introducing an *ideality-factor n* in the Shockley-diode equation

$$I(V) = I_s \left(e^{qV/nk_BT} - 1 \right). \tag{2.2.17}$$

For diffusion dominated transport, the ideality factor is $n = 1$. If recombination dominates, the current will depend on the recombination and generation rates R. For a trap in the middle of the bandgap, R will scale as the product of hole and electron concentrations and be proportional to $e^{qV/2kT}$, resulting in an ideality factor of $n = 2$. Figure 2.2.4 shows the forward current of a diode for these different

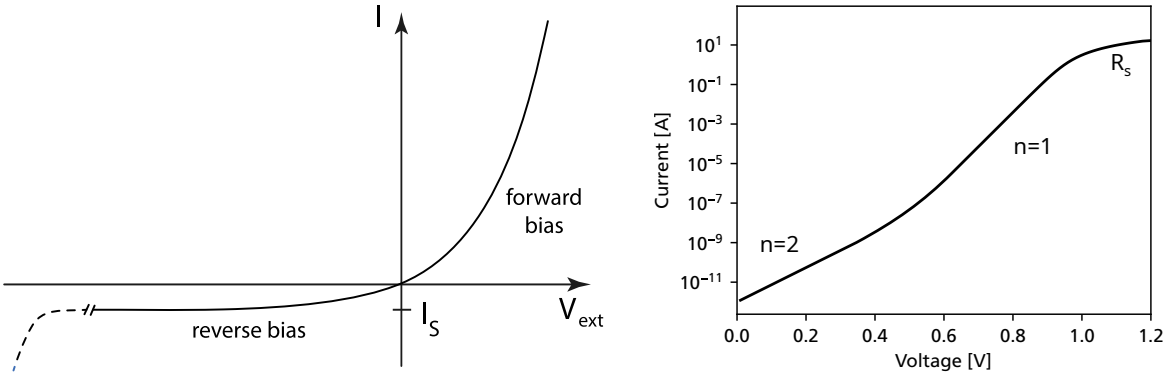

Figure 2.2.4: Left: Shockley diode equation. Taken from [57]. Right: Current-voltage characteristics of a diode in forward bias with different ideality factors and a series resistance R_s.

charge transport regimes. At low bias voltages, the recombination current (with an ideality factor of 2) dominates. At higher bias voltages and currents, the recombination saturates as all traps are filled, and the recombination length increases, and the diffusion current starts to dominate ($n = 1$). Real diodes will also always feature a series resistance R_s, which will limit the conduction in the limit of very high currents.

Electric Field in Reverse Bias

In a p-n junction with a constant doping, the electric field can be calculated using Poisson's equation

$$\vec{\nabla}^2 \cdot \phi = -\frac{\rho(\vec{x})}{\epsilon}. \tag{2.2.18}$$

Substituting the electric field as the gradient of the electric potential $\vec{E} = -\vec{\nabla} \cdot \phi$ and a charge density $\rho(\vec{x})$ given by a doping concentration $qN(\vec{x})$, yields

$$\vec{\nabla} \cdot \vec{E} = \frac{qN(\vec{x})}{\epsilon}. \tag{2.2.19}$$

Assuming a constant doping concentration $N(\vec{x}) = N_0$ and just one dimension, the electric field can be solved to be

$$E(x) = \frac{qN_0}{\epsilon}(w - x), \tag{2.2.20}$$

where w is the depletion width. The depletion width is defined such that the total voltage is equal to a bias voltage $V = V_{ext} + V_{bi}$

$$V = -\int_0^w E(x)\,dx = -\int_0^w \frac{qN_0}{\epsilon}(w-x)\,dx = \frac{qNw^2}{2\epsilon}. \tag{2.2.21}$$

This can be reformulated to specify the depletion width as a function of the bias voltage

$$w = \sqrt{\frac{2\epsilon(V_{bi}+V_{ext})}{qN}}. \tag{2.2.22}$$

For large bias voltages $V_{ext} \gg V_{bi}$, the depletion width will scale with the square root of the bias voltage, $w_d \propto \sqrt{V_{ext}}$. If the device is fully depleted, the electric field is offset by a constant value, in order to still fulfill Equation (2.2.21). Splitting up the bias voltage in the full depletion voltage V_{dep} and an over-voltage $\Delta V = V_{ext} + V_{bi} - V_{dep}$ allows rewriting the electric field as

$$E(x) = \frac{qN_0}{\epsilon}(d-x) + \frac{\Delta V}{d}. \tag{2.2.23}$$

with d the physical device thickness. The electric field $\Delta V/d$ is simply the electric field of parallel plates without any space charge.

Figure 2.2.5 illustrates this for a 50 µm thick 4H-SiC diode. Below the full depletion voltage (100 V), the electric field is linear and grows with the depletion width. After the full depletion, the electric field is still linear, but shifted upwards everywhere by an offset. Particle detectors are typically operated in a regime where the bias voltage is significantly larger than the full depletion, in order to ensure a uniform electric field and maximum charge carrier drift velocity in the entire detector.

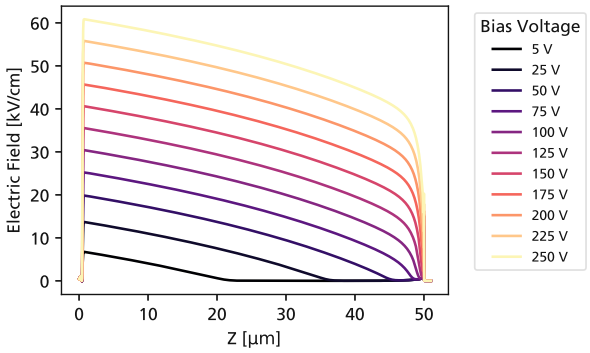

Figure 2.2.5: Simulated electric field inside a 50 µm thick 4H-SiC diode. The doping concentration (approximately $1 \times 10^{14}\,\mathrm{cm}^{-3}$) has been extracted from a C-V measurement and is non-constant as a function of the depth, which is why the electric field is not perfectly linear.

Capacitance-Voltage Characteristics

The depleted region in a semiconductor can be treated as a parallel-plate capacitor with area A and thickness w, where the capacitance is given by the well-known formula

$$C = \frac{A\epsilon_r\epsilon_0}{w}, \tag{2.2.24}$$

with ϵ_r the relative permittivity of the semiconductor and ϵ_0 the vacuum permittivity. For the example of 4H-SiC ($\epsilon_r = 10.3$ [61]), the capacitance per area for a thickness of 50 µm is equal to

$$\frac{C}{A} \approx 1.8\,\mathrm{pF/mm^2}. \tag{2.2.25}$$

The capacitance formula can be solved for the thickness of the depletion zone w

$$w = \frac{A\epsilon_r\epsilon_0}{C}. \tag{2.2.26}$$

As the depletion depends on the doping concentration of the device, the capacitance characteristic as a function of the voltage can be used to extract information about the device doping (known as capacitance-voltage, C-V-profiling) [62]. Taking the definition of capacitance (change in charge with change in voltage) yields

$$C = \frac{A\epsilon_r\epsilon_0}{w} = \frac{\mathrm{d}Q}{\mathrm{d}V} = \frac{qN(w)\mathrm{d}w}{\mathrm{dV}}, \tag{2.2.27}$$

where dQ has been written as a function of the local doping concentration $\mathrm{d}Q = qN(w)\mathrm{d}w$. Additionally, d$w$ can be expressed as a function of the capacitance (see Equation (2.2.26)), which yields

$$\mathrm{dw} = \mathrm{d}(A\epsilon_r\epsilon_0 C^{-1}) = -A\epsilon_r\epsilon_0 C^{-2}\mathrm{dC}. \tag{2.2.28}$$

Inserting into Equation (2.2.27) finally results in

$$\mathrm{dV} = \frac{qN(w)\mathrm{d}w}{C} \Leftrightarrow \mathrm{dV} = -qN(w)A\epsilon_r\epsilon_0 C^{-2}\mathrm{dC}/C. \tag{2.2.29}$$

which can be solved for the doping concentration $N(w)$ as a function of the measured capacitance

$$N(w) = \frac{-C^3}{qA\epsilon_r\epsilon_0}\left(\frac{\mathrm{dC}}{\mathrm{dV}}\right)^{-1} = \frac{2}{qA\epsilon_r\epsilon_0}\frac{\mathrm{d}(1/C^2)}{\mathrm{dV}}. \tag{2.2.30}$$

The second expression is commonly used to extract doping concentrations experimentally. Figure 2.2.6 shows this expression plotted as a function of the voltage. At the beginning, the slope is constant and proportional to the doping concentration. As soon as the depletion width reaches the geometrical limitations of the device, the $1/C^2$ curve will saturate. Depending on the manufacturing process, the depletion width is limited by different strategies, either by the physical extent of the device or by employing a highly doped buffer layer.

While capacitance-voltage profiling works well for extracting the doping of larger regions (such as the bulk doping), there are limitations for smaller features and rapidly changing doping concentrations [62]. The Debye length L_D provides a characteristic length over which the electric field induced by dopants (with concentration $p + n$) is screened by other charge carriers

$$L_D = \sqrt{\frac{k_B T\epsilon_r\epsilon_0}{q^2(p+n)}}. \tag{2.2.31}$$

If this length is on the same order of magnitude as the doping to be resolved (or even smaller), the effective doping is blurred, as the electric field of the dopants can not be fully screened and the assumption $\mathrm{d}Q = qN(w)\mathrm{d}w$ no longer holds. For 4H-SiC at room temperature typical values are $L_D = 384\,\mathrm{nm}$ for $(p+n) = 1\times10^{14}\,\mathrm{cm^{-3}}$ and $L_D = 12\,\mathrm{nm}$ for $(p+n) = 1\times10^{17}\,\mathrm{cm^{-3}}$.

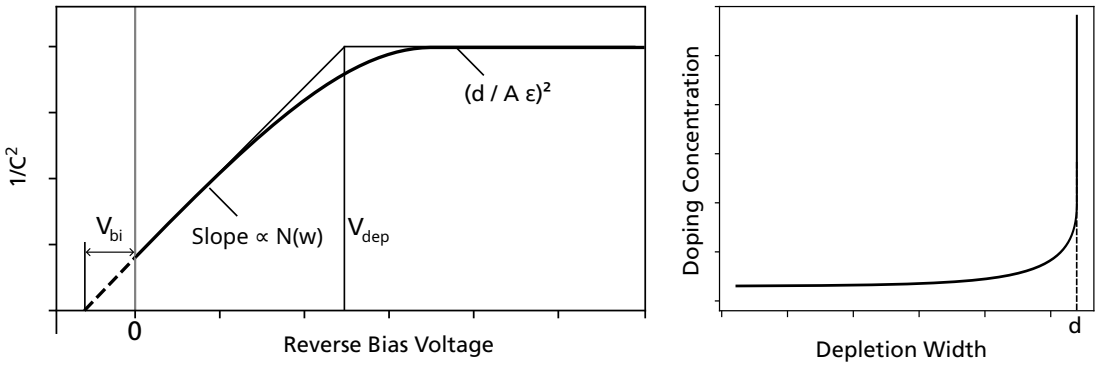

Figure 2.2.6: $1/C^2$ characteristics of a p-n junction. Before full depletion, the slope of $1/C^2$ (and therefore the doping concentration) is constant. At higher voltages, the depletion width reaches a maximum at the device thickness d, and the effective doping concentration increases accordingly.

2.2.3 Shockley-Reed-Hall Recombination

Crystal defects, whether introduced during the growth of the crystal or by radiation damage, can result in additional energy levels in the band diagram that can be occupied by electrons or holes, as depicted in Figure 2.2.7. Depending on the position of these defects, they can act as effective donors or acceptors. These energy levels can either be filled or empty, depending on their position and the charge carrier statistics inside the device. This process can be described by Shockley-Reed-Hall statistics [63, 64]. In thermal equilibrium, the generation rates for electrons and holes are given by [59]

$$R_e = n_T \sigma_e N_C e^{\frac{E_T - E_C}{k_B T}}, \tag{2.2.32}$$

$$R_h = n_T \sigma_h N_V e^{\frac{E_V - E_T}{k_B T}} \tag{2.2.33}$$

with n_T the number of traps, σ_e and σ_h the electron and hole capture cross-section, E_T the energy level of the trap and N_C, N_V the density of states in the conduction and valence bands. Intuitively, it can be seen that emission rates grow exponentially for electrons towards the conduction band (or holes towards the valence band). If the trap energy level is far away ("deep" traps, more than 0.1 eV away from a band edge), the emission rate will be very low and most charge carriers will stay inside the traps, therefore not being able to contribute to any current conduction. Due to the temperature dependency, trap levels and concentrations can be studied by measuring changes in electrical properties (such as the capacitance or current) as a function of the temperature, for example, in deep-level transient spectroscopy (DLTS) or thermally stimulated current (TSC) spectroscopy [7].

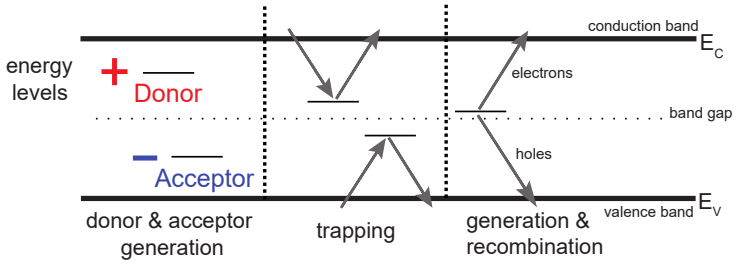

Figure 2.2.7: Generation and recombination in the Shockley-Reed-Hall model. Taken from [65].

2.2.4 Charge Carrier Mobility

Free charge carriers inside a semiconductor move according to the Lorentz force $\vec{F}$

$$\vec{F} = q\left(\vec{E} + \vec{V} \times \vec{B}\right) \tag{2.2.34}$$

for an electric field $\vec{E}$ and a magnetic field $\vec{B}$. In a semiconductor with a non-zero field, charge carriers would therefore continue accelerating without stopping. However, in reality, charge carriers are scattered by interacting with phonons, defects, or other charge carriers and lose part of their kinetic energy, resulting in a fixed drift velocity [61]. The relation of the drift velocity v and the electric field magnitude E can be expressed as

$$v = \mu(E) \cdot E\,, \tag{2.2.35}$$

where the factor $\mu(E)$ is the *charge carrier mobility*. At low electric fields, the mobility is dominated by interactions with phonons or impurities (dopants) [61]. At higher electric fields, charge carriers will approach a maximum value, the saturation velocity. Typically, both regimes are combined by using a model for the low-field mobility μ_{low} and a model for the case of high electric fields. Additionally, the mobility depends strongly on the temperature, generally increasing towards lower temperatures as phonon scattering is reduced [57]. In 4H-SiC, there exists an anisotropy in the charge carrier mobility parallel and perpendicular to the c-axis, which stems from the difference in effective electron and hole masses along the crystal axes. Care has to be taken to use measurements and models in the correct axis (parallel to the vertical c axis for detectors), or to apply a correction factor, typically around $\mu_{\perp}/\mu_{\parallel} = 0.83$ [61]. The low-field mobility for 4H-SiC can be described by a doping dependent model [66]

$$\mu_{\text{low}}(N) = \mu_{\text{min}} + \frac{\mu_{\text{max}} - \mu_{\text{min}}}{1 + (N/N_{\text{ref}})^{\alpha}}. \tag{2.2.36}$$

This model assumes a minimum and maximum mobility, and scales in between them using an exponential factor α and a reference doping concentration N_{ref}. The corresponding parameters for 4H-SiC are shown in Table 2.2, with the resulting mobility as a function of the doping concentration shown in Figure 2.2.8. At low doping concentrations (below 10^{15}cm^{-3}), such as typically found in particle physics detectors, the mobility is maximal.

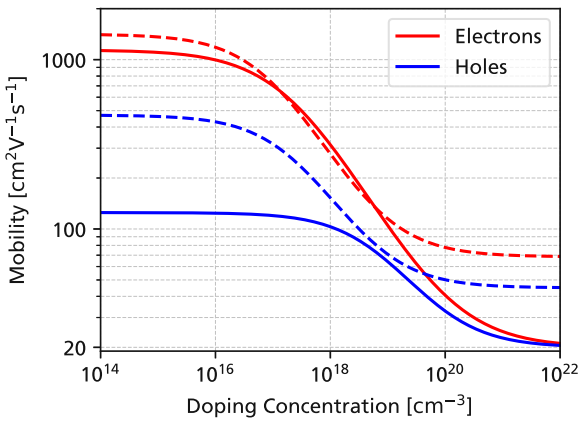

Figure 2.2.8: Low field mobility for 4H-SiC parallel to the c-axis [67, 68] (solid lines) and for silicon [69] (dashed lines) at room temperature.

The high-field mobility can be described in terms of the low-field mobility and the electric field E

$$\mu_{\text{high}}(E) = \mu_{\text{low}} \left(\left[1 + \left(\frac{\mu_{\text{low}} E}{v_{\text{sat}}} \right)^{\beta} \right]^{1/\beta} \right)^{-1} . \tag{2.2.37}$$

In this model, the charge carrier mobility is identical to the low-field mobility for low electric fields, until the charge carrier velocity converges to the saturation velocity v_{sat} at high electric fields (with the high-field mobility decreasing accordingly). The model parameters can again be found in Table 2.2, and the high-field mobility is plotted in Figure 2.2.9. The corresponding parameters for the low-field and high-field mobilities are listed in Table 2.2. For 4H-SiC, the high-field mobility starts to set in from electric fields of approximately $10\,\text{kV}\,\text{cm}^{-1}$, where the drift velocity of electrons starts to surpass that of silicon. Going to higher and higher electric fields shows a saturation of the drift velocity at electric fields around $100\,\text{kV}\,\text{cm}^{-1}$, whereas the velocity for holes is still increasing up to $1\,\text{MV}\,\text{cm}^{-1}$. This shows that while higher drift velocities than in silicon can be reached using silicon carbide, significant electric fields are required to reach those. If the doping concentration is non-negligible (or the detector has a considerable thickness), this will result in very high bias voltages, which would already lead to a breakdown for silicon devices, making the efficient operation of SiC detectors challenging.

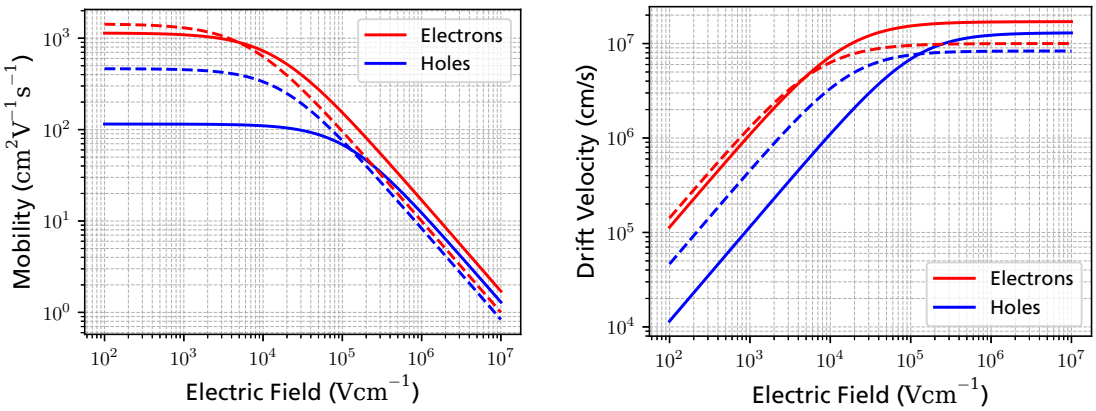

Figure 2.2.9: High-field mobility and resulting drift velocity for 4H-SiC parallel to the c-axis [70] (solid lines) and for silicon [71] (dashed lines) at room temperature. At electric fields above $10\,\text{kV}\,\text{cm}^{-1}$, the drift velocity of electrons in 4H-SiC exceeds that of silicon.

Parameter	Electrons	Holes
μ_{min}	$20\,\text{cm}^2\,\text{V}^{-1}\,\text{s}^{-1}$	$20\,\text{cm}^2\,\text{V}^{-1}\,\text{s}^{-1}$
μ_{max}	$1140\,\text{cm}^2\,\text{V}^{-1}\,\text{s}^{-1}$	$125\,\text{cm}^2\,\text{V}^{-1}\,\text{s}^{-1}$
N_{ref}	$2 \times 10^{17}\,\text{cm}^{-3}$	$6.4 \times 10^{18}\,\text{cm}^{-3}$
α	0.64	0.72
v_{sat}	$1.7 \times 10^7\,\text{cm}\,\text{s}^{-1}$	$1.3 \times 10^7\,\text{cm}\,\text{s}^{-1}$
β	1.1	1.2

Table 2.2: Parameters used to describe the low-field [67, 68] and high-field mobility [44, 70] in 4H-SiC.

2.2.5 Impact Ionization

At sufficiently high electric fields, charge carriers can accelerate to energies high enough between collisions that they can themselves ionize new electron-hole pairs. These newly created charge carriers can then generate further electron-hole pairs, leading to the creation of an avalanche. While this is carefully avoided in many semiconductor devices to avoid an uncontrolled breakdown, it can also be leveraged to multiply charge. For example, in Geiger-Müller tubes, avalanche breakdowns induced by ionizing particles are used to obtain a large charge multiplication ($> 10^5$), which results in large signals and allows for relatively simple readout electronics [57]. Charge multiplication is not only used in gas detectors, but also in semiconductors, in devices such as silicon photomultipliers [59] or low-gain avalanche diodes (see Section 2.9). For impact ionization, the expected gain in the number of charge carriers $\langle G \rangle$ can be defined as

$$\langle G \rangle = e^{\alpha l} \tag{2.2.38}$$

for a drift length l, and an *impact ionization coefficient* α. More generally, if the impact ionization coefficient changes with the electric field and position

$$\langle G \rangle = \int_0^l e^{\alpha(E(x))x} \, \mathrm{d}x. \tag{2.2.39}$$

A popular choice to describe the dependency of the impact ionization coefficient on the electric field is Chynoweth's law [72], which takes the form of $\alpha(E) = a \exp(-b/e)$, where a and b are (temperature-dependent) material constants. The character α is typically used for the impact ionization of holes, whereas for electrons, β is used. Okuto and Crowell [73] proposed a modification to Chynoweth's law, introducing an additional exponent m

$$\alpha(E) = a \cdot e^{-\left(\frac{b}{E}\right)^m}. \tag{2.2.40}$$

This model can be used to describe impact ionization in 4H-SiC, and the model parameters are given in Table 2.3 on the following page. Figure 2.2.10 plots the impact ionization coefficients for 4H-SiC compared to silicon. Opposite to silicon, the impact ionization coefficient for electrons is smaller than the one for holes ($\beta < \alpha$), which means that avalanches in 4H-SiC are mainly driven by hole multiplication. Additionally, the required electric field for significant impact ionization (critical electric field E_c) is one order of magnitude higher.

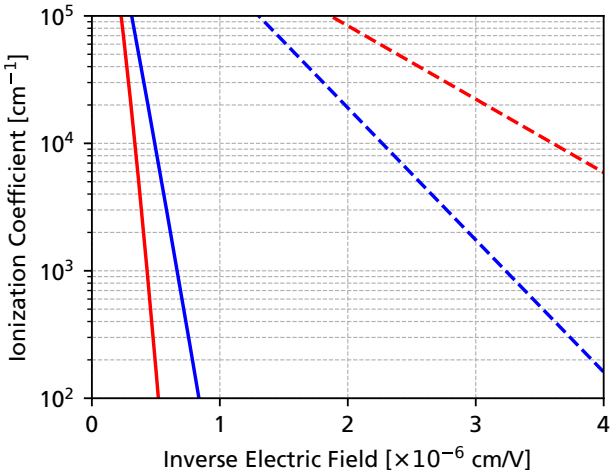

Figure 2.2.10: Impact Ionization coefficients for holes (blue) and electrons (red) in 4H-SiC [74] (solid lines, parallel to the c-axis) and silicon [75] (dashed lines) at room temperature.

The gain value $\langle G \rangle$ is an expectation value. Each individual charge carrier will undergo a statistically independent multiplication process, with the distribution of the total gain given by a Gamma distribution. For an integer number of charge carriers n, where the Gamma function is equal to $\Gamma(n) = (n-1)!$, the distribution of the Gain will be given by

$$G(x) = \frac{\alpha^n x^{n-1} e^{-\alpha x}}{(n-1)!}. \tag{2.2.41}$$

For a single charge carrier, this distribution corresponds to an exponential distribution. In the limit of a large number of carriers, this distribution will converge towards a Gaussian distribution (due to the central limit theorem).

Parameter	Electrons	Holes
a	$2.78 \times 10^6\,\mathrm{cm}^{-1}$	$3.51 \times 10^6\,\mathrm{cm}^{-1}$
b	$1.05 \times 10^7\,\mathrm{V\,cm}^{-1}$	$1.03 \times 10^7\,\mathrm{V\,cm}^{-1}$
m	1.37	1.09

Table 2.3: Impact ionization model in 4H-SiC parallel to the c axis at room temperature [74].

2.3 Precision Electrical Characterization Methods

Characterizing the properties of semiconductor devices is a crucial aspect of semiconductor manufacturing. While a large part of the industry works on verifying that devices work as intended (functional verification), there are many non-destructive techniques that can give detailed insights into the devices (such as doping or trap concentrations), that can then be used to adjust process parameters or to fine-tune simulations [62].

Characterizing silicon carbide presents special challenges in the laboratory. Due to the wide bandgap and extremely low number of thermally generated charge carriers in SiC, the typical device currents to be measured are extremely low, below 10 pA. Together with high voltages (> 200 V) that need to be used to fully deplete epitaxial layers, this presents significant measurement challenges that need to be addressed using special precision measurement techniques. This section introduces these techniques, required for low-level DC measurements (Section 2.3.1) and for impedance (capacitance) measurements with very high bias voltages (Section 2.3.2). Valuable resources on semiconductor characterization include the *Keithley Low Level Measurements Handbook* [76], *Keysight Parametric Measurements Handbook* [77], and *Keysight Impedance Measurement Handbook* [78], which are all published by manufacturers of semiconductor characterization equipment.

2.3.1 Low Level DC Current Measurements

When measuring devices with very large resistances (such as a diode in reverse bias), leakage paths can form where the current does not flow through the device under test (DUT), but through a part of the experimental setup (such as mechanical components) or cable insulation, impacting the measurement accuracy. For example, the resistance between individual traces on a PCB is typically in the range of tens of GΩ, but can significantly decrease with surface contamination [76]. If high quality insulators, such as Teflon or sapphire are used, these leakage currents can be minimized (given that the materials are handled with care), however, it is generally not feasible to reach resistances above 1 TΩ in practical laboratory settings.

Guarding

In order to measure very small currents, special precautions need to be taken. Generally, the limiting factor in the measurement of low currents (or high resistances) is the insulation (resistance) of the measurement cable itself. Assuming a cable resistance $R_{\text{cable}} = 300\,\text{G}\Omega/\text{m}$, a 1 m long cable with an applied voltage of 100 V already results in a current of

$$\text{I}_{\text{leak}} = \frac{100\,\text{V}}{300\,\text{G}\Omega} = 0.33\,\text{nA}. \tag{2.3.1}$$

As there are physical limitations in the insulation performance that can be obtained in practice, the concept of *guarding* is used for the most demanding applications. This is implemented using triaxial cables, as depicted in Figure 2.3.1. Here, the central conductor is surrounded by a guard conductor

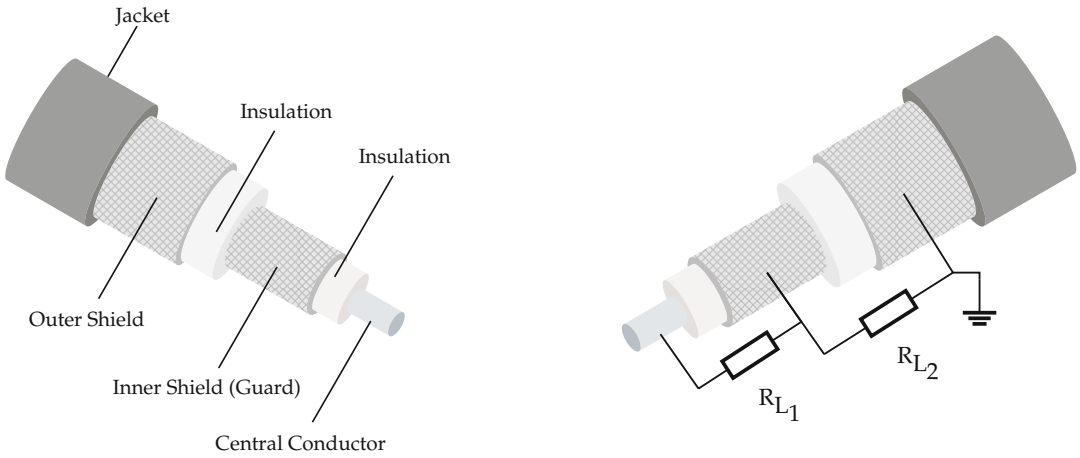

Figure 2.3.1: Components of a triaxial cable (left) and equivalent circuit (right).

(separated by a high-performance insulator such as Teflon). Because the guard and the central conductor are at the same potential, the current flowing between the inner conductor and guard is zero

$$\text{I}_{\text{L}_1} = \frac{\text{V}_{\text{central}} - \text{V}_{\text{guard}}}{\text{R}_{\text{L}_1}} = \frac{0\,\text{V}}{\text{R}_{\text{L}_1}} = 0\,\text{A}. \tag{2.3.2}$$

A further shield is located outside of the guard at ground potential, in order to allow for safe handling of the cable and to shield it from external noise. Figure 2.3.2 shows the circuit implementation of an SMU driving a guarded triaxial cable. The voltage source and ammeter use a buffer ($\times 1$) amplifier to drive the current of the guard such that the voltage closely follows the voltage of the central conductor, and no current can flow through R_{L_1} The leakage current between R_{L_2} is driven by the buffer amplifier and therefore is not measured by the ammeter. Guarding can also be applied to test fixtures, by using a driven guard (as for triaxial cables), or by measuring the leakage current by an additional instrument and subtracting it from the measurement, further detailed in Section 4.1.

Source-Measure Units and Electrometers

Source-measure unit (SMU) instruments can source voltage (or current) and measure while doing so, which can simplify testing circuits. Almost all SMUs can operate in all four *quadrants*, that means negative and positive voltages, as well as sourcing negative or positive currents.

For the most sensitive measurements, where the lowest noise floor and accuracy is required, *electrometers* are used. Electrometers, depicted in Figure 2.3.3, are more sensitive, have a higher input impedance

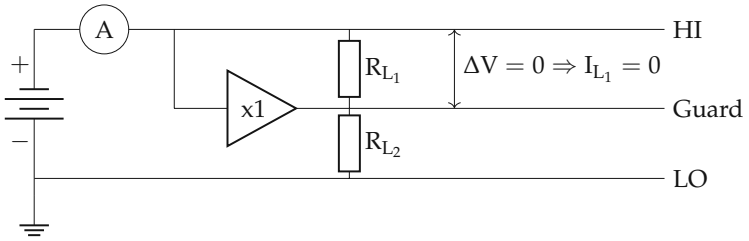

Figure 2.3.2: Triaxial cable connections and buffer amplifier of a triaxial SMU.

and present a lower voltage burden than regular digital multimeters (DMMs) or SMUs [76]. Most modern electrometers are based on a feedback ammeter circuit, where an operational amplifier is used together with a feedback resistor to convert the input current to a voltage. This has multiple advantages over a shunt ammeter (where simply a voltage drop over a resistor is measured). First, the gain added by the operational amplifier reduces the general noise levels and allows for more precise measurements. Second, by using an operational amplifier with a very low input current (such as the Texas Instruments LMP7721 with an input current of 3 fA [79]), the voltage drop over the feedback resistor is extremely low, leading to negligible *voltage burden* even for the most challenging applications. Finally, by replacing the feedback resistor by a capacitor, the same instrument can be used to measure charge instead of current. This is commonly used to read out ionization chambers in radiotherapy, with extremely high accuracy. It can also be used to measure very small currents by integrating the current over long timescales.

(a) Keithley 2400 series SMU [80] (b) Keithley 6500 series electrometer [81]

Figure 2.3.3: Source-measure units and electrometers manufactured by Keithley Instruments.

2.3.2 AC Impedance Measurements

In the simplest terms, a complex impedance Z can be measured by applying a known AC voltage V and measuring the AC current I,

$$Z = \mathrm{V}/\mathrm{I}. \tag{2.3.3}$$

In a real measurement, the measured impedance will never exactly correspond to a "pure" capacitance C or a pure inductance L, and therefore the phase information of the current needs to be acquired as well. For measurements of electronic components (either discrete or on-chip), the component can have unwanted parasitic contributions from other component types. For example, a capacitor might have a series resistance, or an SMD resistor might have unwanted parasitic inductance at high frequencies. Therefore, to describe the measured impedance, an equivalent circuit model is chosen, as depicted in Figure 2.3.4. Typically, two-component equivalent circuit models are used, with a component in parallel or series with another. Other representations also exist, for example, splitting the impedance into its real and imaginary parts (or the inverse of them, respectively). Most instruments measuring AC impedance have a set of circuit models built-in, and are referred to as LCR-meters, indicating the ability to obtain inductance, capacitance, or resistance values (although they all measure the complex impedance).

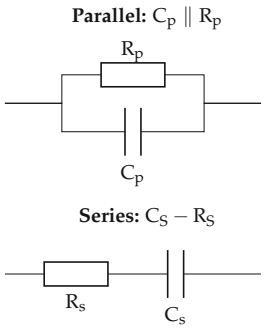

Model		
Z, Θ	$\lvert Z\rvert$	$\Theta = \operatorname{atan}(X/R)$
R + jX	$R = \mathrm{Re}(Z)$	$X = \mathrm{Im}(Z)$
G, B	Re(1/Z)	Im (1/Z)
Cp - Gp	$C_p = 1/(\omega\lvert Z\rvert \sin(\Theta))$	$G_p = 1/(\lvert Z\rvert \cos(\Theta))$
Cs - Rs	$C_s = 1/(\omega X)$	$R_s = R$
Cp - D	$C_p = 1/(\omega\lvert Z\rvert \sin(\Theta))$	$D = 1/(\omega R C_p)$
Cs - D	$C_s = 1/\omega X$	$D = R/X$
Y, Θ	$\lvert Y\rvert = 1/\lvert Z\rvert$	$\Theta = \operatorname{atan}(B/G)$

Figure 2.3.4: Commonly used equivalent circuit models and representations of the complex impedance.

In order to measure impedance, modern LCR meters make use of an *auto-balancing bridge* [78], depicted in Figure 2.3.5. At the *high* input, an AC voltage is driven at H_c, with the voltage measured at H_p. Together with the known resistance R_s, this determines the I_1 current flowing into the device under test (DUT). On the other side, the instrument is connected through an operational amplifier via L_p, which forces the potential of L_p to 0 V. The output of the operational amplifier therefore drives a current equal to I_1 into L_c through a feedback ranging resistor R_2 (i.e., automatically balancing I_1). By measuring the voltage V_2 over a known ranging resistor, the impedance of the device can be obtained as

$$Z = \frac{V_1}{I_2} = \frac{V_1 R_2}{V_2}. \tag{2.3.4}$$

The virtual ground in an auto-balancing bridge has the advantage that no voltage drops in the "low" side connections (L_p and L_C), removing the effect of parasitic cable inductance or capacitance.

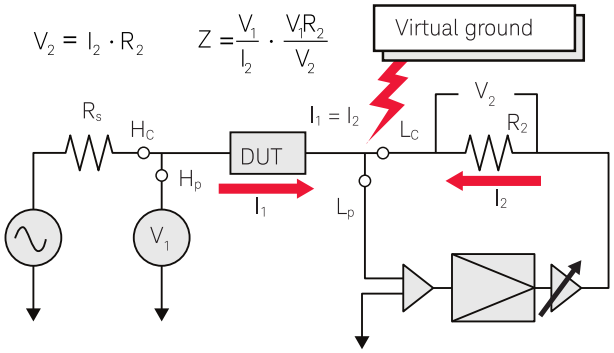

Figure 2.3.5: Auto-balancing bridge used in modern LCR meters. Taken from [77].

Connection Compensation

Because cables and test fixtures are not ideal components and have a resistance, parasitic inductance, and parasitic capacitance themselves, they can distort measurements, especially for very low or very high impedances. The effect of cable parasitics and other contributions can be formulated as an equivalent circuit with a parallel and series impedance to the true impedance of the device under test Z_{DUT}, as shown in Figure 2.3.6. If the series impedance Z_S and parallel admittance $Y_O = 1/Z_0$ are known, the measured impedance Z_m can be corrected, and the DUT impedance can be obtained.

$$Z_{\mathrm{DUT}} = \frac{Z_m - Z_s}{1 - (Z_m - Z_s)Y_O}. \tag{2.3.5}$$

The series impedance can be measured by replacing the DUT with a short connection, while the parallel admittance can be measured by removing the DUT entirely (assuming $Z_s \ll 1/Y_O$). LCR meters can typically store these measured impedances and correct for them automatically, referred to as open and short corrections.

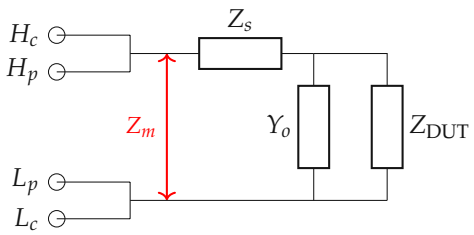

Figure 2.3.6: Circuit model for connection compensation.

Decoupling Boxes

In capacitance-voltage (C-V) measurements, a DC voltage is applied together with an AC voltage, which probes the impedance of a device under test. In order to split and separate the AC and DC components, a so-called "bias-tee" is used, which is composed of a high-pass filter for the AC and a low-pass filter for the DC. Most LCR meters feature an integrated bias-tee and DC voltage source as a hardware option, which can operate in ranges up to ± 30 V [77]. However, if higher bias voltages are required (for example, in C-V measurements of a diode-based particle detector), then an external bias-tee needs to be used. In sensor characterization for high-energy physics, such high-voltage bias-tees are commonly called *decoupling boxes*, as they decouple the DC component from the signal and protect the LCR meter from high voltages. Section 4.1.8 will discuss the challenges associated with bias-tees that can handle very high voltages (> 1 kV).

2.4 Interaction of Ionizing Radiation

The Bethe-Bloch formula [82] describes the mean energy loss $\left\langle -\frac{\mathrm{d}E}{\mathrm{d}x} \right\rangle$ of massive ionizing particles inside a material as a function of the distance x. It is given by

$$\left\langle -\frac{\mathrm{d}E}{\mathrm{d}x} \right\rangle = \frac{4\pi n z^2}{m_\mathrm{e} c^2 \beta^2} \left(\frac{e^2}{4\pi\epsilon_0} \right)^2 \left[\ln\left(\frac{2 m_\mathrm{e} c^2 \beta^2}{I(1-\beta^2)} \right) - \beta^2 \right], \tag{2.4.1}$$

where e is the elementary charge, m_e is the electron mass, ϵ_0 the vacuum permittivity, z the charge of the incoming particle, β it's velocity in terms of the speed of light c and I the mean ionization energy of the medium. The electron density n inside of the medium (which the impinging particle ionizes), can be calculated as $n = {}^{N_A Z \rho}/_{A M_\mathrm{u}}$ with N_A and M_u Avogadro's and the molar mass constants respectively, and Z, A, ρ the atomic number, atomic mass and density of the medium. Figure 2.4.1 shows the energy loss of muons as a function of their energy. Two main regions of interest can be identified: At low momentum ($< 10\,\mathrm{MeV\,c^{-1}}$), the ${}^1/_{\beta^2}$ in Equation (2.4.1) dominates the energy loss. At higher particle momenta, the energy loss decreases until a minimum is reached. Particles at this minimum are also called *Minimum Ionizing Particles (MIP)*. Except for a hydrogen target, the energy loss of MIPs in all other materials is very similar, inside a range of $1 - 2$ MeVcm^2/g, increasing with the atomic number of the material. For common semiconductor and gaseous detector materials, a value of 2 MeVcm^2/g is a very good estimate [59]. This minimum ionization (energy loss) determines the smallest signal that is realistically expected in the detection of ionizing particles and can be used as a reference standard.

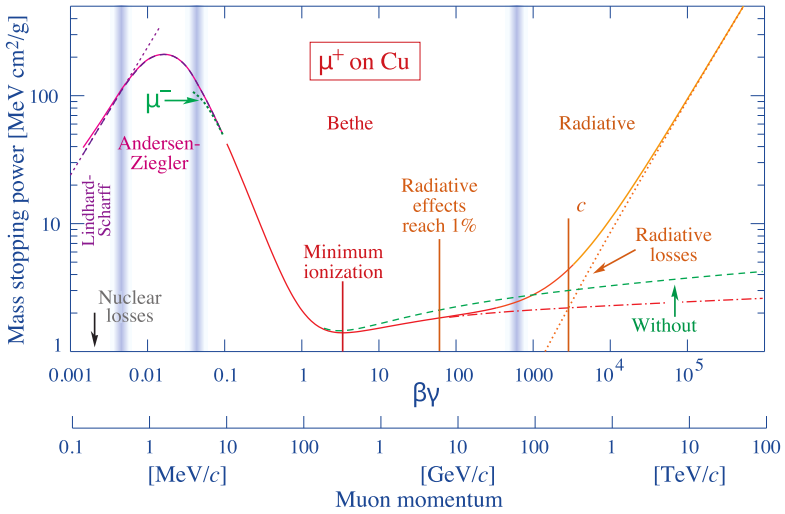

Figure 2.4.1: Energy loss of muons in copper as a function of the momentum. Taken from [83].

For mixtures of different materials, such as SiC, Bragg's additivity rule states that the mean stopping power of the individual materials can be added together as [83]

$$\left\langle \frac{\mathrm{d}E}{\mathrm{d}x} \right\rangle_{\text{total}} = \sum_i w_i \cdot \left\langle \frac{\mathrm{d}E}{\mathrm{d}x} \right\rangle_i , \tag{2.4.2}$$

with w_i the mass fraction of the i-th element. However, corrections have to be applied, such as the mean ionization energy I being different for compounds of elements, among other effects [83, 84]. Ideally, however, tables with measured stopping power should be used for mixtures of elements if they are available.

2.4.1 Energy Loss Fluctuations

The Bethe-Bloch equation ((2.4.1)) describes the *mean* energy loss. However, the energy loss is a stochastic process, and it is worthwhile to investigate the energy loss distribution, especially for thin absorbers, where the number of interactions of a particle experiences is limited. As shown in Figure 2.4.2, the energy loss in a thin absorber is a very asymmetrical distribution, because there exists a probability for a very high energy transfer in an individual interaction, for example by δ-electrons. The first analytical description of this process was given by Landau [85] and later extended by Vavilov [86]. Vavilov introduced a parameter κ

$$\kappa = \frac{\xi}{T_{\max}} \tag{2.4.3}$$

with ξ given as

$$\xi = \frac{1}{2} K \frac{Z}{A} \rho \frac{z^2}{\beta^2} \delta x , \tag{2.4.4}$$

which describes the shape and asymmetry of the energy loss distribution. For thick absorbers ($\kappa \gtrsim 1$), the distribution converges to a symmetric Gaussian (due to the central limit theorem). For thin absorbers ($\kappa \approx 0$), the energy loss distribution is asymmetric and can be described by (under some simplifying assumptions [57]) by the *Landau distribution* f_L

$$f_L(\lambda) = \frac{1}{\pi} \int_0^\infty e^{-t \ln(t) - \lambda t} \sin(\pi t). \tag{2.4.5}$$

Due to the long tail of the energy loss distribution, the mean of the distribution is heavily affected by fluctuations in the tail, and in practice, the most-probable value of the distribution might be a better measure of the expected energy loss in a sensor [57]. For very thin detectors (less than $\sim 10\,\mu m$), the Landau-Vavilov theory can fail to properly describe the energy loss. Here, numerical simulations (performed, for example, by Bichsel [87]) have to be employed to correct for factors such as the energy levels of the shell electrons.

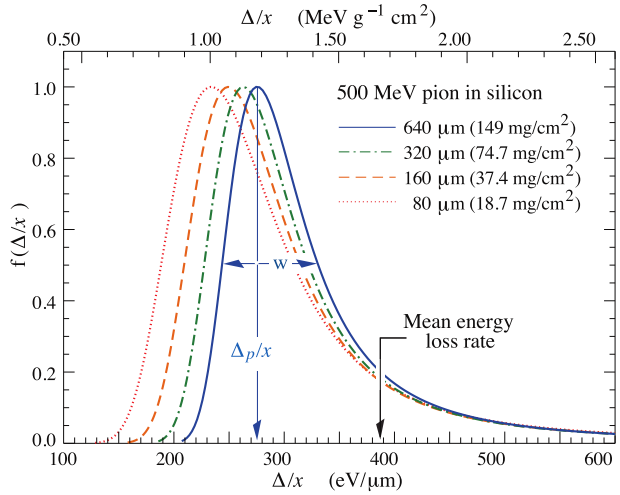

Figure 2.4.2: Energy loss distribution for a 500 MeV for different silicon detector thicknesses [83]. The distribution features a very long asymmetric tail.

2.4.2 Thick Absorbers

For a particle with sufficiently low energy (or a sufficiently thick absorber), the particle energy will be completely absorbed. In order to obtain the energy loss as a function of distance, the Bethe-Bloch equation (Eq. 2.4.1) can be integrated, resulting in the curve depicted in Figure 2.4.3. This assumes that the particle loses only energy through ionization or atomic excitation and is only valid for lower energy hadrons, where the range is smaller than the nuclear interaction length (continuous-slowing down approximation [83]). When the particle reaches a low momentum ($< 10\,\mathrm{MeV\,c^{-1}}$), the $1/\beta^2$ term dominates, and the energy loss per unit length rapidly increases. This results in a "peak" of energy deposition at the end of the particle's travel, known as the *Bragg* peak. The Bragg peak has applications in medical physics (see Section 2.5), as the energy loss in the Bragg peak is very localized and can be used to treat tumors in a localized manner.

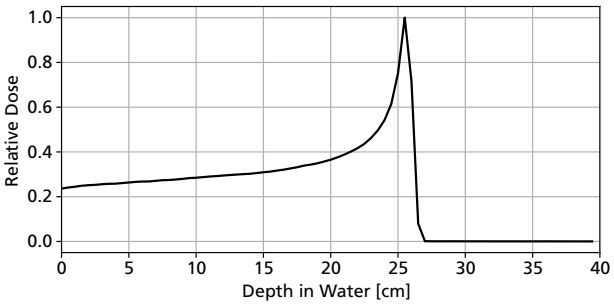

Figure 2.4.3: Bragg curve for 200 MeV protons in water. Taken from [88].

Under the continuous-slowing-down approximation, the *range* R of a particle may be defined by the distance required until it has lost all its energy

$$R = \int_0^E \left\langle \frac{\mathrm{d}E}{\mathrm{d}x} \right\rangle^{-1} \mathrm{d}E \tag{2.4.6}$$

One thing to note is that this range is the *expected* range, as the Bethe-Bloch equation describes the *expected* energy loss. In practice, statistical fluctuations in the energy loss can lead to energy straggling, where different particles lose different amounts of energy, even though the thickness of the absorber is fixed. If the particles are stopped completely, the energy straggling corresponds to range straggling, which can be an issue in radiotherapy (if a tumor is missed or a sensitive organ is hit).

2.4.3 Interaction of Photons

The absorption of photons inside 4H-SiC can by described by the *Beer-Lambert*–Law [89, 90]

$$I(x) = I_0 \cdot e^{-\alpha x}, \tag{2.4.7}$$

where the intensity I_0 is decreased by an absorption coefficient α with the distance inside the material x. The absorption coefficient α is wavelength-dependent, and is depicted for 4H-SiC in Figure 2.4.4a. Because SiC has an indirect bandgap, the probability of photon absorption is relatively small (compared to a direct bandgap, as discussed in Section 2.2.1), evidenced by the weak absorption of UV light in SiC with a slope of $\alpha \propto E^2$ [91]. Figure 2.4.4b shows the absorbed fraction of 370 nm light in 4H-SiC for typical detector thicknesses. A length of around $\lambda = 240\,\mu\mathrm{m}$ is required to reduce the transmitted intensity by a factor of $1/e$. If no impurities are present in the crystal, 4H-SiC appears transparent at visible wavelengths, similar to diamond. The typical greenish color of 4H-SiC wafers manufactured by the power electronics industry is a result of light absorption by nitrogen impurities (doping).

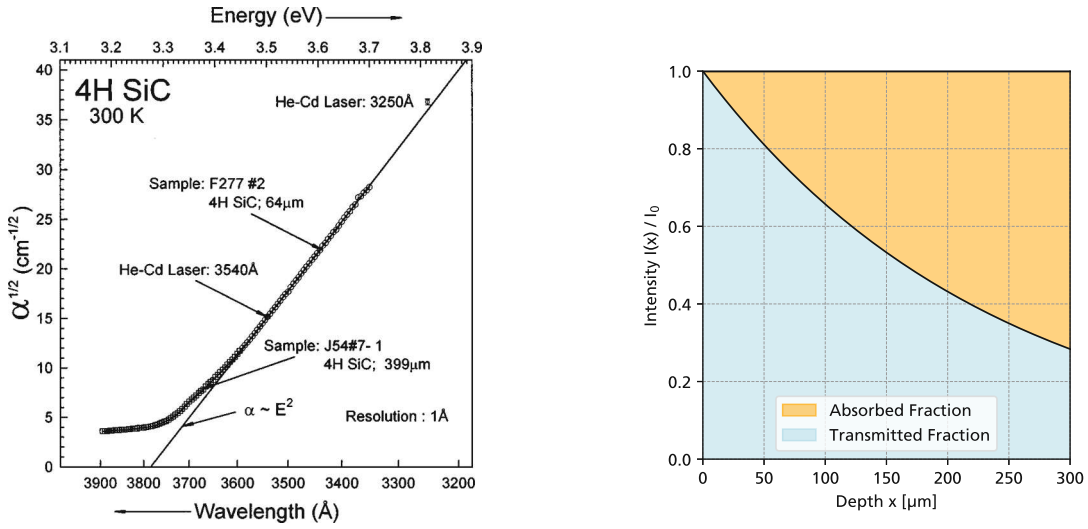

(a) (b)

Figure 2.4.4: Left: Measured square root of the absorption coefficient α in 4H-SiC as a function of the wavelength [92]. Reproduced with permission. Right: Absorbed and transmitted light for UV light at 370 nm ($\alpha \approx 42\,\mathrm{cm}^{-1}$) in 300 µm 4H-SiC.

2.4.4 Electron-Hole Pair Creation by Ionizing Radiation

As highlighted in the previous sections, charged particles or photons lose energy inside a material, which then creates electron-hole pairs. For a given deposited energy E, the *ionization energy* ϵ_i (also referred to as the *electron-hole pair creation energy*) is simply the ratio of the number of created charge carriers n per deposited energy E

$$n = \frac{E}{\epsilon_i}. \tag{2.4.8}$$

The ionization energy is a material constant, and Table 4.4 shows an overview of ionization energies for common materials used in particle physics detectors. Generally, the higher the bandgap, the higher the ionization energy.

A linear relationship between ionization energy and bandgap has been proposed by Shockley [94] and later expanded upon by Klein [93], commonly referred to as *Klein's relation*, depicted in Figure 2.4.5. While Klein's relationship is a good way to get an initial guess for materials where the electron-hole pair creation energy is not yet known, the data has not been controlled for material quality or temperature, and predictions using this can be inaccurate [95]. For detecting ionizing radiation, a lower ϵ_i is advantageous, as more charge will be available to be read out for the same energy deposition. However, semiconductors with a lower ionization energy also have smaller band gaps, leading to increased leakage currents. Therefore, a compromise between ionization energy and bandgap has to be found depending on the specific application, or detectors with a small bandgap need to be cooled down to cryogenic temperatures (such as HPGe-based detectors) [59]. As the ionization energy depends on the bandgap, it can also be affected by the temperature. For the example of 4H-SiC, the ionization energy decreases from around 7.8 eV to 7.6 eV going from room temperature (300 K) to 750 K [23].

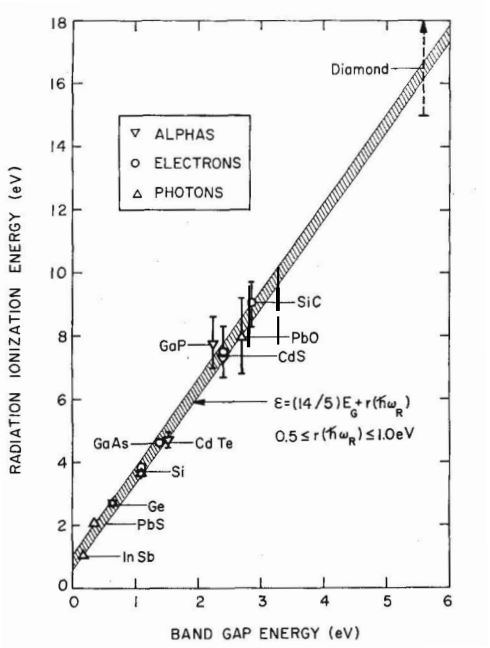

Figure 2.4.5: Klein's relation [93]. Reproduced with permission.

Material	ϵ_i	Material	ϵ_i
Si	3.62 eV	GaN	8.9 eV
4H-SiC	7.83 eV	Air	33.7 eV
Diamond	13 eV	Ge	2.96 eV

Table 4.4: Electron-hole pair creation energies for common materials [14, 46, 56, 83, 96].

2.5 Ion Therapy

Ion therapy is the treatment of cancer (or other diseases) by destroying cells using ionizing radiation deposited by high-energy ions in a patient. Compared to the more commonly used photon therapy, the interaction of ions with matter (inside the patient) is very different, as discussed already in Section 2.4. Heavy particles (such as protons or carbon ions), specifically, have a high linear energy transfer (LET), meaning that they lose a large amount of energy per unit length. Coupled together with the Bragg-peak effect (see Section 2.4.2), this allows to deliver a very high and localized dose to tumor tissue, which yields a two-fold improvement: The higher LET can destroy cancer cells more effectively (an increased *relative biological effectivness, RBE* compared to photons [97]), and, the Bragg peak reduces dose to healthy organs (or organs at risk, i.e. especially sensitive to radiation) at the entry of the beam in the patient, which allows for increasing the dose delivered to the tumor. The different dose-depth profiles for photons and proton/carbon ions are depicted in Figure 2.5.1. However, ion therapy is not without limitations. Due to the much heavier particles involved (compared to the electron accelerators used to generate photon beams), the acceleration is non-trivial and typically requires circular accelerators to reach energies sufficiently high to penetrate deep enough into the patient. Compared to photon radiation therapy, ion therapy machines have significantly higher capital costs and higher operational costs [98].

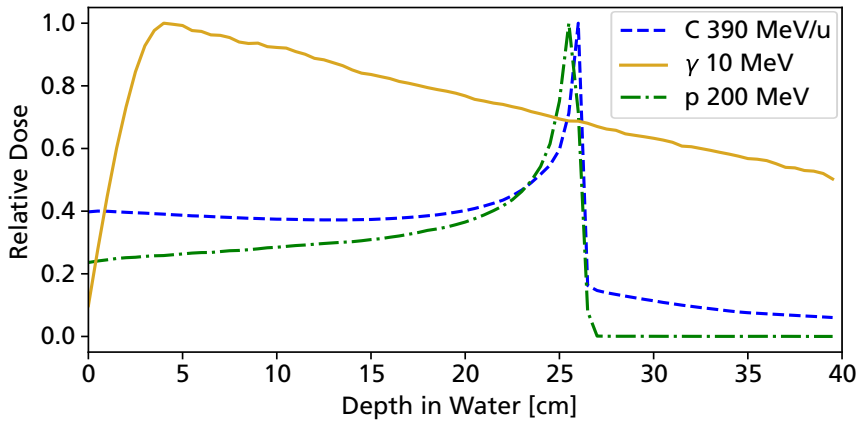

Figure 2.5.1: Normalized dose-depth curves for photons and ions in water, adapted from [88]. Ion therapy shows a pronounced peak (the Bragg peak), while in photon therapy, the dose at the entrance of the patient is highest, and a significant dose is delivered to tissue behind the tumor.

2.6 Radiation Damage

When ionizing radiation reacts with matter, not only can it transfer energy to the electrons of an atom (ionization), but it can also transfer momentum to the nucleus. If the energy transfer exceeds the displacement threshold of the atom in a lattice, it can be displaced from its position in the crystal, forming an interstitial and leaving a vacancy (an empty site in the lattice). These defects in the lattice constitute energy levels and can trap or emit charge carriers, strongly affecting and possibly degrading the electrical performance of a semiconductor.

2.6.1 Non-Ionizing Energy Loss

The fraction of energy lost by highly energetic particles that does not go into ionizing electrons of atoms is known as the non-ionizing energy loss (NIEL). Similarly to the ionizing energy loss, the NIEL can be computed using theoretical approaches and simulations or measurements, depicted for silicon in Figure 2.6.1. The NIEL hypothesis [99] states that the effective radiation damage is independent of particle properties that were used in the irradiation and scales only with the non-ionizing energy loss. This allows for radiation damage from different particle types at different energies to be compared with each other, which is a very important result, as no two irradiation facilities have the exact same particle type and energy spectrum.

The NIEL hypothesis has been widely validated in silicon and is used in high-energy physics to formulate radiation hardness requirements. However, there are certain areas where the NIEL hypothesis fails to be accurate. For the example of protons, low energies (10 MeV) will result in a homogeneous distribution of point defects, while higher energies (24 GeV) can create significant defect clusters [100]. Depending on the specific defect type, the microscopic structure of the defects can have a large influence on the electrical properties. Nevertheless, NIEL scaling is a widely used tool for studying radiation damage in silicon detectors and provides a foundation for comparing different irradiation types (even if the quantitative comparison might be inaccurate in some cases). While the NIEL equivalent depends on the material being irradiated (as the atomic cross-sections and displacement thresholds change), a common choice in the high-energy physics community is to use the NIEL equivalent in silicon.

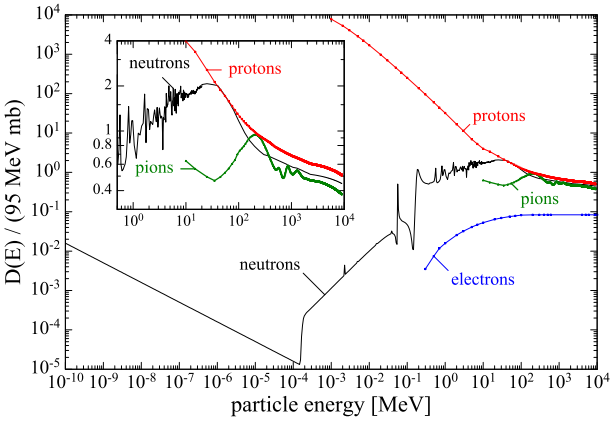

Figure 2.6.1: Non-ionizing energy loss for different particles in silicon. The energy loss has been normalized to the energy loss of 1 MeV neutrons. Taken from [7].

2.6.2 Effect of Radiation-Induced Defects in 4H-SiC

Defect Types in Silicon Carbide

When atoms are knocked out of the lattice in 4H-SiC, multiple defects can materialize, as depicted in Figure 2.6.2. Empty lattice sites leave over a vacancy, and atoms that have been kicked out of the lattice form an interstitial (not aligned with the crystal lattice). As SiC consist of both carbon and silicon, vacancies (V_{Si}, V_C) and interstitial (Si_i, C_i) are possible for both atoms, with differing electrical properties. If a carbon atom replaces a silicon atom in the lattice (C_{Si}, or other way around, Si_c) an antisite is formed. These can occur in pairs (Si_c-C_{Si}), although it is also possible that one of the antisite pairs is not occupied (antisite-vacancy pair). If different impurities are used for doping (such as nitrogen, boron, etc.), *extrinsic* defects are also possible, but they have been omitted from Figure 2.6.2. Figure 2.6.3 shows the energy levels and charge states of traps associated with these crystal defects.

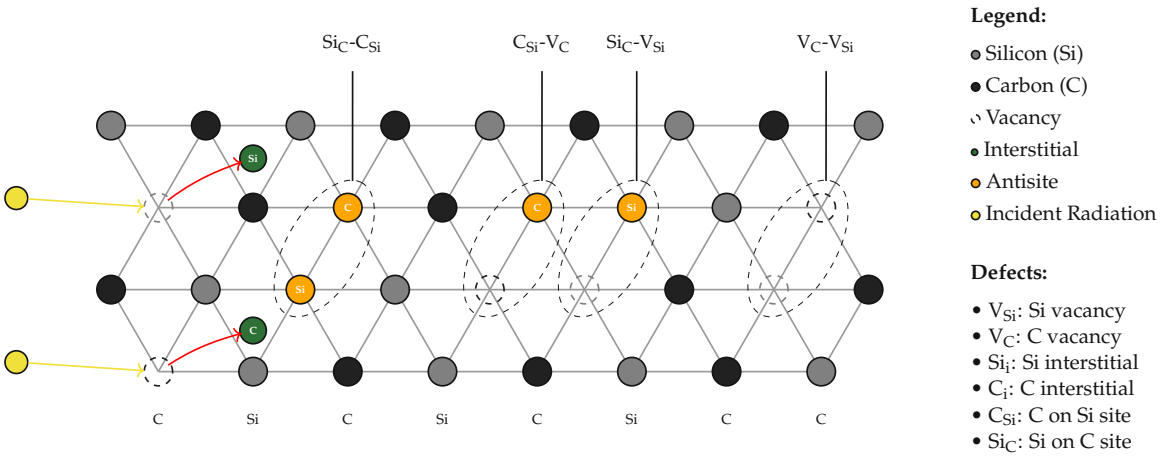

Figure 2.6.2: Simplified overview of the most important defect types in 4H-SiC. The same defect type can manifest at different crystal lattice sub-sites, resulting in different electrical behavior [101].

An in-depth discussion of these defects can be found in [101]. Separate to the other defects, the carbon vacancies Z_1 / Z_2 and EH_6 / EH_7 are notable, as they occur already in unirradiated material (in concentrations of about 10^{11}-10^{13}cm^{-3}) and therefore must originate from the crystal growth and processing [102]. Because the energy levels of these traps are deep (shallow traps typically being only 0.1 eV away from the band edges), they can trap free charge carriers, while the probability of thermal emission is extremely low (compare to Section 2.2.3), significantly impacting the conductivity and charge carrier lifetime. For this reason, $Z_{1,2}$ is often referred to as a "life-time killer" [101] and carries the main responsibility of charge collection losses in 4H-SiC detectors [103, 104].

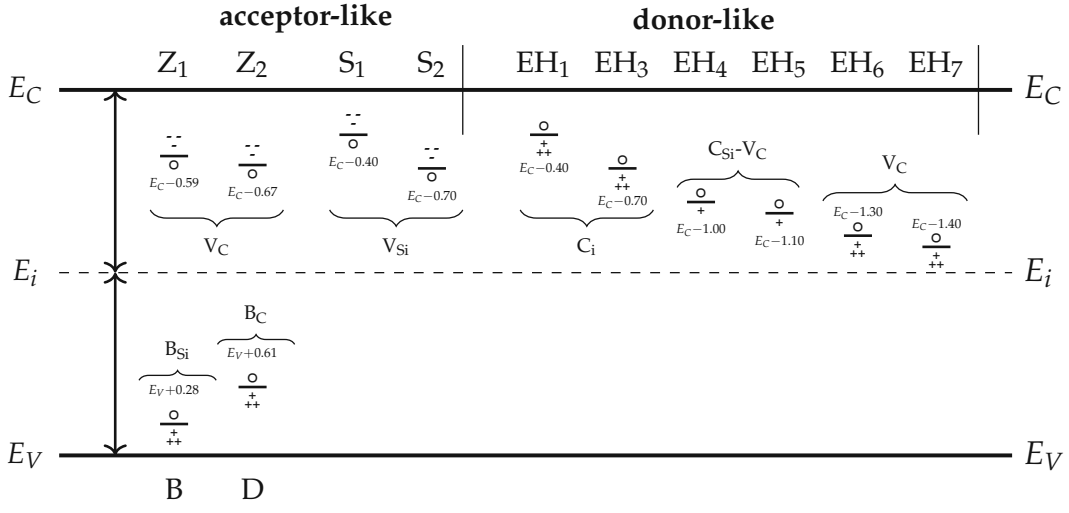

Figure 2.6.3: Overview of electrically active defects in 4H-SiC, with energy levels and charge states from [101] (and references therein). The solid line indicates the energy level, and the charge states are indicated by negative (−) and positive (+) charges, or a neutral charge state (○).

Current Generation by Electrical Defects

As discussed in Section 2.2.3, energy levels in between the valence and conduction band can act as a "ladder", capturing electrons from the valence band and emitting them to the conduction band, therefore resulting in a charge carrier generation. This increased current ΔI can be described as

$$\Delta I = \alpha \Phi_{\text{eq}} V \,, \tag{2.6.1}$$

where α is the *current-related damage rate*, Φ_{eq} the irradiation fluence (normalized to 1 MeV equivalent neutrons according to the NIEL hypothesis) and V the volume of the depletion zone [7]. In silicon, relatively shallow trap levels exist, which can act as generation-recombination centers, leading to an α of $3.99 \times 10^{-17}\,\text{A}\,\text{cm}^{-1}$ [7]. This results in significant leakage currents, which is why silicon detectors typically need to be cooled in high radiation environments, in order to keep noise tolerable and prevent thermal runaway.

However, for 4H-SiC, the majority of the radiation-induced traps are deeper in the bandgap (and the bandgap is much larger as well), which means that current generation by the SRH mechanism is orders of magnitude less effective [14]. This allows 4H-SiC detectors to be operated without any cooling, even after irradiation to high fluences [105]. The reduction in charge carrier lifetime reduces the current to very low levels after irradiation, as depicted in Figure 2.6.4. At high irradiation fluences, the current in forward bias is almost identical to the current in reverse bias.

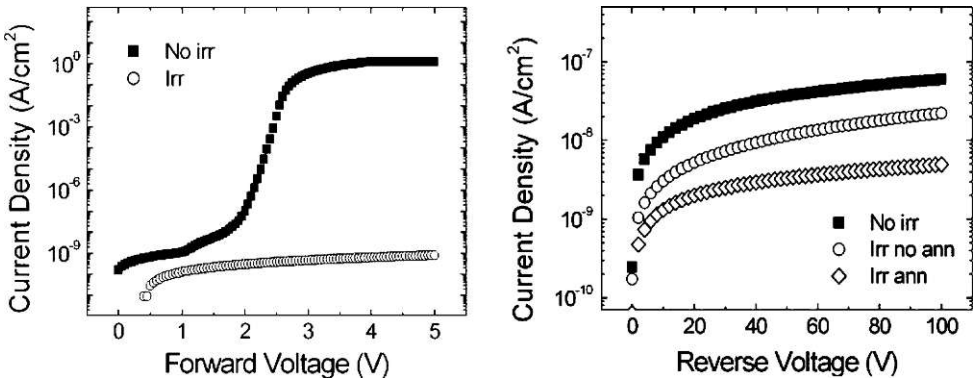

Figure 2.6.4: I-V Characteristics of neutron-irradiated ($3 \times 10^{14}\,\text{n}_{\text{eq.}}/\text{cm}^2$) 4H-SiC p-n diodes [13].

Change in Effective Doping Concentration

If the number of traps is comparable to the number of dopants in the crystal, traps can significantly affect the effective doping concentration. In n-type silicon, acceptor-like traps can compensate the doping fully, and at high enough irradiation, even start to dominate, flipping the n-type silicon to p-type ("type-inversion" [106]). This results in an increase in the full depletion voltage and requires higher bias voltages to be used in high-energy physics experiments, such as the CMS detector at the LHC. For silicon carbide, however, the main impact of radiation damage is a trapping of n-dopants, which will *remove* the dopants until they are fully trapped, with no free charge carriers in the bulk. This can be modeled by a donor removal rate A, which decreases the effective doping N_{eff} as

$$\text{N}_{\text{eff}} = \text{N}_0 - A\Phi \,, \tag{2.6.2}$$

where N_0 is the original doping concentration and Φ the irradiation fluence. Typical donor removal rates for 4H-SiC are on the order of $10\,\text{cm}^{-1}$ [107], but depend on the type of particle as well as the temperature [108, 109]. Contrary to silicon, acceptor-like traps in 4H-SiC are unlikely to be filled by

thermally generated charge carriers, which is why no type-inversion is observed for SiC [104]. This is highlighted in Figure 2.6.5, which shows that after irradiation, the capacitance of SiC detectors is independent of the bias voltage and equal to full depletion, as all free electrons inside the device bulk are captured by deep traps.

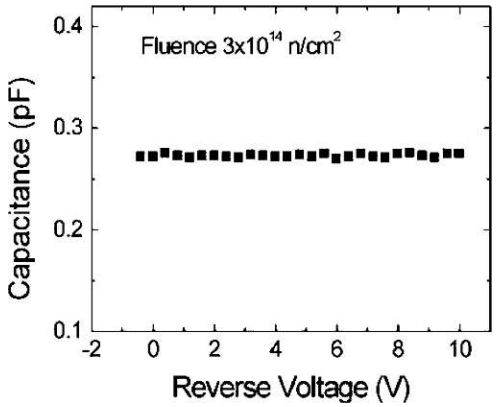

Figure 2.6.5: C-V characteristics of a 4H-SiC p-n diode irradiated to 3×10^{14} $n_{eq.}/cm^2$ [13].

Reduction of Charge Carrier Lifetime

Apart from having an effect on the space charge, traps that are not filled can trap free charge carriers introduced by ionizing radiation, effectively reducing the charge carrier lifetime. If the trap energy level is sufficiently deep so that the charge carriers are not "re-emitted" in a short time, the charge carriers will be "lost", and the charge collection efficiency of a detector is impacted. This can be described by an effective charge carrier lifetime $\tau_{\text{eff.}}$, which reduces the charge Q from Q_0 to [7]

$$Q(t) = Q_0 e^{-t/\tau_{\text{eff.}}}. \tag{2.6.3}$$

The charge carrier collection time t depends on the drift velocity and the thickness of the detector. Intuitively, thinner detectors with higher electric fields will be able to sustain a higher charge collection after irradiation. The effective lifetime $\tau_{\text{eff.}}$ can be modeled by

$$1/\tau_{\text{eff.}} = 1/\tau_{\text{eff.},0} + \beta\Phi_{\text{eq.}}\,, \tag{2.6.4}$$

which depends on the effective lifetime before irradiation $\tau_{\text{eff.},0}$, limited by intrinsic defects during the crystal growth, and a reduction proportional to the number of traps (trapping constant β and irradiation fluence Φ_{eq}). Figure 2.6.6 shows a typical curve of the reduction in collected charge as the charge carrier lifetime (or charge collection distance, CCD) decreases.

Instead of an effective charge carrier lifetime, the fraction of collected charge can be written in terms of the charge collection length L, which is given by the mobility-lifetime product $\mu E \tau_{\text{eff.}}$. For electrons and holes, this yields

$$\frac{Q}{Q_0} = \frac{L_e}{d}\left(1 - \exp\left(\frac{x-d}{L_e}\right)\right) + \frac{L_h}{d}\left(1 - \exp\left(\frac{x}{L_h}\right)\right), \tag{2.6.5}$$

which is commonly referred to as the *Hecht-equation* [110]. By integrating the Hecht equation over the thickness of the detector (assuming a uniform charge deposition), Figure 2.6.7 can be obtained. As the drift velocity saturates towards higher electric fields, the collected charge begins to saturate with decreasing charge carrier lifetime. This is a reason why thinner detectors (such as "3D"-detectors [111]) are preferable in applications that demand extreme radiation hardness (if the detector is thick enough to produce sufficient charge).

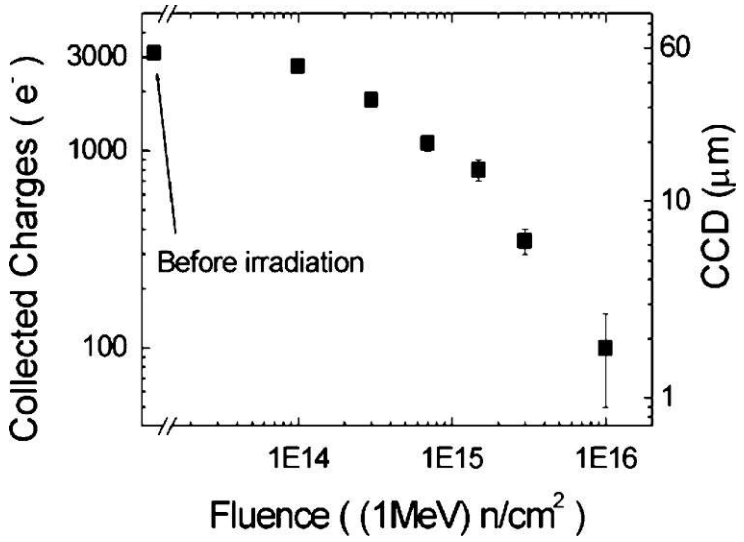

Figure 2.6.6: Reduction of the collected charge in a 4H-SiC p-n diode after irradiation [13].

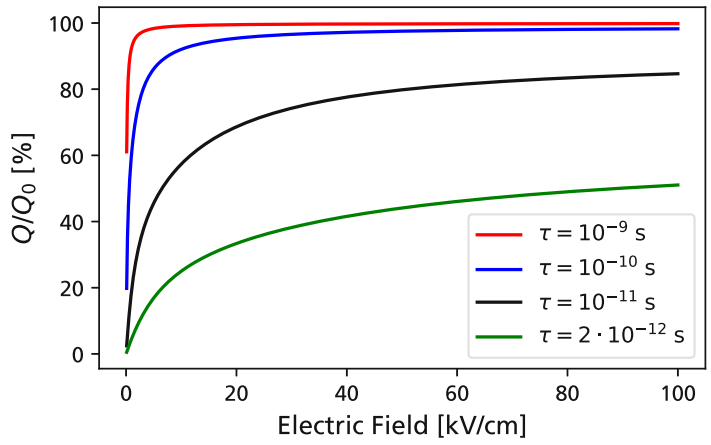

Figure 2.6.7: Fraction of collected charge for a 50 µm 4H-SiC detector with a constant electric field and different lifetimes τ for electrons and holes. Calculated using the Hecht-equation (see Equation (2.6.5)).

2.6.3 Annealing of Radiation Damage

Given enough time (and energy), defects such as interstitials or vacancies can recombine with other defects and "heal" the crystal lattice. For silicon, room-temperature annealing is a significant effect that can have a positive impact on short timescales, and a negative impact on longer timescales (which is why silicon sensors operating at high radiation levels need to be constantly cooled) [7]. However, for 4H-SiC, where the displacement threshold of the Si and C atoms is relatively large [112], high temperatures are typically required for annealing to take place. At room temperature, no annealing is observed, with neutron-irradiated samples stored for multiple years showing no change in electrical properties [113]. Annealing of carbon vacancy effects (which are already present before irradiation) can be performed by implanting additional carbon and annealing [114, 115], however, this requires temperatures around 1600 °C, which makes it infeasible to perform after a device has been processed (let alone in-situ in a detector).

Recently, results have been reported for low-temperature ($< 600\,^{\circ}\mathrm{C}$) annealing of radiation defects, showing improvements to the forward current and charge collection efficiency [116–118]. Additionally, SiC detectors can be operated at elevated temperatures (due to the wide bandgap), where annealing can already take place during the irradiation of the detector [26]. However, compared to silicon, the annealing behavior of 4H-SiC is not understood as well, and more systematic investigations are required.

2.7 Signal Formation in Solid State Detectors

2.7.1 Shockley-Ramo Theorem

As charge carriers (electrons and holes) drift through an electric field inside a sensor, they will induce a current in the cathode and anode. This happens instantaneously with the movement of the charge carrier as the electrostatic flux lines terminate either on the anode or cathode [119, 120]. In fact, "charge" is "collected" even before the charge carrier arrives at the readout electrode (and the rise time of the current signal is practically infinite [121]). The induced current is given by the *Shockley-Ramo* theorem

$$I = q \cdot \vec{E_w} \cdot \vec{v}\,, \tag{2.7.1}$$

with q and v the charge and velocity of the charge carrier and $\vec{E_w}$ the gradient of the *weighting potential*. The weighting potential describes the coupling strength of a charge to a specific electrode and can be obtained by setting the electrode to a unit potential, while grounding all other electrodes [59]. For a planar geometry (single electrode, infinitely long) with thickness d and a bias voltage V, the charge carrier movement and induced charge can be described as [59]

$$E = \frac{V}{d} \qquad v = \mu E \qquad E_w = \frac{1}{d}. \tag{2.7.2}$$

As the electric field E is constant, the drift velocity v will be constant as well. Therefore, the current induced by the charge carrier will be

$$I = q \cdot E_w \cdot v = q\mu \frac{V}{d} \cdot \frac{1}{d} = q\mu \frac{V}{d^2}. \tag{2.7.3}$$

The drift time t is given simply by the distance d divided by the drift velocity v, and the total induced charge Q can be calculated as

$$Q = I \cdot t = \frac{d}{\mu V/d} \cdot \mu \frac{V}{d^2} = \frac{d^2}{\mu V} \cdot q\mu \frac{V}{d^2} = q. \tag{2.7.4}$$

This means that no matter the drift velocity or the length of a detector, the induced charge is always constant and equal to the number of generated charge carriers. If an electron-hole pair at a position x

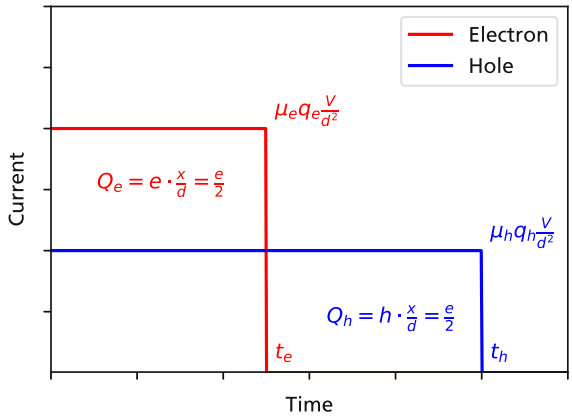

Figure 2.7.1: Current induced by a single electron-hole pair injected in the center ($x = d/2$) of a planar detector for $\mu_e = 2 \cdot \mu_h$. Because the electron-hole pair starts in the center of the detector, the area under both the electron and hole current curves is the same, both inducing half an electron of charge in the readout electrode.

is considered (with electrons drifting a length of x, and holes $d - x$), the charge induced by both charge carriers can be calculated to be

$$Q_e = q_e \cdot E_w \cdot v_e \cdot t_e, \qquad t_e = \frac{x}{v_e} \tag{2.7.5}$$

$$Q_h = q_h \cdot E_w \cdot v_h \cdot t_h, \qquad t_h = \frac{d-x}{v_h}. \tag{2.7.6}$$

which is graphically depicted in Figure 2.7.1. Depending on the starting position of the electron-hole pair, more current is proportionally induced by the electron or the hole, respectively. Again, the sum of induced charge is constant, no matter where the electron-hole pair starts off

$$Q = Q_e + Q_h = e \cdot \left(\frac{x}{d} + 1 - \frac{x}{d}\right) = e. \tag{2.7.7}$$

Considering a line of charge carriers (such as induced by a particle penetrating the entire sensor volume), the current can be calculated as a sum of all N individual charge carriers

$$I_{tot} = \sum_i^N q_i E_w v_i. \tag{2.7.8}$$

Over the thickness of the detector, different positions have different drift times, which results in a triangular current shape, depicted in Figure 2.7.2, described by

$$I_e(t) = \frac{2Q}{t_e}\left(1 - \frac{t}{t_e}\right), \qquad t_e = \frac{d}{v_e} \tag{2.7.9}$$

$$I_h(t) = \frac{2Q}{t_h}\left(1 - \frac{t}{t_h}\right), \qquad t_h = \frac{d}{v_e} \tag{2.7.10}$$

$$\tag{2.7.11}$$

The instantaneous current (at $t = 0$) is proportional to the sum of the electron and hole drift velocities, which can be used to extract the electric field, as is done in the transient-current-technique [122].

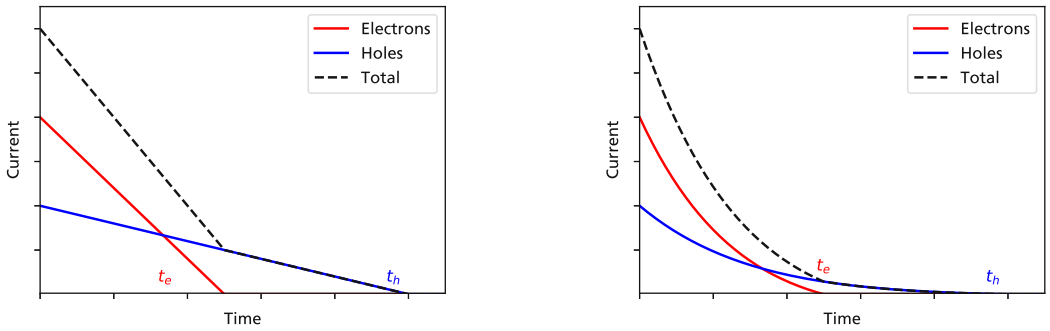

Figure 2.7.2: Left: Induced current by a MIP-like particle (uniform charge deposition with depth) in an idealized detector. The drift of the electrons and holes induces the same amount of charge ($Q/2$) and has a triangular shape. Right: Induced current in the presence of diffusion. Especially if the electric field is small (and the drift time is long), diffusion can significantly spread out the charge carriers, resulting in an exponential signal tail.

2.7.2 Diffusion

Diffusion not only plays a role in diode conduction but can also have an effect on the charge cloud generated by ionizing radiation. After a drift time t, the charge cloud will expand to a Gaussian distribution with a standard deviation of

$$\sigma(t) = \sqrt{2Dt}\,, \tag{2.7.12}$$

where D is the Einstein diffusion coefficient $D = \mu kT/q$. At very high charge concentration levels, the charge carriers will also interact with each other due to Coulomb forces, which leads to a further expansion of the charge cloud and can even shield it from the electric field inside the semiconductor (leading, for example, to *gain-suppression* in low-gain avalanche diodes [123]).

Diffusion also plays a significant role in partially depleted detectors. Charge carriers outside the depletion zone have a chance to diffuse into it and be collected by the electric field, which means that the collected charge is generally larger than expected from the width of the depletion zone, as shown in Figure 2.7.3. For very long charge carrier lifetimes (>100 ns) and partially depleted detectors, the charge collected by diffusion might even fall outside of the shaping time by the readout electronics, and different results will be obtained for different electronics.

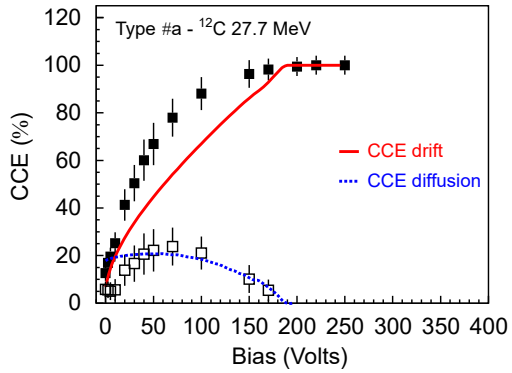

Figure 2.7.3: Drift and diffusion contributions to the collected charge in a 4H-SiC Schottky diode detector [124], reproduced with permission. With higher bias voltages, the depleted thickness (and drift contribution) grows as $\propto \sqrt{V}$ until the device is fully depleted.

2.8 Timing with Solid State Detectors

While some experiments are only interested in the presence (or absence) of a particle, or the position of a hit, many other experiments also require timing information. Examples include time-of-flight measurements, where the momentum of a particle is inferred from the time between two detectors at a fixed distance [125]. Also, detectors at hadron colliders need to cope with pile-up of events (collisions happening essentially at the same time), and in order to distinguish between different events, precise timing information is necessary [6]. In order to determine the time-of-arrival of a particle, the detector signal needs to be converted to a timestamp. This is most commonly done by using a threshold crossing (which should be high enough that no false positives are recorded) and a precise clock. However, due to electrical noise and other effects, there are limitations on the precision and therefore time resolution that can be obtained.

In the presence of electronic noise, a detector signal might cross a fixed threshold slightly before or after where it would in a noise-free case. Typically, the first threshold crossing on the rising edge is chosen, as this slope is higher than the slope of the falling edge. Figure 2.8.1 shows a rising edge of a detector signal with electronic noise. Intuitively, if the rise time is shorter, the slope will be higher and the effect of noise smaller. Similarly, if the signal is larger with respect to the noise, the fluctuation in the threshold crossing time will be smaller. This can be written as [126]

$$\sigma_{\text{jitter}} \approx \frac{\Delta t}{\Delta V} = \frac{\text{t}_{\text{rise}}}{\text{SNR}}\,, \tag{2.8.1}$$

where SNR is the signal-to-noise ratio of the signal. For planar sensors, the current rises almost instantaneously (as discussed in Section 2.7.1). However, the bandwidth (BW) of the readout electronics being used also contributes to the rise time t_{rise}, as

$$t_{\text{rise}} \approx \frac{0.35}{\text{BW}}\,, \tag{2.8.2}$$

for a low-pass filter of the first order. Furthermore, electronics with higher bandwidth typically feature higher noise densities [59]. Therefore, the readout electronics have to be adapted optimally to the frequency content of the expected signal, which will be discussed further in Sections 3.2 and 5.3.

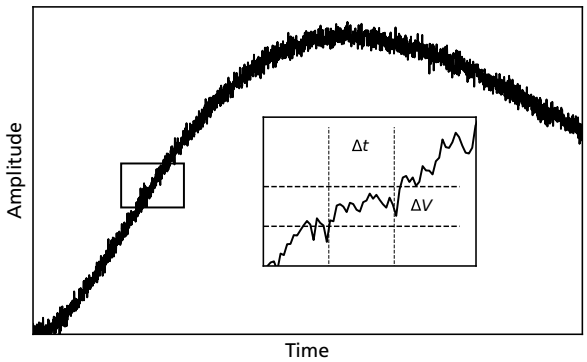

Figure 2.8.1: The rising edge of a signal with non-zero noise. Fluctuations in the amplitude around a threshold will result in a corresponding shift in the time of the threshold crossing.

When using a fixed threshold value, this threshold might be crossed earlier (or later), depending on the absolute size of the signal (which can vary with different amounts of deposited charge in a detector), as depicted in Figure 2.8.2a. The resulting shift in crossing times depending on the signal amplitude is

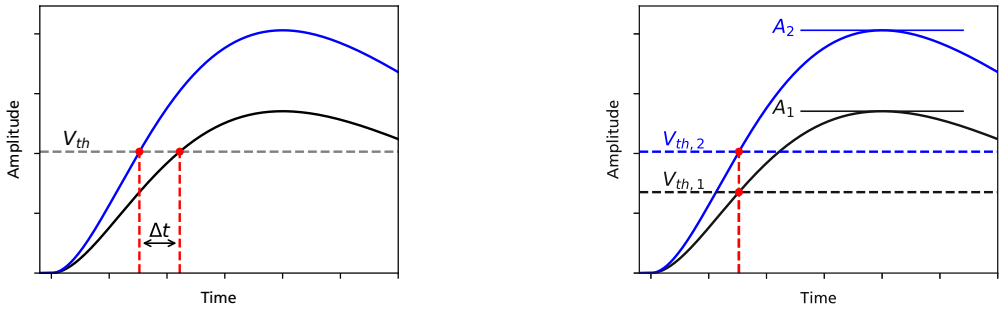

(a) Time walk for a fixed threshold.

(b) Constant fraction discrimination at 50 %.

Figure 2.8.2: Working principle of constant-fraction discrimination (CFD). By setting the trigger threshold to a fraction of the signal amplitude ($V_{th,i} = 0.5 \cdot A_i$), the threshold crossing time is independent of the signal amplitude.

also known as "time-walk". In order to address this issue, instead of using a fixed threshold, a threshold relative to the signal amplitude can be used. This ensures that the threshold is always at the same relative position of the signal waveform, therefore eliminating time-walk. It is also possible to implement constant-fraction discrimination in analog electronics by multiplying the signal with an inverted and delayed version of itself [56]. If the data analysis (extracting timestamps from threshold crossing times) is done offline (after the data has been acquired by an oscilloscope), it can, however, be performed digitally.

Measured timestamps will be discrete values, either given by the sampling rate of an analog-to-digital converter (ADC) or the bin size of a time-to-digital converter (TDC). If the other sources of timing uncertainty are small enough, timestamps will fall in only a single bin of the measurement resolution size t_{sample}, and the timing resolution is then given by

$$\sigma_{TDC} = \frac{t_{\text{sample}}}{\sqrt{12}}, \tag{2.8.3}$$

the factor $\sqrt{12}$ resulting from the standard deviation of a uniform distribution between $[0, t_{\text{sample}}]$. For oscilloscope waveforms and a very good SNR, a limited timing resolution (t_{sample}) can be overcome by interpolating in-between values. In the simplest case, this is accomplished by a linear interpolation of the two data points immediately before and after the threshold crossing.

The statistical nature of ionizing particles not only results in fluctuations in the amount of charge deposition but also in its spatial distribution. This can result in a shift of the center of gravity of the signal, and lead to a threshold being crossed slightly earlier or later, and yields a time resolution limit which is referred to as the *Landau* term [121]:

$$\sigma_{\text{Landau}} \approx w(d/\lambda). \tag{2.8.4}$$

The spatial fluctuations in charge deposition scale with the thickness of the detector d and the mean free path λ of the particle between interactions. The Landau fluctuations mainly present a limitation if all other contributions to the time resolution are well controlled (for example, low-gain avalanche diodes are used to improve the gain), which has driven the push to thinner and thinner detectors [127].

2.9 Low-Gain Avalanche Diodes

As mentioned in Section 2.2.5, impact ionization can be used to multiply the charge deposited by an ionizing particle, resulting in larger signals that can be more easily read out. This is leveraged in semiconductor devices with built-in gain, where a highly doped gain layer results in a high local electric field where impact ionization can occur. By keeping the thickness of this gain layer thin ($\sim 1\,\mu m$), the bias voltages that need to be applied can be kept relatively moderate [126]. One area where devices with gain have found a large success is silicon photomultipliers (SiPMs), which can detect single photons and provide large output signals [128].

While detectors with internal gain have been proposed earlier already [1], *low-gain avalanche diodes* (LGADs) gained prominence from 2013 on [9] and are widely used in particle physics experiments nowadays [129]. Low-gain avalanche diodes (LGADs) combine the advantages of diode-based detectors (fast rise time, low noise, radiation hardness), with the advantages of APDs (large signals) [130]. Figure 2.9.1 shows a schematic of an LGAD. At the top of the device, a highly doped gain layer is implanted (or epitaxially) grown, which results in a localized high electric field. When charge carriers are deposited in the bulk of the device, they drift to the anode and cathodes, and one carrier species will pass by the gain layer, where they multiply and result in a larger signal. As the charge carriers first have to drift up to the gain layer, this results in a triangular shape of the detector signal, as depicted in Figure 2.9.1.

Although this increases the rise time compared to a diode-based detector (which has essentially infinite rise time), the larger signal improves the SNR and allows for very good timing resolutions to be reached [126]. Alternatively, for the same signal charge, an LGAD detector can be made a fraction of the thickness of a planar diode detector, which reduces timing uncertainties due to Landau fluctuations [1]. The reason that the gain in LGADs is limited is that not only is the signal multiplied by the gain, but also the shot noise of the current flowing through the detector. Because this noise grows faster than the signal with the gain, there exists an optimum signal-to-noise ratio for LGAD sensors, where the timing resolution will also be optimal [126]. LGAD sensors are a very attractive technology for silicon carbide [20], as the typical detector thicknesses that can be manufactured (and depleted) are rather low, and together with the electron-hole pair creation energy being higher than for silicon, this makes it very challenging to detect minimum ionizing particles.

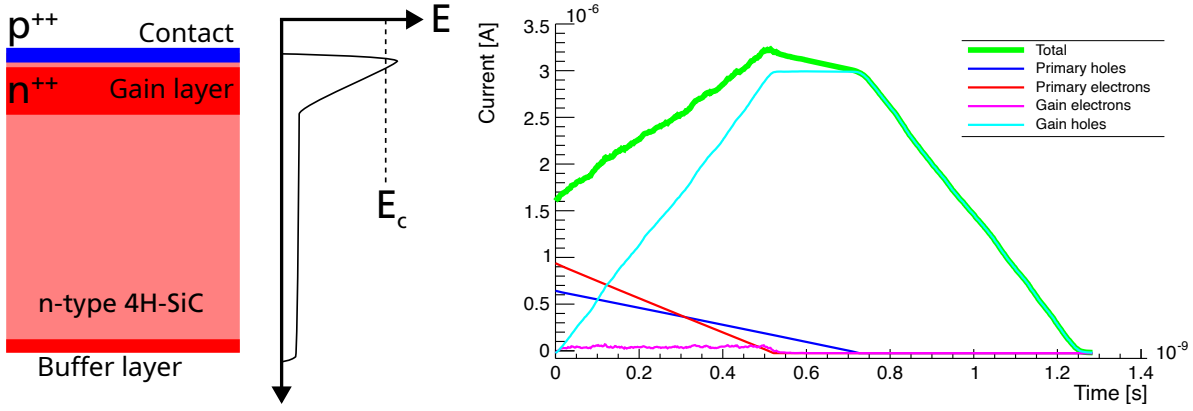

Figure 2.9.1: Left: Working principle of a SiC-based low-gain avalanche diode (LGAD). The highly doped gain layer depletes only very slowly and creates a high electric field. If this electric field is high enough, charge carriers multiply, resulting in a signal gain. Right: Transient currents of primary and secondary electrons and holes simulated using *Weightfield2* [131].

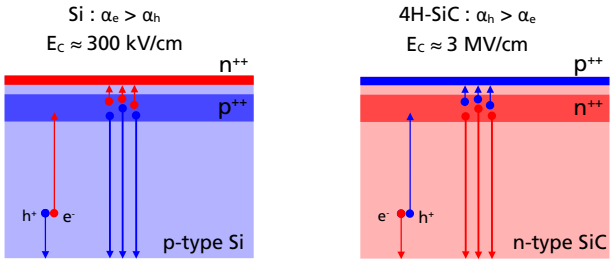

Figure 2.9.2: Comparison between typical silicon and silicon carbide LGADs.

Figure 2.9.2 shows a comparison between typical silicon LGADs and SiC LGADs. As electrons drive the charge multiplication in silicon, silicon LGADs are typically manufactured using p-type material, where the electrons drift up to a highly doped p^{++} gain layer. Si-LGADs based on n-type material also exist (referred to as nLGADs [132]), but these devices are mainly optimized for detecting low-penetrating particles, as the electrons created below the gain layer will not drift through it and experience no gain. SiC-LGADs, on the other hand, are driven mainly by hole multiplication and are built using n-type material. Although the drift of holes in 4H-SiC is slower than that of electrons (which will lead to an increased rise time compared to n-type LGADs), the drift is still approximately as fast as electrons are in silicon [61]. As the breakdown electric field in 4H-SiC is an order of magnitude higher than that of silicon, higher bias voltages and gain layer doping concentrations are typically required.

2.10 Silicon Carbide Detectors in Particle Physics

Particle detectors based on silicon carbide have been investigated since the 1960s [43] and have matured as a technology, being used in various high-energy physics experiments [14, 17, 133]. While the thermal generation of charge carriers in undoped bulk 4H-SiC is sufficiently low (due to the wide bandgap) to directly construct particle detectors, the highest crystal qualities and charge carrier lifetimes are obtained using nitrogen-doped 4H-SiC [44]. Due to this doping, the resistivity of the material is decreased, which therefore requires a junction to reduce the current induced by a bias voltage. It is possible to obtain high-resistivity 4H-SiC material by compensating the n-doping with vanadium [134, 135], however, this reduces the charge carrier lifetime and is generally not viable for use as a particle detector. Generally, SiC particle detectors can be split into three different categories:

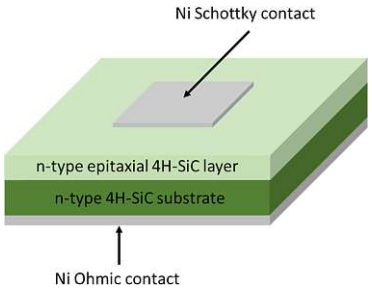

Figure 2.10.1: SiC Schottky diode detector. Taken from [136].

Schottky-diodes [104], depicted in Figure 2.10.1 are the easiest to manufacture, as they require only a a metal to be deposited on an epitaxially grown SiC wafer and some annealing to form the contact. Due to this, a large amount of pioneering work on SiC detectors has been performed using Schottky diodes. Additionally, as very thin (< 10 nm) metal layers can be deposited [137], Schottky diodes excel in spectroscopic applications, where the absorption in the entry window to the detector has to be minimized.

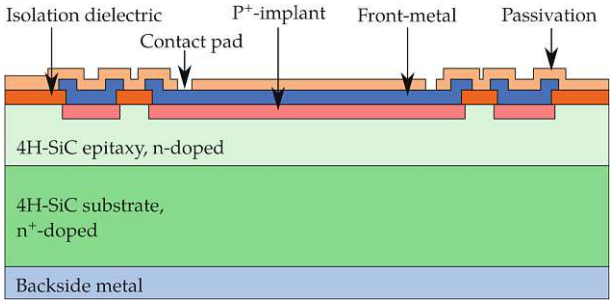

Figure 2.10.2: SiC PiN diode, taken from [105].

PiN diodes (p-n junction with a large low doped "intrinsic" layer) [138], shown in Figure 2.10.2 require a more sophisticated manufacturing process, as p implants are required to create a junction. PiN detectors typically offer lower leakage currents than Schottky diodes, but are not used as heavily in power electronics, due to their higher turn-on voltage [44]. The manufacturing processes typically associated with PiN diodes allow for very complex devices, incorporating not only planar sensors, but also segmented designs, such as strips or pixels [139, 140]. Finally, by implanting (or epitaxially growing) a gain layer, the signal collected by a detector can be increased, overcoming the limitations of planar SiC detectors and excelling in timing applications [19, 141].

SiC-CMOS-based active pixel sensors are an upcoming type of SiC detectors, with a cross-section of a SiC-CMOS process shown in Figure 2.10.3. By integrating analog electronics into a detector, high integration densities can be obtained (for example, in pixel detectors), and higher performance can be obtained (as parasitic capacitances or inductances between the sensor and readout electronics are removed). SiC-CMOS detectors are still an emerging field in detector applications [21], however, pixelized detectors have already been demonstrated for UV-light detection [142], and the processes and technology might benefit from interest in high-temperature compatible electronics [22].

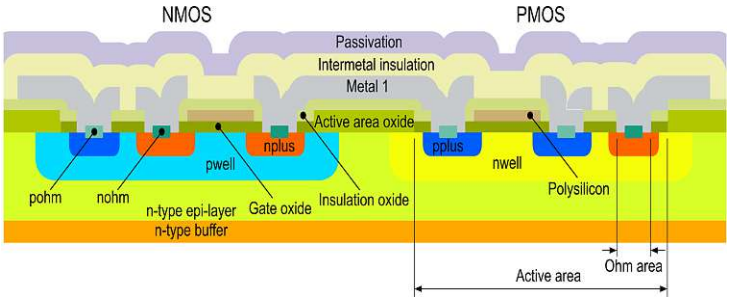

Figure 2.10.3: Cross-section of a SiC-CMOS process. Taken from [143].

3 Fast Detector Readout Electronics

3.1 Current and Voltage Sensitive Amplifiers

Depending on the construction of an amplifier, it can act as a voltage-sensitive or a current-sensitive device. Amplifiers are typically implemented using an operational amplifier with some feedback resistance or capacitance, as depicted in Figure 3.1.1. If only a capacitive feedback is used, the current of the detector will be integrated on the feedback capacitor C_F, generating a voltage which is proportional to the collected charge. The charge on the capacitor will remain until it is discharged, either by a manual reset or by a resistor parallel to it. If this parallel resistor is small enough, such that the discharge time of the system $\tau = R_F C_{\text{det}}$ is smaller than the length of the detector signal Δt, then the output of the amplifier will closely follow the transient current of the detector, with $V_{\text{out}} = -R_F I_{\text{det}}$ [57]. These two extreme cases are referred to as charge (or voltage) sensitive amplifiers (CSAs) and *transimpedance* amplifiers (TIA). Typically, CSAs are used in spectroscopic applications to measure charge very precisely (or other applications where the faintest signals need to be detected), whereas TIAs are used for fast readouts, for example, in timing detectors.

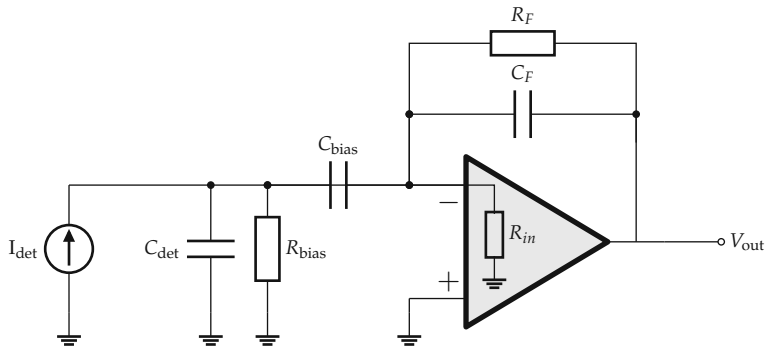

Figure 3.1.1: Diagram of a generic detector readout using a bias tee. Generally, the bias resistor is much larger than the input impedance of the amplifier $R_{bias} >> R_{in}$, and at high frequencies, the impedance of the large decoupling capacitor C_{bias} is negligible. The performance and time constant of the front-end is determined by the feedback resistor R_F and capacitor C_F.

3.2 Noise and Shaping

Every amplifier will experience noise, generated either by the amplifier itself or by the detector connected to it. Three main types of noise exist, as summarized in Figure 3.2.1. Thermal noise results from fluctuations in the thermal noise of charge carriers inside a resistor, which can generate a noise voltage. It is proportional directly to the temperature and the resistance, which is why large resistance values should typically be avoided in noise-critical amplifier paths [59]. Shot noise originates from statistical fluctuations in charge carrier transport and is proportional to the flowing current I_0. Finally, $1/f$-noise

(also referred to as flicker noise), is a type of noise that increases toward lower frequencies; however, it is typically not relevant for detector applications.

$$\begin{aligned} \text{Thermal (Johnson) Noise :} \quad & \langle I^2_{\text{therm}} \rangle = \frac{4k_B T}{R}\,\text{df}, \\ \text{Shot Noise} \quad & \langle I^2_{\text{shot}} \rangle = 2eI_0\,\text{df}, \\ 1/f\ \text{Noise} \quad & \langle I^2 \rangle = K_\alpha \frac{1}{\text{f}^\alpha}\,\text{df}. \end{aligned}$$

Figure 3.2.1: Main noise sources and their frequency content.

It can be shown that thermal noise can be reduced by integrating over a long time period τ, and scales as $1/\sqrt{\tau}$ [57]. In contrast to this, the shot noise acts as a current source, and its contribution to the noise will increase as $\sqrt{\tau}$. This behavior is shown in Figure 3.2.2. For every detector (and amplifier), there will be an optimum shaping time, where the sum of all noise contributions is the lowest. *Shaping*, which employs a band pass filter typically constructed using CR-RC elements, can be used to filter the amplified detector signal to only include frequencies close to the optimal shaping time. This cuts away other parts of the spectrum, where the signal-to-noise ratio is lower, and allows for a direct measurement of the signal amplitude in the best SNR conditions, without the need for additional pulse processing.

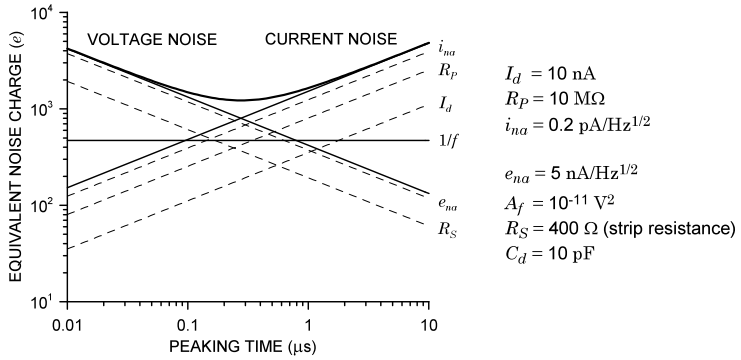

Figure 3.2.2: Noise as a function of the frequency for a silicon strip detector. Taken from [59].

3.3 Frequency Response of Transimpedance Amplifiers

Fast amplifiers (where the time constant of the amplifier is much smaller than that of the signal) are often used in timing applications, where the lowest jitter (best slope-to-noise ratio) is desired. Additionally, fast transimpedance amplifiers are used in transient-current-technique (TCT) measurements, which aim to reconstruct the transient current of a detector signal and gain information about the charge carrier transport inside a detector. High frequency transimpedance amplifiers are also used in optical communications, where a TIA amplifies the signal of an infrared laser hitting a photodiode and bandwidths of more than 50 GHz are routinely achieved [144].

The simplest transimpedance readout is shown in Figure 3.3.1a. No amplifier is used; the current signal of the detector is simply passed over a resistor R_L, which converts it to a voltage that is then digitized. The transimpedance $\text{Z} = \text{U}_{\text{out}}/\text{I}_{\text{in}}$ of this circuit is given by

$$\text{Z}_{\text{simple}} = \frac{R_L}{1 + 2\pi f R_L C_D} \tag{3.3.1}$$

for a detector capacitance C_D. For low frequencies or a small detector capacitance ($2\pi f R_L C_D \ll 1$), the transimpedance is simply given by the shunt resistor

$$Z_{\text{simple}} \approx R_L. \tag{3.3.2}$$

This type of "amplifier" can easily be realized by connecting the detector directly to an oscilloscope. The input impedance of the oscilloscope (and indeed the PCB where the detector is mounted, as well as the cables to the oscilloscope) will typically be 50 Ω and serve as the resistor R_L. For this readout, the 3 dB bandwidth can be calculated to be

$$\text{BW}_{\text{simple}} = \frac{1}{2\pi f R_L C_D}. \tag{3.3.3}$$

For $R_L = 50\,\Omega$ this yields a bandwidth of 160 MHz for $C_D = 20$ pF and 1.6 GHz for $C_D = 2$ pF. While increasing the value of the shunt resistor allows for a higher gain, this will also increase the thermal noise introduced by it, and for most detector readouts, the signal-to-noise ratio will be insufficient to detect particles.

A more sophisticated circuit can be implemented by using a bipolar transistor in a common-emitter configuration, depicted in Figure 3.3.1. The transimpedance of this circuit is given by

$$\text{Z}_{\text{TIA}} = \frac{g_m(R_C \parallel R_F)}{1 + s(R_C \parallel R_F)C_{out}}, \tag{3.3.4}$$

where g_m is the gain of the transistor, R_F a feedback resistor and R_C a bias resistor. This circuit features a low input impedance and high output impedance and is used widely in detector readouts in high-energy physics [145]. The common-emitter TIA configuration features two frequency poles, at

$$p_1 = 1/\left(2\pi R_F C_{in}\right), \qquad p_2 = 1/\left(2\pi (R_C \parallel R_F) C_{out}\right). \tag{3.3.5}$$

The first pole (p_1) is identical to the case of a shunt-resistor based TIA, and is usually dominating if the capacitance of the diode C_D is the main contributor to the input capacitance C_{in} and larger than the output capacitance C_{out}.

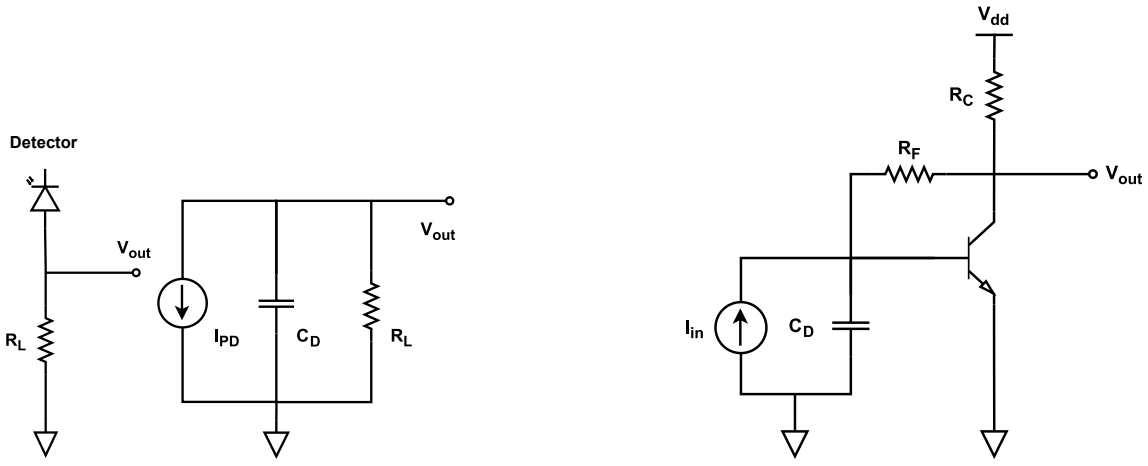

(a) Single-resistor TIA (b) Common-Emitter Feedback TIA

Figure 3.3.1: Transimpedance amplifier topologies. Taken from [146].

3.3.1 Effect of Inductance

Not only can the capacitance of the detector influence and decrease the achievable bandwidth, but other components also can have parasitic inductances and capacitances, which can negatively affect the system. One of the leading parasitic contributions that can reduce bandwidth is that of bond wire inductance. A bond wire with a diameter of 25 µm diameter has a typical inductance of approximately $1\,\mathrm{nH\,mm^{-1}}$ [147]. Together with the detector capacitance C and the input impedance of the amplifier R

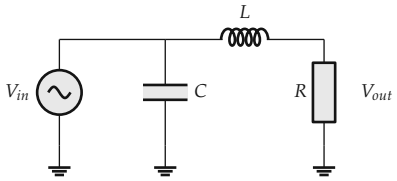

Figure 3.3.2: RLC low pass filter.

(typically 50 Ω), this will constitute a low-pass filter, as depicted in Figure 3.3.2 The magnitude of the response function $H(i\omega)$ is given by

$$|H(i\omega)| = \frac{1}{\sqrt{1 + \frac{\omega^2}{\omega_n^2}(4\zeta^2 - 2) + \frac{\omega^2}{\omega_n^4}}}, \tag{3.3.6}$$

with $\omega_n = \sqrt{1/LC}$ and $\zeta = 1/2 \cdot R\sqrt{C/L}$. The circuit has two poles at p_1, p_2 given by

$$p_{1,2} = -\zeta\omega_n \pm \omega_n\sqrt{\zeta^2 - 1}. \tag{3.3.7}$$

Figure 3.3.3 shows the resulting Bode diagram for typical detector capacitances and bond wire inductances. The detector capacitance decreases the bandwidth of the system in a straightforward fashion.

For a capacitance of 5 pF, the bandwidth is already reduced below 1 GHz, which is why for fast timing detectors, the active area of the detector needs to be limited to around $1\,\mathrm{mm^2}$ or smaller. For varying values of the inductance, however, a more interesting behavior is observed. Together with the capacitor, the inductance can form a resonance, which increases the gain at a specific frequency (given by the poles p_1 and p_2). While this is typically undesirable, it can also be leveraged to extend the bandwidth, if the resonance is placed exactly at the position where the bandwidth starts to be limited by the capacitance [148].

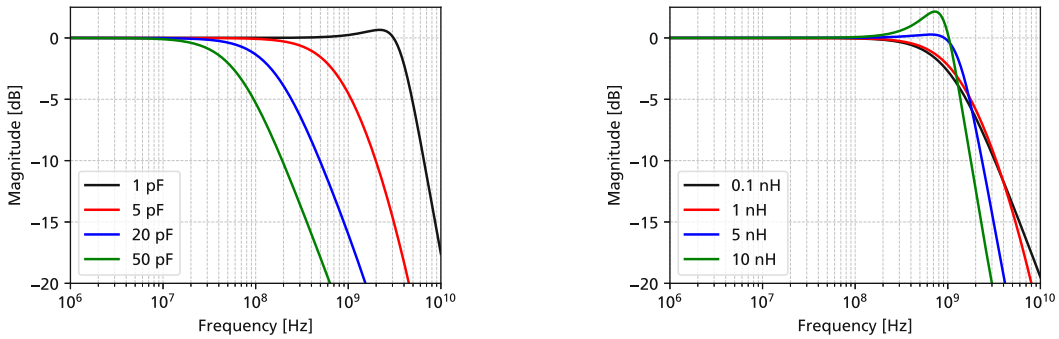

Figure 3.3.3: Bode diagrams for typical detector capacitances and bond wire inductances. Left: Varying capacitance for $L = 2\,\mathrm{nH}$. Right: Varying inductance for $C = 3\,\mathrm{pF}$.

3.4 Transfer Function Measurements for Fast Readout Electronics

For fast readout electronics (used, for example, in timing detectors), knowledge of the exact performance of the amplifier is essential. Metrics such as the gain, bandwidth, and noise need to be characterized in order to validate the electronic design and identify issues that need to be improved. While SPICE simulations can (theoretically) give very detailed insights into the performance of an amplifier, there will always be effects observable in real-life devices, for example, due to manufacturing uncertainties or parasitic contributions from components that can not be modeled (or only with a big effort). This section focuses on the measurement of amplifier gain as a function of frequency, which is essential to specify the bandwidth of the system. Different approaches are presented, using a sinusoidal sweep and a Dirac-like pulse, and finally, measurements of detector readout electronics are shown.

3.4.1 Measurement Methods

In order to describe an amplifier in a simulation (or to evaluate its performance), the transfer function $H(s)$ needs to be known. For a linear time-invariant system, $H(s)$ can be defined as the ratio of the Laplace-transformed input $X(s) \coloneqq \mathcal{L}\left(x(t)\right)$ and the Laplace-transformed output signal $Y(s) \coloneqq \mathcal{L}\left(y(t)\right)$

$$H(s) = \frac{Y(s)}{X(s)}\,, \tag{3.4.1}$$

with the complex frequency $s = \sigma + i\omega$. For purely imaginary frequencies $s = i\omega$, the Laplace and Fourier transformations are identical. Therefore, the inverse Fourier transformation can be applied to obtain the transfer function in he time domain $h(t)$, also referred to as the *impulse response*

$$h(t) = \mathcal{L}^{-1}\,H(s) = \mathcal{F}^{-1}\,H(i\omega) = \mathcal{F}^{-1}\left(\frac{Y(i\omega)}{X(i\omega)}\right) = \mathcal{F}^{-1}\left(\frac{\mathcal{F}\,y(t)}{\mathcal{F}\,x(t)}\right). \tag{3.4.2}$$

This means that the impulse function can be determined by measuring the frequency-dependent behavior of the input versus output voltage. Measuring the frequency response can be done in multiple ways: The most straightforward way is to excite the system with a sinusoidal at a single frequency ω with a known amplitude A. This yields

$$h(t) = \mathcal{F}^{-1}\left(\frac{Y(i\omega)}{A}\right), \tag{3.4.3}$$

where $Y(i\omega)$ is the measured output signal (and phase) at a frequency ω. An alternative way is to use a Dirac-like pulse as an input signal. A Dirac pulse has an equal frequency response for all frequencies ($X(i\omega) = 1$, which yields

$$h(t) = \mathcal{F}^{-1}\left(\frac{\mathcal{F}\,y(t)}{1}\right) = y(t). \tag{3.4.4}$$

This means that the measured time-domain signal $y(t)$ at the output directly corresponds to the impulse response of the system.

Sinusoidal Sweep

A sinusoidal sweep can be used to compute the frequency response $Y(i\omega)$ at each frequency, and reconstruct the impulse response according to Equation (3.4.3). Usually, such measurements are performed using a vector network analyzer (VNA), which can measure not only the transfer function of an amplifier but also reflection coefficients. However, no VNA was available to measure amplifiers, and instead a sine-sweep system was implemented, based on a Rohde&Schwarz RTP164 oscilloscope combined with a Rohde&Schwarz SMA100B signal generator, depicted in Figure 3.4.1. The sinusoidal sweep method is a very common method to determine transfer functions and create Bode plots. The oscilloscope features

an analog bandwidth of 16 GHz (and a sample rate of 40 GSa/s), while the signal generator can generate sinusoidal signals up to a frequency of 12.75 GHz with an output power of up to 30 dBm (20 V peak-to-peak). A custom Python-based software [149] was implemented to perform sine-sweeps: For each frequency (and input power to be applied), the oscilloscope records multiple acquisitions and computes the frequency, RMS, and peak-to-peak values of the waveforms. When measuring at low frequencies ($\sim$ MHz), digital low-pass filters can be automatically enabled to reduce the effective bandwidth of the oscilloscope and to remove high-frequency noise, improving the accuracy. In the current version, only the magnitude of the signal is measured, and the phase is not recorded. However, this could be implemented by using a 50 Ω matched power splitter after the output of the signal generator, and comparing the phase after an amplifier to the original phase of the signal generator, measured by an additional channel of the oscilloscope. Care has to be taken, however, to use phase-stable and phase-matched cables if these measurements are to be done with good accuracy.

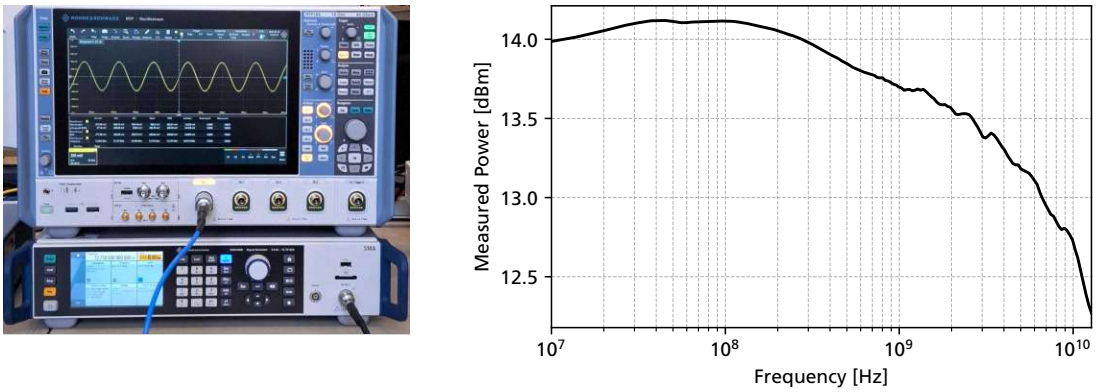

Figure 3.4.1: Left: RTP164 oscilloscope measuring sinusoidal signals connected directly to a SMA100B signal generator using RT-ZA16 BNC to SMA adapters. Right: Measured RMS power at the oscilloscope as a function of the frequency for a signal generator output power of 14 dBm.

Figure 3.4.1 also shows the measured frequency response for a Crystek CCSMA-MM-LL142-36 cable connected directly from the signal generator to the input of the oscilloscope. The frequency response is very flat, only decreasing by around 2.5 dB up to a frequency of 12.75 GHz. This attenuation is most likely a result of cable attenuation, as both the oscilloscope and signal generator state an amplitude accuracy better than 0.5 dB up to 15 GHz [150, 151].

Pulse Injection

As detailed in Equation (3.4.4), the impulse response can also be directly measured by applying a Dirac pulse. The RTP164 offers a hardware option (*RTP-B7*) for a 16 GHz differential pulse source, with a rise time better than 22 ps, which was used to measure impulse response functions. Figure 3.4.2 details how transfer functions can be obtained using the RTP-B7 pulse source. The pulse source outputs a voltage step with a very short rise time, which is then fed into an amplifier. By taking the derivative of the voltage step in time, the response of the amplifier to a very short pulse (Dirac pulse) can be computed, which is the impulse response. In order to obtain the frequency response, the Fourier transform of the impulse response is then computed. This is opposite to a sine-sweep, where the frequency response is the starting point and an inverse Fourier transform is performed to compute the impulse response. Figure 3.4.3 shows a measurement of the voltage step output by the RTP-B7 pulse source directly into the RTP164 oscilloscope. The data points have been acquired with a sample rate of 40 GSa/s and interpolated using a *sinc*-function. In order to reduce noise, 10 000 waveforms have been averaged. Noise reduction is especially important in order to be able to compute the derivative in time of the step response to obtain the

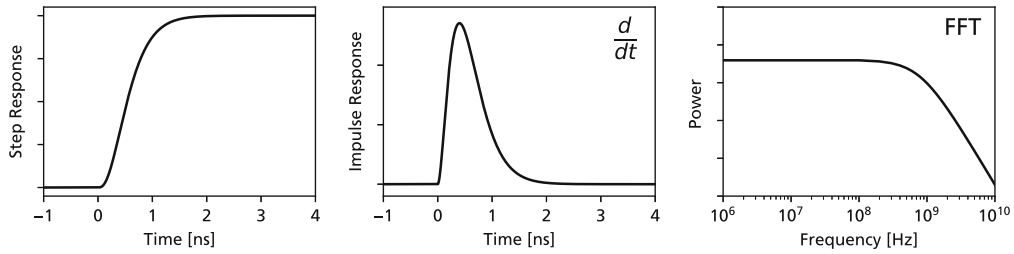

Figure 3.4.2: Working principle of voltage-step-based determination of the transfer function.

impulse response (depicted in Figure 3.4.3b), as small fluctuations can have a significant effect at high frequencies. The impulse response presents as a *sinc* function with a period of approximately 60 ps, which can be attributed to the limited analog bandwidth of the oscilloscope (16 GHz), as the impulse response of a low-pass filter is a *sinc* function. By applying the Fourier transform, the frequency response can finally be computed. Comparing this to the results obtained using a sine-sweep (see Figure 3.4.1), a slightly higher attenuation is observed, already at frequencies around 10 GHz. This could be related to limitations in the oscilloscope reconstructing the waveform from its measured samples, as for a Dirac pulse, it has to take into account the entire frequency range, while for a sinusoidal signal, only a single frequency is present in the signal.

3.4.2 Effect of SMA Cables

As a first measurement, different SMA cables were compared using the sine-sweep method. Using high-quality cables with low attenuation is a prerequisite for performing accurate measurements of the frequency response. If a cable is well characterized (and not bent or moved between measurements), its frequency response can be subtracted from the measurements. Figure 3.4.4 shows the measured attenuation for different SMA cables. The cables manufactured by Crystek and Rohde&Schwarz are rated for 18 GHz and show the lowest attenuation, around 2 dB at 12 GHz. The cables sold by RS PRO are only rated up to 6 GHz and show a higher attenuation. In general, cables at high frequencies (> 2 GHz) should be kept as short as possible to minimize losses. Additionally, broadband amplifiers should be used close to the detector readout electronics to boost the signal to a level much higher than the noise floor of the instrument reading out the signal, such that an attenuation of several dB does not degrade the signal-to-noise ratio of the signal. For lower frequencies (< 2 GHz), most SMA cables show negligible

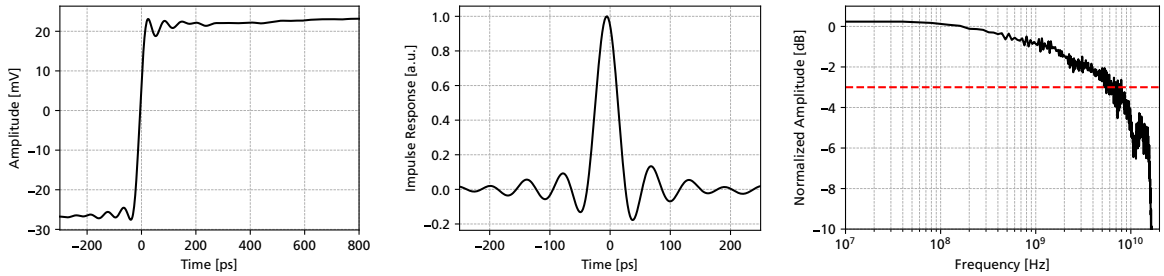

(a) Measured step response (b) Computed impulse response (c) Frequency Response

Figure 3.4.3: Step, impulse and frequency response of the Rohde&Schwarz RTP164 oscilloscope to a fast 50 mV voltage step generated by the RTP-B7 pulse source. The 3 dB bandwidth is indicated using a red line.

losses.

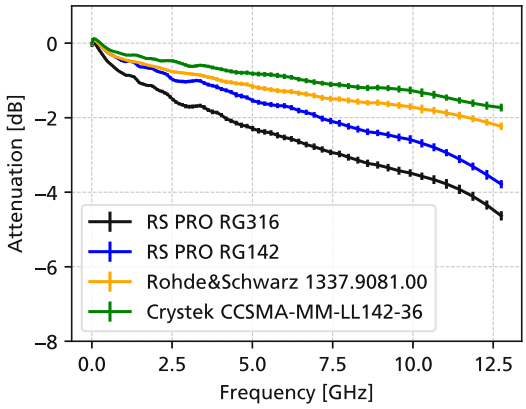

Figure 3.4.4: Measured attenuation for different SMA cables with a length of approximately 1 m.

3.4.3 Cividec Broadband Amplifiers

Broadband amplifiers manufactured by Cividec are widely used in instrumentation, either to directly read out detectors [152] or as secondary amplifiers [153]. These amplifiers feature 50 Ω-matched SMA connectors at the input and output, with a gain of approximately 40 dB and a bandwidth of 2 GHz. Figure 3.4.5 shows the measured frequency response obtained using a sine sweep with an input power of −50 dBm. At low frequencies (below 1 MHz), the input DC blocking capacitor of 1 nF [152] results in a high-pass filter. Between 3 MHz and 1 GHz, the voltage gain is very stable (slightly above 40 dB), decreasing at higher frequencies as the bandwidth limitation of the amplifier is reached. Between the two amplifier models measured, differences in the high-frequency behavior can be observed, with the C2TCT amplifier exhibiting a peak around 1 GHz, indicating a resonance or imperfect impedance matching.

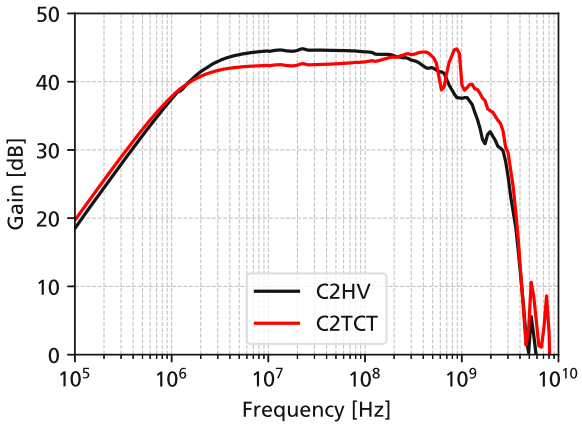

Figure 3.4.5: Measured gain vs. frequency for a Cividec C2HV and a C2TCT broadband amplifier.

3.4.4 Mini-Circuits Low-Noise Amplifiers

While broadband amplifiers up to several GHz are available in the instrumentation community [152, 154], higher frequencies are not typically used. Bandwidths in excess of 2 GHz typically result in a reduced signal-to-noise ratio (as the bandwidth of the detector signal is limited) [126], however, as will be shown in Section 6.5, there exist applications (such as transient-current-technique measurements), where a lower signal-to-noise ratio is accepted in favor of higher bandwidth.

(a) PMA3-14LN+ evaluation board [155]. (b) ZX60-14LN-S+ [156].

Figure 3.4.6: Mini-Circuits MMIC low-noise amplifiers with a bandwidth of 50 MHz-10 GHz.

Figure 3.4.6 shows microwave integrated circuits (MMIC) low-noise amplifiers (LNA) manufactured by Mini-Circuits, which were chosen to be investigated as detector readout electronics. Both amplifiers, PMA3-LN14+ and ZX60-14LN-S+, feature a bandwidth of 50 MHz to 10 GHz, albeit in different form factors. The PMA3-14LN+ amplifier [155] is contained in a QFN package and can be mounted on a PCB (such as the TB-PMA3-14LN+ evaluation board), while the ZX60-14LN-S+ amplifier is connectorized with SMA connectors and is intended to be used in-line. Figure 3.4.7 shows the measured frequency response for the ZX60-14-LNS+ measured using a sine sweep and a fast voltage step. The amplifiers exhibit a very stable and flat gain of around 22.5 dB, with a -3 dB bandwidth of 50 MHz to 10 GHz. Both measurement methods agree very well with each other, even for high frequencies.

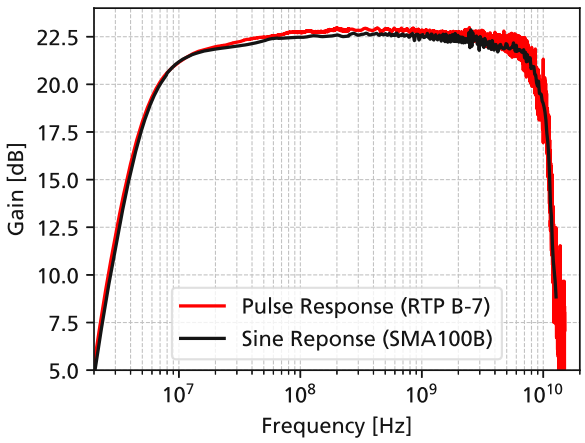

Figure 3.4.7: Voltage gain of the Mini-Circuits ZX60-14LN-S+ low-noise amplifier.

The evaluation board of the PMA3-14LN+ amplifier (depicted in Figure 3.4.6a) features both a connection line for the amplifier, as well as a "through"-line, which only features the waveguide on the PCB as well as some decoupling capacitors. As both the through-line and the amplifier line are constructed identically (except for the presence of the amplifier), any effects or reflections of the waveguide or SMA connectors can be measured and calibrated out by measuring the through-line. This practice is also commonly referred to as "de-embedding" and removes the effect of any cables or test fixtures, allowing for the measurement of the device under test only.

Figure 3.4.8a shows the measured gain for the amplifier and through-line on the TB-PMA3-LN14S+ evaluation board. The through line shows a lower bandwidth limit, due to 10 nF DC-blocking capacitors, and an upper bandwidth limit to losses both in the PCB waveguide and the cables to and from the oscilloscope and signal generator. Compensating for this frequency response allows for the de-embedded frequency response of the amplifier to be obtained, depicted in Figure 3.4.8b.

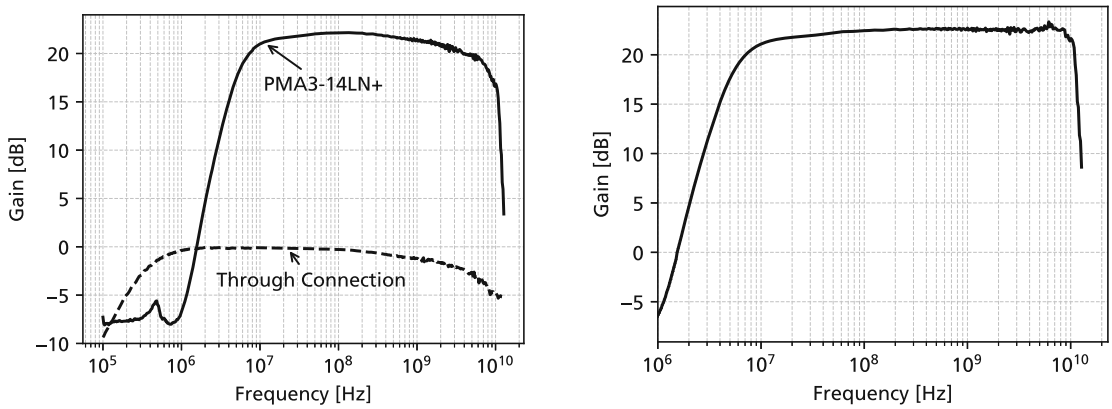

(a) Measured gain

(b) De-embedded gain

Figure 3.4.8: Measured gain of the Mini-Circuits TB-PMA3-14LN+ evaluation board using a sine-sweep up to 12.75 GHz. By performing a measurement using a through line with an identical geometry as the amplifier, the effect of cables, connectors and the PCB can be compensated.

3.4.5 UCSC LGAD Board

The readout board developed for LGAD timing detectors by the Santa Cruz Institute of Particle Physics, referred to as the "SCIPP-board" or *UCSC LGAD* board, has become a standard readout option in the instrumentation community [157], and its circuit has spawned many derivatives [158, 159]. It features an Infineon silicon-germanium npn-transistor in a common-emitter configuration, as depicted in Figure 3.4.9. The readout board is optimized for the lowest noise, with a bandwidth of around 1.6 GHz [160]. By varying the values of the feedback resistor R_F, the transimpedance and bandwidth can be adjusted, as derived in Equation (3.3.4). In order to measure the transfer function (so that the amplifier impulse response can be used in simulations), a SMA connector has been soldered onto the detector input of the amplifier. The SMA connector is terminated with 50 Ω by two 100 Ω resistors in parallel and connected to the bond pad at the amplifier input by a thin wire. Although a calibration input is available on the board via a 0.3 pF capacitor parallel to the input of the amplifier, this connection was not used, due to the possibility of reflections at the unterminated bond pad. Figure 3.4.10 shows transfer functions measured by applying a fast voltage step using the RTP-B7 pulse source. As the output voltage of the pulse source is known, the input current to the amplifier can be calculated assuming an impedance of 50 Ω, and therefore the gain of the amplifier can be expressed as a transimpedance.

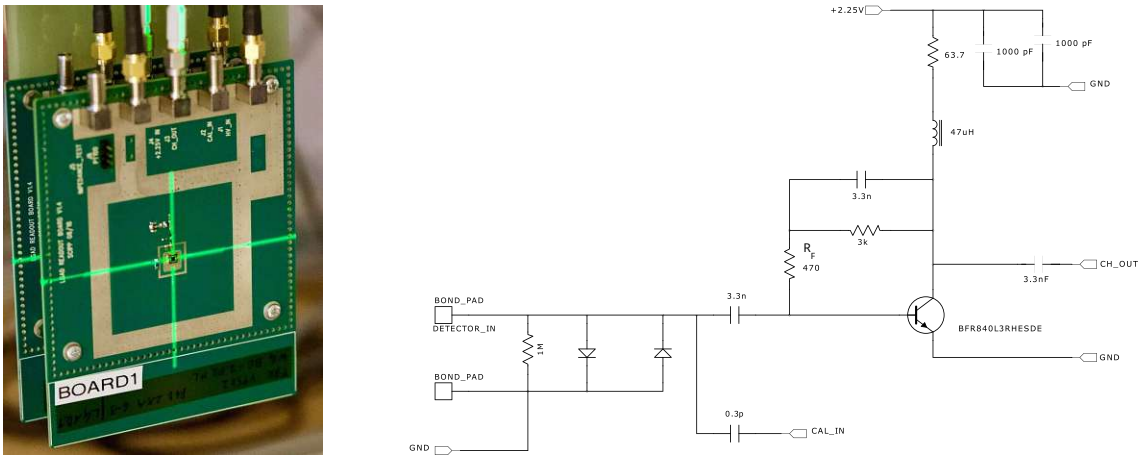

Figure 3.4.9: Photograph [145] and circuit diagram of the UCSC LGAD board.

For higher feedback resistances, the measured transimpedance grows, albeit non-linearly, because the bias resistor of the transistor has not been adapted, therefore changing the bias current. At the highest frequencies (above 1 GHz), the transfer function can not be determined reliably, most likely due to reflections and impedance mismatching between the SMA connector at the amplifier input and the rest of the circuit. For different detector capacitances, simulated by a parallel SMD capacitor to ground, Figure 3.4.10b directly shows the decrease in the bandwidth. For a capacitance of 22 pF, the bandwidth is already reduced to around 200 MHz. Therefore, in order to meet the full design specification of the bandwidth, the detector capacitance should be below 2 pF. Using this technique, measurements of other readout boards (such as a 96-channel board designed for the HADES experiment [161] or a 16-channel board designed by Fermilab [162]) have also been performed, although they are not present here.

Instead of applying a short pulse through an SMA connector, the signal of a detector itself can also be used as a Dirac pulse. Figure 3.4.11 shows a comparison of the pulse shapes and frequency spectra obtained using 50 µm thin 4H-SiC detectors of different capacitances and for different values of the feedback resistor R_F. For detectors with a large capacitance $C_D = 18$ pF, the signal is broadened significantly, as the bandwidth is not sufficient to respond to the transient current of the detector.

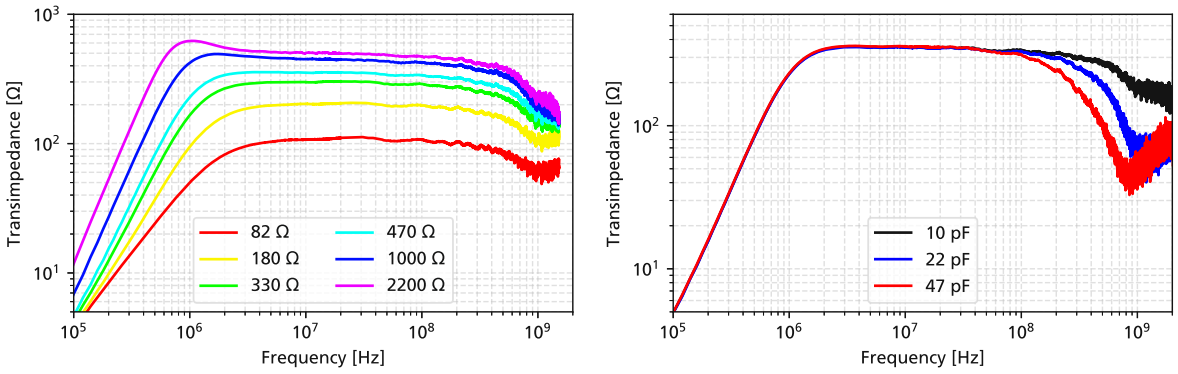

(a) Varying R_F for $C_D = 0$

(b) Varying C_D for $R_F = 470\,\Omega$

Figure 3.4.10: Transimpedance measured for different feedback resistors (R_F) and simulated detector capacitances (C_D parallel to ground at the detector input.

While faster signals can be obtained by using smaller values of the feedback resistor R_F, achieving a bandwidth similar to the signal bandwidth of the detector requires using a very small feedback resistance, as well as a detector with a small capacitance. However, as visible in the time-domain signal and in the frequency response, for such small feedback resistances, the circuit becomes unstable and exhibits high-frequency ringing. For $R_F < 82\,\Omega$, an instability of the readout board was observed, even without applying any input signals.

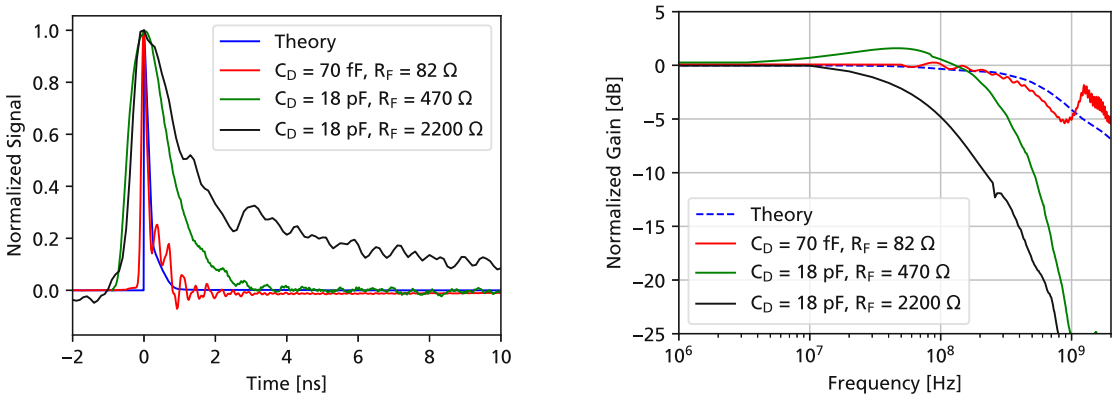

(a) (b)

Figure 3.4.11: Time and frequency domain response of the UCSC LGAD board for different SiC detectors. The expected detector current is indicated in blue. As the charge carriers require a certain time to drift through the detector, the power density of the input signal starts to decrease at GHz frequencies.

4 Detector Characterization Infrastructure

Fully exploiting the material advantages of 4H-SiC (such as its wide bandgap and high charge carrier velocity) requires characterization infrastructure and instruments that can meet this performance. For example, the high bias voltages used for SiC detectors require probe stations and high-voltage power supplies that can source at least 1 kV. Furthermore, as SiC sensors are typically thinner than standard planar silicon sensors (50 to 100 µm vs. 300 µm), the detector signals are expected to be much shorter in time, requiring a higher readout bandwidth to leverage the full signal power spectrum. As a part of this thesis, upgrades have been made to a probe station to enable measurements up to 3 kV (Section 4.1), a UV laser based TCT setup has been commissioned (Section 4.2), and a new alpha spectroscopy vacuum setup has been built (Section 4.3).

4.1 High-Voltage Upgrade of a Probe Station

Electrical characterization of devices and detectors is the first step undertaken after the production of a wafer has been finished and can yield information about the quality of the fabricated devices, including yield, doping concentration, or even defect densities. To perform these electrical measurements directly on a detector die, *probe stations* are used, where the die is electrically contacted using probe needles. Probe stations come in many different flavors, from manual probe stations where a single die is measured to fully automated systems that can characterize an entire wafer without supervision.

Characterizing silicon carbide devices poses special challenges, as depicted in Figure 4.1.1. Due to the wide bandgap, the thermal generation of charge carriers is extremely low, and the currents to be measured are typically at the pA level or below. Combining these low currents with high bias voltages in reverse bias (required to fully deplete devices) necessitates the use of triaxial cables and guarding, as will be detailed in Section 4.1.1. Furthermore, performing capacitance-voltage measurements at these high voltages requires specially adapted bias-tees, see Section 4.1.2.

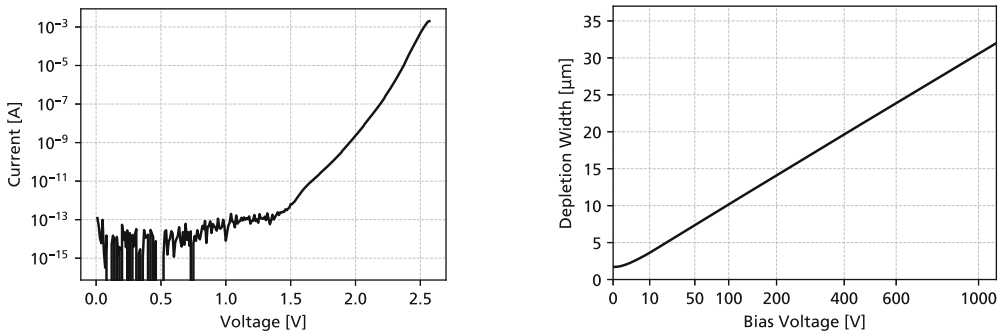

Figure 4.1.1: Left: Forward bias current-voltage (I-V) characteristics of a 4H-SiC PiN diode. The current measurement range spans more than 10 orders of magnitude. Right : Measured depletion width for a 100 µm thick SiC diode with a doping concentration of approximately $5 \times 10^{14}\,\mathrm{cm}^{-3}$ up to 1.1 kV. For full depletion, a bias voltage of 4.5 kV would be required.

4.1.1 Guarding for Low-Level Current Measurements

As discussed in Section 2.3.1, measuring very small currents requires the use of guarding to prevent excessive leakage currents. This becomes more and more relevant at high voltages ($> 200\,\mathrm{V}$) where coaxial cables already have leakage currents of several nA. Triaxial cables can solve this problem using a driven guard. However, leakage currents can occur not only in cables but also in the test fixture to which the device under test (DUT) is attached.

Figure 4.1.2 illustrates an unguarded test fixture. Not only does the current of the DUT (I_{DUT}) show up in the measurements, but also the leakage currents I_L of the test fixture to ground. Especially at high voltages, the insulators in a test fixture might not be good enough for the current to be negligible. Furthermore, parasitic capacitances might be present, which leads to long settling times [81]. By connecting the test fixture to the high-voltage guard connection of an SMU using a triaxial cable, the entire test fixture can be raised to the same potential as the DUT, which eliminates the leakage current in the measurement, as depicted in Figure 4.1.2b. The leakage current is still present, but is driven by the buffer amplifier of the SMU.

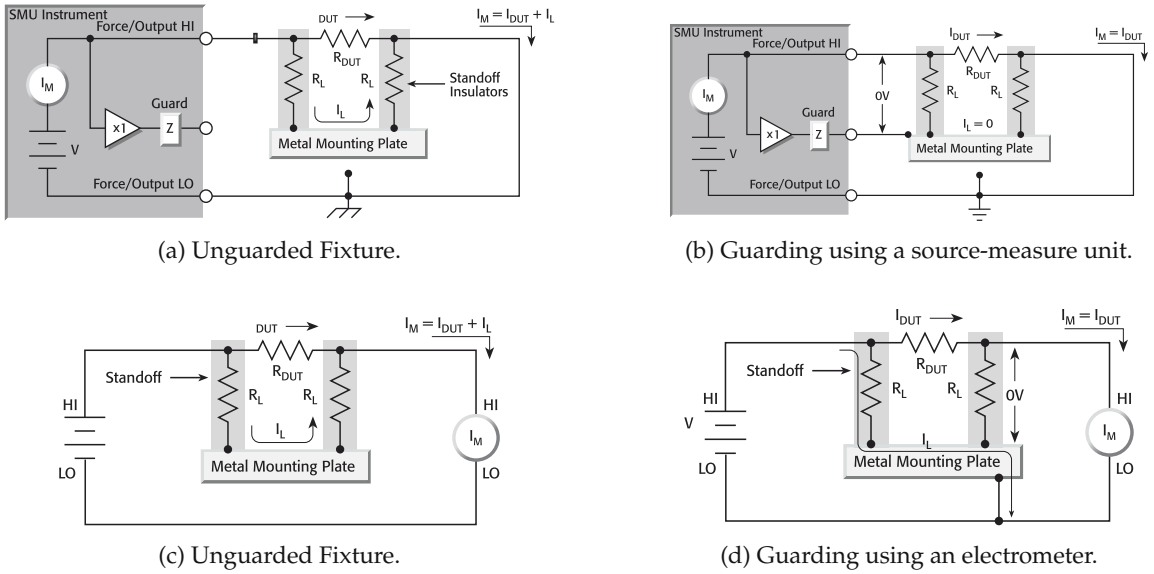

(a) Unguarded Fixture.

(b) Guarding using a source-measure unit.

(c) Unguarded Fixture.

(d) Guarding using an electrometer.

Figure 4.1.2: Guarding of test fixture leakage currents using a driven guard (top) and by measuring the current on the low-potential side of the circuit (bottom). Adapted from [76].

Instead of using a driven guard, the same principle can also be implemented by measuring the current on the low-potential side after the DUT using an additional instrument. The leakage current of the test fixture will then directly flow to ground, bypassing the current-measuring instrument (Figure 4.1.2d). This can be implemented in a rather simple way, for example by connecting an electrometer in series to the probe needle. As the connections after the DUT are at ground potential (and the electrometer has only a very small voltage drop), coaxial cables can be used on the low-potential side of the circuit.

Figure 4.1.3 shows how both of these techniques can be combined to achieve an optimal high-voltage performance. The chuck (on which the DUT rests) is split up into two parts: An outer part, which is mechanically and electrically isolated from its mechanical mount, and an inner part, which is used for measurements. The outer part of the chuck is driven by the guard connection of the SMU, which allows its leakage current to ground (I_{chuck}) to be removed from the measured device current I_{DUT}. By using an electrometer, additional guarding can be implemented, and employing multiple probe needles connected to ground allows for different parts of a detector (such as the guard ring or adjacent strips/pixels) to be guarded and their current to be removed from the measurement.

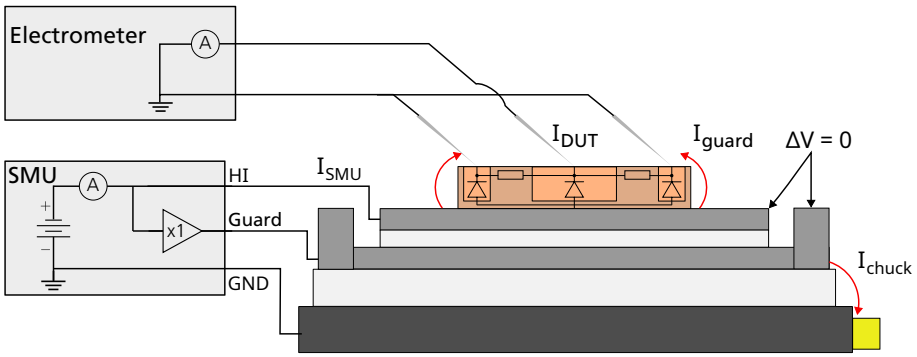

Figure 4.1.3: Schematic view of a guarded chuck mounted on a stepper motor stage. In between the inner and outer part of the chuck, as well as below the chuck a high quality insulating material (such as Teflon) is used.

Figure 4.1.4 shows the probe station "P3" in the HEPHY clean room, which has been upgraded as a part of this thesis. A Keithley 2657A SMU is available to source and measure voltages up to 3030 V. For precision DC current measurements, a Keithley 6571b electrometer can be used. C-V measurements can be performed using the Keithley 4215-CVU capacitance voltage unit in a Keithley 4200A semiconductor analyzer together with high-voltage bias tees (that will be described in Section 4.1.2). The high-voltage guarded chuck is mounted on top of a motorized XYZ stage, which, together with a camera-equipped microscope, can be used to perform automated measurements of multiple samples or segmented devices. The probe station is contained in a light-tight, interlocked, and electrostatically shielded box for which the air humidity can be controlled. All instruments can be operated by a Python-based data acquisition software (available at [163]).

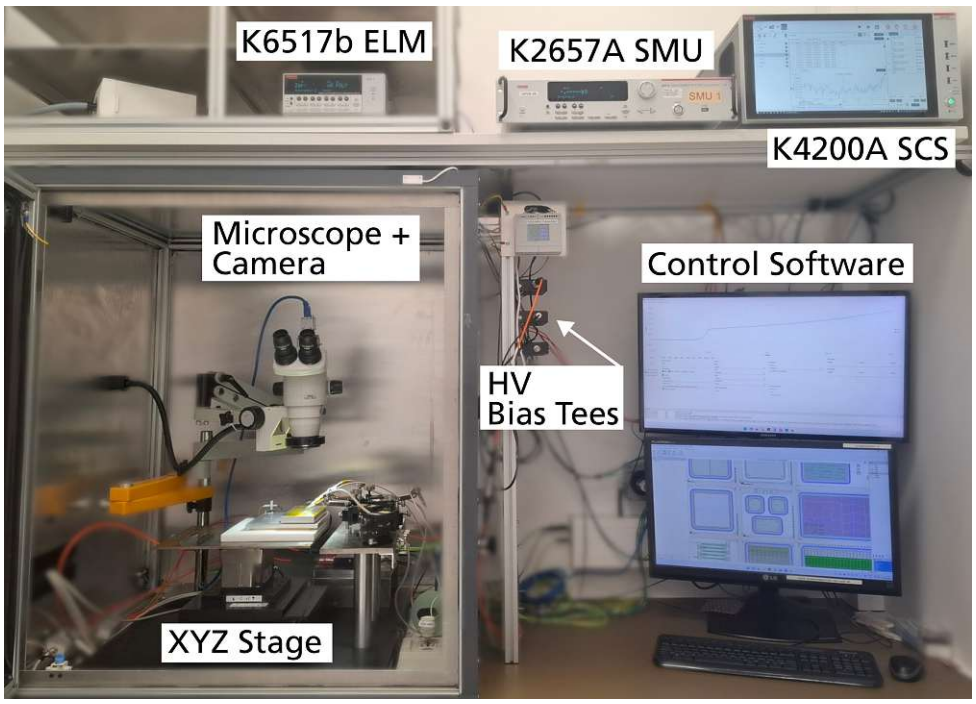

Figure 4.1.4: Photograph and components of the "P3" probe station in the HEPHY clean room.

Figure 4.1.5 shows the performance of the guarded chuck measured by a Keithley 2657A SMU. Even for voltages up to 3 kV, the leakage current stays below 1.5 pA. A voltage-dependent leakage current of 0.3 fA V^{-1} is obtained, equating to a resistance of $3 \times 10^{15}\,\Omega$. Due to the guarding, the settling time of the current is very low, below 10 s even for very large voltage steps of 100 V. Very low noise measurements of the current can be performed by the SMU, with a maximum accuracy of around 50 fA, as depicted in Figure 4.1.5.

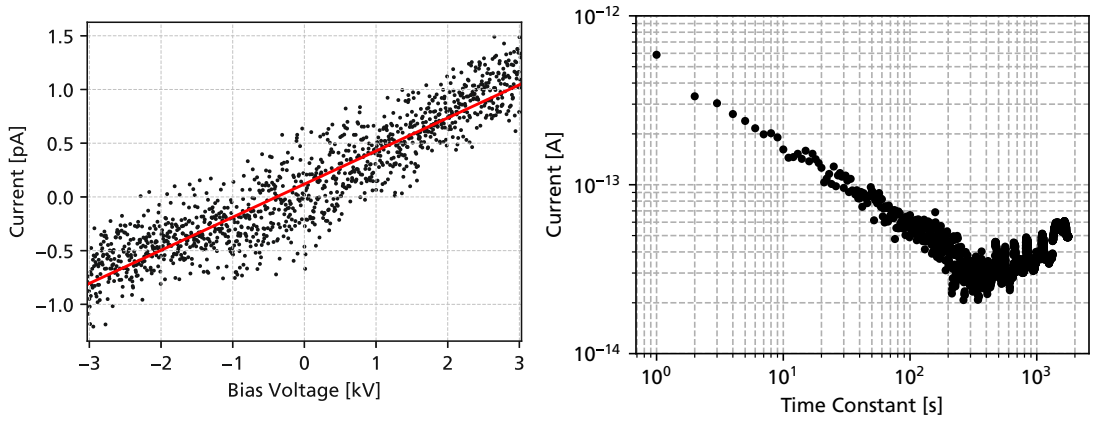

Figure 4.1.5: Left: I-V measurement of an empty chuck up to a voltage of ±3 kV with a linear fit of the leakage current (red). Right: Allan deviation of the current measured by the Keithley 2657A SMU at a bias voltage of 3 kV. At integration times of around 20 s, a current noise below 100 fA can be obtained.

High-Voltage Protection Modules

Although the measurement setup and chuck itself demonstrate a very good performance at high voltages, there still exist high-voltage risks if a device under measurement breaks down. Such a breakdown will result in a sudden decrease of the resistance of the sample, allowing a much higher current to flow, potentially damaging the sensitive electrometer and other instruments. Additionally, as the cables on the low-potential side of the circuit are only rated up to 600 V, this will present a safety risk to the human operator. Figure 4.1.6 shows a photograph of a 4H-SiC detector after a breakdown event, which can occur suddenly if the maximum rated voltage of the device is exceeded.

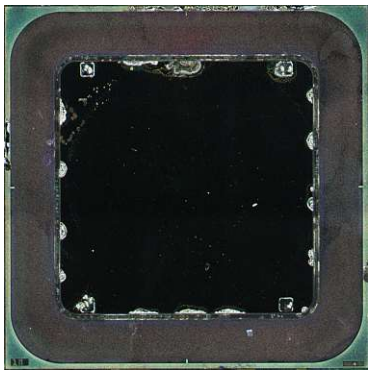

Figure 4.1.6: 4H-SiC sample after a catastrophic device breakdown at 1.6 kV. The breakdown was most likely caused by sparking in air on the surface of the sample, not inside the SiC bulk.

In order to protect the instruments (and operators), protection modules have been employed. The probe needles are connected to Keithley 2657A-PM200 protection modules, depicted in Figure 4.1.7. These protection modules clamp the voltage to a maximum of $\pm 300\,\mathrm{V}$ relative to ground, which is inside the safety limits for the cables used in the low-voltage side of the circuit. However, as a breakdown results in a very fast rise of the voltage, high currents might still be induced in the circuit before these protection modules can act, potentially damaging the electrometer. Therefore, an additional protection circuit has been implemented for the electrometer, depicted in Figure 4.1.7. At the input, two 1N3595 anti-parallel rectifying diodes bypass the input of the electrometer if a significant voltage difference relative to ground is induced by a device breakdown. These diodes have been specifically chosen for a low leakage current, as the voltage burden of the electrometer (although extremely low, below $15\,\mu\mathrm{V}$) can result in a DC current through the diodes [76]. After the diodes, a current-limiting resistor is employed, in case the maximum forward current of the anti-parallel diodes is exceeded. For measurements with large currents ($> 1\,\mathrm{mA}$), such as forward I-V curves of diodes, the protection module needs to be removed because of its series resistance.

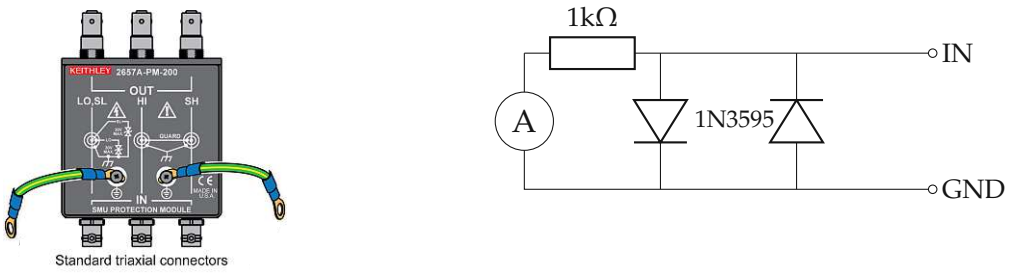

Figure 4.1.7: Left: Keithley 3kV protection module [164]. Right: Electrometer protection circuit.

4.1.2 High-Voltage Capacitance Measurements

As previously mentioned, the full depletion voltage of SiC detectors can be in the hundreds of volts, even for thin devices. For thick devices ($\geq 100\,\mu\mathrm{m}$), bias voltages $\geq 1\,\mathrm{kV}$ are typically required. In order to facilitate capacitance-voltage measurements up to $3\,\mathrm{kV}$, high-voltage bias tees have been procured from Keithley Instruments. These bias tees have recently become available as the needs of the power electronics industry have grown in accordance with the technological process in SiC Schottky diodes and MOSFETs. Figure 4.1.8 shows a schematic diagram of the 2600-RBT-200 and 2650-RBT-3K bias tees that have been acquired as a part of the CVU-3K-KIT bias tee kit [165]. The bias tee uses high-voltage capacitors to decouple the AC signal from the DC bias. Additionally, the DC input is isolated from

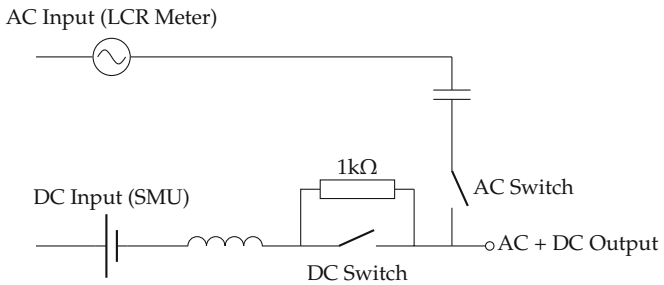

Figure 4.1.8: Simplified circuit of the Keithley2600-RBT-200 and 2650-RBT-3K bias tees.

the AC voltage by a large inductance. Two switches are available to configure the bias tees for I-V and C-V measurements. In the C-V mode, the AC signal is coupled in with a decoupling capacitor, and the DC voltage source is isolated from the AC signal by a series resistor and an inductance. In the I-V mode, the series resistor is bypassed, and the C-V decoupling capacitor is disconnected. This allows for a similar DC performance to be reached with the bias tee in place [165], removing the need to connect and disconnect cables when switching between the two modalities. The switches themselves are implemented as transistors instead of the more commonly used relays, which allows for a faster switching speed as well as a longer switch lifetime. Switching between the I-V and C-V modes can be done by applying a $\pm 10\,\mathrm{V}$ DC bias voltage at the AC input, generated by the internal bias tee of the LCR meter.

Figure 4.1.9 shows a C-V measurement of a capacitor up to a voltage of 3 kV. With the triaxial guarding (and inductance shielding the SMU from the AC voltage), the leakage currents during C-V measurement remained below 10 nA (likely limited by the series resistance of the capacitor). Such low leakage currents for C-V measurements allow for the current compliance of the SMU to be set much lower than usual, providing additional protection in case of device breakdown.

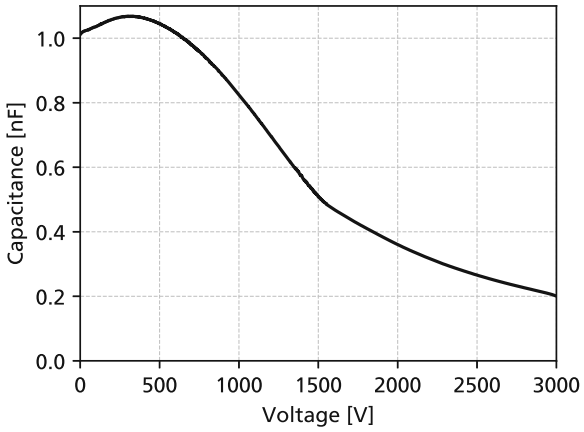

Figure 4.1.9: C-V measurement of a 6kV-rated ceramic disc capacitor with a nominal capacitance of 1 nF using a LCR frequency of 100 kHz. Due to the poor dielectric used in this capacitor (Y5U), the capacitor shows a significant voltage dependency.

4.2 UV-TCT

In the transient-current-technique (TCT), the detector signal (electrical current) is analyzed in the time domain in order to obtain detailed information about the charge carrier drift velocity, lifetime, and electric field distribution. The current induced by charge carrier drift is given by the Shockley-Ramo theorem (see Section 2.7.1):

$$I(t) = q \cdot \vec{E_w}(\vec{x}(t)) \cdot \vec{v}(t). \tag{4.2.1}$$

This technique has been applied since the 1960s in order to determine the mobility of charge carriers in silicon and other semiconductors ("time-of-flight technique" [71, 166, 167]). If the injected charge q and the weighting field $\vec{E_w}$ are known, the induced current will only depend on the local electric field, as this defines the drift velocity via the charge carrier mobility. This has been leveraged to great success to study radiation damage in silicon detectors[168, 169], using techniques where charge is injected with a laser from the side (edge-TCT [170]) or in a small focal point (two-photon absorption TCT, TPA-TCT [171]). By using lasers or heavy ions, large amounts of charge can be injected, which yields large signals and a good signal-to-noise ratio. Additionally, lasers typically feature a trigger signal, which allows for multiple waveforms to be averaged, again significantly reducing noise levels.

Figure 4.2.1 shows the laser-TCT setup at HEPHY. Two picosecond pulsed lasers are available; IR with a wavelength of 1060 nm and UV with a wavelength of 370 nm, used for 4H-SiC (compare with Section 2.4.3). Both lasers are fiber-coupled to Galilean focusing optics, which can be moved along the focus axis (Z), while the detector can be moved in the XY plane. A Peltier element and liquid chiller allow for temperature control and cooling down to $-40\,^{\circ}\mathrm{C}$, which is especially relevant for irradiated

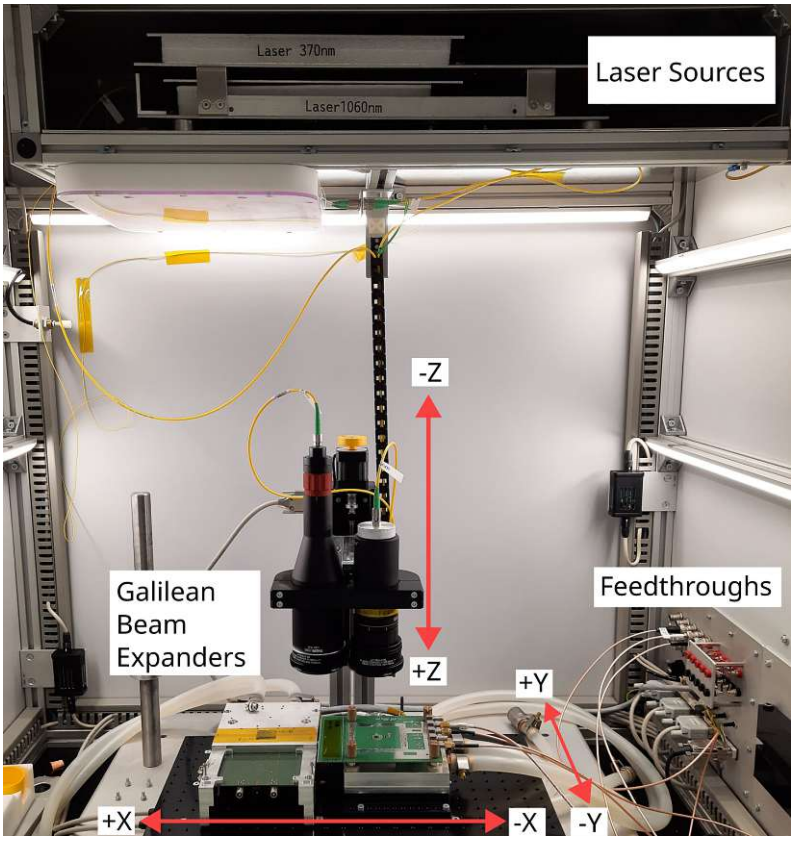

Figure 4.2.1: Laser TCT setup in the HEPHY clean room

silicon detectors. On the XY stage, a Thorlabs PM100 laser power meter is mounted, which allows for calibration and monitoring of the laser intensity. For the IR laser, fiber splitters implementing an online intensity monitoring and a splitter-delay-line are present [172]. These components also exist for the UV laser, but have been bypassed due to excessive losses between fiber couplings (as the wavelength of 370 nm is at the limit of what is possible for optical fibers). The entire setup is enclosed in a light-tight and humidity-regulated box with interlocks to the laser sources. Both of the laser drivers provide electric trigger connections, which allow individual laser pulses to be triggered externally and which send out a low-jitter trigger signal synchronized to the laser pulse. The trigger signal can be used to trigger an oscilloscope and perform waveform averaging. Figure 4.2.2 shows XY scans of the detector response obtained for a 4H-SiC PiN diode, demonstrating the spatial resolution of the system (which will be quantified in Section 4.2.2).

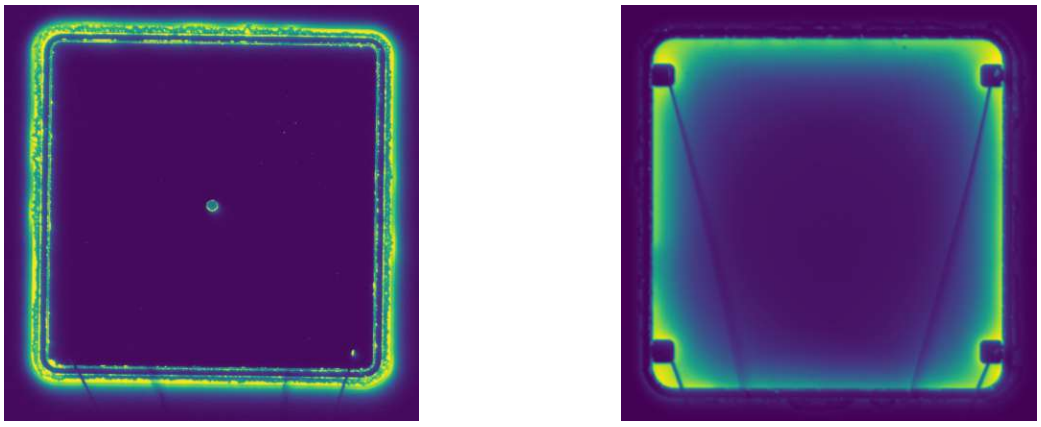

(a) Fully metallized diode. CNM Run 16886 (b) No Metal. CNM Run 13575

Figure 4.2.2: XY UV-TCT scans depicting the signal amplitude for $3 \times 3\text{mm}^2$ 4H-SiC PiN diodes wire-bonded to the UCSC LGAD readout board. The diode on the left is covered completely by metal (except for a hole in the center). The diode on the right has no metallization on the active area, only around the edge and for the bond pads. Here, a decrease of the signal amplitude with the position is visible, which is due to the resistivity of the p-implant [173]. For both samples, shadows of the bond wires are visible.

4.2.1 Energy Calibration

In order to perform measurements at an absolute charge scale (or to compare different measurements), the power delivered by the laser must be known precisely. For example, when timing measurements are performed, the injected charge needs to be calibrated to correspond to the charge of an MIP. The infrared laser at HEPHY features a motorized attenuator, which can be used to reduce the laser intensity by a maximum of 60 dB [172]. However, for the UV laser, this attenuator is again bypassed to avoid power losses in the fiber couplings.

Both the IR and UV lasers (PiLas series, manufactured by NKT photonics) are based on a gain-switched laser diode, and different intensities can be obtained by changing the drive current of the gain-switching operation. This can be user-specified by the *tune* value, between 0 % and 100 %, with a tune of 0 % corresponding to the highest intensity. Changing the tune value allows for a fast way to change the laser intensity, without the need to modify any optical components. Figure 4.2.3a shows a calibration measurement performed for the 370 nm UV laser using a Thorlabs PM100 power meter with a S150C sensor. Up to a tune value of 5 %, the power-per-pulse delivered by the laser is constant,

at almost 6 pJ. For higher tune values, the power starts to decrease linearly, up to around 45 %, after which the decrease in power accelerates. It has to be noted that the power not only depends on the tune value, but also on the frequency, as depicted in Figure 4.2.3b. While the power is almost constant in the range of 1 kHz to 1 MHz, a pronounced peak in power is apparent at 20 MHz, before decreasing again towards the maximum repetition rate of the laser (40 MHz). Therefore, care should be taken, that if the laser intensity is tuned to correspond to a MIP equivalent, the same laser repetition rate is used for all measurements.

Figure 4.2.4 shows a long-term measurement of the power delivered by the UV laser on a SiC PiN diode. For integration times up to 10 s, the laser stability is better than 1 %. At even longer averaging times (1000 s), the variations of the laser power can be further reduced, before long-term fluctuations start to dominate.

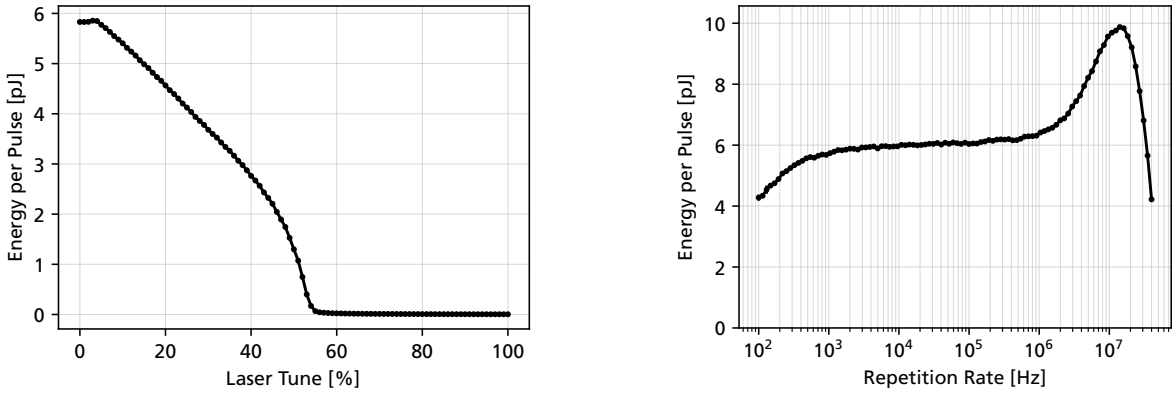

(a) Tune dependence at 1 kHz

(b) Frequency Dependence at tune 0 %.

Figure 4.2.3: Dependency of the energy per pulse delivered by the 370 nm PILAS PIL 1-037-40FC laser as a function of the laser tune value and repetition rate.

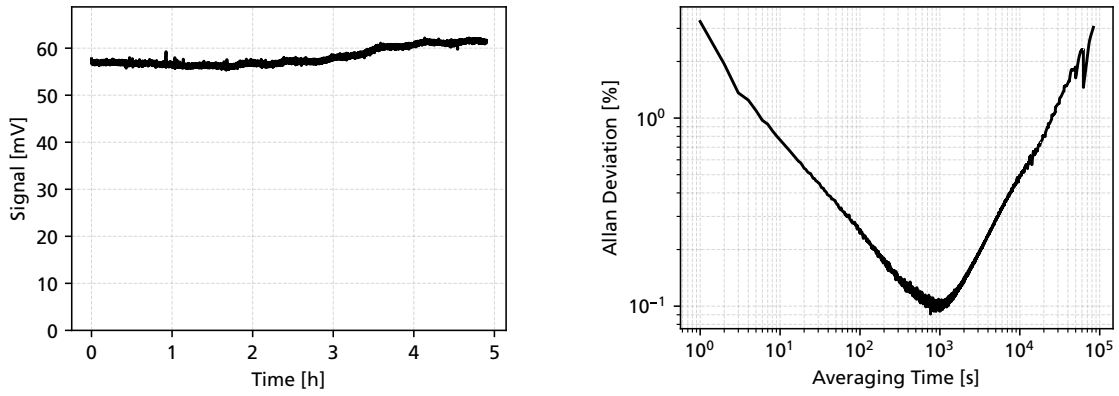

(a) Laser intensity over time

(b) Relative Allan deviation

Figure 4.2.4: Typical long-term stability of the laser intensity at a repetition rate of 10 kHz and tune 0 %. The laser intensity (signal) has been measured by the signal amplitude of a SiC-LGAD manufactured by OnSemi on a UCSC LGAD readout board. During the measurement, the temperature in the clean room stayed constant at $(22.0 \pm 0.1)\,^{\circ}\mathrm{C}$.

4.2.2 Beam Profile Characterization

As detector structures and features can be very small (below 10 µm), good focusing optics are required in laser TCT. Modern stepper motors (as are used in the TCT setup at HEPHY) can achieve a movement precision of 1 µm (or below), and the achievable spatial resolution will typically be limited by the width of the laser beam. The intensity I of a laser beam in the fundamental (TEM_{00}) mode can be described by [174]

$$I(x,y,z) = I_{max} \exp\left(\frac{-8(x^2+y^2)}{w(z)^2}\right), \qquad I(r,z) = I_0 \frac{w_0}{w(z)} \exp\left(\frac{-2r^2}{w(z)^2}\right). \tag{4.2.2}$$

The width of the beam along its direction of travel, $w(z)$ is given by

$$w(z) = w_o \sqrt{1+\left(\frac{z}{z_R}\right)^2}, \qquad z_R = \frac{\pi w_0^2 n}{\lambda}, \qquad \theta = \frac{w_0}{z_R}. \tag{4.2.3}$$

where w_0 is known as the beam waist, z_R as the Rayleigh length (the distance after which the area of the beam has doubled), and θ the divergence. Figure 4.2.5a depicts the intensity distribution of a Gaussian laser beam, highlighting the influence of the beam parameters. For a larger Rayleigh length, the beam width will remain close to the beam waist for a longer distance, which equates to a lower divergence. The focusing optics at the HEPHY laser-TCT setup use a Galilean beam expander (a combination of a diverging and converging lens) in order to decrease the divergence, at the cost of an increased beam diameter. A low beam divergence is necessary for the beam width not to significantly change inside a detector (with a thickness of up to 300 µm).

Experimentally, the beam parameters for a Gaussian beam can be obtained using the *knife-edge* technique. Here, a sharp edge is used to partially block the laser beam. The convolution of the Gaussian laser beam with the knife edge will then result in an intensity profile described by the error function, as shown in Figure 4.2.5b. By either fitting the error function or taking the derivative with respect to the distance, a description of the Gaussian beam profile can be obtained.

Figure 4.2.6 shows the measured beam width in both X and Y axes, measured using the knife-edge technique on the bond pad of a 4H-SiC detector. Step sizes of 2.5 µm have been used, and the intensity of the laser has been measured as a DC current induced in the detector bias. By using different distances from the optimal focus (in Z), Equation (4.2.3) can be fitted in order to extract the beam parameters, which are indicated in Figure 4.2.5. For both the X and Y axes, a 1-σ beam waist of around 30 µm is obtained, with a Rayleigh length of 0.4 mm.

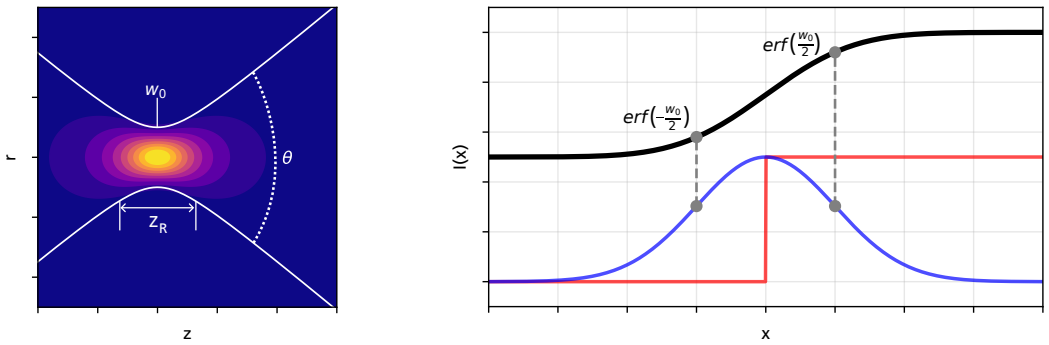

(a) Two-dimensional view of the laser intensity at the beam waist with a diameter of w_0

(b) Convolution of a Gaussian beam profile with a step function, resulting in the error function.

Figure 4.2.5: Intensity profile and knife-edge technique for a Gaussian laser beam.

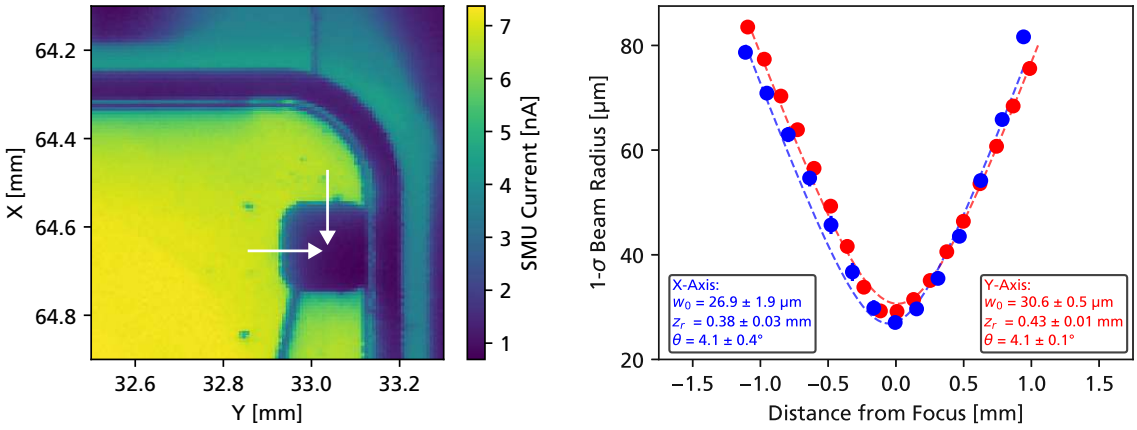

(a) Scan direction over metalized bond pad

(b) Fitted 1-σ beam radius and beam parameters.

Figure 4.2.6: Beam width measurement on a 4H-SiC PiN diode using the bond pad as a knife edge. The rest of the detector is not covered by any metal and is transparent to the UV laser.

4.2.3 Temporal Profile

While gain-switched lasers can provide pulses as short as picoseconds, the exact temporal profile will depend on how fast charge carriers are injected and how fast they recombine [175]. This means that the exact temporal profile can change for different operating conditions, for example, by changing the tune value of the laser. Figure 4.2.7 shows the typical pulse widths obtained for different tune values at a laser repetition rate of 40 MHz, as measured by the manufacturer. At higher tune values (45 %), the full-width half maximum is around 40 ps, increasing to 58 ps for a tune value of 45 %. Even though the FWHM is short, a pronounced tail pulse can be observed for low tune values. While for slower readout electronics (with a bandwidth of less than 2 GHz), i.e., a rise time larger than 180 ps) this is not an issue it can affect measurements of faster readout electronics.

Figure 4.2.8 shows a measurement of a 4H-SiC detector read out by a broadband low-noise amplifier with a bandwidth of about 6 GHz (which will be detailed in Section 6.5). By taking the derivative in time, the temporal profile of the charge injection can be obtained. An ideal laser pulse will be sufficiently short

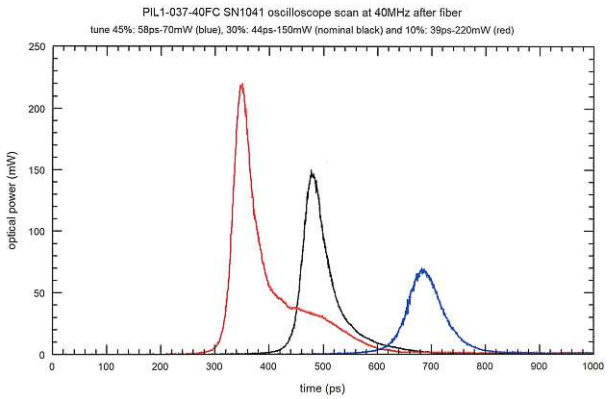

Figure 4.2.7: Test report data for the pulse widths of the PILAS PIL 1-037-40FC54750A UV laser measured by the manufacturer using a Newport 1024 fiber-optic detector [176].

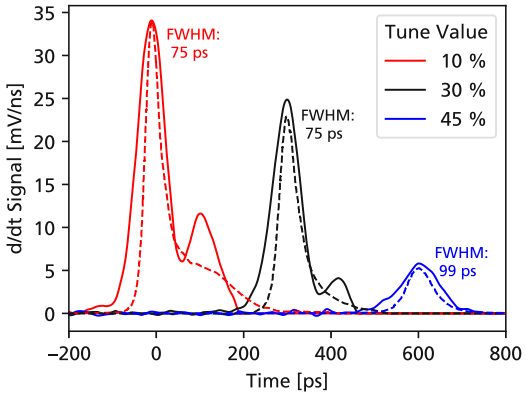

Figure 4.2.8: Slope of the rising edge for 1kHz UV-TCT beams in a 4H-SiC PiN diode read out with a bandwidth of 6 GHz (solid lines). The time profile of the laser pulse measured by the manufacturer for a repetition rate of 40 MHz is indicated using dashed lines. The second peak for tunes 10 % and 45 % likely originates from an inductive resonance in the detector readout (see Section 6.5).

such that the rise time (or instrument response function) will only depend on the readout electronics. For tunes 10 % and 30 %, the FWHM of the measured signal stayed constant. However, after increasing the tune to 45 %, an increase of the FWHM to 99 ps was observed. As the readout electronics are the same for all measurements, this indicates that the laser pulse is slower than the impulse response of the readout electronics at high tune values.

4.2.4 Trigger Jitter Characterization

As previously mentioned, the laser controller for both the IR and UV lasers provides a trigger signal, which has a very low jitter relative to the laser pulse ($<$ 3 ps according to the manufacturer [176]). In order to quantify how accurate the laser trigger is, measurements were performed using a 4H-SiC detector, comparing the timestamp obtained from the detector to the laser trigger signal. For the IR laser, this has been previously performed using a silicon LGAD, reaching a minimum jitter of 5.5 ps [172].

Figure 4.2.9 shows a typical UV-TCT detector signal, together with the laser trigger signal. A small area detector with a capacitance of 70 fF and a thickness of 50 µm was used, read out by the UCSC LGAD board (detailed in Section 3.4.5). The signal from the detector was maximized by applying a bias voltage of 500 V (ensuring full depletion) and using a laser tune value of 0 %, which corresponds to the largest power-per-pulse. In order to compute the respective timestamps, a CFD crossing of 50 % has been used, interpolating between the two samples below and above the threshold. Interpolating is necessary, as the jitter is much smaller than the resolution of the oscilloscope (25 ps for 40 GSa/s). By comparing the timestamp of the detector signal to the laser trigger, the jitter time resolution can be calculated, which reaches as low as 5 ps. This indicates that the laser trigger is very well aligned to the laser pulse, and that using the laser trigger as a time reference in the oscilloscope to average multiple waveforms is possible without any degradation of the signal.

As the signal of the detector contains only a limited bandwidth (due to the drift time of the charge carriers), the signal-to-noise ratio will decrease for higher and higher analog bandwidths. However, as will be shown in Section 2.8, this is compensated by the rising edge of the detector signal becoming steeper, as the rise time in the current of a planar sensor is essentially infinitely short. Figure 4.2.10 shows the effect of applying a digital low-pass filter on the detector signal, which has been acquired with an analog bandwidth of 16 GHz.

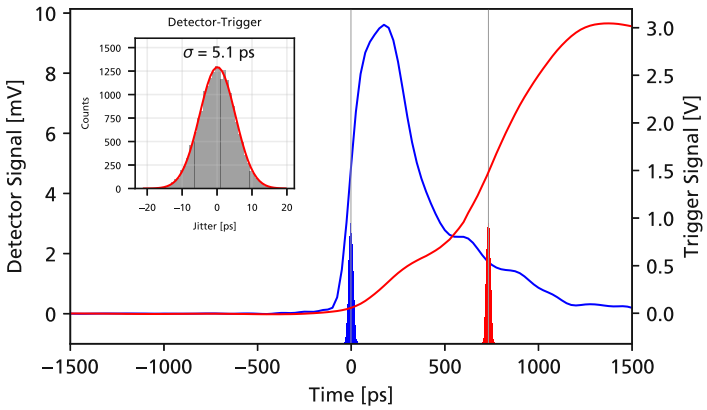

Figure 4.2.9: Averaged UV-TCT induced detector signal (blue) and laser trigger signal (red). For both signals, the 50 % CFD crossing time is indicated by a vertical line, together with a histogram of the statistical fluctuations in crossing times for 20 000 acquisitions. Digital low-pass filters with a cutoff of 2.5 GHz for the detector signal and 1 GHz for the laser trigger have been applied to achieve the optimal slope-to-noise ratio (see Figure 4.2.10). The inset shows a histogram of the difference between the detector and laser trigger timestamps.

For filter cutoffs below 1 GHz, the rise time of the signal is significantly reduced, and the jitter is increased. Above a frequency of around 2.5 GHz, the jitter is minimal and does not change significantly anymore. A small rise towards higher frequencies is observed, which could be due to the spectral noise density increasing towards higher frequencies. For the laser trigger signal, a similar study was performed, which yielded an optimal bandwidth of 1 GHz. The right-hand side of Figure 4.2.10 shows the measured jitter as a function of the signal-to-noise ratio (SNR), which has been swept using different tune values of the laser. As expected (see Section 5.3), for a fixed signal rise time, the jitter scales as $\propto 1/\mathrm{SNR}$. Below an SNR of 5, no jitter could be calculated, as this SNR is insufficient to distinguish a detector signal from noise. For the highest SNR ($\sim$25), the jitter is still decreasing; however, it is expected to converge towards a fixed value given by the intrinsic jitter of the laser trigger signal relative to the laser pulse.

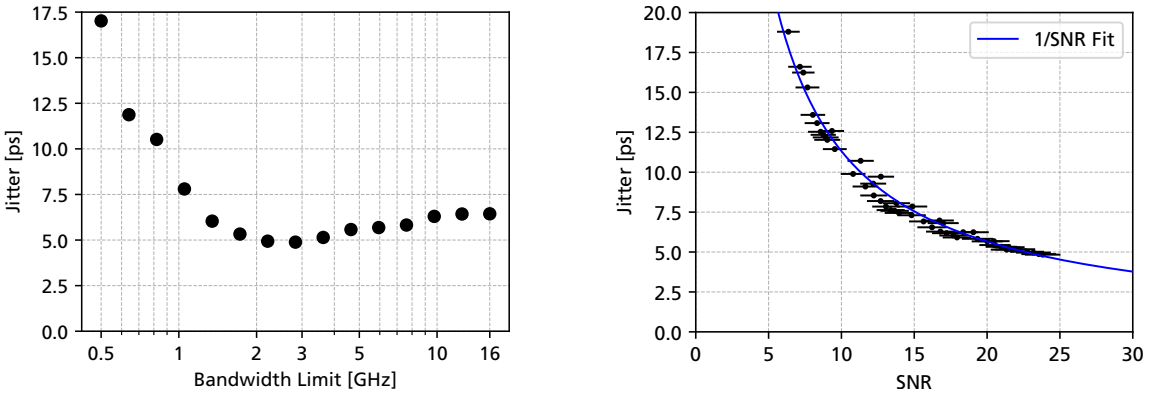

Figure 4.2.10: Left: Measured jitter between the detector signal and the laser trigger as a function of the analog low-pass filter cutoff applied to the detector signal and as a function of the SNR. Right: Jitter vs. SNR for an optimal low-pass filter (2.5 GHz).

4.3 Alpha Spectroscopy

Alpha particles from radioactive sources provide a convenient way to test detectors in a laboratory setting, as they deposit a large energy ($\sim 5\,\mathrm{MeV}$) and are monochromatic in energy [57]. However, due to their low momentum (compared to high-energy ion beams), alpha particles are readily stopped in air for distances less than 5 cm. Therefore, either a very small distance to the detector, or more preferably, a vacuum, is required. As a part of this thesis, a new vacuum setup for alpha spectroscopy (shown in Figure 4.3.1) was planned, procured, and built [177].

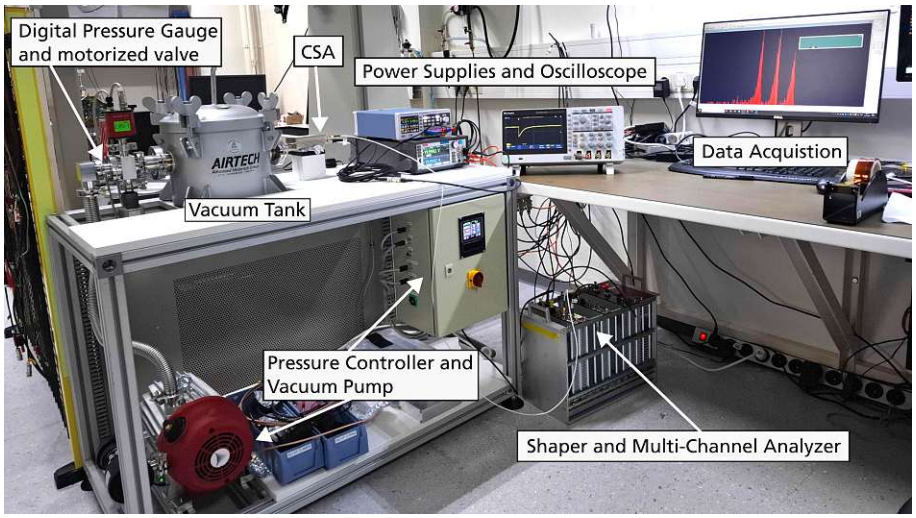

Figure 4.3.1: Newly built alpha spectroscopy setup in the HEPHY clean room.

The setup features a vacuum tank with a volume of approximately 10 L, with a feedthrough for 4 SMA connectors. Together with a Pfeiffer RPT200 pressure gauge, a valve to the surrounding air (Pfeiffer EVR116) can be used to leak air into the vacuum tank, allowing the pressure to be regulated in between 500 mbar down to 5×10^{-3} mbar using a PID controller. Different charge-sensitive amplifiers are available to perform spectroscopic measurements, a Cx-L amplifier [179] manufactured by Cividec, as well as an Amptek CoolFET [180]. Additionally, an Ortec shaper and multi-channel analyzer can be used to directly capture energy spectra.

Figure 4.3.2 shows the radioactive source that was procured for alpha spectroscopy measurements. It features three nuclides (^{239}Pu,^{241} Am,^{244} Cm), with decay energies that are spaced approximately

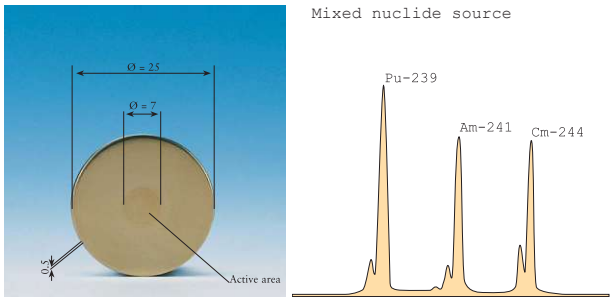

Nuclide	Energy [keV]	Rel. Intensity [%]
^{239}Pu	5105.5	11.9
^{239}Pu	5144.3	17.1
^{239}Pu	5156.6	70.8
^{241}Am	5388.0	1.7
^{241}Am	5443.8	13.1
^{241}Am	5482.6	84.8
^{244}Cm	5762.6	23.1
^{244}Cm	5804.8	76.9

Figure 4.3.2: Left: Mixed-nuclide source for alpha spectroscopy produced by Eckert&Ziegler [178]. The source contains three nuclides with an approximate activity of 1 kBq each. Right: Relevant decay energies [178].

0.5 MeV apart. As any dead material on top of the alpha-emitting nuclides will result in absorption (and an increase of the energy spread [181]), the nuclides are electrochemically deposited in an extremely thin layer, which allows for line widths down to 20 keV FWHM to be reached [178]. The alpha source, with a combined activity of around 3 kBq, is contained in a custom-made aluminum source holder with a collimator, ensuring that the alpha particles hit the detector at a perpendicular angle. Using an HPK s3590-19 photodiode together with the CoolFET amplifier and a shaping time of 2 µs, FWHM linewidths of 22 keV have successfully been obtained.

4.3.1 Vacuum and Pressure Control

Due to the typical high epi-doping of 4H-SiC diodes ($\gtrsim 1 \times 10^{14}\,\mathrm{cm}^{-3}$), bias voltages of more than 100 V are necessary for full depletion. For irradiated sensors, even higher electric fields are required to minimize charge losses due to trapping. Already at air pressure, bias voltages of 1 kV present special challenges, and require adequately rated components (capacitors) to avoid dielectric breakdown. Going to lower gas pressures will increase the mean-free path of air ions between collisions, and if the mean free path is sufficiently long that the ions can gain enough speed in an electric field to ionize further gas molecules, this will lead to an avalanche, akin to impact ionization in semiconductors (see Section 2.2.5). At very low pressures, the mean free path will further increase, however, fewer and fewer gas molecules will be available for collisions, which makes impact ionization less likely. The electric field required for an avalanche breakdown in air (which first decreases with pressure, before increasing again) can be described by Paschen's law [182].

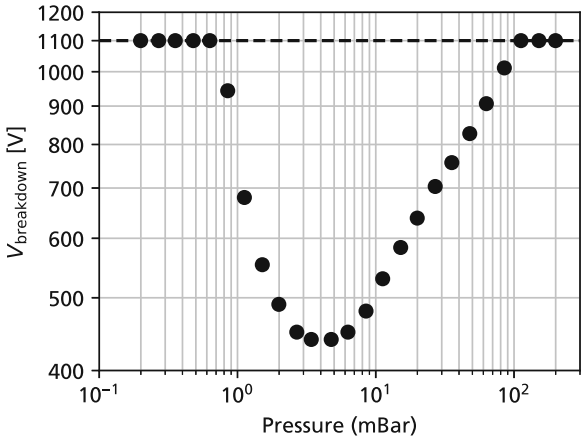

Figure 4.3.3: Breakdown voltage as a function of pressure for 1206 SMD capacitors. Above 100 mbar and below 0.5 mbar, the breakdown voltage is limited by the maximum voltage of the SMU.

Figure 4.3.3 shows a measurement of the breakdown voltage for 1206 SMD capacitors on the UCSC LGAD board. For each pressure (adjusted by changing the PID set-point of the pressure controller), the bias voltage of the PCB (without any sensor) was increased in 5 V steps, until the compliance of the source measure unit was triggered by a breakdown event. A minimum breakdown voltage of 400 V is reached at around 5 mbar. Only at a pressure of less than 1 mbar, a breakdown voltage of more than 1 kV is again achieved, which highlights the necessity of a good vacuum, even though the absorption of alpha particles in the residual air might already be negligible at mbar pressures [177]. The breakdown voltage (as described by Paschen's law) does not depend on the pressure alone, but also on the distance between the electrodes. If, for example, smaller capacitors are used, the bias voltage required for a breakdown will also shrink.

4.4 Ion Beams at MedAustron

The ion therapy facility MedAustron [183, 184] features a synchrotron that can accelerate protons, carbon ions [185] and helium ions [30]. MedAustron has four beamlines, with three irradiation rooms dedicated to the treatment of patients, and one irradiation room (IR1) available for non-clinical research [29]. Figure 4.4.1 shows a picture of IR1, where detector characterization studies can be carried out. All irradiation rooms feature a beam nozzle with an integrated dose-delivery system that can be used to deliver a precise dose (or particle count) to different positions using steering magnets [186, 187]. The minimum and maximum beam energies that can be achieved are shown in Table 4.1.

Particle	Minimum Energy [MeV/u]	Maximum Energy [MeV/u]
Protons	62.4	252.7/ 800*
Carbon	120.0	402.8
Helium	62	403

Table 4.1: Overview of clinical beam energies available at MedAustron [188].

The highest energy available is for protons at 800 MeV (used only in non-clinical research), which is limited by the thickness of the radiation shielding of the irradiation room. At this energy, protons are not yet minimum-ionizing particles (which requires about 2.4 GeV [189]), and their energy loss is equivalent to around 1.2 MIPs [190]. In clinical operation, an entire synchrotron spill (containing 10^{10} protons) is extracted in about 10 s, which leads to very high (GHz) particle rates. As most particle detectors (and readout electronics) can not cope with such high hit rates, *low-flux* operation modes have been commissioned for protons and helium ions, which can reduce the particle flux to MHz or even kHz rates, thereby avoiding pile-up [191].

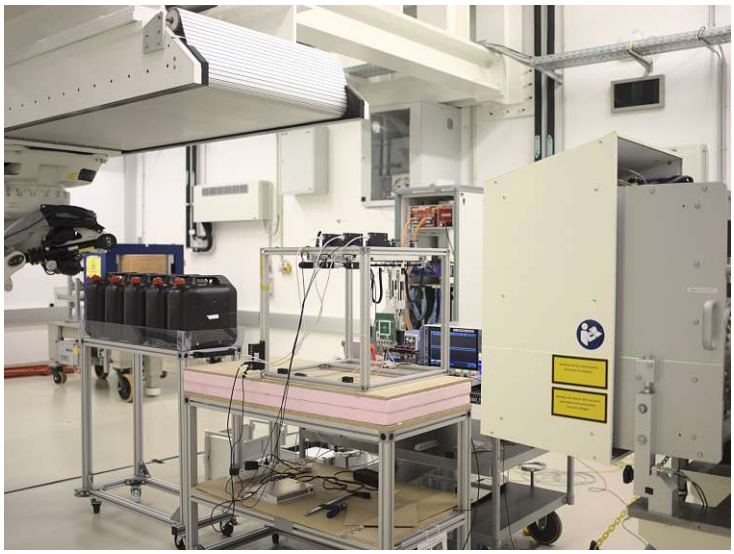

Figure 4.4.1: IR1 Beamline at MedAustron. The beam enters from the right side through the nozzle containing the dose-delivery system. In the isocenter, a detector mounted on a UCSC LGAD board is visible. Photo credit: Simon Waid.

5 Simulation of Silicon Carbide Detectors

Simulations are an essential part of detector research and development. Typically, manufacturing a prototype sensor in a semiconductor process can take six months or more, depending on the process technology and complexity. For the silicon carbide wafers produced as a part of the RD50-SiC-LGAD project (detailed in Section 6.3), the first samples only arrived in mid-2024, although the design was submitted for production a year before that. Therefore, it is imperative that different designs are simulated and validated as far as is possible in simulations before a first physical prototype sensor is produced. Simulations can also provide detailed insights into semiconductor devices, which are impossible (or very hard) to obtain experimentally, allowing for a deeper understanding and optimization of the detector.

Detector simulations in high-energy physics are typically split up into two parts: The first type uses Technology Computer-Aided Design (TCAD) tools to simulate the electrical performance of the detector and to validate that the design is working. These simulations can also cover the production and processing of the devices, for example, simulating the ion implantation or dopant diffusion processes. The second type of simulation is Monte-Carlo simulations, which aim to quantify the performance of a complete detector in response to different types of ionizing radiation. As the energy loss of ionizing radiation in matter is stochastic (see Section 2.4.1), these simulations typically require large amounts of statistics, which is not possible to do in TCAD tools. Additionally, the simulations might include multiple layers of detectors in complex arrangements, allowing for the full reproduction of an experimental setup and assessing the performance in conditions close to the real world.

In this thesis, the focus is on the second type of simulations, Monte-Carlo simulations of 4H-SiC detectors performed using Allpix^2. Section 5.1 will first introduce the Allpix^2 simulation framework, after which the necessary simulation input to simulate 4H-SiC is presented in Section 5.2. With 4H-SiC implemented in Allpix^2, measurements of PiN diodes are compared to simulations in Section 5.3. Furthermore, SiC-LGADs are simulated in Section 5.4, and the results are compared to TCAD simulations. Finally, the time resolution of PiN diodes and LGADs based on wide-bandgap materials is compared to silicon in Section 5.5. Results are presented for the jitter contribution to the time resolution, as well as the time resolution limit due to Landau fluctuations.

5.1 The Allpix^2 Simulation Framework

Allpix^2 [192, 193] is a Monte-Carlo based detector framework written in C++, intended primarily for simulating pixel detectors. It has been used with great success to simulate monolithic pixel sensors [194, 195] and has also found many applications in related tasks, such as 3D detectors [196], LGADs [197], and wide-bandgap materials [198–200]. Figure 5.1.1 shows an overview of the simulation process in Allpix^2.

At the beginning, the geometry of the detector is built and the interaction of ionizing radiation is simulated using Geant4 [48, 201, 202]. The resulting three-dimensional energy deposition is the starting point of Allpix^2. For each deposition, electron-hole pairs are generated according to the ionization energy ϵ_i and Fano factor of the material, which are then transported in discrete steps through the detector volume using the Runge-Kutta method. In contrast to TCAD simulations, Allpix^2 deals with individual electrons and holes instead of continuous charge distributions. The charge carrier transport takes into account the charge carrier mobility resulting from electric fields (and the doping concentration), which can be imported from TCAD simulations. If the electric field is high enough, impact ionization can be simulated as well (for example, in LGADs). It is also possible to model the effect of radiation damage

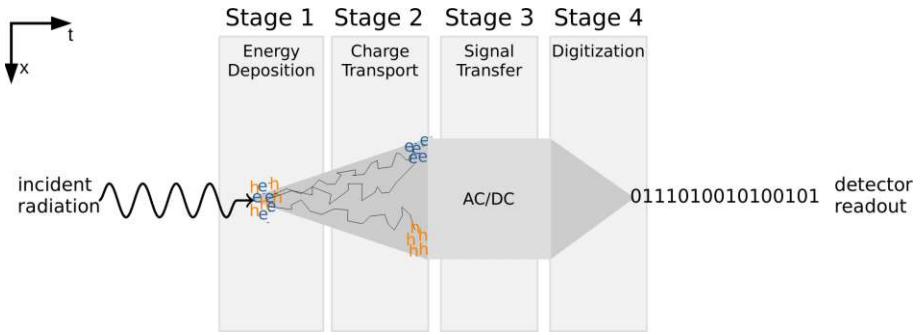

Figure 5.1.1: Overview of the simulation process in Allpix². Taken from [203].

by introducing a finite charge carrier lifetime. During the charge transport, the induced current on the readout electrodes is calculated according to the Shockley-Ramo theorem and the weighting potential of the simulated device. Allpix² can handle complex weighting potentials, with multiple electrodes next to each other (for example, in pixel detectors). The induced current can be integrated to obtain the total charge or be treated as a time-dependent signal, which can then be convolved with a user-specified front-end electronics transfer function.

Compared to TCAD simulations (where the interaction of ionizing radiation can be simulated using the *HeavyIon* model), Allpix² provides several advantages. First, Allpix² can simulate the interaction of ionizing radiation (and the production of charge carriers) in a realistic manner, which is not possible in TCAD (as no Geant4 integration exists for commercial TCAD tools). Second, Allpix² typically has a much faster execution speed than TCAD, as it assumes fixed electric fields and weighting potentials, while TCAD recalculates these for each time step. As each charge carrier is independent of the others, this allows for a high level of parallelization. Finally, as Allpix² simulates discrete quantities of electrons and holes, it is able to describe statistical fluctuations (such as in the gain of an LGAD) that TCAD is not able to.

However, there are also certain drawbacks. Allpix² is not able to simulate the interaction between individual charge carriers. At high charge densities, the electric field generated by the drifting charge carriers can shield the external field, leading to *gain suppression* in LGADs [204]. Furthermore, weighting potentials in Allpix² are fixed in time and can not accurately reproduce detectors with resistive readout elements (such as DC-LGADs), which require time-dependent weighting potentials [205] (or TCAD simulations).

5.2 Implementing 4H-SiC in Allpix²

Figure 5.2.1 shows an overview of the typical simulation workflow in Allpix². Each step of the simulation is split up into modules, and the output of each module can be saved or directly passed to the next module. In a first step, charges are created inside the detector volume, using Geant4 or other methods (such as a point charge at a fixed position). Next, the electric fields and weighting potentials are imported to prepare for charge carrier transport. For simple structures (i.e., planar detectors), Allpix² can analytically calculate these fields, but in general, fields simulated using TCAD are required. The deposited charges can then be transported in the detector volume (using the `TransientPropagation` module), where they induce a current pulse in each step. The induced pulses for each charge carrier can then be combined by the `PulseTransfer` module, before the current pulse is passed through a front-end electronics simulation (for example, using the `CSADigitizer` module). Allpix² has recently also added the possibility of writing the simulation output to a SPICE netlist, which can be used as an input to external SPICE simulations of analog amplifiers [206].

While some default values for 4H-SiC are available in Allpix^2 (for example, the ionization energy in `DepositionGeant4`), most modules require additional input from the user to work correctly for 4H-SiC (as indicated in Figure 5.2.1). In the following, an overview of the input and 4H-SiC physics models for simulations in Allpix^2 is provided.

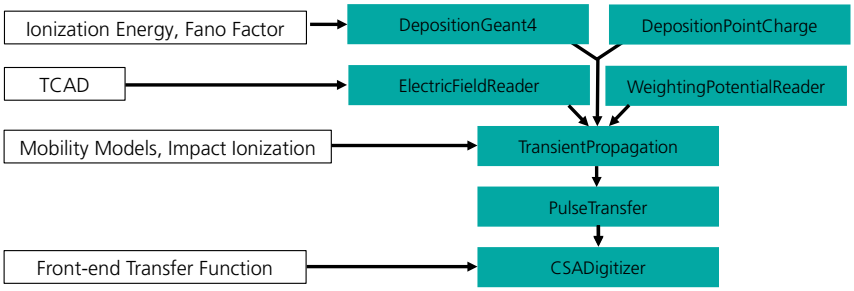

Figure 5.2.1: AllPix^2 modules and experimental input needed for simulations.

Charge Deposition

4H-SiC is modeled by Allpix^2 in Geant4 as a homogeneous mixture of Si and C, with a density of 3.21 g/cm^3. To use 4H-SiC as a detector material, the key `sensor_material = "silicon_carbide"` can be passed to the detector configuration. Additionally, the ionization energy (ϵ_i) can be adjusted in the `DepositionGeant4` module in order to agree with the most recent experimental values (see Section 6.4 and [46]). The default Fano factor used by Allpix^2 for 4H-SiC is 0.1 [207]. Additionally, the photo-absorption ionization (PAI) model can be enabled, which better describes the charge deposition in very thin detectors ($< 50\,\mu$m) [208].

```
[Geant4Deposition]
charge_creation_energy = 7.83eV
fano_factor = 0.1
enable_pai = true
```

Figure 5.2.2: Input to the `Geant4Deposition` module for 4H-SiC.

TCAD Electric Fields and Weighting Potentials

While for simple planar devices, Allpix^2 can calculate the electric and weighting potential analytically, more complex devices typically require TCAD simulations to compute these fields. For example, the electric field might be impacted by a highly-doped gain layer (for LGADs), or the weighting potential could be non-trivial due to segmented electrodes (for pixel sensors). In order to import simulated electric fields (and other quantities, such as the doping concentration), Allpix^2 offers the `meshconverter` tool. This tool can read in TCAD data in the *DF-ISE* format and convert it to a format appropriate for Allpix^2. Text-based data formats can be imported as well. Figure 5.2.3 shows an imported electric field and weighting potential for a SiC-LGAD. The weighting potential has been computed by subtracting the electrostatic potential from two simulations that were performed 1 V apart. As the simulated device geometry is planar, the weighting potential is linear.

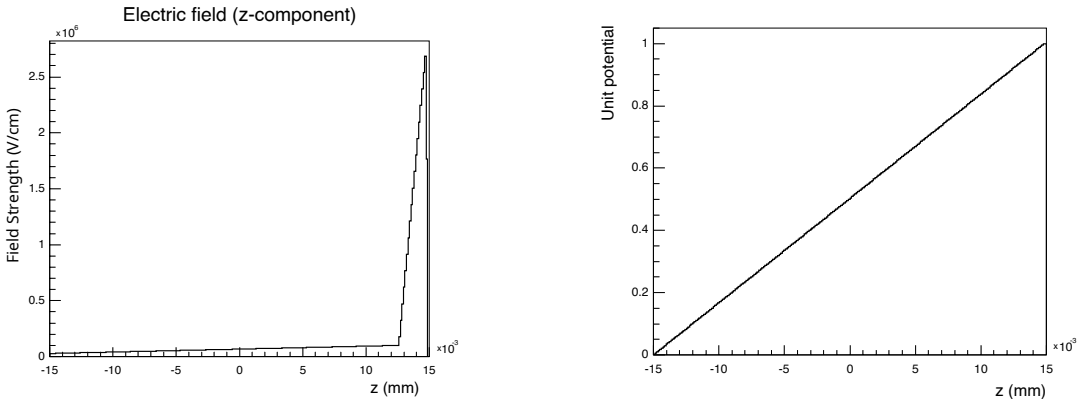

Figure 5.2.3: Left: Electric field of a SiC-LGAD imported into Allpix². At the top of the device (positive z-coordinates), the high electric field of the gain layer is visible. Right: Imported weighting potential. For a simple device in a planar geometry, the weighting potential is linear.

Mobility Models

For 4H-SiC, no default charge carrier mobility models are available in Allpix². Custom mobility models can be implemented in two ways: Either by implementing an additional material for already existing mobility models in the source code (such as the Canali or Arora model), or by implementing it as a "custom" mobility model in the `TransientPropagation` module. A "custom" mobility model can be defined directly in the simulation configuration and requires no changes to the code (which avoids the need to recompile the Allpix² framework if any changes are made). Figure 5.2.4 shows the electron and hole mobility model configurations for 4H-SiC used in this thesis. The low-field mobility is calculated using the Masetti model [67, 68], and the high-field velocity saturation using the Caughey-Thomas model [70]. Plots of both mobility models can be found in Section 2.2.4. The low field mobility depends on the doping concentration, which can be imported from TCAD simulations using the `DopingProfileReader` module. If no doping profiles are available, a constant doping profile can be defined by using the option `model = "constant"`.

```
[TransientPropagation]
mobility_model = "custom"

# mu_low = mu_min + (mu_max - mu_min) / (1 + (N/N_ref)^alpha)
# mu = mu_low * 1 / (1 + (mu_low * E / vsat)^beta)^(1/beta)
mobility_function_electrons = "([0] + ([1]-[0]) / (1 + pow(y/[2], [3]))) / pow(1 + pow(([0] +
    ([1]-[0]) / (1 + pow(y/[2], [3]))) * x / [4], [5]), 1/[5])"
mobility_function_holes = "([0] + ([1]-[0]) / (1 + pow(y/[2], [3]))) / pow(1 + pow(([0] +
    ([1]-[0]) / (1 + pow(y/[2], [3]))) * x / [4], [5]), 1/[5])"

# Parameters: mu_min, mu_max, N_ref, alpha, vsat, beta
mobility_parameters_electrons = 20cm*cm/V/s, 1140cm*cm/V/s, 2e17/cm/cm/cm, 0.64, 1.70e7cm/s,
    1.1
mobility_parameters_holes = 20cm*cm/V/s, 125cm*cm/V/s, 6.4e18/cm/cm/cm, 0.72, 1.3e7cm/s, 1.2
```

Figure 5.2.4: Custom mobility model used for 4H-SiC in Allpix². The electric field enters as `x` and the doping concentration as `y`. The mobility parameters have been taken from [67, 68] and [70].

Impact Ionization

Similarly to the mobility models, the impact ionization coefficients can also be implemented in the `Transient Propagation` module as a custom model, depicted in Figure 5.2.5. Here, the parameters found in [74] were used, which are plotted in Section 2.2.5. In addition to the impact ionization coefficients, a threshold electric field can be defined, below which no impact ionization will be calculated. This helps save computation time in areas of the detector where no impact ionization is expected. Additionally, a maximum multiplication level can be defined to avoid infinite loops for simulations close to the breakdown voltage.

```
[TransientPropagation]
multiplication_model = "custom"
multiplication_threshold = 1000kV/cm
max_multiplication_level = 5

multiplication_function_electrons = "[0] * exp(-pow([1] / x,[2]))"
multiplication_function_holes = "[0] * exp(-pow([1] / x,[2]))"

multiplication_parameters_electrons = 2.78e6/cm, 1.05e7V/cm, 1.37
multiplication_parameters_holes = 3.51e6/cm, 1.03e7V/cm, 1.09
```

Figure 5.2.5: Impact ionization model in Allpix^2 based on [74].

5.3 Simulation of SiC PiN Diodes

With the material properties of 4H-SiC, implemented in Allpix^2, simulations of PiN diodes can be performed and compared to experimental results. One of the first simulations that were performed aimed at reproducing the timing jitter of a $3 \times 3\,\mathrm{mm}^2$ PiN diode manufactured by CNM in run 13575 (which will be detailed in Section 6.2). This work was partially performed as part of a Master's thesis [209] and has been presented at the 4th Allpix^2 User Workshop [200]. The simulated diode features a 50 µm thick epitaxial layer, with a doping concentration of $1.5 \times 10^{14}\,\mathrm{cm}^{-3}$ and a full depletion voltage of approximately 400 V. From C-V measurements, the doping concentration of the bulk was extracted and imported into TCAD to simulate the electric field as an input to Allpix^2. Measurements of the charge-collection efficiency were performed using a UV laser (see Section 4.2 for a description of the experimental setup).

The diode was read out using the UCSC LGAD single-channel readout board (see Section 3.4.5). Because of the high capacitance of this large area diode (around 18 pF), the bandwidth of the readout electronics was limited by *RC* effects. This meant that the measured waveforms are identical to the impulse response of the amplifier, as the transient current of the detector is too short for the readout electronics to properly resolve. In Allpix^2, the impulse response of the UCSC LGAD readout board, previously measured using a sine-sweep and an SMD capacitor mimicking the detector capacitance (see Section 3.4.5), was imported into the `CSADigitizer` module. After the simulation, white noise was added to the waveforms. The charge deposition was simulated using a uniform deposition along a line, which is a reasonable approximation to a UV laser beam in 4H-SiC. Figure 5.3.1 (left) shows typical measured and simulated waveforms, which agree very closely.

The measured charge collection efficiency (CCE) as a function of the bias voltage is shown in Figure 5.3.1 (right). The CCE has been computed by the amplitude of the waveforms, which is proportional to the charge collected by the detector (as the amplifier acts as a fast charge-sensitive amplifier). With higher and higher bias voltages, the depletion width of the detector grows, and so does the collected charge, until full depletion is reached. A good agreement is obtained between the Allpix^2 simulations

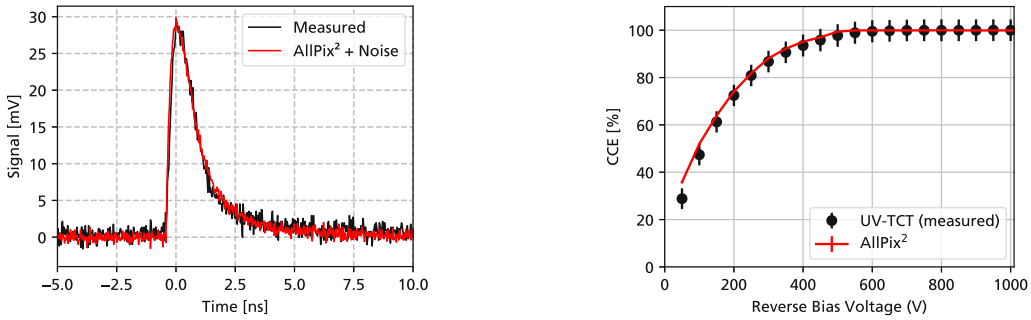

Figure 5.3.1: Left: Measured UV-TCT waveforms of a 4H-SiC diode at a reverse bias of 1 kV on the UCSC LGAD readout board compared to Allpix^2 simulations. Right: Measured and simulated charge collection efficiency (CCE) as a function of the bias voltage.

and the measurements. At lower voltages, a small discrepancy of around 5 % can be observed. This can be attributed to the fact that the shape of waveforms changes in the experimental measurements at low bias voltages, as the effective readout bandwidth drops with an increasing detector capacitance. For the Allpix^2 simulations, the impulse response is constant for all bias voltages and does not take into account the changing detector capacitance. For more accurate simulations, the readout electronics would need to be modeled by an equivalent circuit in SPICE, with a different detector capacitance for each bias voltage.

Figure 5.3.2 shows measurements and simulations of the jitter timing resolution. For the experimental data, the jitter has been obtained by the threshold crossing of the detector signal relative to the laser trigger using a constant-fraction discrimination of 50 % (see also Figure 4.2.10 in Section 4.2.4 for a comparable measurement). A bias voltage of 1000 V has been applied to the detector, and the signal-to-noise ratio has been swept by changing the tune value of the laser. For the detector waveforms simulated in Allpix^2, white noise has been added, and the amount of injected charge has been tuned to reproduce the experimentally measured jitter values.

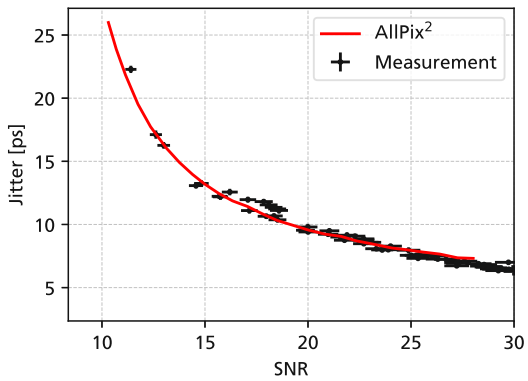

Figure 5.3.2: Measured and simulated UV-TCT jitter time resolution at a bias voltage of 1 kV.

By importing electric fields from TCAD simulations, charge collection efficiency curves can be accurately reproduced. Furthermore, realistic detector waveforms and values of the jitter time resolution can be reproduced by importing the impulse response of readout electronics in Allpix^2. No quantitative impact of the 4H-SiC mobility models was observed in these simulations yet, as the readout electronics in the measurements are too slow (or the detector capacitance is too large) to resolve the transient current.

5.4 Simulation of SiC-LGADs

As previously discussed in Section 2.10, the high electron-hole pair creation energy of 4H-SiC, combined with the limited epitaxial thickness that can be depleted in practice, makes it very challenging to reliably detect minimum-ionizing particles (MIPs), especially if a good timing resolution is to be achieved. SiC-LGADs [18, 141] overcome this limitation by introducing a gain layer, where impact ionization provides a larger signal. While the electrical characteristics and gain can be investigated in TCAD (using the *HeavyIon* model), TCAD software lacks tools to describe the statistical nature of the energy loss of ionizing radiation in matter. Especially for timing, the fluctuations in energy loss can result in a limit of the timing resolution that can be achieved (see Section 2.8). For this reason, SiC-LGADs, which have been simulated in TCAD as a part of the RD50-SiC-LGAD project, were simulated in Allpix^2, with the results of these simulations shown in Section 5.4.2.

5.4.1 Impact Ionization in Allpix^2

In Allpix^2, impact ionization is implemented based on a Yule-Furry process [210, 211]. For each step x that a charge carrier is transported, the expected gain is computed as

$$g(E) = e^{\alpha(E)\cdot x} \quad \text{for } E > E_{\text{thresh.}} \tag{5.4.1}$$

where $\alpha(E)$ is the local impact ionization coefficient. In order to save on computational resources, impact ionization only occurs above an electric field threshold $E_{\text{thresh.}}$. The actual number of generated gain electrons (and holes) n_{gain} is then sampled according to

$$n_{\text{gain}} = \frac{\ln(u)}{\ln(1-1/g(E))} = \frac{1}{\log_u(1-1/g(E))}. \tag{5.4.2}$$

where u is randomly sampled from an uniform distribution $U \sim [0,1]$. This method of simulating impact ionization is also found in Garfield++[212], which is used in the community to simulate gaseous electron multipliers [213]. As impact ionization has only recently been added to Allpix^2, it is still not widely validated [214]. Therefore, as a first step, a simple simulation was performed to validate that impact ionization is working as expected. A 4H-SiC diode with a thickness of 1 µm and a uniform electric field was simulated. A single charge carrier (either an electron or hole) was injected into the device, and

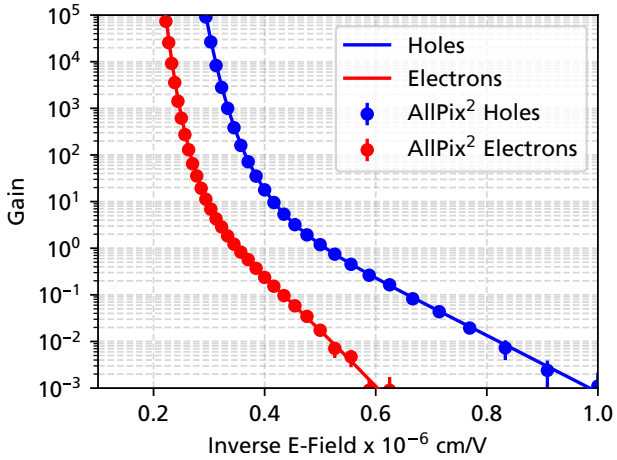

Figure 5.4.1: Simulated electron and hole gain inside a 1 µm 4H-SiC device with a constant electric field. The solid line shows a theoretical prediction based on the impact ionization coefficients [74].

the number of gain electrons and holes was calculated by averaging 10 000 events and compared to the analytically expected amount of $G = \exp(\alpha \cdot 1\,\mu\text{m})$. Electron and hole multiplication were simulated separately, by disabling the impact ionization for the other species. By averaging multiple events, a gain below 1 was able to be simulated, even if only a single electron or hole was injected.

Figure 5.4.1 shows the resulting gain-voltage curves. A very good agreement between the theory prediction and Allpix^2 simulations is found. For low electric fields, the simulation statistics are limited, as at a gain of 10^{-3} only 10 of the 10 000 simulated charge carriers undergo multiplication. As the simulated device has a uniform electric field, the step size (i.e., time step) is irrelevant. However, in realistic LGADs, which have a thin gain layer, the step size needs to be sufficiently small for the gain layer to be adequately "sampled" by the charge carrier traversing it.

5.4.2 RD50-SiC-LGAD

After verifying that the impact ionization works as expected in Allpix^2, TCAD simulations of the SiC-LGAD structure of the RD-50-SiC-LGAD project were reproduced in Allpix^2. The electric fields and weighting potentials were imported from TCAD simulations with a step size of 1 V. Figure 5.4.2 shows a cross-section of the simulated device. The SiC-LGAD consists of an epitaxial layer with a total thickness of 30 µm. The top 2.4 µm forms a gain layer with a target doping of $7.5 \times 10^{16}\,\text{cm}^{-3}$, although doping concentrations between $6.5 \times 10^{16}\,\text{cm}^{-3}$ and $8.5 \times 10^{16}\,\text{cm}^{-3}$ have been simulated. The gain layer is grown instead of implanted, as the combination of a deep implant (which requires ion implantation energies above 1 MeV) and the high doping concentration is very challenging to achieve with the commercially available implantation services. The p^{++} implant (forming the p-n junction) is directly implanted into the epitaxial gain layer. As the gain layer covers the entire wafer, it needs to be terminated to avoid a breakdown at the edge of the devices, which has been implemented using a trench. Together with the trench, a deep p^+ implant is also used to enhance the termination. The possibility for such a deep implant only became commercially available very recently, after the design of the epitaxially grown gain layer was fixed [15].

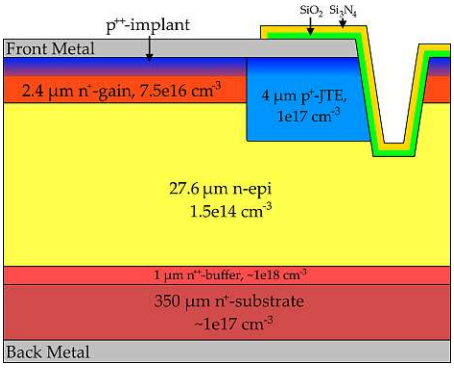

Figure 5.4.2: Cross-section of the simulated SiC-LGAD. The guarding structure at the edge of the device was not simulated. Taken from [18].

The aim of the Allpix^2 simulations in this section was to reproduce the results obtained in TCAD simulations, and to lay the foundation for more in-depth Monte-Carlo studies of the RD-50-SiC-LGAD in the future. Figure 5.4.3 shows the resulting gain-voltage curves for SiC-LGADs of different gain layer doping concentrations. A uniform deposition of charge carriers (MIP-like) and a time step of 0.25 ps has been used, and 1000 events have been simulated for each data point. The reference PiN diode (without gain) fully depletes at around 100 V, after which the collected charge stays constant. For the LGAD devices, the signal is almost zero up to the gain layer depletion around 300-400 V. After reaching full

depletion, the gain slowly grows exponentially with the bias voltage. As the gain layer doping was chosen rather conservatively (to ensure that the device can be fully depleted before a gain-layer induced breakdown occurs), the simulated gain values are in the range of 3 to 12. For gain values larger than 5, an errorbar can be observed, which is a result of statistical fluctuations in charge carrier multiplication.

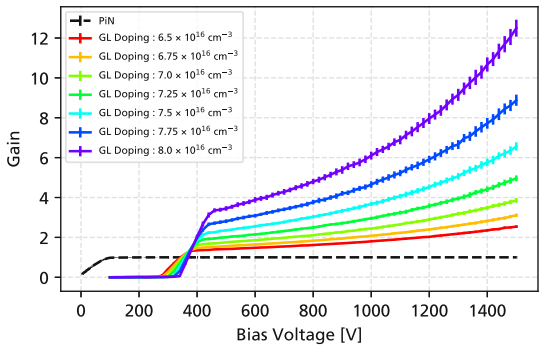

Figure 5.4.3: Gain characteristics as a function of the bias voltage for a 30 µm thick SiC-LGAD simulated in Allpix^2. The gain is calculated relative to a PiN diode with the same thickness (i.e., a gain layer doping identical to the bulk of the device).

The results are compared to TCAD simulations (using the identical impact ionization model) in Figure 5.4.4. A very good agreement can be observed. Some small discrepancies are visible around the gain-layer depletion (approximately 300 V), where the TCAD simulation predicts a higher gain than the Allpix^2 simulations do. This can be attributed to the fact that the TCAD simulations used a very long integration time (up to 10 µs), compared to the 5 ns of the Allpix^2 simulation. Such a long integration time allows for charge carriers outside the depleted volume to drift inside it and be collected at later times. As the TCAD simulations can use adaptive step sizes, such long simulation times can be implemented, which are not feasible for Allpix^2 simulations with a fixed step size.

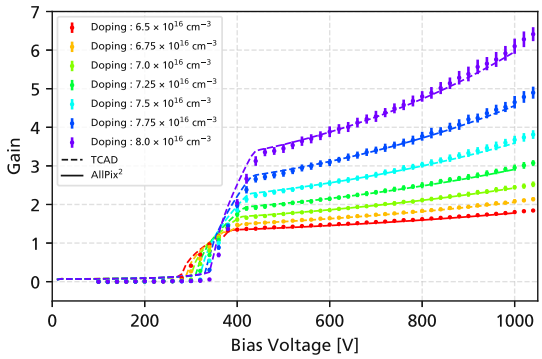

Figure 5.4.4: Comparison of the simulated gain for the RD50-SiC-LGAD design in TCAD and Allpix^2.

Figure 5.4.5 shows exemplary transient currents obtained in Allpix^2 for a gain layer concentration of $7.5 \times 10^{16}\,\mathrm{cm}^{-3}$. For low bias voltages $< 400\,\mathrm{V}$, the induced current looks similar to a device without gain, where two triangular currents are visible, attributed to the hole and electron drift. At higher voltages, the impact ionization begins to set in, and the current displays a trapezoidal shape. First, the current increases as more and more holes drift upwards to the gain layer and multiply. This continues until approximately 300 ps, where the last primary hole (in the case of 4H-SiC) reaches the gain layer.

After this, the current decreases as the gain electrons arrive at the cathode on the bottom of the device. As this device is only 30 µm thick, the signals are exceptionally fast, shorter than 400 ps for bias voltages above 1 kV.

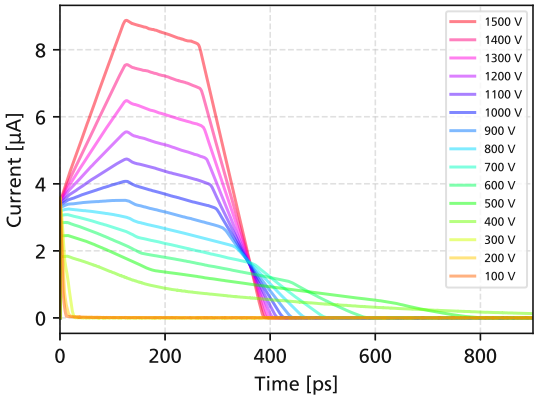

Figure 5.4.5: Transient currents simulated using Allpix^2 for the RD50-SiC-LGAD design at different bias voltages with a gain layer doping of $7.5 \times 10^{16}\,\mathrm{cm}^{-3}$.

In this section, it has been shown that Allpix^2 can be a valid simulation tool for simulating SiC-LGADs. This sets the groundwork for more sophisticated simulations in the future, for example, to study the time resolution that can be obtained for these devices (and how to improve it). However, in order to obtain realistic results, this will need experimental input of the noise levels (due to leakage currents) and specific readout electronics, as well as an experimental verification of the impact ionization models used in the simulation, in order to confidently state the performance that can be achieved. For idealized SiC-LGADs, Section 5.5.3 will provide simulations of the expected Landau timing limit.

5.5 Time Resolution of Wide-Bandgap Semiconductors

The high charge carrier saturation velocity of wide-bandgap (WBG) materials is often stated as an advantage for timing detectors [215–217]. This forms the basis of the recent work towards SiC-LGADs, which are expected to have a better timing resolution than Si-LGADs [20]. However, even though the charge carrier drift velocity is higher in WBG semiconductors (and the leakage currents are lower), the large bandgap also results in a much higher ionization energy. The aim of this section is to investigate (using Allpix^2 simulations), which time resolution can be expected from WBG detectors and how it compares to silicon detectors.

First, sensors without internal gain are investigated. For these types of sensors (especially if they are thin), the jitter time resolution usually dominates, which is quantified using a simple analytical model in Section 5.5.1. The impact of Landau fluctuations is investigated in Section 5.5.2 for different detector thicknesses. For sensors with internal gain (LGADs), the jitter contribution to the time resolution is usually not a dominating factor (if the gain is high enough) [126]. Instead, the lower time resolution limit of LGADs is given by the impact of Landau fluctuations, which has driven the push for thinner Si-LGADs [127]. The Landau limit for LGADs is simulated in Section 5.5.3 for silicon, 4H-SiC, and diamond.

A part of these results have been presented at the 2nd DRD3 week on Solid State Detectors R&D [15]. While the presented studies are based on Monte-Carlo simulations, analytical descriptions also exist, and a detailed treatise for the time resolution of silicon detectors (with and without gain) can be found in publications by Werner Riegler et al. [121, 218].

5.5.1 Jitter Time Resolution and Frequency Content of Sensors without Gain

The problem statement to be solved in timing can be formulated as a parameter estimation problem of a known signal s shifted by an unknown time τ in the presence of white noise w. The measured signal $r(t)$ is then given by

$$r(t) = s(t-\tau) + w(t). \tag{5.5.1}$$

To obtain a lower bound on the uncertainty of estimating τ, the Cramér-Rao bound [219] can be used. This bound states that any (unbiased) estimator of τ, $\hat{\tau}$ must have a variance of at least

$$\sigma_\tau^2 = \mathrm{Var}(\hat{\tau}) \geq \frac{1}{I(\tau)}, \tag{5.5.2}$$

with $I(\tau)$ the Fisher information. The Fisher information of the signal s in respect to τ is given by

$$I(\tau) = \frac{2}{N_0}\int_{-\infty}^{\infty}\left(\frac{\partial s(t-\tau)}{\partial \tau}\right)^2 dt \tag{5.5.3}$$

for a (white) noise density N_0. Using $\frac{\partial s(t-\tau)}{\partial \tau} = -\frac{ds(t-\tau)}{dt}$, this can be written as

$$I(\tau) = \frac{2}{N_0}\int_{-\infty}^{\infty}\left(\frac{ds(t)}{dt}\right)^2 dt. \tag{5.5.4}$$

The Fisher information can be written in the frequency domain (using Parseval's theorem), resulting in

$$I(\tau) = \frac{2}{N_0}\int_{-\infty}^{\infty}(2\pi f)^2|S(f)|^2 df = \frac{8\pi^2}{N_0}\int_{-\infty}^{\infty} f^2|S(f)|^2 df \tag{5.5.5}$$

for the Fourier transform of the signal $S(f) = \mathcal{F}(s(t))$. Inserting this in Equation (5.5.2) yields

$$\sigma_\tau^2 \geq \frac{1}{I(\tau)} = \frac{N_0}{8\pi^2\int_{-\infty}^{\infty} f^2|S(f)|^2\,\mathrm{d}f}. \tag{5.5.6}$$

By defining the signal power P_s as

$$P_s = \int_{-\infty}^{\infty}|S(f)|^2\,df, \tag{5.5.7}$$

the second moment of the signal normalized to the signal power (referred to as the *effective signal bandwidth* $B_{\mathrm{eff.}}$) can be written as

$$B_{\mathrm{eff}}^2 := \frac{\int_{-\infty}^{\infty} f^2|S(f)|^2 df}{\int_{-\infty}^{\infty}|S(f)|^2 df} = \frac{\int f^2|S(f)|^2 df}{P_s}, \tag{5.5.8}$$

which simplifies Equation (5.5.6) to

$$\sigma_\tau^2 \geq \frac{N_0}{8\pi^2 B_{\mathrm{eff}}^2 P_s}. \tag{5.5.9}$$

For a fixed noise bandwidth B_{noise}, the signal-power to noise-power ratio $\mathrm{SNR}_{\mathrm{power}}$ is given by

$$\mathrm{SNR}_{\mathrm{power}} = \frac{P_s}{N_0 B_{\mathrm{noise}}}. \tag{5.5.10}$$

Inserted in the previous equation, this yields

$$\sigma_\tau^2 \geq \frac{N_0}{8\pi^2(\mathrm{SNR}_{\mathrm{power}}\cdot N_0 B_{\mathrm{noise}})B_{\mathrm{eff}}^2} = \frac{B_{\mathrm{noise}}}{8\pi^2 B_{\mathrm{eff}}^2}\cdot\frac{1}{\mathrm{SNR}_{\mathrm{power}}}. \tag{5.5.11}$$

If the noise bandwidth is matched to the effective signal bandwidth $B_{\text{noise}} = B_{\text{eff}} = B$, and if the rise time is inversely proportional to the bandwidth ($t_{\text{rise}} \propto 1/B$), the jitter can be written as

$$\sigma_\tau \propto \frac{1/B}{\sqrt{\text{SNR}_{\text{power}}}} = \frac{t_{\text{rise}}}{\sqrt{\text{SNR}_{\text{power}}}} = \frac{t_{\text{rise}}}{\text{SNR}_{\text{amplitude}}}, \tag{5.5.12}$$

which is the commonly known formula for the jitter time resolution (see Section 2.8).

Analytical Model for Planar Sensors

For a planar sensor and uniform charge deposition along a line, as well as a uniform electric field, the resulting induced current can be calculated analytically using the Shockley-Ramo theorem. According to Equation (2.7.1) in Section 2.7.1, the induced current (which has a triangular shape) can be described by

$$I(t) = \frac{2Q}{T}\left(1 - \frac{t}{T}\right), \qquad \int I(t)\,\mathrm{d}t = Q, \tag{5.5.13}$$

where Q is the total charge deposited in the detector and $T = d/v$ is the drift time for a charge carrier velocity of v and a detector thickness d. The frequency spectrum $I(i\omega)$ of the current induced by the charge carrier drift can be evaluated by applying a Fourier transformation [121]

$$I(i\omega) = \frac{1}{\sqrt{2\pi}} \int_{-\infty}^{\infty} I(t) \cdot e^{-i\omega}\,\mathrm{d}t \tag{5.5.14}$$

$$= \frac{1}{\sqrt{2\pi}} \frac{2Q}{T^2\omega^2}\left(1 - e^{-i\omega T} - i\omega T\right). \tag{5.5.15}$$

Figure 5.5.1 shows the power spectral density for different drift velocities (per injected unit charge). At low frequencies, the power density is constant and directly proportional to the deposited charge. For higher frequencies, the power density follows a $1/\omega^2$ behavior, where the frequency at which this dependency sets in is given by the drift velocity of the charge carriers.

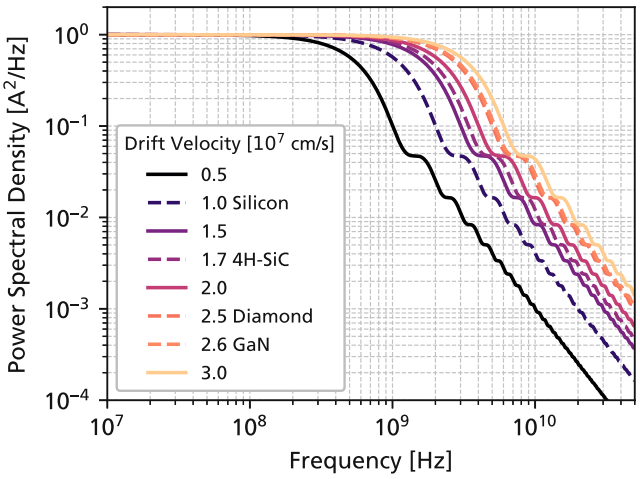

Figure 5.5.1: Power spectral density for different electron drift velocities in a 50 µm thick sensor. Lines are shown for the saturation electron drift velocities of silicon and WBG semiconductors.

	Silicon	4H-SiC	Diamond	GaN
dQ/dx	$72\,e\,\mu m^{-1}$	$57\,e\,\mu m^{-1}$	$35\,e\,\mu m^{-1}$	$138\,e\,\mu m^{-1}$
$v_{sat,e}$	$1 \times 10^7\,cm\,s^{-1}$	$1.7 \times 10^7\,cm\,s^{-1}$	$2.6 \times 10^7\,cm\,s^{-1}$	$2.5 \times 10^7\,cm\,s^{-1}$
$v_{sat,h}$	$0.8 \times 10^7\,cm\,s^{-1}$	$1.3 \times 10^7\,cm\,s^{-1}$	$1.6 \times 10^7\,cm\,s^{-1}$	$0.66 \times 10^7\,cm\,s^{-1}$
X_0 rel. to Si.	1	1.18	0.77	3.9

Table 5.1: Number of charge carriers produced by a MIP per unit length, electron and hole saturation velocities, and normalized radiation length for different detector materials [14, 47, 190, 220].

The analytical results for electron and hole drift (added together) in silicon and wide-bandgap semiconductors are presented in Figure 5.5.2. The simulations assume that the charge carriers move with the saturation velocity, summarized for all materials in Table 5.1. For a detector thickness of 50 µm, gallium nitride (GaN) provides the largest spectral power density, as it has the highest amount of charge carriers created per unit length (given its high density). However, for the same radiation length (50 µm silicon equivalent), depicted in Figure 5.5.2 (right), silicon will provide the largest signals at low frequencies, as it has the smallest ionization energy. At higher frequencies, WBG materials will still surpass silicon due to their higher charge carrier saturation velocities. For the same radiation length, 4H-SiC and diamond yield very similar results.

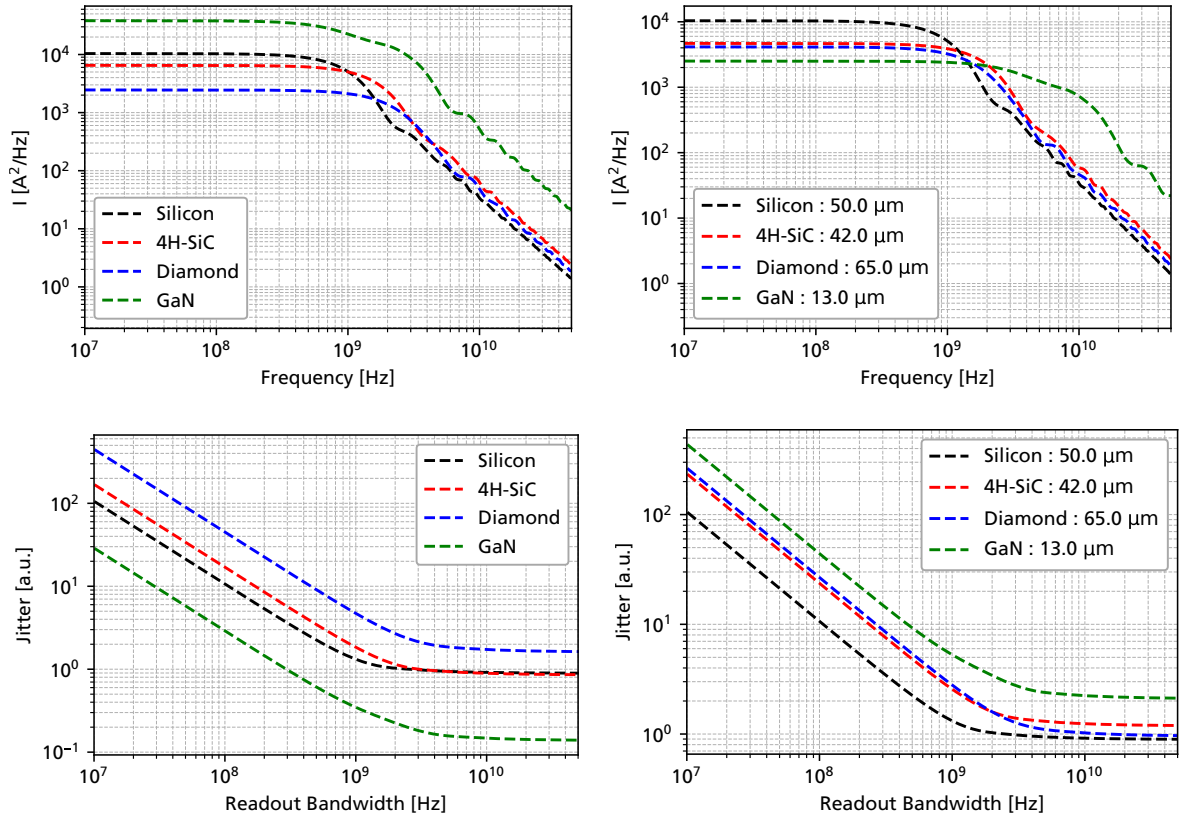

Figure 5.5.2: Top: Spectral Power Density of a minimum ionizing particle (MIP) in a 50 µm thick detector for different materials at the charge carrier saturation velocity, for equal thickness and 50 µm silicon equivalent radiation length. Bottom: Timing jitter as a function of the bandwidth for equal thickness (left) and radiation length (right).

Assuming a white noise density, Figure 5.5.2 also directly shows the power signal-to-noise ratio. At low frequencies (long shaping times), the best SNR can be obtained. However, this does not mean that the timing resolution is also maximal at this frequency. For a rise time inversely proportional to the readout bandwidth, the jitter time resolution ($\propto t_{\text{rise}}/\text{SNR}_{\text{amplitude}}$) is shown in the lower part of Figure 5.5.2. At low frequencies, the SNR is constant, and a slope of $1/\omega$ can be observed for the jitter due to the decreasing rise time of the signal. At higher frequencies, the $1/\omega^2$ dependency of the power SNR (equating to a $1/\omega$ dependency for $\text{SNR}_{\text{amplitude}}$) cancels with the decrease in rise time, resulting in a fixed jitter time resolution. This represents the upper limit of the time resolution that can be achieved, regardless of whether a particle can be detected in the first place (if the SNR is insufficient). For the same detector thickness, GaN again results in the best performance, due to its high charge deposition per unit length. However, for the same radiation length, silicon shows the best results, closely matched by diamond. For 4H-SiC, the performance is approximately 30 % worse than silicon.

These results (obtained using a simple analytical model), indicate that, even though WBG semiconductors features charge carrier velocities that are twice as high as for silicon, the jitter time resolution is worse for the same radiation length. This is a result of the high ionization energies that are associated with the bandgap of WBG semiconductors. Therefore, for planar sensors, which are usually limited by the signal-to-noise ratio, no advantage in using WBG materials can be identified. For sensors with gain, which will be discussed in Section 5.5.3, the situation is different, as the time resolution is usually limited by Landau fluctuations, not the jitter term.

5.5.2 Landau Fluctuations in Sensors without Gain

After studying the jitter time resolution for silicon and WBG materials, the time resolution limit due to stochastic fluctuations in the energy deposition is investigated in this section. In order to focus on materials that are currently available (and have previously been used in experiments), gallium nitride (GaN) is excluded from these studies. Figure 5.5.3 shows the distribution of charges deposited by a minimum ionizing particle in 4H-SiC. The distribution is very non-uniform, with individual interactions only creating a single charge carrier pair, and others creating 100 or more.

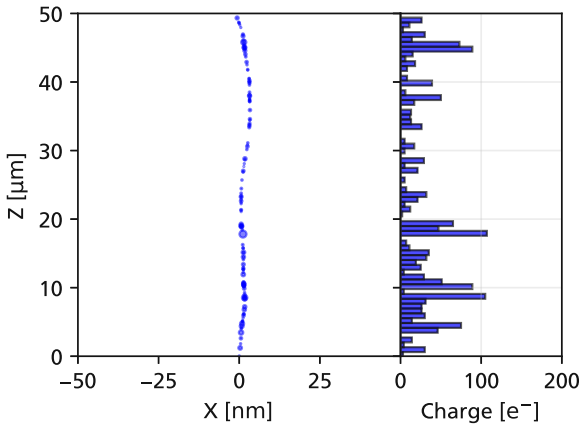

Figure 5.5.3: Deposited charge for a 120 GeV π^+ in 50 µm 4H-SiC simulated using Allpix^2. The number of created charge carriers in each individual interaction is indicated by the size of the marker and shown in the histogram on the right side of the plot. Large fluctuations in the deposited charge are visible, far away from a uniform distribution.

Center of Gravity Time Resolution

For an amplifier with an impulse response $h(t)$, slower than the transient current of the detector, it can be shown [121] that the resulting signal $v(t)$ is equal to

$$v(t) = q \cdot h(t - \tau), \tag{5.5.16}$$

i.e., the impulse response of the amplifier scaled with the deposited charge and shifted in time by the center of gravity of the detector current. The center of gravity (first moment) τ of the detector current $I(t)$ is given by

$$\tau = \frac{\int t \cdot I(t)\,\mathrm{d}t}{\int I(t)\,\mathrm{d}t}. \tag{5.5.17}$$

Neglecting the noise (jitter) contribution, the time resolution of the detector due to fluctuations in charge deposition can therefore be quantified by investigating the fluctuations in the center of gravity of the transient current.

Figure 5.5.4 shows the resulting time resolution for silicon, 4H-SiC, and diamond detectors of different thicknesses simulated using Allpix^2 and the PAI model [208]. For each thickness, 10 000 events of 120 GeV pions (provided for example by the CERN SPS [221]) were simulated. For the transport of the charge carriers, the saturation drift velocity was used by applying a uniform electric field with a very high value. The transient current was simulated with a step size of 1 ps, and the center of gravity of the current was calculated in an external processing step. The values of the center of gravity were then histogrammed and fitted with a Gaussian, in order to obtain the 1-σ center of gravity time resolution.

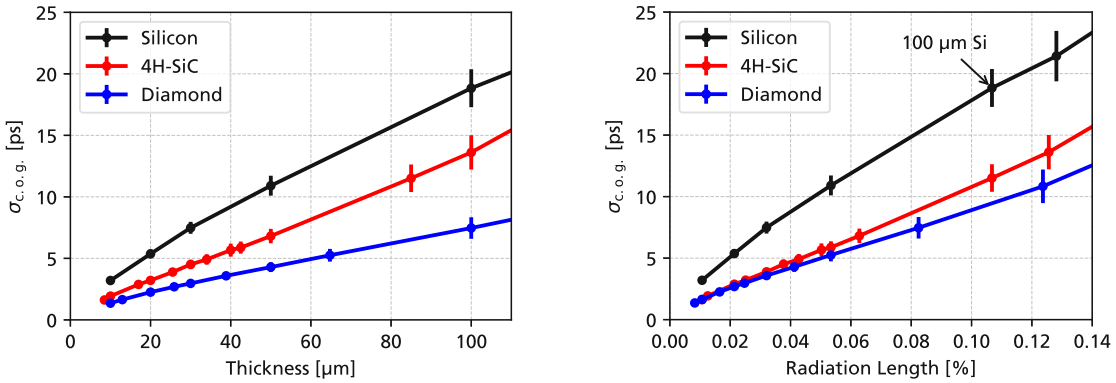

Figure 5.5.4: Landau fluctuation time resolution in planar silicon, 4H-SiC and diamond detectors without gain at saturation velocity for 120 GeV pions simulated using Allpix^2. Data is shown for the same thickness (left) and for the same radiation length (right).

The Landau fluctuations show a linear behavior with the thickness of the detector, as well as the charge carrier drift time (inverse of the saturation velocity), as predicted by analytical calculations [121]. As expected, diamond shows the best center-of-gravity time resolution, as it has the highest drift velocity. The fact that fewer electrons and holes are produced due to the higher ionization energy only plays a minor role, as these simulations do not consider the impact of noise. For the same radiation length, very similar results are obtained for 4H-SiC and diamond, as the lower thickness for 4H-SiC to achieve the same radiation length as diamond results in a very similar drift time for both detectors.

5.5.3 Sensors with Gain (LGADs)

The time resolution of low-gain avalanche diodes is typically limited by Landau fluctuations and not the jitter (if they are operated with a sufficient gain) [126]. In order to study the Landau fluctuations for different materials and detector thickness, a simplified LGAD geometry, depicted in Figure 5.5.5, was used. A gain layer with a thickness of 1 µm was implemented at the top of the device, with the rest of the device constituting the total thickness d. The electric field in the gain layer was uniform, and its value (as well as the impact ionization model for the different materials) was adjusted so that a gain value of 20 was reached in all simulations. This gain value was chosen to be sufficiently large to minimize the

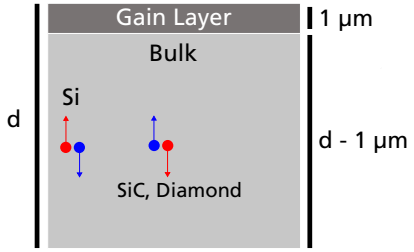

Figure 5.5.5: Cross section of simulated simple LGAD devices. In silicon, LGADs primarily multiply electrons, while in 4H-SiC and diamond, the hole impact ionization coefficient is larger. For these two arrangements, the electric field was inverted so that the correct charge carrier species reaches the gain layer.

impact of the primary charge carriers, while still keeping the number of gain electrons and holes (that need to be simulated and propagated) reasonable. In the bulk of the detector, a uniform electric field was used. This was set high enough such that the saturation drift velocity was reached, but no charge carrier multiplication occurred. Again, 10 000 120 GeV pion events were simulated, and the center-of-gravity of the detector currents was fitted using a Gaussian.

Figure 5.5.6 shows the obtained center-of-gravity time resolution for silicon LGADs, compared to data from WeightField2 (a Monte Carlo framework) and experimental measurements [127]. A very good agreement between the data simulated in Allpix^2 and the literature values was achieved, which gives confidence that this simulation approach produces correct results, even for a simplified LGAD geometry.

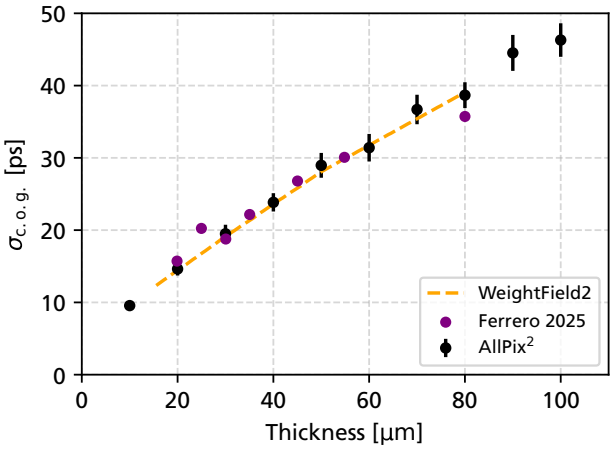

Figure 5.5.6: Center-of-gravity time resolution for silicon LGADs simulated in Allpix^2 compared to experimental data and WeightField2 simulations (Ferrero et al. [127]).

The simulated time resolution for silicon, 4H-SiC, and diamond LGADs is shown in Figure 5.5.7. Compared to the time resolution of planar sensors, higher values are found for LGADs. This is due to the fact that the charge carriers first need to drift to the gain layer before they are multiplied and the bulk of the signal develops. This effectively results in a larger drift time, which stretches out the impact of Landau fluctuations, worsening the time resolution. Again, diamond shows the best timing resolution due to its superior charge carrier velocity. However, for the same radiation length, it is comparable to 4H-SiC. Opposite to the jitter time resolution, the Landau timing limit (which is the dominating timing contribution for LGADs), better results are achieved for WBG LGADs than for silicon LGADs. For the same thickness, SiC-LGADs will have a time resolution approximately 1.3× better than, and diamond LGADs 2.0× better than silicon.

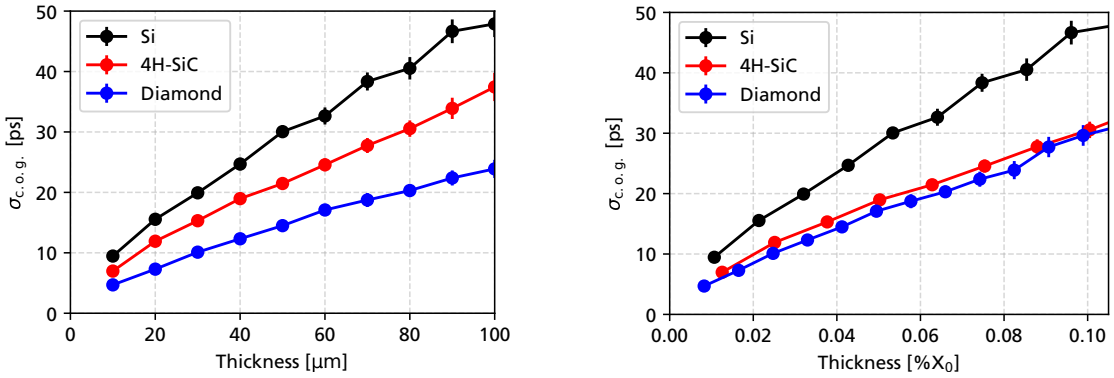

Figure 5.5.7: Comparison of the center-of-gravity time resolution resulting from Landau fluctuations for silicon, 4H-SiC, and diamond LGADs in Allpix^2. Results are shown for equal detector thickness (left) and equal radiation length (right).

Figure 5.5.8 also shows the expected transient currents of a MIP in different detector materials for a gain of 20 and a thickness of 50 µm. While for Si-LGADs the largest integrated charge is expected (as it has the lowest ionization energy), the amplitude of the transient current is comparable to the results for 4H-SiC and diamond, whose signals are twice as short. As is visible in the frequency domain, the signals of WBG LGADs contain a higher spectral power density at frequencies above 1 GHz, which will allow for shorter shaping times (faster amplifier rise times) to be used, possibly aiding in reducing the impact of jitter.

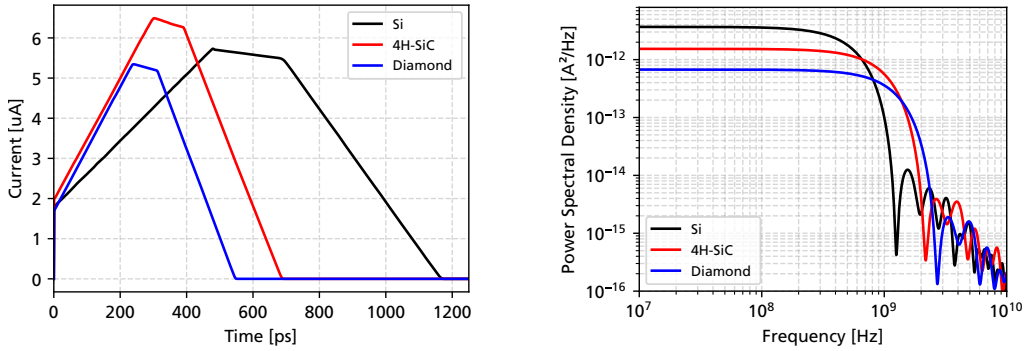

Figure 5.5.8: Current induced by a minimum ionizing particle (120 GeV pion) in 50 µm thick LGADs for different materials and a fixed gain of 20. The image on the left shows the time domain, and the image on the right the power spectral density in the frequency domain.

6 Characterization of 4H-SiC Detectors

As mentioned already in Sections 2.2.4 and 2.4.4, literature values for the material properties of 4H-SiC, such as the charge carrier mobility or electron-hole pair creation energy, scatter widely, and some currently used values are based on different polytypes altogether [61]. In this section, measurements of 4H-SiC detectors are presented, with the overarching goal of improving the understanding of the material properties and achievable particle detection performance. The measurements focus on PiN Diodes produced by IMB-CNM-CSIC in Barcelona, Spain. First, the process technology and samples fabricated by previous productions of CNM will be introduced in Section 6.1 Based on the measurements on these samples (Section 6.2), a wafer layout was designed by HEPHY, and five wafers with PiN diodes were manufactured as a part of the RD50-SiC-LGAD common project [222]. The characterization and yield assessment of these productions will be shown in Section 6.3. Finally, Sections 6.4 and 6.5 present measurements aiming to characterize the material properties of 4H-SiC, such as the ionization energy ϵ_i and charge carrier drift velocities,

6.1 4H-SiC PiN Diodes Manufactured by CNM

Silicon carbide detectors at CNM [138, 223–225] have been developed on the basis of process technology originally developed for power electronics applications [226], such as Schottky diodes for the Bepi-Colombo space mission [227]. Figure 6.1.1 shows a typical cross-section of a 4H-SiC PiN diode detector manufactured by CNM. The device consists of a substrate with a thickness of 350 µm and a high-quality epitaxial layer of around 50 µm, with a doping as low as $1 \times 10^{14}\,\mathrm{cm}^{-3}$. In between the epitaxial layer (which acts as the sensitive volume) and the substrate, a highly nitrogen-doped buffer layer is grown in order to contain the electric field inside the epitaxy. For a low resistance ohmic contact to the Al p^{++} implant, a multi-metal stack made of titanium, nickel, and aluminum is used [226]. An isolation dielectric made of SiO_2 and Si_3N_4 is available to construct MOS devices. In order to achieve high bias voltages (which are required to fully deplete the epitaxial layer), multiple implanted guard rings are used to slowly spread out the electric field, avoiding device breakdown. Around the active area of the detector ($3 \times 3\,\mathrm{mm}^2$), which is either covered by metal or only the passivation, a contactable guard can be grounded to better define the active area in C-V measurements and to remove the effect of surface currents.

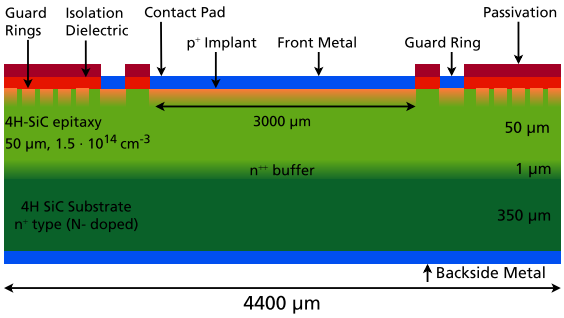

Figure 6.1.1: Typical cross-section of 4H-SiC PiN diodes manufactured by CNM. Taken from [16].

6.2 Characterization of PiN Diodes from Run 13575

Figure 6.2.1 shows a microscope image of $3 \times 3\,\mathrm{mm}^2$ 4H-SiC PiN diodes produced by CNM in run 13575, glued and wire bonded on a UCSC LGAD readout board. Diodes of this type were available at HEPHY from 2021 onward, and have undergone in-depth characterization [228, 229] and an assessment of their radiation hardness (see [230] and Section 7).

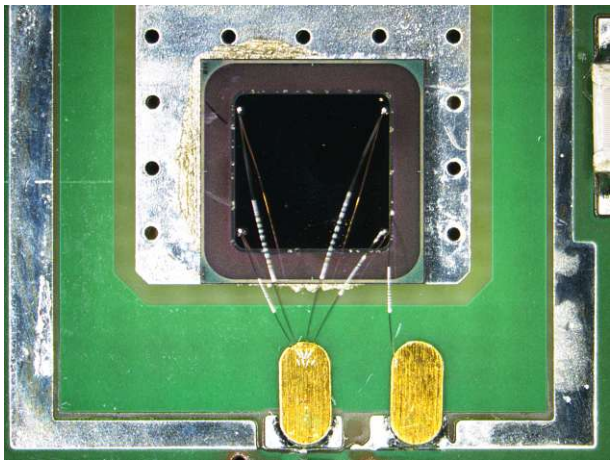

Figure 6.2.1: Microscope image of a $3 \times 3\,\mathrm{mm}^2$ diode from CNM run 13575. Four wire bonds are used to connect the active area of the diode to the input of the amplifier. The guard ring is connected to the ground potential using an additional wire bond.

Figure 6.2.2 shows the typical DC electrical characteristics of these diodes in forward and reverse bias. Two different slopes are visible in forward bias. At low bias voltages (and currents), an ideality factor of approximately 3.5 was measured. This implies that the current is driven by recombination processes in deep traps. These traps generate current less efficiently than mid-bandgap traps [116], which would result in an ideality factor of 2 (see Section 2.2.2). At higher currents (above 10 µA), an ideality factor of 1.5 was obtained, which corresponds more closely to a diffusion-limited charge carrier transport process, where an ideality factor of 1 is expected. In between both regimes, a small "bump" is visible, which is likely a result of $Z_{1,2}$ and $EH_{6,7}$ defects introduced during the crystal growth [231]. In reverse bias, the

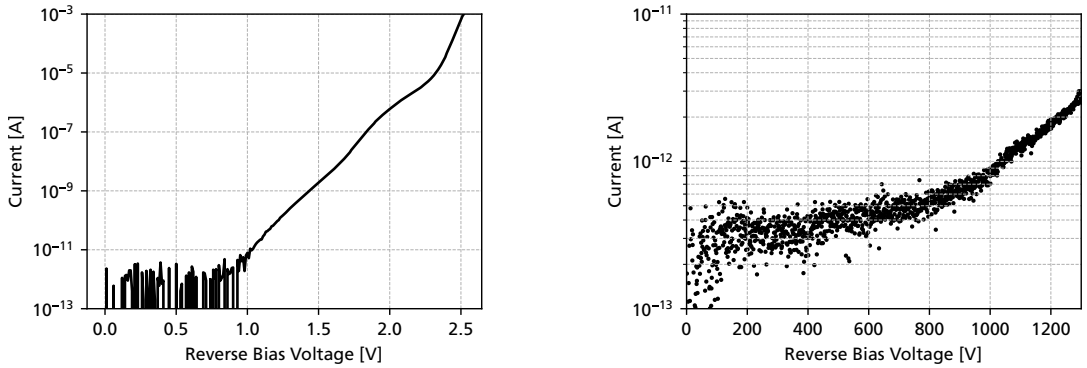

Figure 6.2.2: Typical current-voltage characteristics of PiN diodes produced by CNM (run 13575) in forward bias (left) and reverse bias (right). The guard ring was grounded, and the measurements have been performed at the high-voltage probe station described in Section 4.1.

measured currents are exceptionally low (compared to silicon devices), below 1 pA up to 1 kV. No clear correlation between the depleted volume of the sensor (see Figure 6.2.3) and the current is visible, as would be expected for the thermal generation of charge carriers. Instead, the current is likely dominated by leakage currents, for example, on the surface of the device. The increased current at higher voltages is attributed to charge carrier generation from impact ionization at the guard ring termination structure, with a device breakdown occurring around 1.4 kV.

The typical capacitance-voltage characteristics are shown in Figure 6.2.3. The $1/C^2$ curve first shows a linear increase, which corresponds to the depletion of a sensor with a constant doping concentration. At bias voltages of approximately 400 V, the capacitance starts to saturate as the full depletion of the device is reached. The plots also show that it is crucial to bias the guard ring in C-V measurements. If it is left floating, the effective area of the diode will be larger, which impacts the measured capacitance and can lead to erroneous results. By taking the derivative of the $1/C^2$-curve with respect to the bias voltage, the doping concentration as a function of the depletion width can be obtained, depicted in the right-hand part of Figure 6.2.3. Up to a depth of 40 µm, the doping is constant, at approximately $1.5 \times 10^{14}\,\mathrm{cm}^{-3}$. After this, the doping concentration starts to increase exponentially. This is likely a result of the growth process of the highly doped buffer layer at the bottom of the epitaxial layer. If there is residual nitrogen gas during the CVD growth after the buffer layer has been completed, it might require some time (corresponding to around 5-10 µm of epi growth) for the dopant to be fully purged from the system and the desired concentration of $1.5 \times 10^{14}\,\mathrm{cm}^{-3}$ to be reached. This will lead to a "smoothed" out depletion characteristic, compared to the sharp "kink" typically observed in C-V measurements of silicon diodes [1]. Using a diode area of $3 \times 3\,\mathrm{mm}^2$, the maximum depletion width (at a bias voltage of 1.1 kV) approaches 50 µm, in accordance with the physical dimensions of the device

At zero volts of external bias, the capacitance (and depletion width) will be defined by the built-in potential of the diode (see Section 2.2.2). By fitting the data in Figure 6.2.3, a built-in voltage of $V_{bi} = 2.8$ V is found, which corresponds to a depletion width of about 4.5 µm.

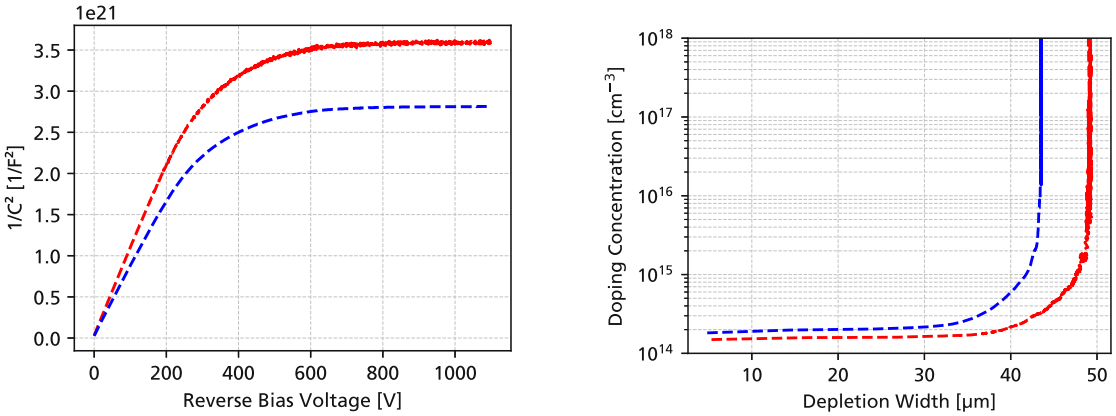

Figure 6.2.3: Left: Typical capacitance voltage characteristics of 4H-SiC PiN diodes for measurements that contact the guard ring (red) and that leave it floating (blue). Right: Extracted doping concentration as a function of the depletion depth. The measurements have been performed for an AC frequency of 10 kHz using an excitation voltage of 1 V.

Figure 6.2.4 shows typical UV-TCT waveforms obtained using the UCSC LGAD single-channel readout board as a function of the detector bias voltage. As the impulse response of the amplifier is longer than the transient current of the detector (expected to be around 300 ps at the saturation velocity), the resulting waveforms are identical to the amplifier impulse response, scaled with the collected charge. For 400 V, the detector is almost fully depleted, with 90 % of the charge collected.

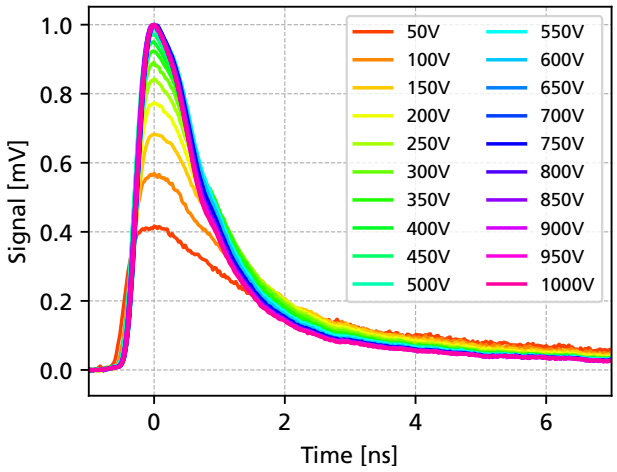

Figure 6.2.4: Typical UV-TCT waveforms for 4H-SiC PiN diodes from CNM run 13575.

For different types of ionizing radiation (as well as simulations), the charge collection efficiency (CCE) as a function of the bias voltage is compared in Figure 6.2.5. The results for UV-TCT and 62.4 MeV protons (measured at MedAustron, see Section 4.4) agree very well with simulations which use a uniform deposition of charge carriers. For alpha particles, the collected charge saturates much earlier, as alpha particles with an energy of around 5 MeV only penetrate approximately 15 µm deep in 4H-SiC.

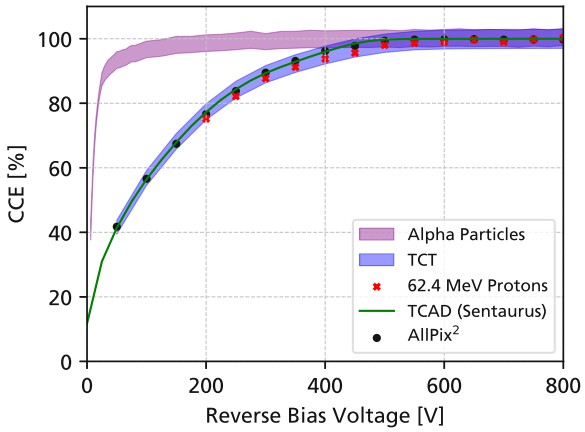

Figure 6.2.5: Charge Collection Efficiency, adapted from [231].

This section has given an overview of the typical electrical characteristics and particle detection performance for $3 \times 3\,\mathrm{mm}^2$ 4H-SiC PiN diodes produced by CNM in run 13575. The electrical characteristics of similar devices, produced in the RD50-SiC-LGAD project, will be discussed in Section 6.3. Radiation hardness studies, where the I-V and C-V characteristics, as well as the charge-collection efficiency, are investigated for neutron irradiation samples, will be presented in Section 7.

6.3 Characterization of 6-inch PiN Wafers (RD50-SiC-LGAD)

In the context of the RD50-SiC-LGAD project [222], a planar wafer run was designed by HEPHY, with the aim to test improved guard ring structures, validate TCAD simulations, and study radiation damage in devices without gain before a LGAD production was undertaken. The production of planar devices started in 2023 and delivered wafers in 2024 and 2025, as summarized in Table 3.1. This production is the first of CNM to use 6-inch 4H-SiC wafers, which allowed for a much larger quantity of devices to be fabricated than in the previous 4-inch productions. This section will present the on-wafer characterization of $3 \times 3\,\mathrm{mm}^2$ PiN diodes, quantifying the yield and electrical characteristics of the produced devices. The characterization was performed on-site in Barcelona, during a 1-month stay in 2024 and a 1-week stay in 2025. After the characterization, the wafers were diced and distributed to the participants of the RD50-SiC-LGAD project[1].

Wafer	Run Number	Epi Thickness	Production Date	Yield (for $3 \times 3\,\mathrm{mm}^2$ diodes)
W2	17407	50 µm	March 2024	39.9 %
W3	16886	50 µm	March 2024	6.4 %
W4	16886	100 µm	March 2024	46.8 %
W1	17560	50 µm	May 2025	72.0 %
W5	17560	100 µm	May 2025	76.2 %

Table 3.1: Overview of 4H-SiC wafers produced by CNM using the mask set 1184 designed by HEPHY.

Figure 6.3.1 shows the layout of the wafer. Around the edge of the 6-inch wafer, a total of 173 $3 \times 3\,\mathrm{mm}^2$ PiN diodes are distributed. These diodes feature a very similar layout to the diodes designed by CNM for run 13575 (see previous section). However, the guard rings have been improved to allow for a breakdown voltage as high as 2 kV [231]. Along the X and Y axes, strip sensors with different pitches are located, together with nine large $1 \times 1\,\mathrm{cm}^2$ strip sensors in the center of the wafer. Furthermore, test structures such as MOSFETs, MOSCAPs, gate-controlled diodes and Van-der-Pauw structures are spread out over the wafer area. These test structures aim to quantify the resistivity of different layers (such as the p^{++} implant or metal) and map the uniformity of the production process.

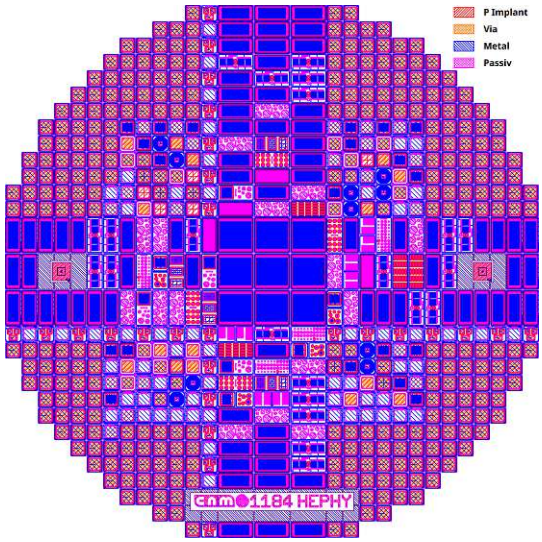

Figure 6.3.1: 6-inch wafer layout 1184 designed by HEPHY and produced by CNM.

[1]OEAW-HEPHY, CSIC-IMB-CNM, CERN, INFN Perugia, IFCA Santander, NIKHEF

Characterization Equipment at CNM

At CNM, different manual and automatic probe stations are available. Because of the large number of samples to be characterized, a semi-automatic MPI TS2000-SE probe station, depicted in Figure 6.3.2, was chosen. This probe station features an XYZ table, allowing for an automated contacting of the wafer, as well as a rotational stage, which can correct for angular errors in the wafer orientation. In a typical configuration, four probe needle holders are used, mounted on top of the probe station on a metal feedthrough. Furthermore, a digital microscope allows for an optical inspection of the wafer.

For current-voltage measurements, a Keithley 2470 SMU together with a Keithley 6514 electrometer was used to implement pA-level current measurements. The chuck of the probe station, as well as the cables leading to it, were fully triaxially guarded. In addition to the SMU and electrometer, a Keithley 4200-SCS semiconductor analyzer was available for C-V measurements up to ± 30 V. The semiconductor analyzer also features four integrated SMUs, which can be used for DC measurements that require multiple voltages to be sourced or measured (for example, for Van-der-Pauw structures).

The wafer designed by HEPHY includes not only more than 35 device types, but also non-uniform die sizes. This makes a fully automatic probing of the wafer very challenging, as most automatic wafer probers assume a uniform die size. Therefore, a custom Python software was written in order to control the position of the chuck in the wafer prober and to perform electrical measurements (I-V and C-V) or to acquire microscope photos. As input to the control software, the position of each device (and its corresponding bond pads) was extracted from the wafer layout. For example, Figure 6.3.2 shows the position of standardized process quality control structures on the wafer.

Automation of the measurements was crucial, as the large number of diodes to be measured (and the time required for each measurement) required the characterization to run throughout the night. By automating the optical inspection, a microscope image of each die was obtained (and correctly labeled with the die coordinates), serving as a reference database and even allowing for computer vision methods to be applied in the future.

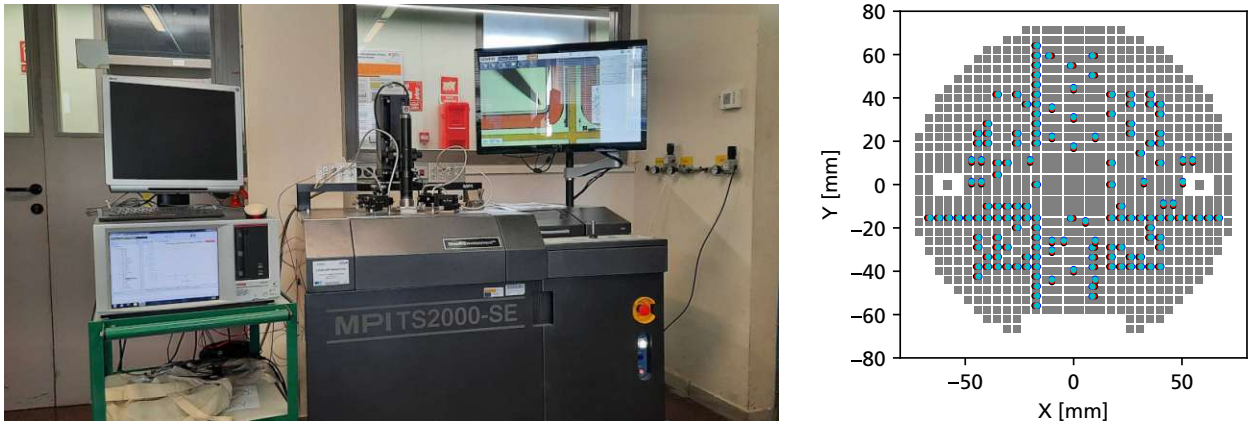

Figure 6.3.2: Left: Semi-automatic probe station MPI TS2000-SE measuring 4H-SiC PiN diodes in the characterization lab at IMB-CNM, Barcelona. Left of the probe station, a Keithley K4200 semiconductor analyzer is visible, conducting C-V measurements. Because 4H-SiC is insensitive to visible light, measurements can be conducted simultaneously with visual inspection. Right: On-wafer coordinates of process quality control structures extracted from the mask layout. Each colored dot corresponds either to a Van-der-Pauw or a cross-Kelvin bridge structure. The gray rectangles indicate the individual dies of the wafer.

6.3.1 First Production: Runs 17047 and 16886

In 2024, two runs of 6-inch 4H-SiC wafers were processed by CNM. As depicted in Table 3.1, this consisted of two wafers with a 50 µm epitaxial layer and one wafer with a 100 µm epitaxial layer. However, due to a mistake in the mask layout, only a few of the devices on the wafer worked correctly.

In this production, a single metal mask was used for the contact metal on top of the silicon carbide, as well as the metal on top of the oxide (for MOS structures). The metal in contact with SiC is made of multiple metals, forming a silicide compound during high-temperature sintering, achieving a low-resistance ohmic contact [226]. However, if this multi-metal stack is deposited on SiO_2 instead of SiC, the silicide can not correctly form, which leaves over unused metal. This unused metal will melt during sintering and spread out over the wafer, creating short circuits. As the same mask was used for the contact metal and the second metal (a layer of aluminum), this created issues for most MOS devices, as shown in Figure 6.3.3.

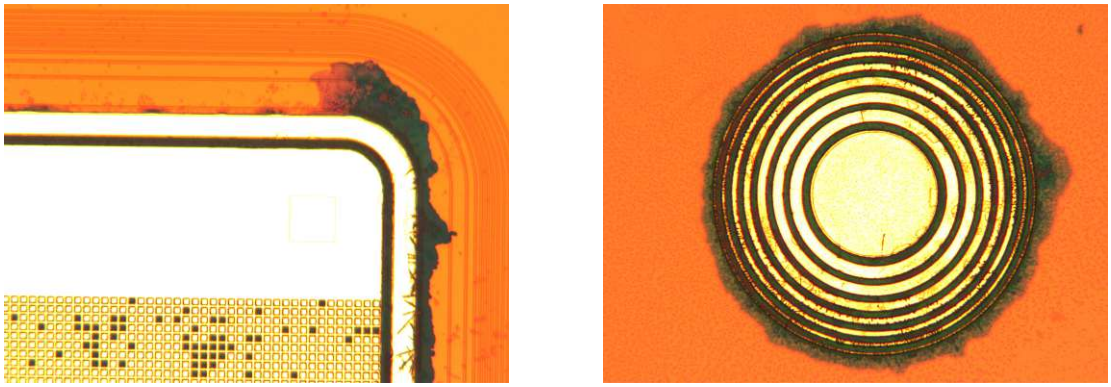

(a) Diode with metal grid (b) Gate-controlled diode

Figure 6.3.3: Microscope images of molten metal for devices of CNM runs 16886 and 17407. The molten contact metal is visible as a dark layer around the edges of the devices. This metal spreads outside of the intended area, which can be seen by a highly reflective aluminum layer. In between individual segments or rings, the molten contact metal can cause a short circuits.

Depending on the device type, this metallization issue can have a minor influence (for example, shorting the guard ring for $3 \times 3\,\mathrm{mm}^2$ diodes), or render a device completely unusable (for MOS devices). As the silicide formed by sintering of the metal stack is extremely chemically stable, it was not possible to remove it from the wafers to attempt the metallization again. Nevertheless, some diode designs were still usable, with the extent of the molten metal varying from wafer to wafer, and characterization of these devices was carried out.

Electrical Characterization of PiN Diodes

The most frequent structure on the wafer layout are $3 \times 3\,\mathrm{mm}^2$ planar PiN diodes. These diodes, depicted in Figure 6.3.4, are similar to diodes from previous runs of CNM (such as run 13575), however, feature an improved guard ring design optimized to allow bias voltages above 2 kV, while respecting process limitations (such as a minimum 5 µm spacing between guard rings) and having a maximum total width of 200 µm [231]. Additionally, the diodes feature a central 100 µm diameter hole in the metallization to allow for light to be injected in UV-TCT studies. While the large area of these devices severely limits the readout bandwidth (with a device capacitance of approximately 17 pF), the large area results in larger values of the measured currents and capacitance, simplifying measurements and minimizing

the impact of edge effects. These diodes are intended to be a vehicle for radiation hardness studies in the future.

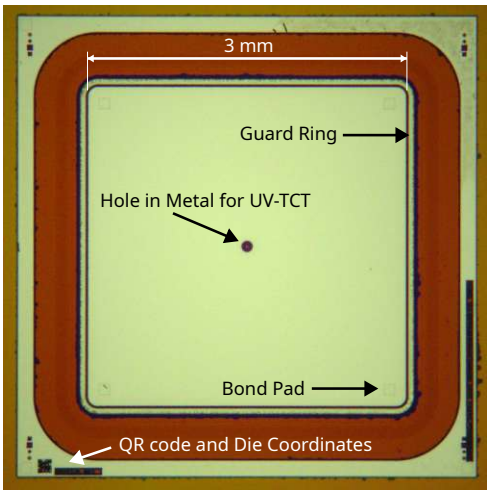

Figure 6.3.4: Overview of the $3 \times 3\,\mathrm{mm}^2$ PiN diodes manufactured by CNM in run 16886. Around the edge of the active area, molten metal from the previously discussed issues can be seen.

In order to assess the yield of the wafers in this first production (and to evaluate the impact of the molten metal issue), current-voltage and capacitance-voltage measurements were performed for all $3 \times 3\,\mathrm{mm}^2$ PiN diodes on the three wafers from runs 16886 and 17407. The main goal of these measurements was to quantify the number of working devices, as well as to map quantities such as the doping concentration as a function of the position on the wafer. Below 1.5 V in forward bias, the measured current should be very low (below 50 pA), and be limited by the settling and averaging time of the electrometer and SMU, rather than the current of the diode. If the measured current is higher than this, then this might point to a leakage path (i.e., a resistance in parallel to the diode), for example, caused by the molten metal shorting a part of the diode. This was applied as a criterion to specify the yield, with a similar criterion for the reverse bias, which had to be below 50 pA at 200 V (although from previous productions, a current of less than 1 pA is expected at 1 kV).

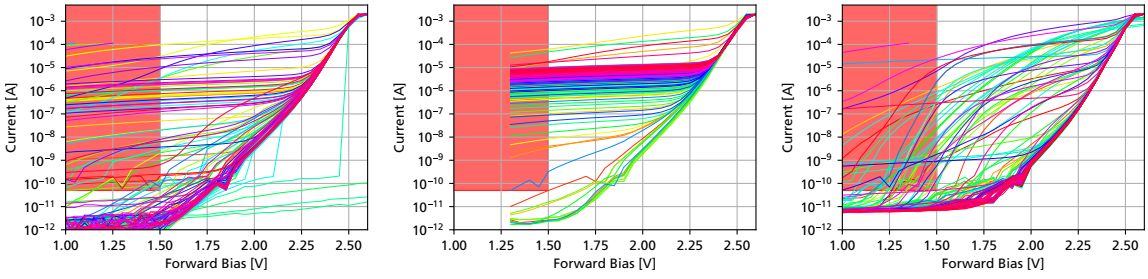

(a) Wafer 2 (50 µm epi) (b) Wafer 3 (50 µm epi) (c) Wafer 4 (100 µm epi)

Figure 6.3.5: Forward I-V curves for all three wafers of CNM runs 16886 and 17407. The red area indicated the leakage current criterion of 50 pA at 1.5 V. The lower limit in the measured current (approximately 1 pA) is a result of the short settling and integration time used in the measurements. A kink is visible around 1.8 V, which is an artifact due to the electrometer switching its measurement range.

Current-Voltage Characteristics and Yield

Figure 6.3.5 (on the previous page) shows the measured forward I-V curves for all 173 $3 \times 3\,\mathrm{mm}^2$ diodes on the three wafers from the first CNM production. For wafers 2 and 4, almost half of the diodes follow very similar I-V curves. For the other half, an increased leakage current is observed already at low bias voltages, which can be attributed to a low-resistance leakage path, caused by the molten contact metal (or other defects). If an increased leakage current is already measurable in forward I-V (only going up to a voltage of 2.5 V), the same leakage resistance will result in an even higher current in reverse bias (which uses hundreds of volts). Wafer 3 shows a much lower yield than the others, with almost all devices exhibiting a leakage resistance as low as 10 kΩ. It is thought that this is a result of process variations, which resulted in a larger impact of the molten contact metal for this wafer than for the others.

The yield as a function of the position on the wafer is depicted in Figure 6.3.6. Here, results from reverse bias I-V measurements up to 200 V were also taken into account, which have been omitted from being plotted graphically, as the current in reverse bias is dominated almost entirely by limitations in the measurement setup (as a result of very large 25 V step sizes), and the only discernible characteristics in the reverse bias I-V curves is a binary indication if the diode is working or not.

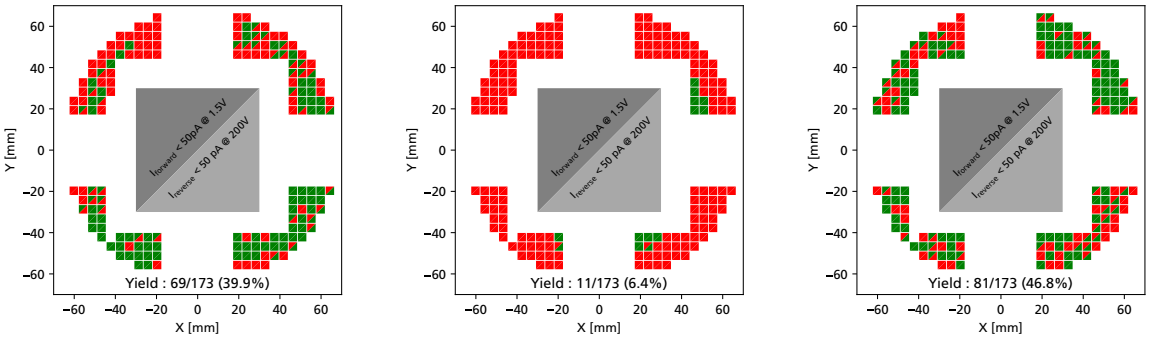

Wafer 2 (50 µm epi) Wafer 3 (50 µm epi) Wafer 4 (100 µm epi)

Figure 6.3.6: Yield assessment combining forward and reverse I-V measurements for all three wafers.

Capacitance-Voltage Characteristics

For wafers 2 and 4 (where approximately half of the diodes are working as intended), a wafer map of the epitaxial layer doping concentration was performed up to a bias voltage of 30 V, with the results shown in Figure 6.3.7. No C-V measurements with an external high-voltage bias-tee were performed, as this would have taken much longer to measure and because the maximum voltage that could be used at the CNM probe station was limited. For devices that were previously characterized as "leaky", C-V measurements were still able to be performed by setting a large current compliance of 1 mA.

For the wafer 2 (with an epitaxial layer of 50 µm), the doping concentration is very low, at $1 \times 10^{14}\,\mathrm{cm}^{-3}$ (or even below), while for the wafer 4 (100 µm epi), it is significantly above $3 \times 10^{14}\,\mathrm{cm}^{-3}$. The manufacturer of the wafers tried to achieve as low a doping concentration as possible (on a "best-effort" basis), which likely explains the non-constant doping concentration for wafer 2. During the epitaxial growth, the effective doping concentration might have been limited by residual nitrogen gas in the growth reactor (or other contaminations), which can not be accurately controlled during the epitaxial growth. For thicker wafers (100 µm), the doping concentration that can be achieved is typically higher than for thinner devices. As a function of the position on the wafer, a smooth gradient in the doping can be observed, which can be attributed to temperature gradients during the CVD growth of the epitaxial layer [44].

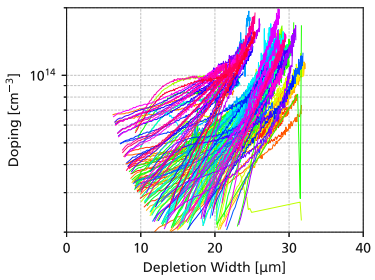

(a) Doping vs. depletion depth for wafer 2

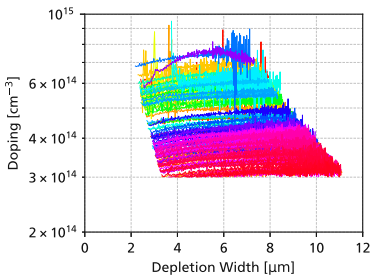

(b) Doping vs. depletion depth for wafer 4.

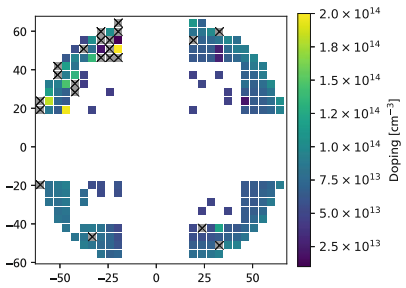

(c) Doping vs. position on wafer 2

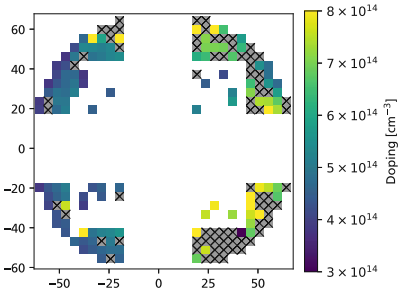

(d) Doping vs. position on wafer 4

Figure 6.3.7: Wafer maps of the doping concentration for wafer 2 of run 17407 and wafer 4 of run 16886 with epitaxial layer thicknesses of 50 µm and 100 µm respectively. Note the different horizontal and vertical axes scales between the different wafers. For dies marked with an X, the doping concentration could not be extracted due to excessive leakage currents. Results are also shown for 20 PiN devices in the central part of the wafer, which have a very similar geometry to the 173 investigated $3 \times 3\,\mathrm{mm}^2$ diodes.

Process Test Structures

As shown in Figure 6.3.2, the wafer features 147 identical process test structures, depicted in Figure 6.3.8, that can be used to measure the resistivity of the epitaxial layer, p^{++} implant and metal (using Van-der-Pauw structures), as well as the contact resistance (using a cross-bridge Kelvin resistor). The Van-der-Pauw technique [232] allows for measuring the resistivity of a material independent of the exact shape of the structure. This is performed by forcing a current I_{12} between two corners (1 and 2), which (due to the resistivity of the material) will result in a voltage drop between the two other corners, V_{34}. These corners are arranged in either a clockwise or counter-clockwise orientation, and the sheet resistance can then be calculated as [55]

$$R_{\mathrm{sheet}} = \frac{\pi}{\ln(2)} \frac{V_{34}}{I_{12}}. \tag{6.3.1}$$

By performing measurements for all four rotations of this arrangement, as well as both positive and negative current polarity, asymmetries and non-idealities can be eliminated and a very accurate measurement of the resistivity can be obtained [233]. The Keithley K4200-SCS semiconductor analyzer at CNM, which has four SMUs, allowed for these different arrangements to be performed entirely using software by switching the operation mode of the SMUs between a current source/sink or voltage measurement, which eliminated the need for cables to be switched between measurements.

Because of the impact of the molten metal, almost all Van-der-Pauw test structures were unusable in

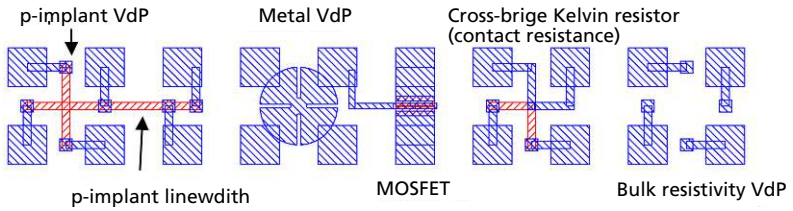

Figure 6.3.8: Process quality control test structure used in mask 1184, adapted from silicon wafers in the CMS tracker production [55]. The metal mask is shown in blue, and red areas indicate the mask the p^{++} implant.

this production, as the current (which should flow through the test structures) took the lowest resistance path through molten metal, shorting all four bond pads. The only structure where successful resistivity measurements were able to be obtained was for the metal leaf clover (see Figure 6.3.8). This structure aimed at measuring the resistivity of the aluminum metal layer deposited on top of the contact metal. As its resistivity is much lower than the resistance of the molten metal between the bond pads, successful measurements were able to be obtained, depicted in Figure 6.3.9. The results show very low sheet resistances on the order of 45 mΩ cm/sheet, as expected from the high conductivity of aluminum metal. A tendency of lower resistivities in the wafer center can be observed, increasing towards the edge of the wafer. This might be a result of non-uniformities in the metal deposition during the processing of the wafers.

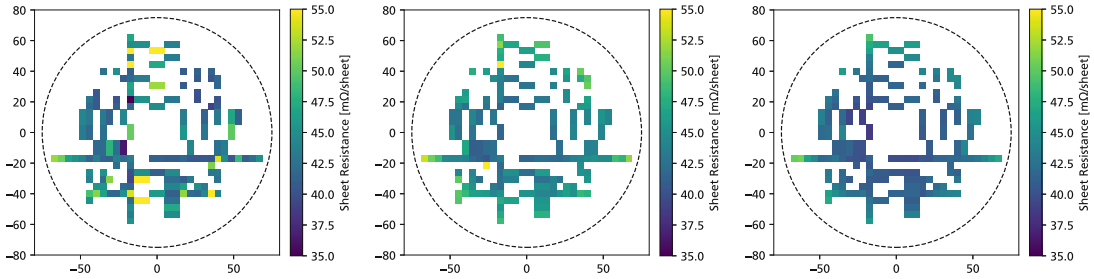

(a) Wafer 2 (50 µm epi) (b) Wafer 3 (50 µm epi) (c) Wafer 4 (100 µm epi)

Figure 6.3.9: Metal resistivity measured using a Van-der-Pauw leaf clover structure for wafers processed in runs 16886 and 17407. The circumference of the wafer is indicated using a dashed circle.

Electrical Characteristics after Dicing

For a subset of devices from wafer 2 (run 17407, 50 µm epi), the electrical characteristics were measured again at HEPHY after the wafer was diced, depicted in Figure 6.3.10. This was performed using the high-voltage compatible probe station detailed in Section 4.1, which allowed for the characterization of devices up to more than 1 kV. Compared to diodes manufactured in run 13575, much higher leakage currents in reverse bias are observed, almost 100 pA at 1 kV (a factor 100 higher). This is very likely a result of the metallization issues for the newly produced wafers, which partially short the termination structure and provide a path for leakage currents to flow. The very low doping concentration of wafer 2 results in a full depletion voltage of approximately 100 V, which is a factor 4 better than for diodes from run 13575. A spread in the full depletion capacitance is visible, which is a result of floating the guard ring during the C-V measurements. The guard ring was not able to be contacted, as it is shorted to the active area of the diode by molten metal. Some C-V measurements were also performed for samples of

wafer 4 (with 100 µm epi), however, for bias voltages up to 1 kV only a depletion width of approximately 50 µm was attained, a result of the high epitaxial doping concentration of this wafer. Although the probe station can handle higher bias voltages (up to 3 kV), the diodes underwent a breakdown around 1.2 kV, likely as a result of the molten contact metal negatively affecting the termination structure.

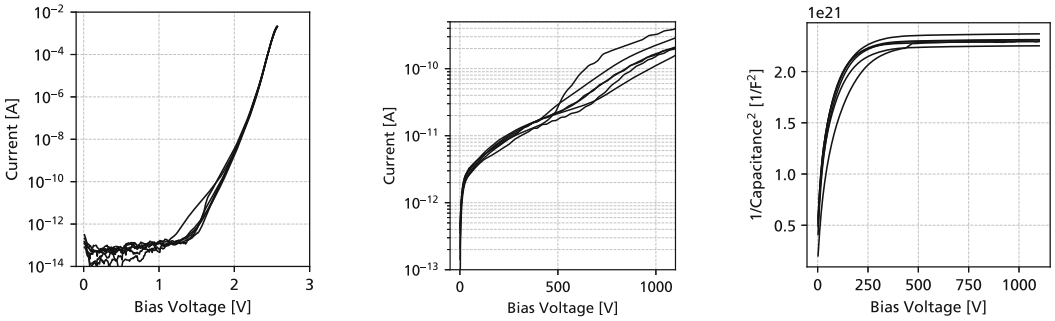

(a) Forward I-V (b) Reverse I-V (c) C-V

Figure 6.3.10: Typical electrical characteristics for 50 µm thick PiN diodes of wafer 2 (run 17407), measured after HEPHY after the wafer has been diced.

6.3.2 Second Production: Run 17560

In order to address the issues with the molten contact metal in runs 16886 and 17407, a second production was undertaken in 2024 with one 50 µm and one 100 µm epitaxial layer wafer, finishing in 2025. An additional metal mask was introduced, which split the metal masks into two masks, one for the contact multi-metal stack (which forms the ohmic contact with the silicon carbide) and one mask for an additional aluminum layer (which can be used for MOS devices). With this, the issues with molten metal were able to be eliminated, as depicted in Figure 6.3.11.

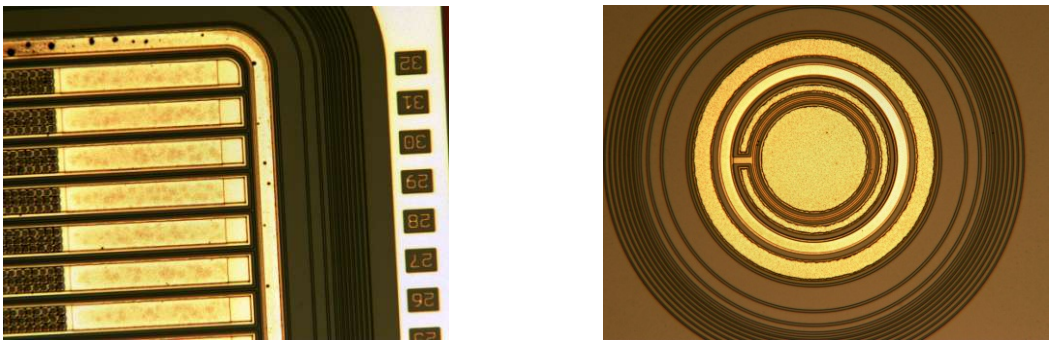

Figure 6.3.11: Microscope images of devices in the second production (run 17560). Taken from [234].

For the $3 \times 3\,\mathrm{mm}^2$ PiN diodes, an identical electrical characterization as presented for the previous production was carried out. Figure 6.3.12 shows the resulting yield for wafers 1 (50 µm epi) and 5 (100 µm), which has been greatly improved. A yield of 75 % is a reasonable result, as most of the diodes are situated at the edge of the wafer, where more defects are expected. Figure 6.3.13 shows the doping as a function of the position. With the high yield of the devices, and the diode area properly defined by biasing the guard ring in C-V measurements, a very uniform distribution of the wafer doping can be observed, ranging between 2-3 $\times$ $10^{14}\,\mathrm{cm}^{-3}$ and 6 $\times$ $10^{14}\,\mathrm{cm}^{-3}$. With the diced wafers of run 17560

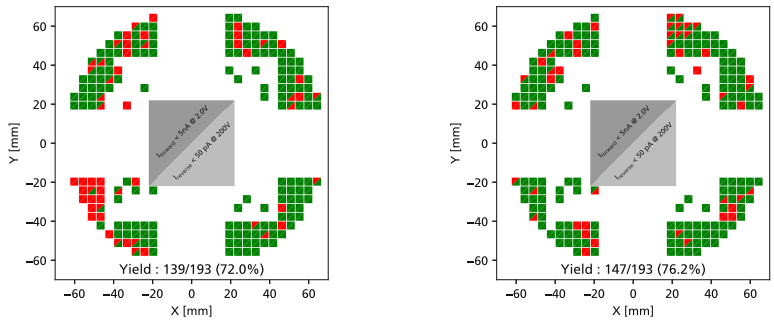

Figure 6.3.12: Yield Assessment combining forward and reverse I-V for all three wafers. Wafer 1 with an epitaxial layer of 50 µm is depicted on the left, and wafer 5 with 100 µm epi on the right.

arriving at HEPHY in August 2025, more detailed characterizations will be able to be carried out. Due to another mask layout issue, measurements of the process test structures (see Figure 6.3.8) did not yield any results (except for, again, the metal resistivity). The exact nature of this issue, however, still needs to be understood.

A total of 253 working PiN diodes will be distributed among the RD50-SiC-LGAD project partners. This large number of samples will provide a very good basis to perform in-depth radiation hardness studies in the future, with a statistically relevant number of samples. Diodes with small areas (and small capacitances) will lend themselves to timing studies and allow for the transient current of the detector to be resolved using high-bandwidth readout electronics (see Section 6.5). Such studies could also be performed for irradiated devices, mapping the electric field inside PiN diodes. Finally, novel structures, such as segmented diodes leveraging the resistivity of the p^{++} to provide a position resolution using charge sharing, will be able to be investigated, laying the groundwork for SiC-DC-LGADs [235].

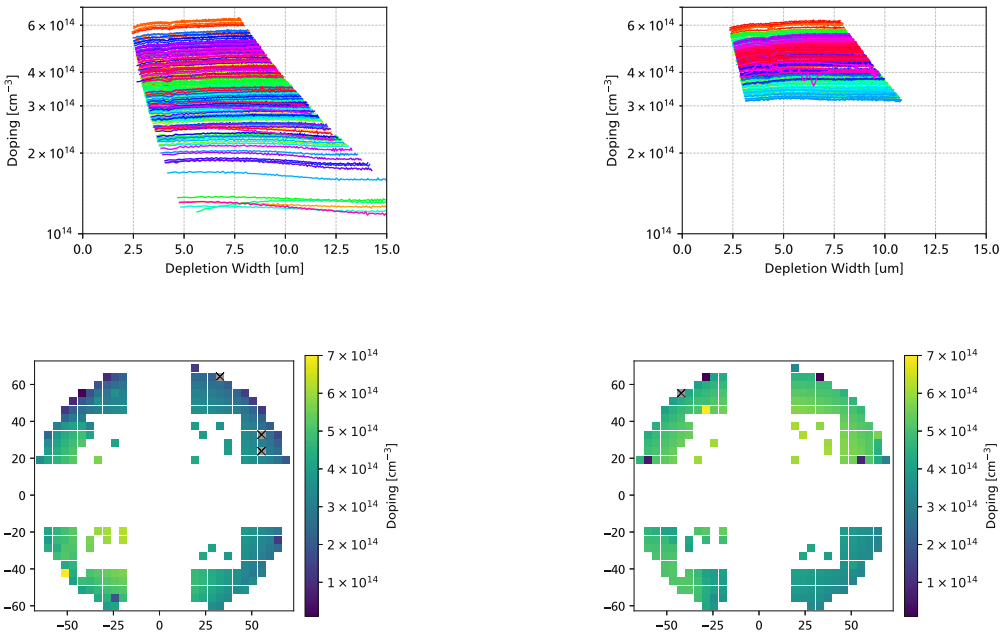

Figure 6.3.13: Doping concentration extracted from C-V measurements for wafers 1 (left) and 5 (right).

6.4 Determination of the 4H-SiC Ionization Energy

The ionization energy or electron-hole pair creation energy ϵ_i (see Section 2.4.4) is an essential material parameter to know when designing a semiconductor detector system. While for silicon the ionization energy has been thoroughly characterized, there has been some confusion in the literature about the ionization energy of 4H-SiC, with values ranging from 5 eV to 8.6 eV as shown in Table 4.2. Most of the measurements have been performed using a cross-calibration with a silicon detector, used to calibrate the experimental setup (and amplifier). The calibrated setup can then be used to measure the ratio between the signals obtained for 4H-SiC and silicon, which is proportional to the ratio of their ionization energies. Other approaches include a calibration using a charge injection into the amplifier via a well-known capacitor, or measurements of the DC current induced in a SiC diode by a known keV electron-beam current.

In order to address the uncertainties in $\epsilon_{i,\,SiC}$ in the literature, measurements were performed using alpha particles in vacuum and a silicon detector to calibrate the readout electronics. The measurements have been partially performed as a part of a Master's thesis [177], and have been published in Gsponer et al. [46], which is reproduced in this section.

Table 4.2: Previously published values of ϵ_i for 4H-SiC. For measurements that use a comparison to silicon, the ionization energy of silicon that was used is given as well (if it is stated in the paper).

Ref.	Year	$\epsilon_{i,SiC}$ [eV]	Radiation	Method	Device Type	$\epsilon_{i,\,Si}$ [eV]
[46]	2023	7.83 ± 0.02	α	Comp. to Si	PiN diode	3.62
[236]	2023	7.78	α	Comp. to Si.	Schottky diode	3.60
[190]	2022	8.06 [1]	252 MeV protons	Comp. to Si.	PiN diode	3.64
[237]	2013	7.82 ± 0.02	α	Charge inj.	Schottky	-
[238]	2013	7.28	α	Charge inj.	Schottky	-
[239]	2006	5.05	e^-	DC Current	PiN diode	-
[240]	2005	7.78 ± 0.05	α	Comp. to Si	Schottky diode	3.62
[240]	2005	7.79 ± 0.09	protons	Comp. to Si	Schottky diode	3.64
[241]	2005	7.6	X-Rays (^{241}Am)	Comp. to Si	PiN diode	3.60
[242]	2004	8.6	α	Comp. to Si	PiN diode	3.62
[243]	2004	7.71	α	Comp. to Si	Schottky diode	3.62
[244]	2003	7.8	X-Rays (^{241}Am)	Comp. to Si	PiN diode	3.67

[1] The ionization energy stated in the paper (5.85 eV) [190] has been measured using protons penetrating the detector. However, for the comparison to silicon, the authors directly compared the signal amplitudes, without taking into account the different amount of energy deposited by protons in silicon and 4H-SiC detectors of the same thickness. Correcting for the deposited energy results in an ionization energy of 8.06 eV.

6.4.1 Measurement Method and Samples

Figure 6.4.1 shows the detector used for the measurement of the ionization energy. In order to calibrate the amplifier, a silicon diode from a test structure of the CMS tracker production [245] was used. This diode has an area of $5 \times 5\,mm^2$, a thickness of 300 µm and a full depletion capacitance of 22 pF. On the surface of the diode, an aluminum metal layer and a passivation layer are present, with an equivalent aluminum thickness of 2.2 µm (simulated using the GATE toolkit [246]). Two $3 \times 3\,mm^2$ 4H-SiC PiN diodes were investigated, produced by CNM as a part of run 13575. One diode has metallization covering the entire active area, which, together with the passivation, results in an equivalent aluminum thickness of 1.72 µm. The other diode has metal only for the bond pads (as well as a ring around the edge of the diode), which results in a reduced material budget of 0.6 µm [46]. Without the metal covering

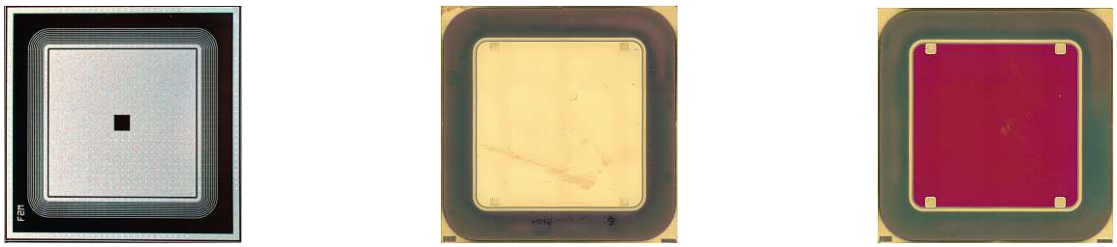

(a) Silicon detector (b) SiC with metallization (c) SiC without metallization

Figure 6.4.1: Microscopy images of the used silicon and 4H-SiC detectors. Taken from [46].

the diode area, the induced current is collected via the p^{++} and bond pads at the circumference of the diode. For fast amplifiers, the resistivity of the implants results in position-dependent *RC* effects [173]. However, if the integration time is sufficiently long ($> 100\,\text{ns}$), the detector signal is independent of the position.

6.4.2 Ionization Energy of 4H-SiC

In order to determine the ionization energy of 4H-SiC, a comparison measurement between the silicon detector (Figure 6.4.1a) and SiC detector with metallization (Figure 6.4.1b) was performed using alpha particles in vacuum (see Section 4.3 for a description of the experimental setup). A Cividec Cx-L [179] charge-sensitive amplifier was used, and both detectors were wire-bonded on passive ceramic boards manufactured by the CERN solid state detector (SSD) lab. A bias voltage of 400 V was applied to both detectors using the internal bias tee of the amplifier to ensure full depletion, and the signal of the amplifier was read out by a Rohde&Schwarz RTO6 oscilloscope with a 16 bit vertical resolution. By using a bleed valve (and a PID pressure controller, see Section 4.3), 25 000 events were acquired for different air pressures in the vacuum vessel, between 0.3 mbar and 1000 mbar.

As the silicon and SiC detectors feature different thicknesses of the passivation and metal layers, it is crucial to accurately assess the energy that is lost in these dead layers if the signals are compared between detectors. Figure 6.4.2 shows the simulated energy deposition in both detectors as a function of the air pressure in the vacuum chamber.

Below a pressure of around 1 mbar, the scattering of alpha particles in air is negligible. At higher pressures, the energy reaching the detector is reduced, with a maximum of around 500 keV lost in the 6 mm between the source and the detector. For an adequate vacuum, the dead material on top of the detector volume results in an energy loss of around 330 keV for the silicon detector and 190 keV for the 4H-SiC detector. This energy loss is also susceptible to statistical fluctuations (*energy straggling*), which will have an impact on the energy resolution that can be achieved (as will be discussed in Section 6.4.3). By comparing the simulated energy deposition E_α to the measured signal, the responsivity of the detector (V/MeV) can be obtained, shown in Figure 6.4.3. The ratio of the results for silicon (0.398 V/MeV) and 4H-SiC (0.184 V/MeV), multiplied by the ionization energy of silicon $\epsilon_{\text{i, si}}$ =3.62 eV [247] yields the ionization energy of 4H-SiC

$$\epsilon_{\text{i, SiC}} = \frac{(0.398 \pm 0.001)\,\text{V/MeV}}{(0.184 \pm 0.001)\,\text{V/MeV}} \cdot 3.62\,\text{eV} = (7.83 \pm 0.02)\,\text{eV}.$$

This result agrees well with recent measurements (which also use a comparison to silicon) [236, 237] and gives confidence to the ionization energy of 4H-SiC being in the region of 7.8 eV.

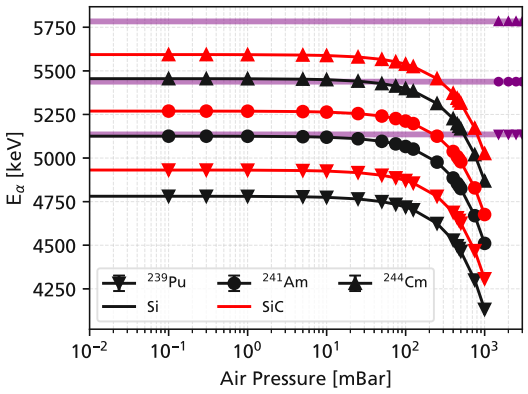

Figure 6.4.2: Energy deposited in detector E_α as a function of air pressure and nuclide for the silicon (black) and 4H-SiC detector with metallization (red). The mean decay energy for the three nuclides is indicated by a purple line. Adapted from [46].

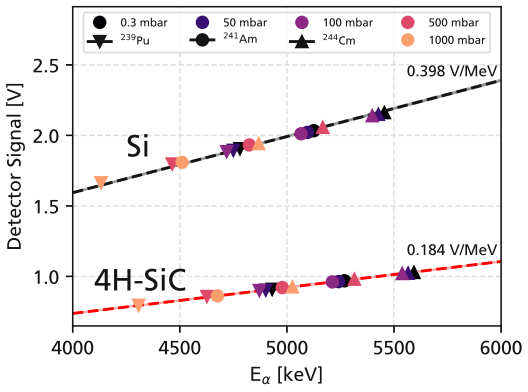

Figure 6.4.3: Detector signal versus simulated energy deposition in the detector. The markers indicate the measured detector signal for different pressures inside of the vacuum chambers and decay energies of the different nuclides. Adapted from [46].

6.4.3 Energy Resolution

After the ionization energy of 4H-SiC was determined, the energy resolution of the detectors for alpha particles was also investigated. The original aim of this study was to try to determine the Fano factor of 4H-SiC, which influences the Poissonian statistics of the electron-hole pair generation. However, for alpha particles of approximately 5 MeV the expected Fano fluctuations (using a Fano factor of 1.0 [248]) are only on the level of 5 keV FWHM [46], which is below even the best energy resolution that can be obtained in alpha spectroscopy using silicon detectors (around 10 keV FWHM [249]). Typically, Fano fluctuations will only be relevant in X-ray spectroscopy, see for example [207]. Nevertheless, the energy resolution for alpha particles is an interesting quantity to investigate, as a charge deposition in this order of magnitude is similar to what is expected in heavy-ion experiments (see, for example, [17, 133]).

For measurements of the energy resolution, a CoolFET charge-sensitive amplifier [180] was used, which provided a lower noise level than the Cividec Cx-L amplifier. Additionally, the output of the charge-sensitive amplifier was passed through an Ortec 671 shaper module and directly histogrammed by an Ortec 928 multichannel analyzer. Figure 6.4.4 shows the electron noise charge (ENC) measured

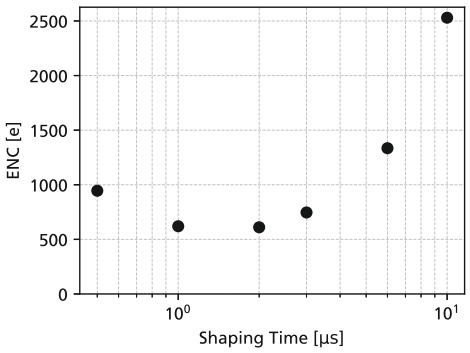

Figure 6.4.4: ENC for a pulse applied to the test input of the CoolFET charge-sensitive amplifier.

for a fast pulse applied to the test input of the CoolFET amplifier using different shaping times. The amplifier was calibrated in terms of the absolute charge using the reference silicon detector. During the measurement of the ENC, a 4H-SiC detector was connected to the amplifier and biased at 400 V in order to take into account the noise introduced by the detector capacitance (as well as the capacitance of the cables between the detector and the amplifier). For a shaping time of 2 µs, a minimum noise of 610 e is reached, which equates to a FWHM energy resolution of 5.2 keV for silicon and 11.2 keV for 4H-SiC. This energy resolution presents the lower limit that can be reached, assuming ideal detectors.

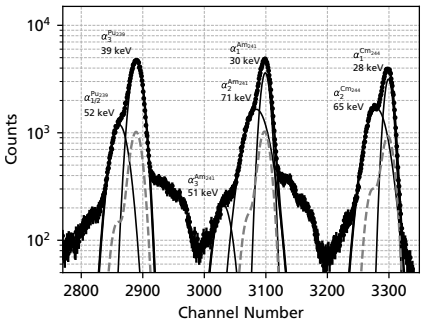

(a) Silicon detector.

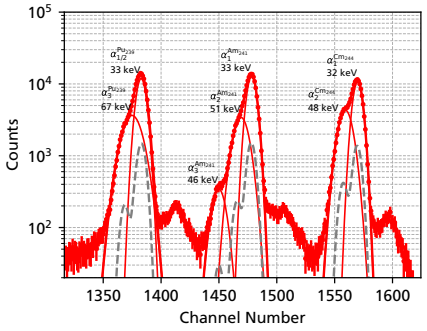

(b) SiC detector with metallization.

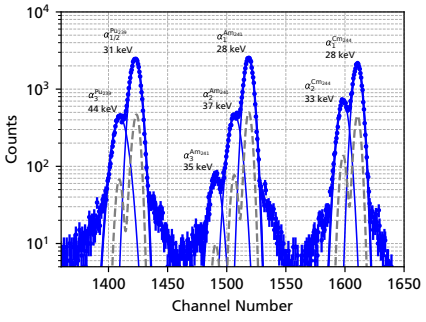

(c) SiC detector without metallization.

Figure 6.4.5: Histograms of the measured alpha-particle spectrum in vacuum for the Si (black) and SiC (red, blue) detectors. Gaussian fits for each decay energy are indicated by dashed lines, with the sum shown using a solid line and the FWHM resolution annotated. Adapted from [46].

For the silicon detector, as well as 4H-SiC detectors with and without metal covering the active area (see Figure 6.4.1), energy spectra were recorded for 100 000 events in vacuum, depicted in Figure 6.4.5. The silicon detector and 4H-SiC with metal reach a similar energy resolution, around 30 keV FWHM. For the 4H-SiC detector with a minimal material budget (no metal covering the active area), the best energy resolution of 28 keV FWHM is reached in Figure 6.4.5c, corresponding to a resolution of 0.5 % FWHM for 5.5 MeV [46]. This energy resolution is almost three times as high as expected from the noise of the amplifier.

While the dead material on the surface of the detector accounts for a line-broadening (simulated using GATE) of 15 keV for the silicon detector, and 12 keV and 9 keV FWHM for the 4H-SiC detectors [46], this is not able to account for the observed energy resolution. Furthermore, tails and other features are visible in the histograms, next to the expected decay lines. These limitations can likely be attributed to the roughness of the passivation and metal layers of the samples. Non-uniformities of the passivation layer of up to 100 nm have been observed for all samples using a Leica DCM8 metrological microscope. Different thicknesses of the dead layer will result in different energy losses, which can be larger than the energy straggling inside the dead layer. To avoid this issue, and to try and reach a better energy resolution in the future (only limited by the noise of the charge-sensitive amplifier), studies where the passivation layer is etched away in a chemical process are currently ongoing.

6.5 TCT Measurements with High Bandwidth Readout Electronics

In the transient current technique (introduced in Section 4.2), the current induced by the charge carrier drift inside of a detector is directly measured with a high temporal resolution. This allows for extracting a significant amount of information and can be used, for example, to measure the charge carrier mobility [166, 167, 250] or the electric field distribution inside irradiated detectors [168, 251]. In the high-energy physics community, TCT is commonly applied to 300 µm thick silicon detectors, where drift times of around 3 ns are expected. Over time, many different flavors of TCT have emerged, such as edge-TCT [252], ion-beam induced current (IBIC) [225] or two-photon absorption TCT (TPA-TCT) [253].

Applying TCT to 4H-SiC would yield previously inaccessible information, such as the electric field distribution inside the detector after irradiation, or give insights into the charge carrier mobility, which is still not precisely known [61]. However, up to now, the only TCT studies for 4H-SiC [225, 252, 254] that have been performed used readout electronics which were not fast enough to resolve the transient charge carrier drift. Instead, in these measurements, the collected charge was measured as a function of the position in the detector (and the electric field). Transient currents have only been able to be resolved in 4H-SiC for cases where significant tails in the transient current of the detector are present, such as for semi-insulating 4H-SiC [255] or neutron-irradiated 4H-SiC samples in forward bias [256, 257].

In order to enable the transient-current-technique to be applied to 50 µm 4H-SiC detectors, new high-bandwidth readout electronics have been developed and combined with low-capacitance SiC diodes to achieve rise times as low as 60 ps. This readout enabled, for the first time, measurements of the transient current in thin 4H-SiC detectors. Differing transient currents were clearly observed for different types of charge injection, such as alpha particles (Section 6.5.2), UV lasers (Section 6.5.3), and protons (Section 6.5.5). The effect of an increasing prompt current has been observed for increasing electric fields, even after the device is fully depleted. With the measurements performed in this section, the drift velocity of electrons and holes is extracted and compared to mobility models of the literature in Section 6.5.4.

6.5.1 Low-Capacitance SiC Diodes and High-Bandwidth Readout

As discussed in Section 3.3, there are different strategies to design transimpedance amplifiers with a high bandwidth. One bandwidth limitation will always be the low-pass filter formed by the detector capacitance C_D and the input impedance of the amplifier Z_{in}, with a bandwidth of

$$\mathrm{BW} = 1/(2\pi Z_{in} C_D). \tag{6.5.1}$$

For an input impedance of $Z_{in} = 50\,\Omega$, this imposes a bandwidth limit of 2 GHz for a detector capacitance of $C_D = 1.6$ pF and 10 GHz for $C_D = 320$ fF. Two options exist to increase the bandwidth: either decrease the input impedance or decrease the detector capacitance. As discussed in Section 3.3, the input impedance for a common-emitter TIA circuit (such as found on the UCSC LGAD single channel readout board) can be reduced by decreasing the feedback resistance. However, this will also reduce the gain, and for the highest frequencies, there will still be a significant limit by the input capacitance of the amplifier (added to by parasitic capacitance). Reducing the detector capacitance itself is the most straight-forward method to decrease the detector capacitance, especially when starting from a very large value of capacitance (such as for the previously shown $3 \times 3\,\mathrm{mm}^2$ 4H-SiC PiN diodes with $C_D \approx 18$ pF).

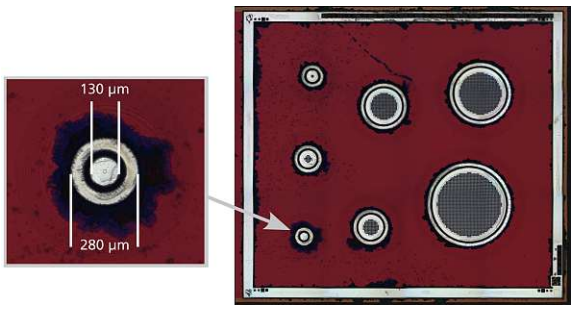

Figure 6.5.1: 4H-SiC die with round PiN diodes of different areas. Each diode features a grid of openings in the metallization to allow for light injection by a laser. Additionally, a guard ring around the diode area can be contacted to contain the depletion zone. Because the hole in the center of the smallest area diode was not opened (due to issues with the metal lift-off process), laser light was injected in the gap between the diode and the guard ring instead.

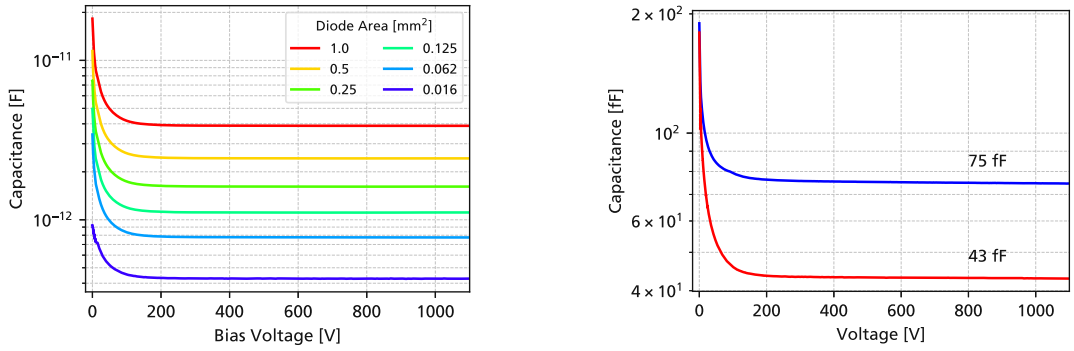

Figure 6.5.2: Left: Capacitance-voltage measurements for 50 µm thick PiN diodes with different areas at a frequency of 10 kHz with a contacted guard ring. Right: Comparison of the measured capacitance for a floating (blue) and grounded guard ring (red).

For the measurements present herein, circular 50 µm thick 4H-SiC diodes produced by CNM in the run 17407 were used, depicted in Figure 6.5.1. Different diode areas are available on the die, from 1 mm^2 to 0.016 mm^2. To minimize the capacitance, the diode with the smallest diameter was used. Figure 6.5.2 shows the typical measured capacitance as a function of the diode area and bias voltage. By grounding the guarding ring, a capacitance as low as 43 fF can be obtained. The depletion voltage is approximately 100 V. Such a low capacitance results in a theoretical bandwidth well above 50 GHz. In practice, however, the bandwidth will be limited by parasitics, such as the bond wire inductance or bond pad capacitance.

In order to read out the detector, a Mini-Circuits PMA3-14LN+ low noise amplifier (LNA) was chosen, introduced in Section 3.4.4. This amplifier features a very stable gain of 22 dB from 50 MHz to 10 GHz with a low typical noise figure of 1.8 dB. Compared to building a transimpedance amplifier using a discrete transistor, such as the Infineon BFR840 used in the UCSC LGAD readout board, the Mini-Circuits LNA is a monolithic microwave integrated circuit (MMIC) and can be treated as a "black-box" with an input and output impedance of 50 Ω. Designing an amplifier as an integrated circuit allows for a much smaller size than using discrete components, reducing parasitic inductances and capacitances, shortening signal paths, and resulting in better performance in general. To test the performance and suitability of this readout electronics, the SiC die was mounted directly on the amplifier input of the TB-PMA3-LN14+ evaluation board, as depicted in Figure 6.5.3. The input SMA connector was removed, and in its place, SMD capacitors have been added, which are connected to a high voltage by a wire to an additional SMA connector. On top of the capacitors, the SiC die was affixed using silver glue and wirebonded to a decoupling capacitor soldered on the PCB trace of the amplifier input. In addition to the decoupling capacitor, a 100 kΩ bias resistor to ground was added at the amplifier input. Care was taken to keep the signal path from the SiC detector to the LNA as short as possible and to minimize the bond wire inductance. Still, the bond wires feature a length of approximately 1.5 mm, limited by the distance from the diode to the edge of the die (approximately 800 µm) and the necessary distance between the bond pad and the detector (at high voltage) to avoid sparking in air.

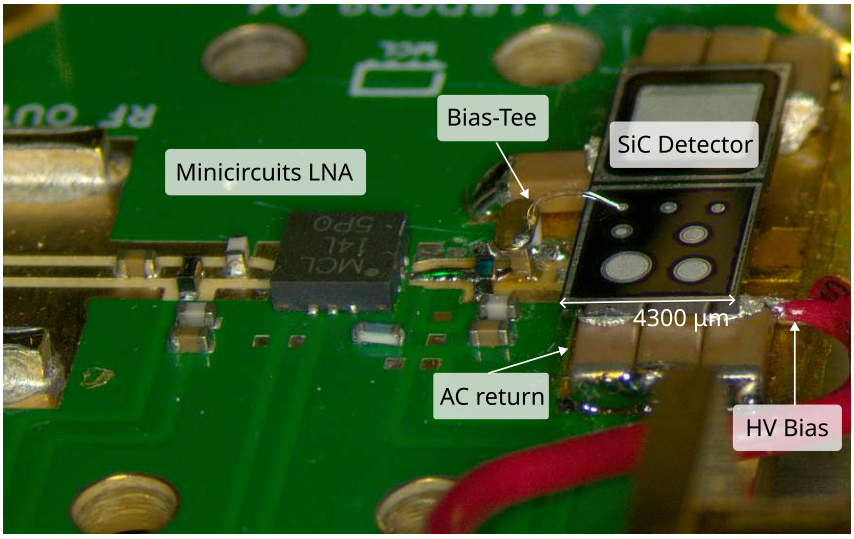

Figure 6.5.3: View of the 4H-SiC detector mounted on top of the TB-PMA3-LN14+ evaluation board.

6.5.2 Alpha Particles

In the first tests, alpha particles in vacuum (see Section 4.3 for a detailed description of the setup) were used. To digitize the signal, a Rohde&Schwarz RTP164 oscilloscope was employed, with an analog bandwidth of 16 GHz and a sample rate of 40 GSa/s. Figure 6.5.4 shows the measured transient current (assuming an input impedance of 50 Ω and an amplifier gain of 22 dB) for a bias voltage of 1.1 kV. The 10-90 % rise time of the signal is extremely low, only around 60 ps. This is expected from the fact that the charge carriers in a planar sensor start moving immediately after they are created (see Section 2.7.1). Additionally, this shows that the MMIC-based readout electronics and low-capacitance detector can provide a very high bandwidth, which can be estimated to be $\approx 0.35/t_{\text{rise}} = 5.8\,\text{GHz}$. The total signal time of only 500 ps is equal to the combined rise and fall time of an amplifier with a bandwidth of 2 GHz. While the signal is very large (more than 200 mV, even without a secondary amplifier), there is a significant spread in the signal amplitude. This is likely caused by variations in the hit position of the alpha particle on the detector. If the particle hits near the edge of the diode, a part of the charge is collected by the guard ring instead of the sensor and "lost". Due to the very small area of the diode, the guard ring represents a significant fraction of the total area. The small area of the detector also resulted in a very slow measurement speed, with a particle hit only every couple of minutes.

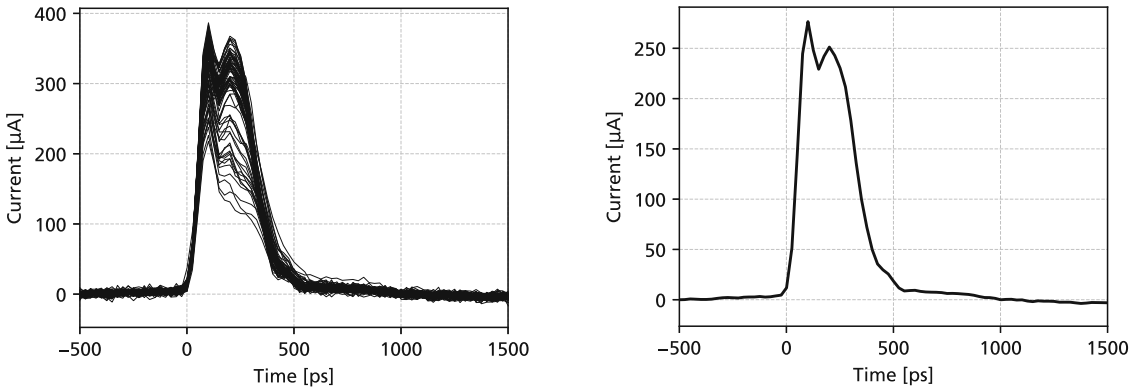

Figure 6.5.4: Measured waveforms for alpha particles in vacuum at a bias voltage of 1100 V. Left: individual events showing noise and variations in the signal amplitude. Right: Result of averaging 100 waveforms, which have been aligned to the rising edge.

Figure 6.5.4 (right) shows the waveforms after averaging, which allows for fluctuations in the signal amplitude to be removed and the noise level to be decreased. Low-amplitude events (near the guard ring) have been removed by applying an amplitude threshold. Care has to be taken to align the events in time before averaging is performed. As the short rise time of 60 ps corresponds to less than 3 oscilloscope samples (with a spacing of 25 ps), there can be a shift in time, depending on which oscilloscope sample first crosses the threshold. The threshold crossing time is therefore first computed using interpolation between samples and a CFD of 50 %, before the events are aligned to an identical threshold crossing time, where they can be interpolated and averaged.

The waveforms for different bias voltages (between 0 and 1100 V) are depicted in Figure 6.5.5. It is clearly visible that the prompt current continues growing with the bias voltage, indicating that the charge carriers' velocity also continues to grow, as the saturation velocity is not yet reached. For very low voltages, the signal is much longer as the electric fields are very low, and in the case of very low bias voltages (< 100 V), the detector is only partially depleted, which means that the charge collection is dominated by diffusion. The waveforms also show a significant feature just after a rising edge of the signal, where the measured transient current temporarily decreases again. This is likely caused by an

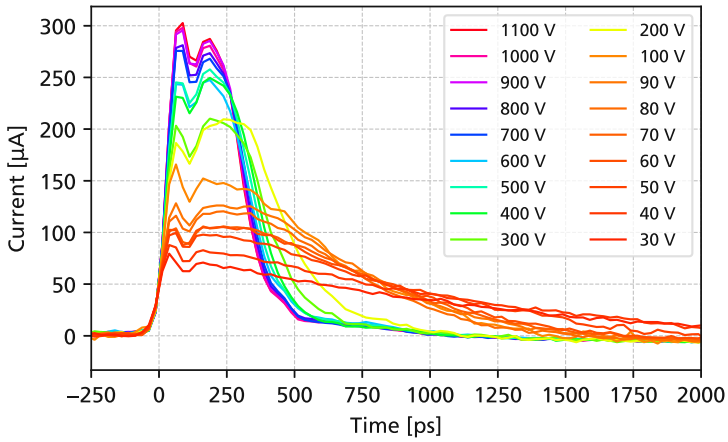

Figure 6.5.5: Averaged induced current for alpha particles for different detector bias voltages. The transient current has been calculated assuming an amplifier input impedance of 50 Ω and a gain of 22 dB.

RLC-resonance, formed by the detector input impedance, the detector capacitance, and the inductance of the bond wire. As the bond wire is rather long (1.5 mm), an impedance of up to around 1-2 nH is expected [147]. In the frequency domain, this effective RLC filter will have a resonance in the GHz region, which can be observed by a damped oscillation with a certain settling time after the rising edge.

6.5.3 UV-TCT

After measurements using alpha particles, measurements were then conducted at the UV-TCT setup detailed in Section 4.2. Because the laser has a trigger output with a very low jitter relative to the laser pulse itself, it can be used to trigger the oscilloscope and average multiple waveforms. Additionally, UV light deposits charge almost uniformly along the depth in 4H-SiC, and the laser strength and repetition rate can be arbitrarily tuned. As the diode has only a small opening in the metallization for the laser light to enter (compare with Figure 6.5.1), an additional Mini-Circuits ZX60-LN14S+ low-noise amplifier (see Section 3.4.4) was used before the oscilloscope to boost the signal of the detector above the noise floor of the oscilloscope.

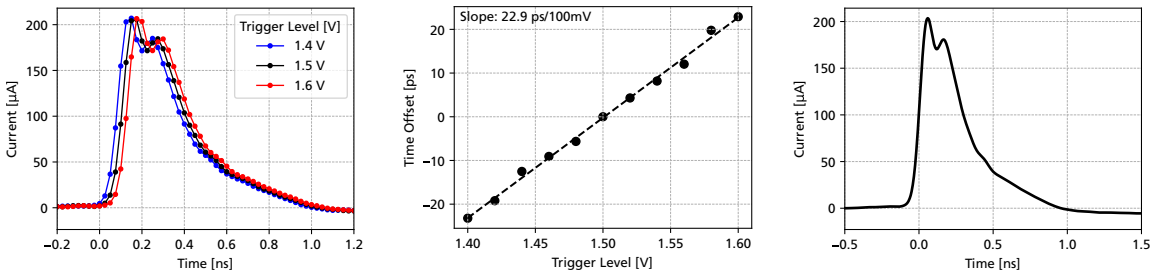

Figure 6.5.6: Left: Measured UV-TCT waveforms at a bias voltage of 1100 V for different trigger thresholds on the trigger provided by the laser. Each time, 1000 waveforms have been averaged. The entire waveform is shifted in time for different thresholds, as the acquisition is started slightly earlier or later in respect to the laser pulse. Middle: Fitted time shift as a function of the trigger level, with a slope of 22.9 ps/100 mV. Right: Resulting interpolated waveform.

By changing the trigger threshold for which the oscilloscope starts its acquisition, the measured waveforms can be shifted in time, as depicted in Figure 6.5.6 (left). The slope of the laser trigger signal was measured to be around 23 ps/100 mV. This means that by changing the trigger threshold in a range of ±50 mV, the start of the oscilloscope acquisition (relative to the laser pulse) can be continuously shifted in the range between two oscilloscope samples (25 ps). This effectively allows for a higher synthetic sample rate to be achieved, the same working principle which is used in a *sampling oscilloscope*. The analog bandwidth of the oscilloscope is still limited to 16 GHz, and this technique is only possible because the laser provides a low jitter trigger signal.

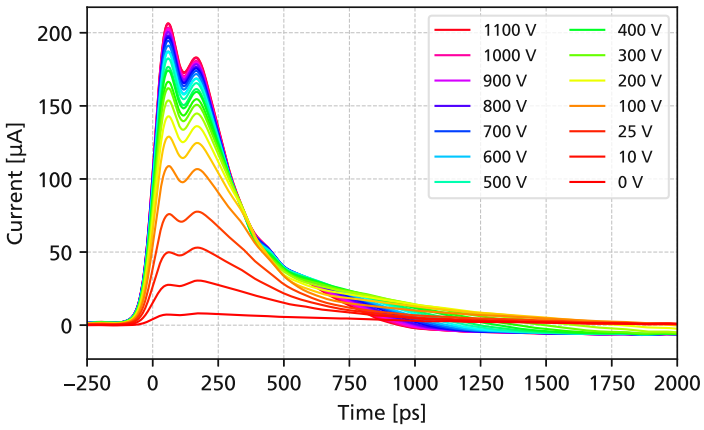

Figure 6.5.7: Averaged and interpolated UV-TCT induced current for different bias voltages. A laser repetition rate of 1 MHz and a tune value of 62 % was used.

This technique has been applied to a voltage scan of the transient current, depicted in Figure 6.5.7. The measured data has been interpolated to a sample rate of 500 GSa/s (2 ps sample spacing). As a function of the voltage, the transient current keeps increasing, even after the full depletion of the detector. Again, a "kink" after the first maximum is visible. This kink can likely be attributed to a damped resonance of the bond wire inductance, detector capacitance, and input impedance of the amplifier, which forms an RLC low-pass filter. This filter is not properly dampened and results in oscillations, which could be reduced by decreasing the detector capacitance or amplifier input impedance. Additionally also a longer bond wire (with a higher inductance) could be used, but this would limit the bandwidth.

Comparing the UV-TCT results to alpha particles in Figure 6.5.8 (left) shows a very similar behavior for the first 250 ps. As the holes (which move faster than electrons) drift upwards in n-type 4H-SiC, alpha particles, which penetrate only approximately 15 µm into the device, will result in shorter transient currents than for a UV laser, where holes have to traverse the entire thickness of the detector. This is in accordance with the measured signals for alpha particles being shorter than those in UV-TCT, which shows two linear regions, associated with the electron and hole drift.

Charge carriers in a detector induce a transient current according to the Shockley-Ramo theorem (see Section 2.7.1). Just after a particle (or laser) creates a number of electron-hole pairs in a detector (with a total charge Q), no charge carriers have been collected by the electrode yet, and the *prompt current* is given by [258]

$$\mathrm{I}_{\mathrm{prompt}} = Q \cdot (v_e + v_h) \cdot 1/d\,, \tag{6.5.2}$$

for a planar detector of thickness d and electron/velocities of v_e, v_h. If the electric field inside the detector is uniform (for example, if a bias voltage much higher than the full depletion voltage is applied), the drift velocity (and therefore the prompt current) will be independent of the charge deposition distribution [259]. Figure 6.5.8 (right) shows the prompt current extracted from UV-TCT and alpha par-

ticle measurements. The prompt current of the UV laser measurement has been scaled to agree with the current for the alpha measurement at 1 kV, as the amount of injected charge by the laser was not controlled for. For the results expected by mobility models found in the literature, a charge of $Q \approx 5.5\,\text{MeV}/7.83\,\text{eV}/e \approx 700\,\text{k}e$ was used. The prompt current expected from mobility models is almost a factor three larger than what was obtained in measurements, although a very good agreement of the shape of the results is found when scaling the theory prediction by a constant. This could be caused by multiple factors: First, the conversion from the measured signal in mV to a transient current in µA might be inaccurate, if the gain of the amplifier or its input impedance differ from the expected values of 22 dB and 50 Ω. Furthermore, the RLC effects of the bond wire inductance and detector capacitance might distort the measurement of the transient current, decreasing the amplitude of the signal.

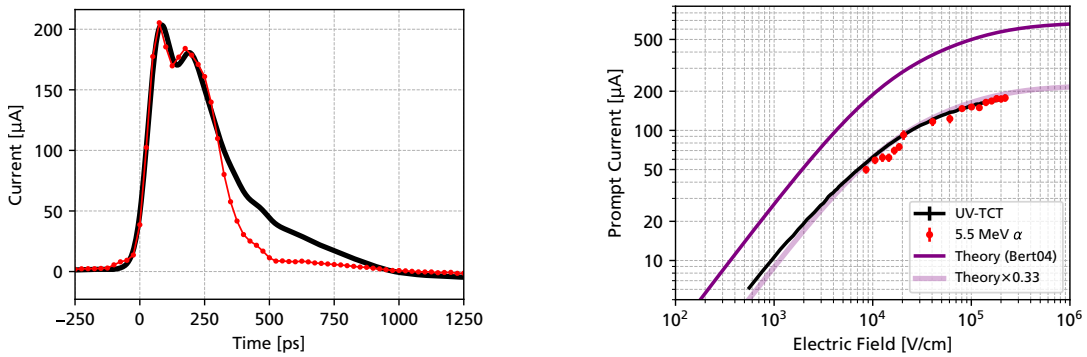

Figure 6.5.8: Left: Comparison between transient current of alpha particles (red, with a sample rate of 40 GSa/s) and UV-TCT (black, interpolated) at a detector bias voltage of 1 kV. Right: Comparison of the prompt current between UV-TCT and alpha particle measurements. The purple line shows the expected result from the Shockley-Ramo theorem, compared to the expected result using the 4H-SiC mobility models described in [70].

6.5.4 Extraction of Charge Carrier Velocities

The exact values of the charge carrier drift velocities in 4H-SiC is a very important quantity, as it directly impacts the performance of timing devices (such as SiC-LGADs, see Section 5.5.3). Additionally, there are large uncertainties in the literature for the drift velocity values parallel to the c-axis, as the industry mainly focuses on lateral drift perpendicular to the c-axis, such as for SiC-MOSFETs [61]. While the prompt current method (previously presented) only yields the sum of the electron and hole velocity, analysis of the transient current in time allows both drift velocities to be disentangled. For example, in the *time-of-flight* method, charge carriers are injected near the electrode or anode, and by measuring the drift time until they arrive at the other end, the drift velocity can be determined [260]. To disentangle electrons and holes, the depth to which charge carriers are injected should be very small compared to the drift distance, such that the signal is not contaminated by the other charge carrier species. In silicon detectors, this can be achieved by using light from red lasers (with wavelengths around 660 nm), which has a very low penetration depth in silicon. By injecting light from the bottom or top of the device, electron and hole injection can be achieved [261, 262]. However, for 4H-SiC, no equivalent to red-laser TCT exists, and UV lasers (with a sufficient photon energy to overcome the bandgap of 4H-SiC) act similarly to IR lasers in silicon, with a very long absorption length. A possibility to obtain electron or hole injection would be to use pulsed x-ray sources (which have been frequently applied to establish charge carrier mobility models for different types of semiconductors [263]), or to use TPA-TCT. However, using the existing data, the contribution of electrons and holes can be distinguished by performing fits of the transient current.

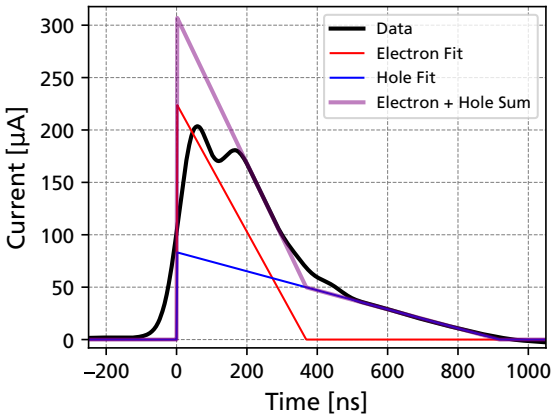

Figure 6.5.9: Measured UV-TCT transient current with linear fits to the electron and hole drift.

Figure 6.5.9 shows the measured transient current for a detector bias voltage 1 kV, where linear fits of the electron and hole drift have been performed. For a uniform MIP-like charge distribution, the electron and hole current is expected to form a triangular shape, with charge carriers gradually collected at the boundaries of the detector. For a time larger than 200 ps, a very good agreement of this simple fit is obtained with the measured waveform. Around the peak of the waveform, however, a higher transient current would be expected than was measured. This is likely due to the effect of the detector capacitance and bond wire inductance, as discussed previously for the prompt current. By extracting the intercept between the fitted electron and hole current, the drift time, and therefore the drift velocity, can be extracted.

Figure 6.5.10 shows the extracted drift velocity as a function of the electric field, compared to literature values. Qualitatively, the saturation of the charge carrier velocity towards higher electric fields can be reproduced, with very similar characteristics observed for the electron drift as in the literature. However, especially for the hole drift, a significant disagreement with the literature is present. This might be a result of the fits working less ideally for the hole drift compared to the electron drift, as the slower hole drift is affected more by tails or an undershoot of the amplifier. A comparison to the prompt current method is shown as well for the sum of the electron and hole drift velocities. Again, the extracted drift velocities from the time-of-flight method are lower than in theory; however, the general shape of the velocity saturation looks very similar.

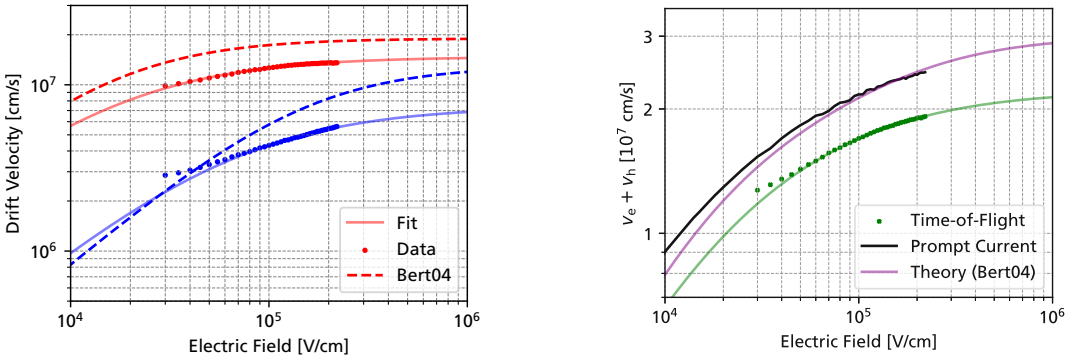

Figure 6.5.10: Left: High-field mobility extracted from fitted electron and hole transient currents. Right: Sum of electron and hole drift velocity compared to literature values [70]. The data for the prompt current has been scaled in order to match the value of the literature curve.

While there is still a significant amount of work to be performed to perform a good quantitative determination of the charge carrier drift velocities in 4H-SiC, the working principle has been demonstrated. If injection of a single charge carrier type could be implemented (using a pulsed x-ray source or TPA-TCT), then the drift velocities could be extracted in a simpler and more robust way using the time-of-flight technique. A TPA-TCT campaign using a similar 4H-SiC sample (and a new version of the high bandwidth readout) has been carried out in June 2025 at the UPV/EHU femto laser facility in Bilbao, Spain [264], with the data analysis still ongoing.

6.5.5 Protons at MedAustron

While measurements using alpha particles and UV lasers have successfully been carried out, the transient current measured in these measurements might not perfectly reproduce the signal expected by a minimum ionizing particle. For alpha particles, the charge deposition is highly localized, and for UV-TCT, the laser pulse is not instantaneous (with a FWHM pulse width of about 50 ps, see Section 4.2.3). In order to study the transient current for particles passing through the entire thickness of the detector, measurements using 62.4 MeV protons were carried out at the MedAustron ion therapy center (see Section 4.4). These measurements used a very similar experimental setup to the previous studies, with

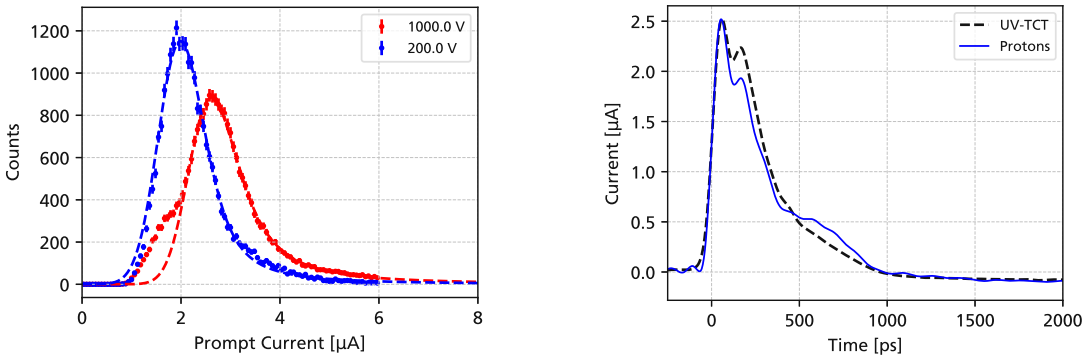

Figure 6.5.11: Left: Histogram of the maximum of the transient current for 62.4 MeV protons fitted using a Landau function. Right: Transient waveforms at a detector bias of 1 kV for protons (blue) and UV-TCT (black, normalized to the proton data).

an 20 dB ZX60-LN14S+ amplifier again being used to boost the signal above the noise floor of the oscilloscope. For each bias voltage between 1.1 kV and 200 V, 25 000 waveforms were acquired at 40 GSa/s using a leading edge trigger on the signal of the detector. Figure 6.5.11 shows the histogram of the resulting prompt current, fitted using a Landau distribution. For a bias voltage of 1 kV a MPV value of 2.52 µA is obtained, which corresponds to a SNR of 8. At a bias voltage of 200 V (approximately the full depletion of the diode), the SNR falls to 5, and below that, the peak of the Landau distribution was no longer distinguishable. Figure 6.5.11 also shows a comparison between an averaged waveform for protons and the waveforms measured in UV-TCT. Due to the low SNR of the proton data, averaging multiple waveforms in time was challenging, because the leading edges needed to be aligned better than 25 ps for the averaging not to "smear out" the waveforms. Therefore, only the 500 events with the largest amplitude (from the high-energy deposition tail of the Landau distribution) have been used for the waveform averaging. The waveforms acquired using proton beams agree well with UV-TCT. Some small discrepancies around the maximum of the waveform (as well as the width of the pulse) are visible, which are likely a result of the instantaneous charge deposition for protons, compared to the 50 ps pulse width of the laser.

The most probable value of the prompt current as a function of the bias voltage is depicted in Figure 6.5.12. The saturation of the prompt current towards higher bias voltages is well reproduced. Slightly higher prompt currents are attained for protons at low bias voltages compared to UV-TCT, which could be attributed to inaccuracies in fitting the MPV of the Landau distribution at low SNR.

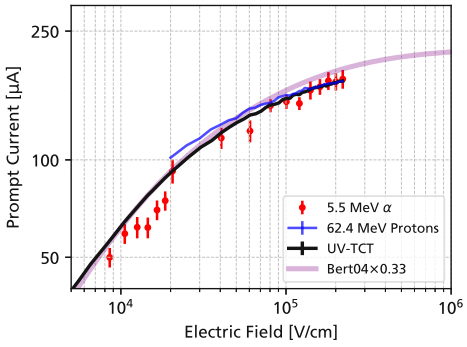

Figure 6.5.12: Prompt current for UV-TCT, alpha particles, and protons. All data points have been scaled to match the current measured using alpha particles at 1 kV. See also Figure 6.5.8.

Based on the high bandwidth obtained using a prototype LNA-based readout board, a custom PCB has been developed, depicted in Figure 6.5.13. This readout board has shown a very similar performance to the prototype for identical 4H-SiC diodes, with slight differences likely due to different bond wire lengths (different parasitic inductances). Tests and measurements are currently ongoing to measure the transient current in thin (50 µm) silicon detectors, such as trench-isolated LGADs

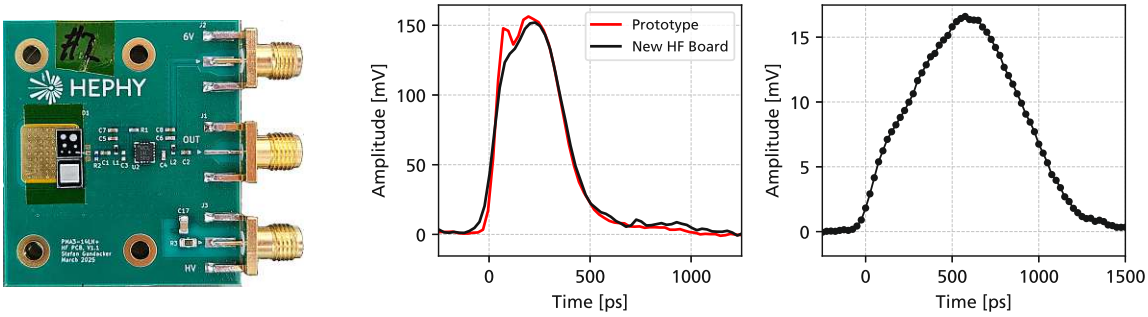

Figure 6.5.13: Left: Newly developed detector readout board based on the Mini-Circuits PMA3-14LN+ low-noise amplifier developed. Middle: Comparison of the new readout board to the prototype version (Section 6.5.1) for alpha particles in 50 µm thick 4H-SiC PiN diodes. Right: Transient signals for 1060 nm IR laser on a trench-isolated LGAD pixel [265] with an area of 370 µm × 240 µm at a bias voltage of 240 V.

7 Radiation Damage in 4H-SiC PiN Diodes

7.1 Irradiation Campaigns

The radiation hardness of solid-state detectors is becoming more important each year, as the luminosities and radiation levels of high-energy physics experiments continuously grow [1]. For the future high-luminosity upgrade of the LHC [2], 1 MeV equivalent fluences of up to $2 \times 10^{16}\,\mathrm{cm}^{-2}$ are expected [3], with the proposed Future Circular Collider reaching extreme fluences up to 1×10^{18} $\mathrm{n_{eq.}/cm^2}$in its hadron collider configuration [4]. Radiation damage in 4H-SiC detectors has been investigated since it was first used as a detector in the 1970s [43]. During the 2000s, when there was a significant interest of the detector community in 4H-SiC detectors, radiation hardness studies have been carried out already to fluences as high as 1×10^{16} $\mathrm{n_{eq.}/cm^2}$ [13]. While the results obtained in the past might still hold true nowadays, it is worth investigating the radiation hardness of 4H-SiC detectors again, as there have been significant improvements in the industry's growth process of 4H-SiC epitaxial layers, resulting in a higher material quality and lower doping (impurity) concentrations.

In order to assess the radiation hardness of $3 \times 3\,\mathrm{mm}^2$ 4H-SiC PiN diodes produced by CNM, two irradiation campaigns have been carried out. The first campaign used diodes produced in run 13575 and focused on fluences between 5×10^{14} and 1×10^{16} $\mathrm{n_{eq.}/cm^2}$. This irradiation was carried out in July 2021 at the TRIGA Mark II reactor of the Atominstitut at the Technical University of Vienna, depicted in Figure 7.1.1. For the irradiated devices in this campaign, the electrical characteristics were measured, and the charge collection efficiency was assessed using different types of ionizing radiation. These studies have been published in [16, 254, 257, 266] and served as a basis for a 4H-SiC TCAD radiation model [267, 268]. In the second irradiation campaign, PiN diodes from CNM runs 17407 and 16886 (produced as a part of the RD50-SiC-LGAD project, see Section 6.3.1) have been irradiated to a fluence of 1×10^{18} $\mathrm{n_{eq.}/cm^2}$ at the TRIGA reactor of the Jožef Stefan Institute in Ljubljana, Slovenia [269]. The electrical characterization results are reported in Section 7.5.

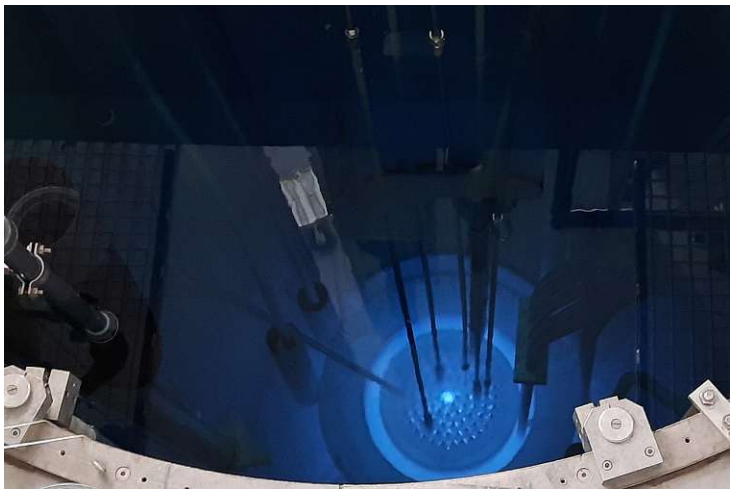

Figure 7.1.1: View into the TRIGA Mark II reactor at the Atominstitut in Vienna. Blue Cherenkov light is visible, emitted by β-decay electrons traveling faster than the speed of light in water.

Nuclear reactors are often used to perform radiation hardness testing of electronics and detectors in high-energy physics. Due to the high neutron flux inside a reactor core, irradiation campaigns are possible in a reasonable amount of time, simulating the radiation exposure experienced in years of operation at high-energy physics experiments. A widespread type of nuclear reactor used for science (and irradiation studies) is the TRIGA (Training, Research, Isotope Production, General Atomic) reactor series, which was built all over the world as a part of the United States' *Atoms for Peace* program [270]. A notable reactor of this type in the high-energy physics community is the TRIGA reactor at the Jožef Stefan Institute in Ljubljana, with a long history of radiation damage testing for silicon detectors [271]. HEPHY has carried out first irradiation studies of silicon detectors at the TRIGA MARK II of the Atominstitut reactor recently in 2020 [272]. The irradiation campaign of 4H-SiC diodes was carried out in 2021, and in order to reach a fluence of 1×10^{16} $n_{eq.}/cm^2$, an irradiation time of around 6 hours was necessary [230, 254]. The energy spectrum of the ATI reactor has been previously simulated and measured [273] in order to compute the radiation hardness factor κ, which can be used to convert the irradiation fluence to a 1 MeV neutron equivalent [272].

7.2 Effect on Electrical Characteristics

7.2.1 Current-Voltage Characteristics

The I-V characteristics of the 4H-SiC PiN diodes irradiated up to 1×10^{16} $n_{eq.}/cm^2$ were measured at room temperature (22 °C) in the HEPHY clean room, using a Keithley 2657A SMU and a Keithley 6571b electrometer. Because the detectors were permanently glued on a UCSC LGAD single-channel readout board from previous tests, measurements were performed by probing the detector on top of the PCB as depicted in Figure 7.2.1. The bond wires were removed, and the high-voltage bias was applied to the backside of the detector using a probe needle connected to the SMU. The current of the PiN diode was then measured using two probe needles, one of which grounded the guard ring, and another connected to the electrometer. Measuring the current with the electrometer instead of the SMU allows for leakage currents through the PCB board to be guarded from the current of the PiN diode (see also Figure 4.1.2d in Section 4.1).

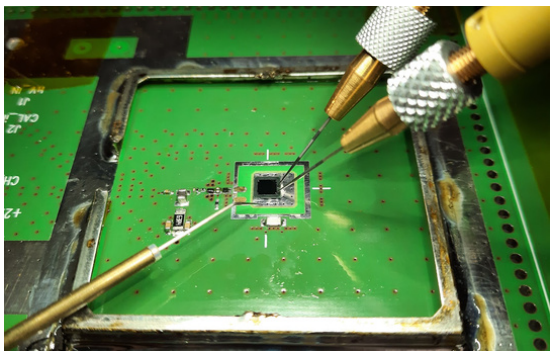

Figure 7.2.1: Neutron-irradiated 4H-SiC samples permanently glued to a readout PCB being characterized electrically using probe needles.

Figure 7.2.2 on the next page shows the measured I-V characteristics in forward and reverse bias up to a voltage of 1.1 kV. In reverse bias, the currents stay very small, less than 10 pA at the highest bias voltages, even for fluences up to 1×10^{16} $n_{eq.}/cm^2$. Compared to silicon, these currents are extremely small. After irradiation to high fluences, silicon detectors will typically require cooling to −20 °C (or below) to remain below µA current levels [7]. This is due to the fact that the bandgap of 4H-SiC is

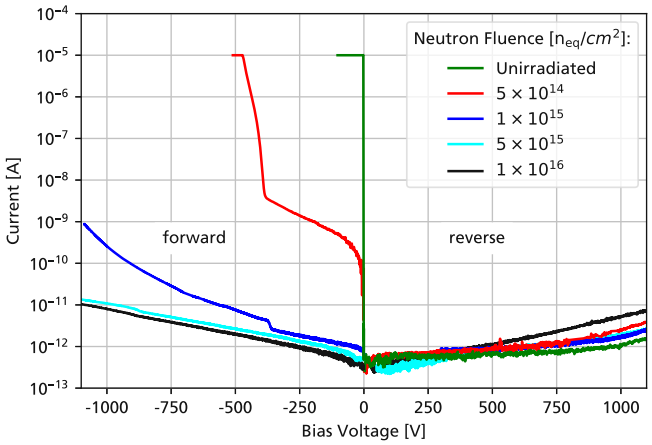

Figure 7.2.2: I-V characteristics for irradiated 4H-SiC diodes in forward and reverse bias. At high irradiation fluences, the current in reverse and forward bias is almost identical. Taken from [16].

almost three times as large as silicon's, which makes it exponentially harder for charge carriers to be thermally generated, even if additional energy levels are introduced to the band structure by radiation defects [224]. While a small increase in current is visible for the sample irradiated to the highest fluence (1×10^{16}), this current is likely a result of leakage currents on the surface of the device, as no increase in the current has been observed for similar studies up to 1×10^{17} $n_{eq.}/cm^2$ [116]. These very low currents make 4H-SiC an attractive candidate for high-energy physics experiments, as the power draw of the detector will be extremely small compared to silicon, and operation at room temperature is possible. This allows for the detector cooling to be removed and requires a less sophisticated powering scheme, both reducing the mass budget of the detector.

In forward bias, an interesting behavior can be observed. Already at the lowest irradiation fluence, the current in the forward direction is substantially reduced, and a bias voltage of around 400 V needs to be applied in order to conduct a significant current (10 µA). The current further decreases for higher irradiation fluences, and above 1×10^{15} $n_{eq.}/cm^2$, an almost identical current is observed in reverse and forward bias. The reduction of current in forward bias can be attributed to a decrease in the charge carrier lifetime as well as an electric field created by space charge, which blocks the electrons and holes from being injected into the device. This effect is illustrated in Figure 7.2.3, which shows the simulated

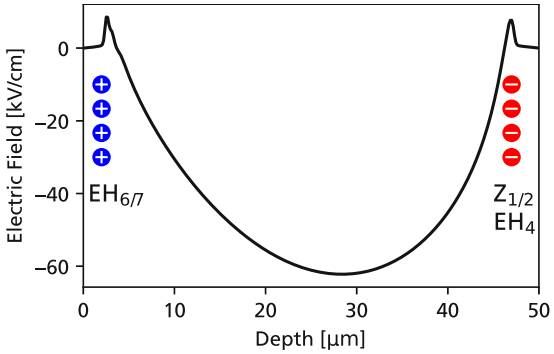

Figure 7.2.3: Electric field in a 4H-SiC PiN diode irradiated to 5×10^{14} $n_{eq.}/cm^2$ at a forward bias of 200 V obtained from TCAD simulations [268]. Space charge by trapped charge carriers at the anode (0 µm) and cathode (50 µm) results in an electric field barrier.

electric field inside an irradiated detector in forward bias. At the anode (the p^+ implant) and cathode (the n^{++} buffer layer), charge carriers injected under forward bias will be trapped by acceptor and donor-like traps, which will result in a large concentration of space charge. The space charge will induce an electric field, which presents a barrier for electrons or holes to be injected into the device. At higher and higher forward bias voltages, the traps will be fully filled, and the space charge can no longer grow to compensate the externally applied voltage. This will reduce the effective electric field barrier, allowing for charge carriers to enter the device again, resulting in a sharp increase of the current [268]. For higher radiation fluences, the number of traps is too large to be completely filled, and much larger electric fields in forward bias would need to be applied to restore conduction. Additionally, the charge carrier lifetime continues to decrease.

7.2.2 Capacitance-Voltage Measurements

The capacitance characteristics of irradiated detectors were acquired using the same setup as for the I-V measurements, using a high-voltage bias tee and an HP4284A LCR meter, and are depicted in Figure 7.2.4. It is immediately obvious that after an irradiation of only 5×10^{14} $n_{eq.}/cm^2$, the capacitance flat-lines and is independent of the bias voltage. This can be attributed to deep acceptor-like traps (such as $Z_{1,2}$) compensating the n-doping of the epitaxial layer. Therefore, the measured capacitance corresponds just to the physical dimensions of the epitaxy. No dependency on the C-V frequency was observed, between 100 Hz and 1 MHz and bias voltages of -1.1 kV to 1.1 kV. While for silicon there is a significant dependency of the capacitance on the frequency [274], the energy levels of the traps in 4H-SiC are so deep that there is no appreciable emission from the traps at room temperature in the timescale of C-V measurements. Essentially, the charge carriers in the traps are "frozen out" and do not respond to an AC excitation in the kHz range. Nevertheless, the space charge after irradiation is not zero. Donor-like traps (such as $EH_{6,7}$ [101]) can become positively charged when they capture an electron, and will introduce a fixed space charge that affects the electric field inside the detector [252, 275].

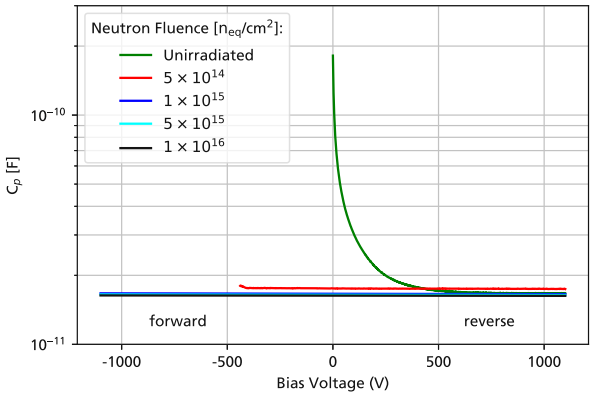

Figure 7.2.4: C-V characteristics for irradiated samples in forward and reverse bias measured, taken from [16]. The measurements used an AC voltage of 0.5 V at a frequency of 10 kHz.

A small difference in the capacitance can be seen between the individual fluences, with the lowest fluence showing a slightly higher capacitance. This can be attributed to the fact that the cathode (formed by a heavily doped n^{++} buffer layer) is not an abrupt junction, but extends by some micrometers in the epitaxial layer. For higher and higher fluences, more and more of the buffer is compensated, slightly increasing the depletion width. In the limit of a very high irradiation fluence (Section 7.5), the buffer layer will be completely compensated and the measured capacitance will correspond to the physical thickness of the device (50 µm epitaxial layer plus the 350 µm substrate).

7.3 Impact on the Charge Collection Efficiency

As the electrical characterization has shown, 4H-SiC PiN diodes can still be operated after irradiation up to 1×10^{16} $n_{eq.}/cm^2$, and the leakage currents remain extremely low (as expected from the wide bandgap of 4H-SiC). While these properties provide significant advantages over silicon (which requires cooling after irradiation), the question remains if the detector can still efficiently detect ionizing radiation. In order to quantify the reduction in charge collection efficiency, measurements have been carried out using high-energy protons [16], alpha particles [266], and UV-TCT [254, 257]

7.3.1 62.4 MeV Protons

The first measurements of the charge collection efficiency for irradiated sensors used 62.4 MeV proton beams at the MedAustron medical synchrotron (see Section 4.4). Protons with the lowest energy were chosen in order to maximize the signal in the detector (with 62.4 MeV protons corresponding to around 6 MIPs). Even though carbon beams are available at MedAustron and would deposit more energy in the detector, these beams can only be delivered in clinical intensities (and not in the low-flux modality as for protons), which, together with the large area of the detectors ($3 \times 3\,mm^2$) would lead to pile-up. During the measurements, the detectors were read out using a Cividec Cx-L charge-sensitive amplifier, by bypassing the electronics of the UCSC LGAD readout board the detectors were permanently glued on. Figure 7.3.1 shows the measured charge collection efficiency as a function of the bias voltage for unirradiated and irradiated sensors. Because of the radiation-induced reduction in the forward current of the detectors, particles were also able to be detected in forward bias operation (see [276] for comparable results of forward-bias irradiated SiC detectors). Data is shown only for a fluence of up to 1×10^{15} $n_{eq.}/cm^2$, as for higher irradiation fluences only the tail of the Landau distribution of the signal was able to be acquired.

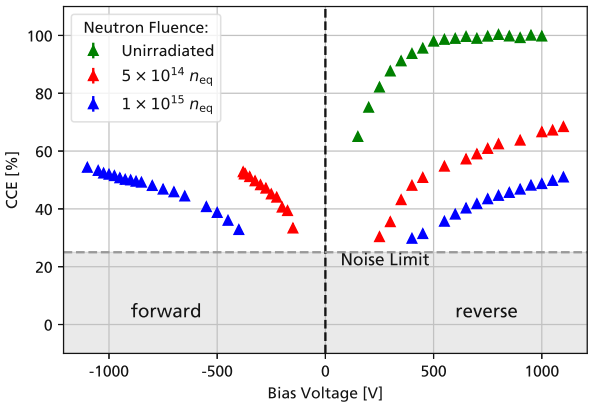

Figure 7.3.1: Charge collection efficiency for neutron-irradiated 4H-SiC PiN diodes measured using 62.4 MeV protons at MedAustron. Taken from [16].

The charge-collection efficiency (CCE) for the unirradiated sensor grows in accordance with the depletion width, reaching a plateau around 400 V. For the detectors irradiated to a fluence of 5×10^{14} and 1×10^{15} $n_{eq.}/cm^2$, a CCE of around 70 % and 50 % can be obtained at a reverse bias of 1 kV. In forward bias operation, slightly higher charge collection efficiencies were observed for the same bias voltage. This is thought to be caused by a more uniform electric field distribution of the detector in forward bias, and partial trap filling by the large injected current. For the sample irradiated to 5×10^{14} $n_{eq.}/cm^2$, the maximum forward bias voltage was limited by the strong increase in current around -450 V.

These results show that 4H-SiC detectors can still detect high-energy particles after neutron irradiation up to 1×10^{15} $n_{eq.}/cm^2$, and that the decrease in CCE can be partially compensated for by increasing the applied bias voltage. Compared to silicon detectors, however, the decrease in charge collection efficiency is drastic. At similar fluences, 300 µm thick silicon detectors can reach similar (or even better) charge collection [7], even though the drift time in these detectors is more than six times longer, which would present more opportunities for charge carriers to be trapped. This apparent disadvantage of 4H-SiC will be further discussed in Section 7.3.3.

7.3.2 Alpha Particles

Alpha particles offer a very high charge deposition (around 5.5 MeV, corresponding to 110 fC in 4H-SiC), which allows for signals to be detected even for very heavily irradiated sensors. Alpha particles deposit most of their charge in the first 15-20 µm, and in *n*-type detectors, holes will therefore have a shorter drift distance than electrons. This will result in a charge-collection efficiency that is different from that of a proton (or a MIP) depositing charge along the entire length of the detector. Still, alpha particles can provide useful information that can then be compared to TCAD simulations. Also, detector applications outside the typical high-energy physics experiment exist, where alpha particles (or similar particles with a low penetration depth) need to be detected, such as in fusion diagnostics, where a significant radiation hardness is also required [24].

Measurements for all irradiated detectors were carried out using an alpha source (with three nuclides, see Section 4.3) in vacuum, and the detectors have again been read out using a Cividec Cx-L charge-sensitive amplifier. Figure 7.3.2 shows the measured charge-collection efficiency in forward and reverse bias, together with a measurement of an unirradiated sensor. As the different nuclides in the alpha source have different decay energies, they will deposit a slightly different amount of charge depending on the nuclide. To take this into account, 5000 events were recorded for each bias voltage, and the signal amplitude was histogrammed to extract the amplitude for each nuclide (^{244}Cm, ^{241}Am and ^{239}Pu), before the signal was normalized by the decay energy. If separating the three decay energies was not possible (in the case of very low charge-collection efficiencies), the entire signal amplitude distribution was instead fitted using a single Gaussian (indicated as "no separation" in the legend of Figure 7.3.2).

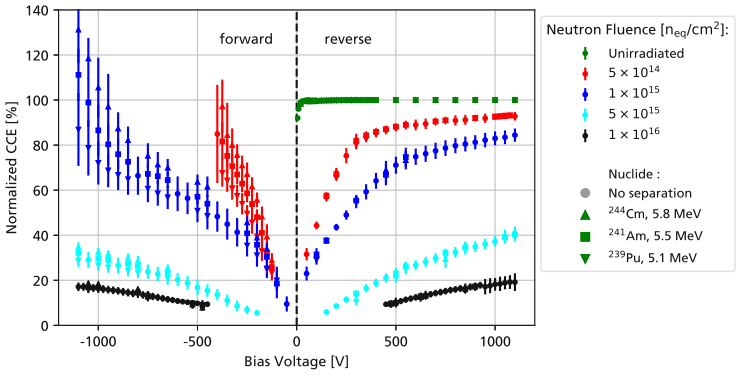

Figure 7.3.2: Charge collection efficiency measured using alpha particles in vacuum for an unirradiated and neutron-irradiated samples in forward and reverse bias. Adapted from [16].

Compared to the data acquired with protons, a much higher charge-collection efficiency is observed for alpha particles, more than 80 % for samples irradiated to 1×10^{15} $n_{eq.}/cm^2$. Additionally, signals were also possible to be recorded for the highest fluences, still reaching a CCE of around 20 % at 1×10^{16}. This increase in the charge collection efficiency can be attributed to the shallow penetration depth of the alpha particle, which results in a lower drift distance for the holes. As the electrons drift almost

twice as fast as the holes in 4H-SiC, this will result in fewer charge carriers being trapped during the charge transport (assuming similar hole and electron lifetimes). In forward bias, very large signals were observed, even exceeding a charge collection efficiency of 100 %. Additionally, the CCE is different for the different nuclides. ^{244}Cm, with the highest decay energy (and therefore penetration depth), yielding a larger signal normalized to its decay energy than the others. This excess charge (CCE > 100 %) can likely be attributed to a transient screening of the space charge at the anode and cathode, which allows for the conduction in forward bias to temporarily resume, adding to the charge created by the alpha particle. This effect has also been observed in IBIC measurements [277], and more in-depth studies of this effect have been performed using UV-TCT, which will be discussed in Section 7.4.

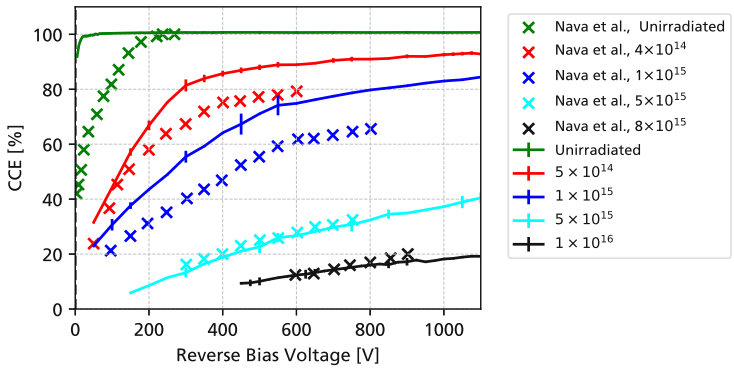

Figure 7.3.3: Charge collection efficiency for alpha particles in reverse bias compared to literature data of a 4H-SiC Schottky diode (Nava et al. [103]).

Figure 7.3.3 shows a comparison of the CCE for alpha particles to a study from literature, measured using a 39 µm thick 4H-SiC Schottky diode with an epitaxial layer doping of 6.5×10^{14} cm^{-3} [103]. For high fluences (>5×10^{15} $n_{eq.}/cm^2$), a very good agreement in the measured charge collection efficiency can be observed. At the lower fluences, however, a larger disagreement is visible, which could be explained by the higher doping concentration of the diode in the literature, or inaccuracies in the neutron fluence (a fluence of 5×10^{14} $n_{eq.}/cm^2$ required an irradiation time shorter than 20 min at the ATI TRIGA Mark II reactor of the Atominstitut [254]).

7.3.3 UV-TCT

In order to investigate the charge collection in more detail in a controlled laboratory setting (without stochastic fluctuations in the charge deposition), measurements were performed using a 370 nm picosecond pulsed UV laser (see [16, 254, 257] and Section 4.2). As the 4H-SiC PiN diodes (produced by CNM in run 13575) were completely covered by metal over the active area of the diode, the laser light was injected at the edge of the device, into a small 3 µm gap between the diode and its guard ring. Figure 7.3.4 shows the measured charge collection efficiency (using a Cividec Cx-L charge-sensitive amplifier) in forward and reverse bias. In reverse bias, a very close agreement to the data acquired using protons is observed. Due to the possibility to perform waveform averaging at the UV-TCT setup, and because a relatively large amount of charge can be injected into to the diode with the UV laser (approximately 60 fC), signals were also able to be obtained for samples irradiated to 5×10^{15} and 1×10^{16} $n_{eq.}/cm^2$, although here the CCE is below 10 %, even for a bias voltage of up to 1 kV. In forward bias measurements, an extreme effect can be observed, with a charge-collection efficiency 3-4 times higher than before irradiation. This is similar to the observations using alpha particles and will be studied in detail in Section 7.4.

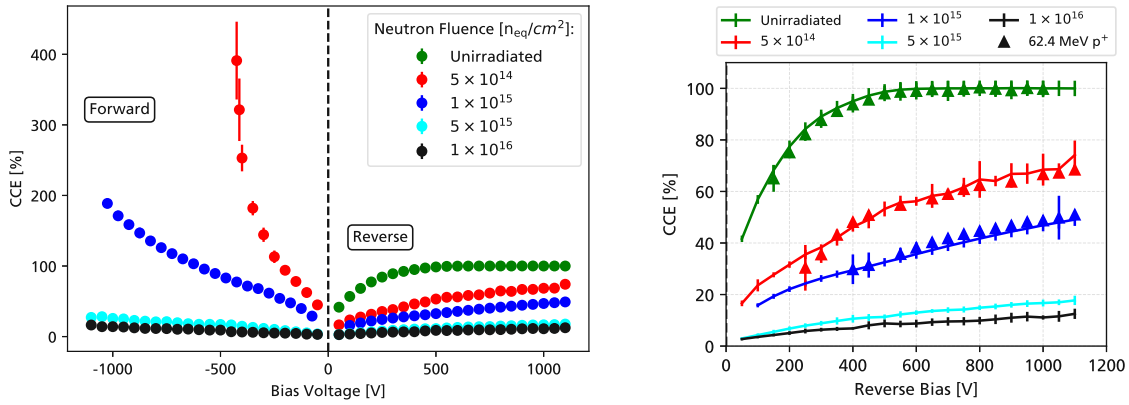

Figure 7.3.4: Left: Charge collection efficiency or neutron-irradiated 4H-SiC PiN diodes in forward and reverse bias measured by UV-TCT. Right: Charge collection efficiency in reverse bias, compared to data acquired using 62.4 MeV protons (see Section 7.3.1). Both plots have been adapted from [16].

Another way of describing the charge collection efficiency of a detector is in terms of the *charge collection distance* (CCD), which relates the amount of collected charge to an effective detector thickness. This interpretation is also found in the Hecht-equation (see Section 2.6), where the CCD is given by the mobility lifetime product $L = \mu E \tau_{\text{eff.}}$. The charge collection efficiency in reverse bias, depicted in Figure 7.3.5 behaves proportional to the square root of the bias voltage ($\sqrt{V}$). This behavior is very similar to the depletion behavior of a diode with space charge. Therefore, an effective doping concentration can be used to describe the CCD, which has been extracted from fits and is depicted on the right-hand side of Figure 7.3.5. For the unirradiated diode, a doping concentration of $1.5 \times 10^{14}\,\text{cm}^{-3}$ (previously extracted from C-V measurements) has been been used, which fits the charge-collection efficiency well up to around 200 V, where it starts to diverge as the doping concentration of the device increases towards the n^{++} buffer layer. For the irradiated sensors, effective doping concentrations between 1×10^{15} and $3.5 \times 10^{16}\,\text{cm}^{-3}$ have been extracted. This can be attributed to donor-like traps (such as $EH_{6,7}$ introduc-

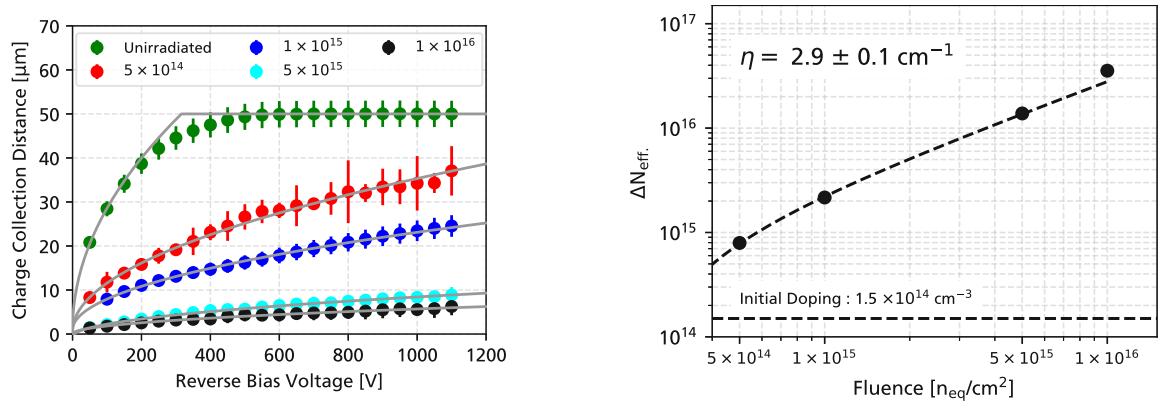

Figure 7.3.5: Left: Charge collection distance in reverse bias UV-TCT measurements fitted using a $\sqrt{V}$ function (solid gray line). Right: Increase in the effective doping concentration as a function of the irradiation fluence, fitted using a linear function with a non-zero intercept.

ing space-charge [252, 275], resulting in an effective doping $N_{\text{eff.}}$

$$N_{\text{eff.}} = N_0 + \eta \cdot \Phi_{\text{eq.}}\,, \tag{7.3.1}$$

where N_0 is the doping before irradiation, η the introduction rate, and $\Phi_{\text{eq.}}$ the 1 MeV neutron equivalent fluence. As previously discussed, this space charge is not measurable in C-V measurements (due to the deep energy level of the trap), but can have an effect on the electric field. A linear fit to the measured effective doping concentration was performed, which fitted the data very well up to a fluence of 5×10^{15} $\text{n}_{\text{eq.}}/\text{cm}^2$, resulting in an introduction rate of $\eta = (2.9 \pm 0.1)\,\text{cm}^{-1}$. For a fluence of 1×10^{16} a slightly higher effective doping is extracted, which could be attributed to the charge-collection distance not only shrinking due to space charge, but also due to a decrease of the charge carrier lifetime (for example, by the life-time limiting defect $Z_{1,2}$ [278]). Figure 7.3.6 shows electric fields and trap occupancies simulated in TCAD [267]. The donor-like trap $EH_{6,7}$ introduces a fixed space charge, which resists the expansion of the electric field.

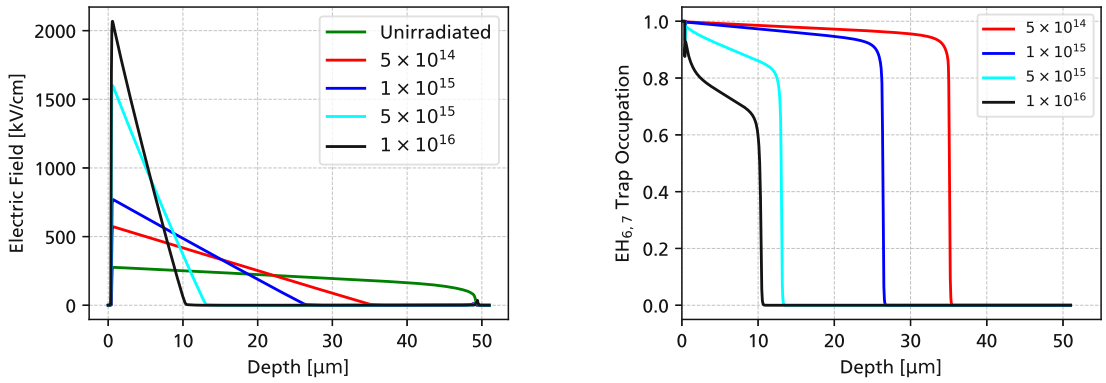

Figure 7.3.6: Left: Electric fields at a reverse bias of 1 kV simulated using the TCAD radiation damage model described in [267] (which used an introduction rate of $\eta = 1.6\,\text{cm}^{-1}$. Right: Fraction of filled $EH_{6,7}$ donor-like traps.

7.4 Charge Enhancement in Forward Bias

The increased charge collection in forward-bias operated irradiated 4H-SiC detectors, observed in UV-TCT and alpha particle measurements, prompted discussions in the community about the origin of this charge excess. Similar results for 4H-SiC diodes from the same production and irradiation campaign were also obtained by other groups using TPA-TCT [279] and IBIC [277]. If the underlying effect of this charge enhancement could be attributed to impact ionization with high electric fields, then this effect could be leveraged to attain larger signals, as has historically happened with the discovery of charge multiplication in irradiated silicon strip sensors, leading to the development of LGADs [1]. However, as has been shown in the previous section, this effect has been primarily observed in UV-TCT (and with a weaker impact for alpha particles), and not for high-energy protons. Any electrical effects that depend on impact ionization should not significantly change with the particle type being measured, and rather decrease instead of increase for higher injected charge densities (see gain suppression in LGADs [204]). The aim of this section is to study the observed charge enhancement in forward bias in more detail using UV-TCT, demonstrating that the measured charge collection efficiency depends on the amount of injected charge and its density. For sufficiently low injected charge densities, the charge collection efficiency remains below 100 %.

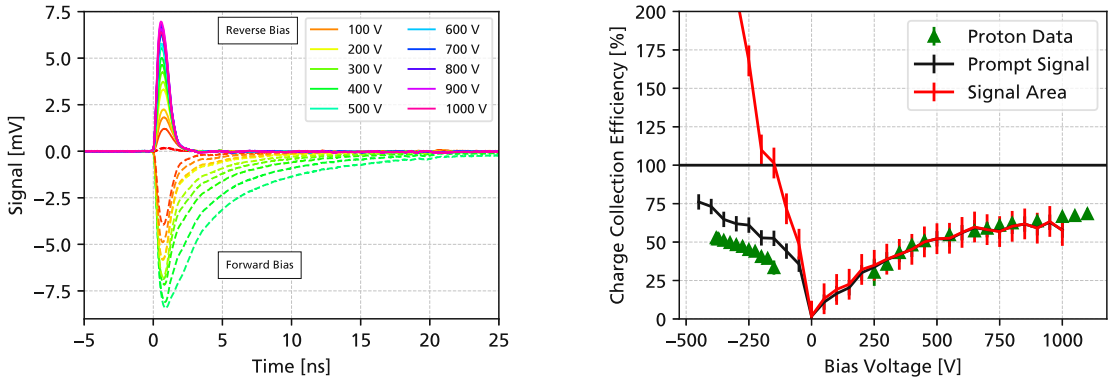

Figure 7.4.1: Left: Transient UV-TCT waveforms for a 4H-SiC PiN diode irradiated to 5×10^{14} $n_{eq.}/cm^2$ in forward and reverse bias, measured using the UCSC LGAD single channel readout board. Right: Comparison of the charge collection efficiency calculated using the amplitude of the waveform (prompt signal) and the signal area.

Figure 7.4.1 shows transient waveforms measured in UV-TCT for a neutron-irradiated 4H-SiC PiN diode in forward and reverse bias, which have been acquired using the fast amplifier of the UCSC LGAD readout board (with a feedback resistance of 470 Ω).

In reverse bias, the waveforms are just the impulse response of the amplifier scaled with the collected charge, as the readout electronics are too slow to resolve the transient current of the detector. The resulting charge collection efficiency is therefore identical when considering just the amplitude of the waveform or the entire integrated signal area. The charge collection efficiency also agrees very well with UV-TCT and proton beam measurements using a charge-sensitive amplifier. However, in forward bias, a pronounced tail of the signal can be observed. Although the amplitude-based CCE stays below 100 %, the signal area increases far above 100 %.

However, the shape and extent of this tail were observed to depend on the amount of injected charge, as depicted in Figure 7.4.2 for different laser power settings. The laser power has been varied using the tune value of the laser (see Section 4.2), and the output power has been calibrated relative to the maximum power using a Thorlabs S150C power sensor. For very low injected charge densities, almost no exponential tail of the signal is present. However, with higher and higher injection densities, this tail becomes more pronounced. The amplitude of the signal (normalized to the injected charge), however, stays constant for all laser power levels. The resulting calculated charge collection efficiency is therefore independent of the amount of injected charge when only considering the amplitude of the waveform, and CCEs similar to measurements using protons are obtained (around 60 % at a bias voltage of −450 V). These results show that the charge increase in forward bias is present only for high injected charge densities. When these high charge densities drift to the anode and cathode, they will partially compensate the space charge of trapped charge carriers. This, in turn, allows for a transient current to flow in forward bias until the electric field barrier induced by trapped space charge recovers, as summarized in Figure 7.4.3. Qualitatively, similar conclusions were also obtained from TCAD simulations [267, 268]. In the transient waveforms that have been acquired, the temporal resolution of the detector current was primarily limited by the large capacitance of the $3 \times 3\,mm^2$, which forms a low-pass filter with the input impedance of the amplifier. Future studies using smaller area diodes (with a lower capacitance) would allow for the transient current of the detector to be studied in more detail, as has been performed in Section 6.5 for unirradiated diodes. This would allow for a determination at which point in time (relative to the particle hit) the exponential signal tail in forward bias forms. Additionally, TPA-TCT or edge-TCT measurements would allow for electric fields to be extracted using the prompt current technique [258].

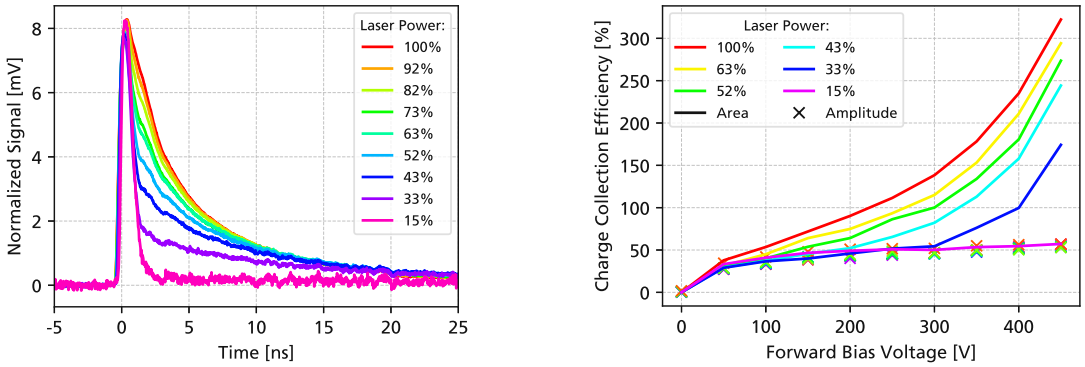

Figure 7.4.2: Left: UV-TCT waveforms (normalized to the injected charge) for a 4H-SiC PiN diode irradiated to 5×10^{14} $n_{eq.}/cm^2$ at a forward bias of 450 V for different UV laser power levels. Right: Amplitude and area as a function of the bias voltage and relative injected charge.

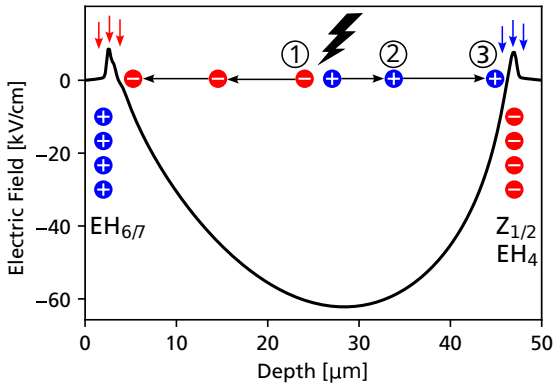

Figure 7.4.3: Mechanism of excess charge collection for irradiated 4H-SiC PiN detectors operated in forward bias. After electron-hole pairs are created by ionizing radiation (1), they will drift according to the negative electric field in the diode (2). When the charge carriers arrive at the cathode and anode (3), they can partially screen the trap-induced space charge, which lowers the field barrier and allows for conduction to temporarily resume.

Another study was carried out, where the total amount of injected charge was constant, but the charge density was varied by focusing and defocusing the laser beam. For these studies, 4H-SiC PiN diodes from the same production (CNM run 13575) and irradiation campaign, which did not feature any metal on top of the diode area, were used (see also Figure 6.4.1c in Section 6.4). This allows for the laser to be freely moved on the diode area and relaxes the requirements on the focus (i.e., size of the beam spot). A Cividec Cx-L charge-sensitive amplifier was used for these measurements to eliminate resistive effects of the p^{++} implant using its long integration time. This amplifier has also previously been calibrated using alpha particles. Figure 7.4.4 shows the measured charge in forward bias for different distances away from the optimal laser focus. Even though the laser was operated at its maximum power (using a tune value of 0 %), no excess charge is visible if the laser is further than 0.5 mm (about one Rayleigh-length) away from its optimal focus. Only when the laser is focused on a very small beam spot (with a 1-σ radius of 30 µm), an increase of the collected charge above a CCE of 100 % can be observed. Measurements in reverse bias were also performed, showing a constant response of the detector as a function of the laser focus, excluding any optical effects that would generate more charge than expected for a highly focused laser beam.

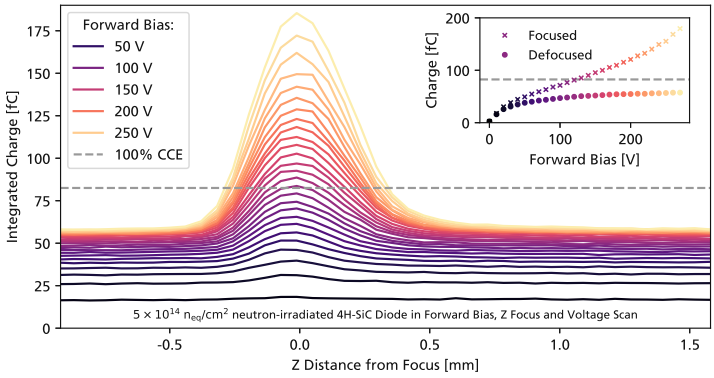

Figure 7.4.4: Collected charge as a function of the distance away from the laser optics focus and as a function of the bias voltage in the forward direction. The inset shows the collected charge as a function of the bias voltage for focused/defocused conditions. Taken from [257].

These results show that if a sufficient charge density can be injected, then the electric field barrier induced by trapped space charge can be *locally* overcome, allowing for charge carriers to enter the device and current to flow. Figure 7.4.5 shows CCE measurements for samples without any metals covering the active area, irradiated to fluences of 5×10^{15} $n_{eq.}/cm^2$, further demonstrating the effect of focusing and defocusing the laser. For a sufficiently low injected charge density, the excess CCE in forward bias can be avoided, and the correct CCE (in response to minimum ionizing particles) is obtained. This effect is something that has to be kept in mind for future TPA-TCT studies of irradiated sensors, and a sufficiently low amount of charge should be injected so as not to affect the electric field inside the detector.

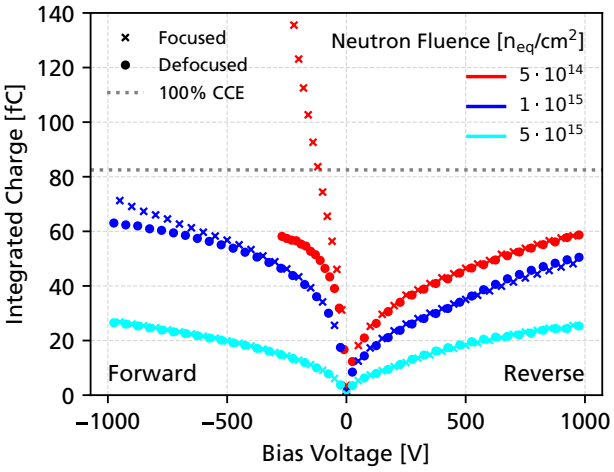

Figure 7.4.5: UV-TCT charge collection efficiency for irradiated 4H-SiC PiN diodes without any metal covering the active area. Two curves are shown, one for an optimally focused UV laser and one for a very broad beam spot outside of the laser focus. Adapted from [257].

7.5 Irradiation to Extreme Fluences

Future hadron colliders (such as the proposed FCC-hh [4]) will have extreme radiation hardness requirements, with fluences up to 1×10^{18} $n_{eq.}/cm^2$. For silicon detectors, radiation damage scaling laws are based on the NIEL hypothesis, which implies a linear scaling of radiation-induced defects with the non-ionizing energy loss dose. However, for very high fluences (>1×10^{17} $n_{eq.}/cm^2$), the increase in radiation damage has been observed to saturate, with smaller changes in the leakage current and trapping time than expected [280]. Radiation hardness studies of 4H-SiC in the literature are typically limited to 1 MeV neutron equivalent fluences of $1 \times 10^{16} n_{eq.}/cm^2$, with recent results reported up to $1 \times 10^{17} n_{eq.}/cm^2$ [116]. Even for these fluences, no appreciable increase in the leakage current has been reported after irradiation.

To assess the radiation hardness of 4H-SiC at extreme fluences, a set of 4H-SiC PiN samples from the first RD50-SiC-LGAD production were neutron-irradiated at the JSI TRIGA reactor in Ljubljana during the Autumn of 2024 [269]. As the production of these SiC samples (CNM runs 16886 and 17407) had numerous issues (see Section 6.3.1), which resulted in a very low yield, only four samples were irradiated in total. Two $3 \times 3\,mm^2$ PiN diodes were chosen from wafer 2 (with an epitaxial layer of 50 µm) and wafer 4 (with an epitaxial layer of 100 µm). The electrical characteristics after irradiation will be reported in Section 7.5.1. No signals were able to be detected from the irradiated sensors using alpha particles and UV-TCT, indicating that the charge collection efficiency has dropped to very low levels, below the measurement noise floor. This is in contrast with silicon devices, such as 3D detectors with a drift distance of 50 µm, where charge collection efficiencies as high as 30 % were recently reported after irradiation to 1×10^{18} $n_{eq.}/cm^2$ [281].

7.5.1 Electrical Characteristics

Figure 7.5.1 shows the capacitance-voltage characteristics before and after irradiation. The full depletion voltage for the 50 µm thick diodes is around 400 V, and the 100 µm thick diodes can not be fully depleted, even for a bias voltage of 1.1 kV (limited to avoid sparking on the surface of the detector). After irradiation, however, a much lower capacitance than expected from the full depletion of the epitaxial layer was measured. This can be explained by not only the n-doping of the epitaxial layer being compensated by deep traps, but also the entirety of the highly doped n^{++} buffer layer being deactivated. Therefore, the measured capacitance will correspond to the entire physical thickness of the device (the 50 µm epitaxial layer in addition to a 350 µm PVT-grown n-type 4H-SiC substrate). Studies performed

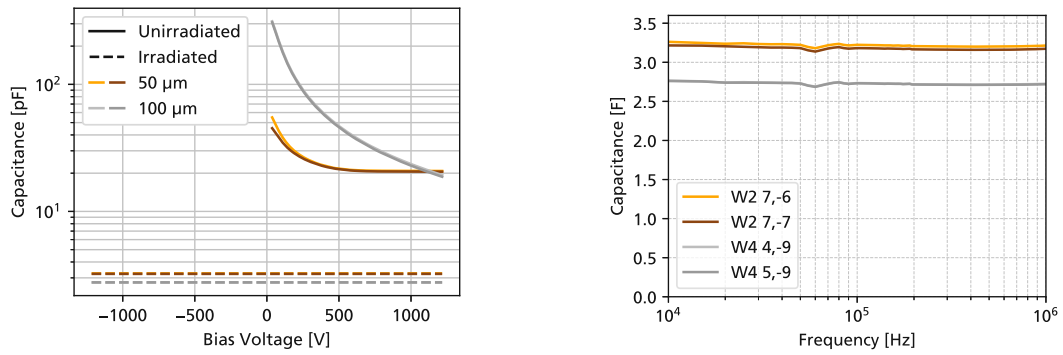

Figure 7.5.1: Left : Capacitance-voltage characteristics of 50 µm (W2) and 100 µm (W4) thick 4H-SiC PiN diodes before and after irradiation to 1×10^{18} $n_{eq.}/cm^2$, measured using 1 V AC at 100 kHz. Right: Capacitance after irradiation as a function of the frequency for zero DC bias.

using similar devices irradiated to 1×10^{17} $n_{eq.}/cm^2$, have shown that the buffer layer is still intact at this fluence (with a measured capacitance in accordance with the 50 µm thick epitaxial layer) [116]. The capacitance as a function of the frequency, depicted in Figure 7.5.1, was measured between 10 kHz and 1 MHz, and no dependency on the frequency was observed. Similar to the results obtained for the previous irradiation campaign (Section 7.2.2), the energy level of the traps capturing the n-dopants are too deep for trap emission at the frequencies probed in the C-V measurement.

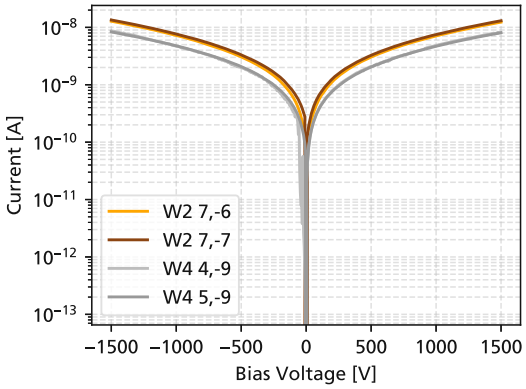

Figure 7.5.2: Room temperature (22 °C) current-voltage characteristics for 50 µm (W2) and 100 µm (W4) thick 4H-SiC PiN diodes irradiated to 1×10^{18} $n_{eq.}/cm^2$.

The n^{++}-buffer layer being removed also has an effect on the I-V characteristics, depicted in Figure 7.5.2. Contrary to the results for lower neutron fluences ($1 \times 10^{16} n_{eq.}/cm^2$), a large increase of the current to 10 nA at 1.5 kV can be observed, with a symmetric behavior in forward and reverse bias. Additionally, the samples with a larger thickness (W4) show a lower current than thinner diodes (W2), opposite to the expected behavior of thermal charge carrier generation (proportional to the detector volume). In order to assess the possible origin of these large currents, I-V measurements have been performed at different temperatures (between −40 °C and 25 °C) in a CTS C-40 climatic chamber, depicted in Figure 7.5.3. The current shows a strong dependency on the temperature, with the shape of the I-V curve, however, only being scaled by a constant. In order to quantify the change of current as a function of the temperature, the data is depicted in an Arrhenius [282] plot on the right-hand side of Figure 7.5.3. For all four irradiated samples, an activation energy of 0.24 eV was extracted in the range of −40 °C to

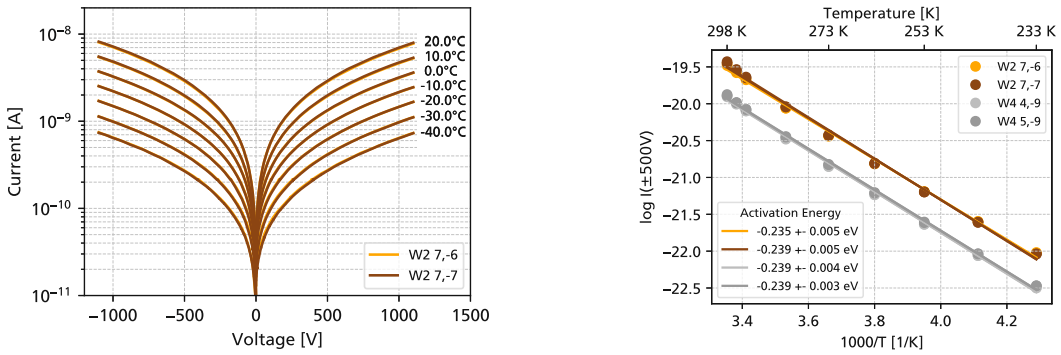

Figure 7.5.3: Left: I-V curves measured at different temperatures. For visual clarity, results are only shown for 50 µm thick diodes (W2), although the characteristics of 100 µm samples are very similar. Right: Arrhenius plot and extracted activation energies at bias voltages of ±500 V.

20 °C. Such a shallow energy level does not correspond to any known radiation-induced intrinsic defects in 4H-SiC [101]. However, the energy level matches very closely to that of Al dopants in 4H-SiC, which are shallow acceptors with energy levels reported to be around 0.19 eV to 0.3 eV [283–285]. It is therefore hypothesized that after irradiation to a very high neutron fluence of 1×10^{18} $n_{eq.}/cm^2$, the p^{+1} implant is still active and can inject charge carriers into the diode, resulting in a behavior similar to a p-type 4H-SiC bulk with a fixed resistivity. The relatively high resistivity is most likely a result of low charge carrier lifetimes. For higher bias voltages, the drift velocity increases, which increases the drift current and reduces the likelihood of trapping, and above 1 kV, the current scales almost linearly with the voltage.

Measurements and annealing studies are currently ongoing, with a maximum temperature of 300 °C available at a thermal chuck that is currently being commissioned. So far, no room temperature annealing has been observed, with unchanged current-voltage characteristics after more than six months. Although the carbon vacancies $Z_{1,2}$ and $EH_{6,7}$ are only expected to anneal at temperatures as high as 1600 °C [286], low temperature ($\leq$ 200 °C) annealing studies have shown a decrease of the leakage current as well as a recovery of the charge collection efficiency [116, 287], and are planned to be performed in future irradiation campaigns.

8 Silicon Carbide for FLASH Beams at a Medical Synchrotron

The material properties of 4H-SiC make it a very attractive candidate for beam monitoring applications. Due to its wide bandgap, leakage currents are extremely low (even after irradiation) [16], allowing for a DC coupled readout [288], highly advantageous for continuous high-intensity beams found in ion therapy centers [288] or x-ray beam position monitoring [289]. Additionally, the insensitivity of 4H-SiC to visible light and changes in temperature make it a suitable material for dosimetry [26]. Recently, significant efforts have been undertaken to develop and establish 4H-SiC diodes for the dosimetry of ultra-high dose rate FLASH radiotherapy [25, 290, 291]

In the context of the *HiBPM* (Hi-Precision Beam Position and Intensity Monitor for Accurate Cancer Treatment with Ions) FFG-funded project [292], HEPHY is developing a beam position monitor based on 4H-SiC strip detectors that will be implemented at the MedAustron ion therapy center [27, 288]. This system is intended to increase the detection sensitivity compared to the currently used beam position monitors based on scintillating fibers [293], which can not detect single particles. Extending the dynamic range of the beam monitors is especially relevant for non-clinical research, where certain applications (for example, detector characterization) demand *low-flux* beams, with intensities as low as $\mathrm{kHz\,cm^{-1}}$ [191].

However, research is not only ongoing for low-flux beam modalities, but also at the other end of the beam intensity spectrum. Currently at MedAustron, spills of the synchrotron (containing around 1×10^{10} protons) are extracted in a time span of at least one second [183]. The extraction speed is limited by safety considerations: at lower extraction times, spikes and ripples in the extracted intensity will have a large effect, which can result in an erroneous dose if the dose-delivery system can not react to these fluctuations in time [294]. Increasing dose rates would not only result in a higher patient throughput [295], but also solve problems with patient movement during irradiation (for example, for lung tumors) that otherwise require gating [296]. Furthermore, ultra-high dose rates ($>40\,\mathrm{Gy\,s^{-1}}$) give rise to the FLASH effect, where decreased damage to healthy tissue is observed, while the cancerous tissue is treated with the same efficiency, allowing for better treatment outcomes [297, 298].

Since 2020, studies to implement ultra-high dose rate beams at MedAustron have been ongoing, with the aim of providing proton beams for non-clinical studies of the FLASH effect [32]. Obtaining these high dose rates in a safe and controlled manner is non-trivial for synchrotrons [299], and different slow-extraction mechanisms have been developed and tested [33]. The currently available dose-delivery systems at MedAustron (ionization chambers) [186], have a limited time resolution and exhibit a non-linear response at very high dose rates and are therefore not suited to investigate ultra-high dose rate beams. In order to address these metrology needs, a beam intensity monitor based on a 4H-SiC PiN diode and a 20 MHz transimpedance amplifier has been built. As a part of this thesis, different extraction modalities have been investigated, with the ultimate goal of a pulsed ultra-high dose rate beam that can be delivered safely and reliably [34]. A special emphasis is put on the time profile of the beam intensity, with the SiC-based beam monitor being able to resolve the extraction for each individual turn of the particles in the synchrotron.

8.1 FLASH Radiotherapy

8.1.1 The FLASH Effect

Fundamentally, radiotherapy works by leveraging the different responses to radiation of healthy and cancerous cells [300]. Healthy cells can repair radiation damage better than cancer cells, which leads to a difference between tumor control and normal tissue complication probabilities, as illustrated in Figure 8.1.1. A wider therapeutic window (difference between tumor control and normal tissue complication) will allow for better tumor control for the same dose, or allow for the dose to the healthy tissue to be reduced while keeping the tumor control identical.

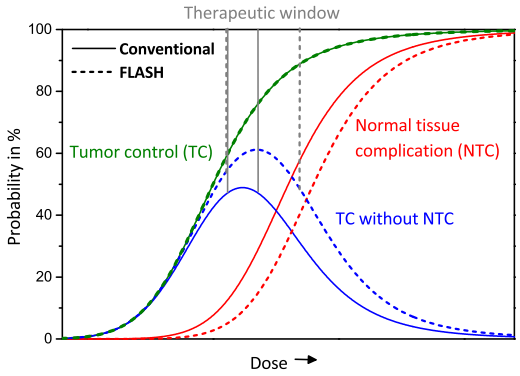

Figure 8.1.1: Tumor control (TC) and normal tissue complication (NTC) probabilities as a function of the applied dose for conventional and FLASH radiotherapy. Taken from [301].

During the 1960s and 70s, it was first observed in cells that radiotherapy with very high dose rate pulsed beams results in a different biological effect than at conventional dose rates [302, 303]. About 10 years ago, this effect was rediscovered in mouse studies [298], and since then, there has been an immense interest in the community [304]. The requirement for the FLASH effect to be observed is typically stated as an ultra-high dose rate (exceeding $40\,\mathrm{Gy\,s^{-1}}$), and a large dose fraction (exceeding 8 Gy) [305]. However, the exact working mechanism behind the FLASH effect is still not yet understood. Radiolytic oxygen depletion, inducing transient cell hypoxia, has often been proposed as a possible mechanism [306]. While the oxygen saturation of tissue is a well-known modulator of radiation damage [307], the radiolytic oxygen depletion hypothesis is under significant scrutiny, as even a dose of 10 Gy is not sufficient to significantly reduce oxygen concentration in tissue [308]. Other hypotheses, including radical-radical interaction, immune modulation, and mitochondrial preservation, have been proposed, but the FLASH mechanism still lacks a clear explanation [305].

The FLASH Effect in Ion Beam Therapy

FLASH beams are typically delivered using electron beams by using modified photon treatment machines [309]. Data on the FLASH effect for other particle types, such as ions, is much rarer, and it is not clear what impact the higher linear energy transfer (LET) of ions will have. The low number of studies using ions can be attributed mainly to the limited availability of ion therapy centers, but also the difficulties in implementing FLASH dose rate beams [299]. Some first studies have shown, however, that the FLASH effect exists for protons [31, 310], with a review of the current status found in [311]. These first studies focused on transmission mode protons [312], which negates the main advantage of ion therapy (being the localized dose deposition using the Bragg peak). Recently, developments have started planning to use the Bragg peak in proton FLASH beams [313, 314], but clinical studies have yet to be performed.

8.1.2 Ultra-High Dose Rate Dosimetry

One of the main challenges in implementing FLASH radiotherapy in the clinic is the inability of conventional ionization chambers to perform accurate dosimetry at ultra-high dose rates [301]. At sufficiently high dose rates, the charge cloud generated by the ionizing radiation will be dense enough for ions and electrons to recombine before they can drift through the ionization chamber, resulting in a decreased ion collection efficiency [315]. Figure 8.1.2 shows a measurement of the ion collection efficiency for an ionization chamber in response to 1.8 µs electron beam pulses. While the decrease of the ion collection efficiency can be described by an analytical model, any changes in the pulse length or operating conditions (such as the bias voltage of the ionization chamber, or air pressure and temperature) can result in a different response, which makes ionization chambers generally unsuitable for accurate dosimetry of FLASH beams [316].

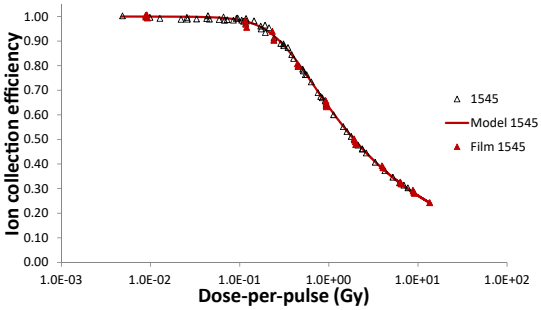

Figure 8.1.2: Ion collection efficiency for an "Advanced Markus" ionization chamber at different dose-per-pulse levels, fitted using the *Boag* model [315]. Reproduced with permission [317].

Instead, FLASH dosimetry requires dosimeters that are dose-rate independent. One prominent class of dosimeters that have shown a very good response to ultra-high dose rate beams are passive chemical dosimeters, such as Fricke-solution, alanine pellets, or Gafchromic films [301]. Additionally, calorimeters (which directly measure the temperature change by the energy deposited during irradiation) can be used. However, these dosimeters can only be analyzed after irradiation (for chemical dosimeters) or require large and intricate experimental setups (for calorimeters), and are not usable for online monitoring. Recently, however, semiconductor-based dosimeters have also demonstrated excellent performance in FLASH dosimetry. Compared to ionization chambers, the density of atoms is much larger and the ionized charge carriers move much faster (due to higher charge carrier velocity and significantly shorter drift distances), which will result in much lower recombination losses [318]. Figure 8.1.3 shows measurements of the dose-rate linearity for silicon, 4H-SiC, and diamond detectors, which all have demonstrated dose-rate linearity up to dose rates of MGy s^{-1}.

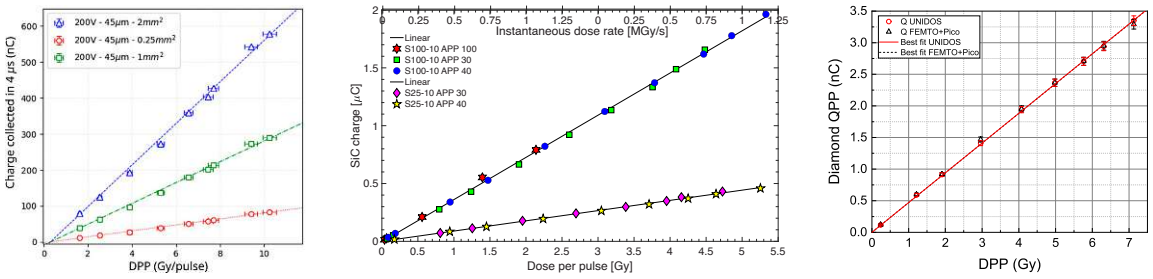

Figure 8.1.3: From left to right: Dose-rate linearity for silicon [319], 4H-SiC [290] (reproduced with permission) and diamond [320] dosimeters for microsecond pulsed electron beams.

8.2 Ultra-High Dose Rate Ion Beams at Synchrotrons

While electron-based FLASH radiotherapy can be implemented in a straightforward manner by modifying photon treatment machines [309], modifying synchrotrons (or other ion accelerating systems) to achieve high dose rates is more difficult [299]. Extracting a beam from a synchrotron in a few turns (or even a single turn) is possible using a kicker dipole magnet; however, such an extraction is not applicable in a clinical setting, as the amount of extracted particles can not be precisely controlled. Additionally, each time the synchrotron ring is emptied, it needs to be filled and accelerated again, a process which takes seconds, instead of the microseconds between pulses of linear accelerators. This means that the entire irradiation needs to be performed in a single synchrotron spill, which limits the volume that can be irradiated [299]. Furthermore, if a three-dimensional covering of the tumor is required, this will need either multi-energy extraction [32] or a passive beam scatterer [321].
The aim for implementing ultra-high dose rate beams (capable of triggering the FLASH effect) at a synchrotron is therefore to develop an extraction method that can deliver a pulsed beam with a high dose rate and duty cycle, which, most importantly, is controllable and reproducible enough for clinical applications.

This can be implemented using *slow-extraction* techniques. The goal of slow extraction is to provide an extraction with a constant beam intensity, which is commonly required for clinical applications [184]. However, pulsed extractions can also be performed [33]. Slow extraction is commonly performed using *resonant third-integer* extraction. Field imperfections in the magnets of a synchrotron ring can accumulate over many turns, which leads to resonances. While these resonances are avoided in the regular operation of a synchrotron, moving the particles into unstable phase space regions allows for these resonances to be exploited to slowly extract a beam with constant intensity [322].

Figure 8.2.1 shows different slow extraction methods, which have been implemented at MedAustron and used for ultra-high dose rate tests [32, 33]. The figure shows a *Steinbach*-diagram, with the vertical axis depicting the amplitude of the excitation (relative to the orbit of the particles) and the horizontal the tune (particle momentum offset) [323]. If a particle crosses in the upper triangle (the unstable region), it will become unstable and be extracted by an electromagnetic septum after some hundreds of turns.

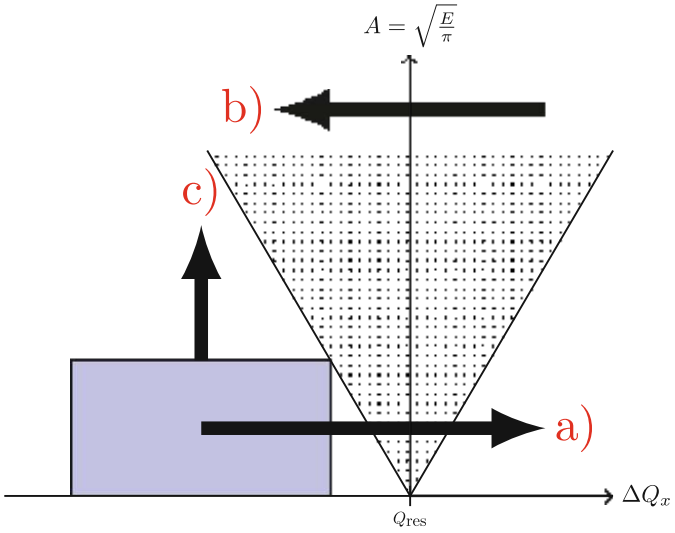

Figure 8.2.1: Steinbach diagram showing different slow extraction techniques. Image taken from [322].

Different methods can be employed to bring particles into the unstable region. First (a), the beam can be moved into the unstable region by increasing its momentum, i.e., accelerating it. This can be implemented by magnetic induction cavities, referred to as betatron core extraction [324], or using an RF

cavity (phase-displacement extraction) [325]. Next (b), the unstable region itself can be moved into the waiting beam by changing the magnetic field inside the accelerator, for example, using the constant optics slow extraction (COSE) technique [326]. Finally (c), the amplitude of the particle oscillation around the reference orbit can be directly increased by applying transverse kicks using an RF field, known as RF-knockout (RF-KO) [327]. At MedAustron, research into slow extraction techniques alternative to betatron core extraction is ongoing [32], not only to achieve ultra-high dose rate beams for FLASH radiotherapy, but also to improve the extraction used in conventional radiotherapy by reducing intensity ripples [322], or to enable new modalities such as multi-energy extraction [32].

8.2.1 Safety Considerations

As mentioned previously, patient treatment can not be implemented safely if all of the synchrotron is extracted in a single turn. Even if the dosimetric verification can be performed at a sufficiently fast rate, termination of the irradiation (using a beam chopper) requires at least 150 µs at MedAustron [328]. Instead, a better approach is to use an extraction method that can be quickly enabled and disabled, without relying on an interlock system to abort the irradiation [34]. Safety requirements for ion therapy machines require that less than 0.25 Gy be delivered to the patient in case of a failure [329]. For 40 Gy s^{-1} (without considering ripples in the dose rate), this allows for only 6.25 ms to detect the error and abort the irradiation.

Figure 8.2.2 shows a possible FLASH extraction scheme using pulsed beams. Each pulse is measured using a fast detector, which integrates the charge (and checks other safety-relevant parameters, such as the position), and verifies that the pulse has been delivered as required. Only if the pulse has passed verification, a go-ahead is given, and the next pulse is delivered. If the dose-per-pulse is kept below 0.25 Gy, then the irradiation safety limits can be respected.

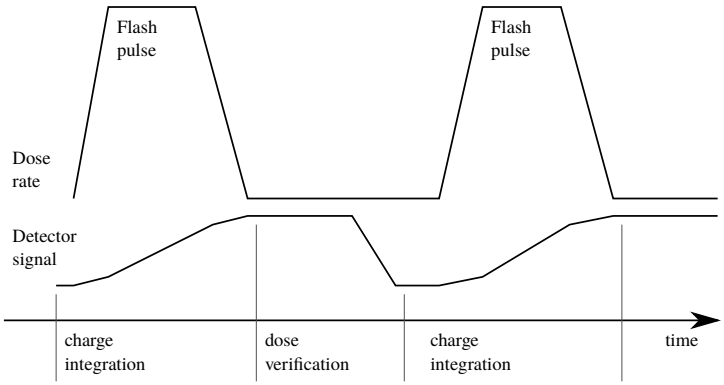

Figure 8.2.2: Pulsed extraction FLASH scheme. Taken from [34].

The challenge for this scheme is that not only the dose rate during irradiation, but the average dose rate (taking into account the measurement time of the detector) needs to remain above 40 Gy s^{-1} for the FLASH effect to be triggered. Therefore, very fast detectors and processing of the detector signals are required to maximize the duty cycle of the irradiation.

8.3 Silicon Carbide Based Beam Intensity Monitor

As previously mentioned in Section 8.1.2, ionization chambers encounter issues when facing very high dose rates and show saturation effects. Additionally, ionization chambers have a very limited temporal resolution, dominated by the long drift time of ions in air [299]. In order to address these issues, a beam intensity monitor with a high temporal resolution, based on a $3 \times 3\,\mathrm{mm}^2$ 4H-SiC PiN diode and a 20 MHz transimpedance amplifier was designed. The beam intensity monitor, together with the experimental setup used to investigate different extraction modalities at MedAustron, is depicted in Figure 8.3.1. The current in the synchrotron ring can be measured by a transformer (CTS) with a sample rate of 1 kHz. After extraction from the synchrotron ring, the beam travels to the irradiation room and through the dose-delivery system (DDS), which contains two ionization chambers. In front of the beam nozzle, the SiC-based beam intensity monitor is placed in the isocenter. Gafchromic EBT3 films are used for reference dosimetry, in front of the detector and at 80 % of the Bragg peak (R80) using an RW3 solid water phantom.

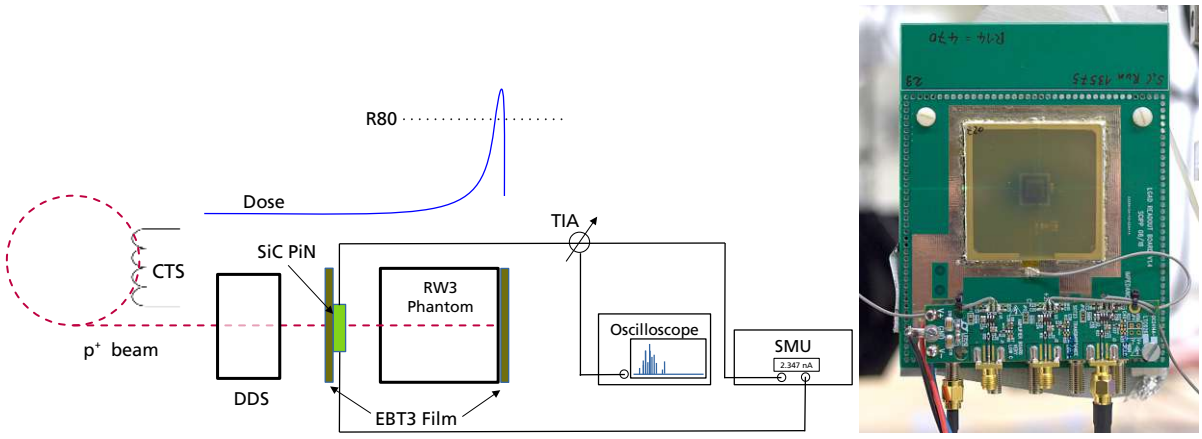

Figure 8.3.1: Left: Experimental setup used in ultra-high dose rate measurements. Right: Photograph of the SiC-based beam intensity monitor in the isocenter. The UCSC LGAD single-channel readout board is used as a carrier board, with a daughter board hosting the transimpedance amplifier. On top of the detector, an EBT3 film is attached for reference dosimetry.

At the high intensities expected in UHDR beams, individual particles will arrive almost simultaneously at the detector (especially for a detector of such a large area), resulting in a DC current. This current is amplified and read out by a transimpedance amplifier based on an Analog Devices LTC6268-10 operational amplifier in a negative feedback circuit (with different feedback resistances that can be chosen). The signal of the transimpedance amplifier is read out by an oscilloscope (Rohde&Schwarz RTP164) with a sample rate of 100 MSa/s. Due to the large internal memory of the oscilloscope (2 GSa), up to 20 s of the transimpedance amplifier can be recorded in one acquisition, more than sufficient to measure the entire synchrotron extraction. The current induced by the particle beam passing through the detector can also be measured by a source-measure unit, which provides the high-voltage bias for the detector (albeit with a much lower sample rate of only 2.8 kHz).

Figure 8.3.2 shows a comparison of a 10 ms beam extraction measured using the SMU and the transimpedance amplifier. While both signals show a similar envelope, the signal measured by the transimpedance amplifier has a much higher temporal resolution, which allows features of the extraction to be resolved and correlated with different accelerator settings. In fact, the bandwidth of the transimpedance amplifier (20 MHz) is much higher than the revolution frequency of the particles in the synchrotron, 2.36 MHz for 252.7 MeV protons.

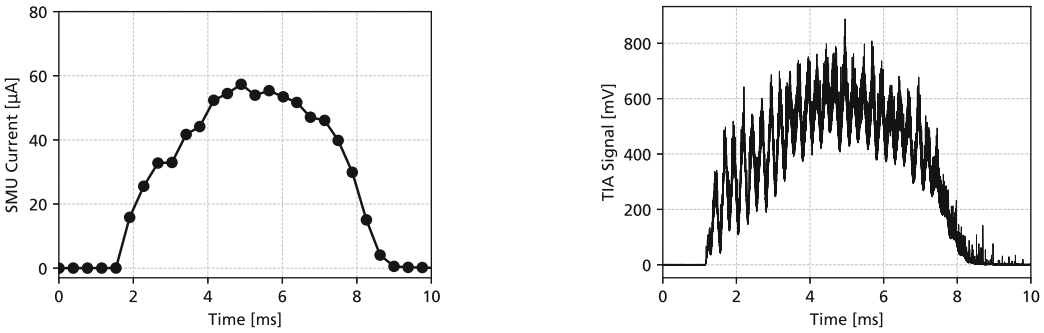

Figure 8.3.2: Left: Transient detector bias current measured by the SMU using a sample rate of 2.8 kHz. Right: Output of the fast transimpedance amplifier measured at 100 MSa/s. Both plots show a constant optics slow extraction with a nominal extraction time of 10 ms.

While the SiC-based beam intensity monitor can measure the temporal profile of the beam extraction, it can not directly measure the delivered dose, as it only covers a fraction of the beam spot (with a FWHM of 7.6 mm for 252.7 MeV, compared to the detector size of 3 mm) Therefore, a reference dosimeter is required to obtain the total dose. EBT3 films, which are dose-rate independent (up to a total dose of 10 Gy [330]), were used to correlate the dose measured by the detector to the total delivered dose. These self-developing films, depicted in Figure 8.3.3, darken when irradiated and are a standard tool in FLASH research. In order to analyze the films after irradiation, the change in optical depth (OD) is measured, which corresponds to the number of particles that have interacted with the film. The optical density can be calculated as the logarithm of the 16-bit brightness value of a pixel (PV) [331]

$$\mathrm{OD} = \log\left(\frac{2^{16}}{\mathrm{PV}+1}\right). \tag{8.3.1}$$

As the optical density of the film is already non-zero before the irradiation, a scan before the irradiation needs to be subtracted to obtain the net change in optical density $\mathrm{OD}_{\mathrm{net}} = \mathrm{OD}_{\mathrm{irrad.}} - \mathrm{OD}_{\mathrm{unirrad.}}$. An EPSON Expression 11000XL scanner was used to scan the films (after a development time of 24 h), and the conversion factor between dose and optical depth was calibrated for the red color channel using a reference ^{60}Co irradiation.

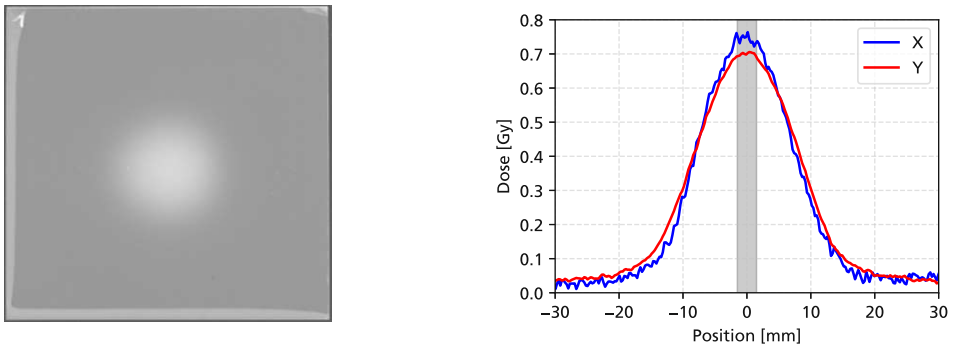

Figure 8.3.3: Left: Red image channel extracted from a scan of an irradiated EBT3 film. Right: Dose distribution in X and Y calculated from the increase in optical density of the EBT3 after irradiation. The gray area indicates the width of the detector (3 mm).

In order to measure the performance of the SiC beam monitor, a comparison measurement using phase-displacement extraction (at dose rates below 1 Gy s^{-1}) was performed, depicted in Figure 8.3.4. The number of extracted particles was measured by a beam current transformer, and the linearity of the dose-delivery system (based on an ionization chamber) and SiC beam monitor was investigated. As expected, the measurement of the dose-delivery system correlated very closely to the number of extracted particles, which also implies a good extraction efficiency. For the SiC beam monitor, a good linearity has been demonstrated as well, albeit with higher noise levels (a result of the low dose rate).

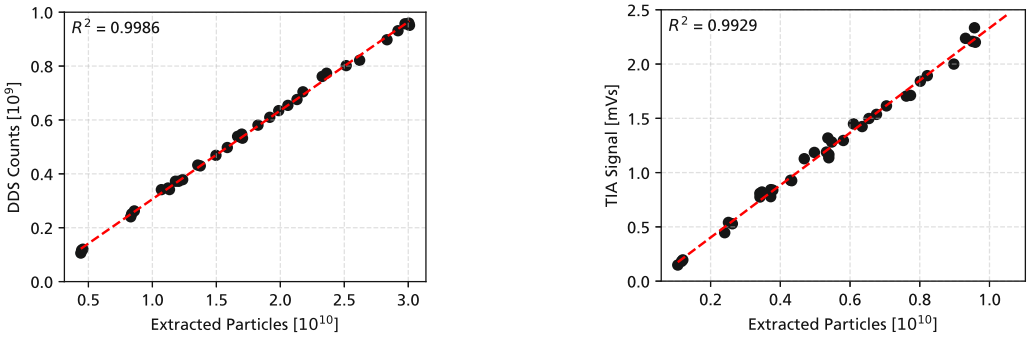

Figure 8.3.4: Measurements of the dose-delivery system (left), and the SiC beam intensity monitor (right) vs. the number of 252.7 MeV protons extracted from the synchrotron. A linear fit is indicated by a red line, together with the coefficient of determination.

At high dose rates, the ionization chambers of the dose-delivery system will show saturation effects. In order to investigate the saturation threshold, phase-displacement extractions of the synchrotron were performed, extracting 1×10^{10} protons with an energy of 252.7 MeV in a single pulse with a duration between 1 s to around 10 ms. As shown in Figure 8.3.5, for average dose rates larger than approximately 10 Gy s^{-1}, the response of the ionization chamber starts to decrease from the expected value. At even higher dose rates (>100 Gy s^{-1}), the response of the dose-delivery system approaches a minimum, as the air in the ionization chambers is completely ionized. Even though the instantaneous dose rate can be much higher (>1 kGy s^{-1}) than the average dose rate, no saturation effects for the SiC-based detector have been observed, proving that it (and its readout electronics) are suitable for FLASH dosimetry of proton beams.

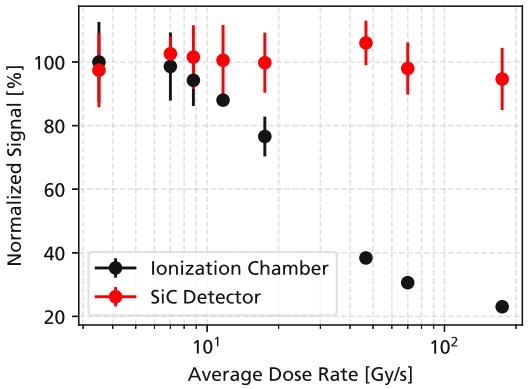

Figure 8.3.5: Comparison of the dose-delivery system (using ionization chambers) and the SiC beam intensity monitor at different dose rates using phase-displacement extraction.

8.4 Constant-Optics Slow Extraction (COSE)

In constant-optics slow extraction, all magnets of the synchrotron (dipoles, quadrupoles, and sextupoles) are simultaneously ramped in order to move the unstable region of the phase space into the waiting beam [326]. A typical COSE extraction is shown in Figure 8.4.1, where the magnetic field was ramped in a single pulse with a duration of 200 ms. In the time domain, large ripples in the extracted intensity (up to 60 Gy s^{-1}) can be observed. These intensity variations, clearly visible in the Fourier spectrum as a peak around 4 kHz, are a result of ripples in the power converters driving the accelerator magnets [332]. Similar ripples are also present for clinical extraction modalities, and MedAustron employs *empty-bucket channeling* to reduce the impact of these ripples by channeling the beam more quickly into the resonance at the boundary of the unstable region [294]. Due to a non-ideal ramping of the magnetic field, part of the beam is lost, and the measured dose rate drops significantly after around 140 ms, with only around 2/3 of the beam arriving at the irradiation room.

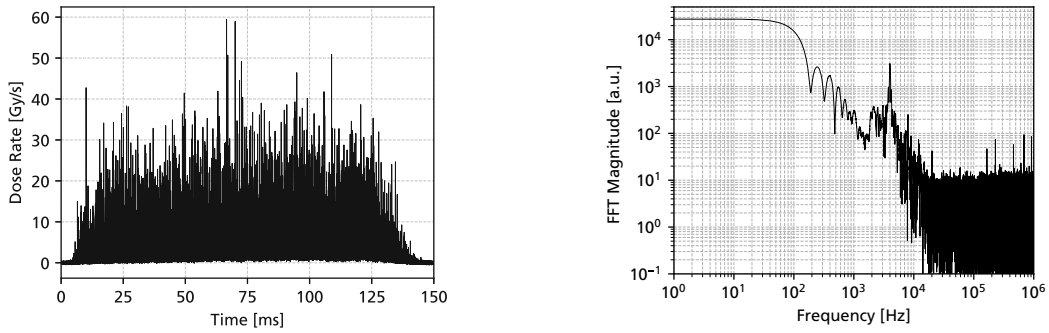

Figure 8.4.1: Left: Measured extraction time profile for a single-pulse COSE extraction with a nominal length of 200 ms. Right: Frequency spectrum of the measured dose rate.

In order to establish the maximum dose rates that could be obtained using COSE, beams were extracted using different sweeping speeds between 1 s and 1 ms, as depicted in Figure 8.4.2. For each measurement, an EBT3 film was mounted on top of the detector to measure the total extracted dose. In order to show the extraction time profile visually in the left-hand side of the plot, a notch filter has been applied to the measured dose rate to remove the 4 kHz intensity ripples.

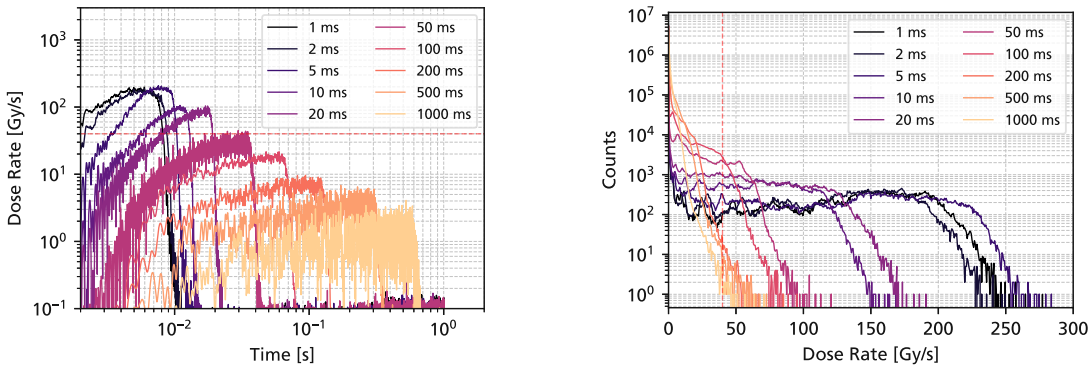

Figure 8.4.2: Left: Measured and filtered dose rate time profiles for COSE extractions with different nominal extraction times. Right: Histograms of the dose rate during the extraction. In both plots, the FLASH threshold of 40 Gy s^{-1} is indicated by a dashed red line.

For higher and higher extraction speeds, the instantaneous dose rate continues to grow, until a maximum around 200 Gy s^{-1} for a 5 ms short extraction is reached, well above the FLASH threshold of 40 Gy s^{-1}. However, for even shorter extraction times, the dose rate does not increase further, and a limit is reached. Figure 8.4.3 shows the dose rate averaged over the entire extraction duration. For extractions shorter than 5 ms, the average dose rate is limited to a value of 100 Gy s^{-1}, limited by the ramping speed of the magnets.

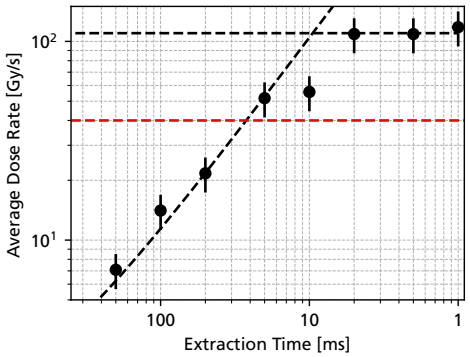

Figure 8.4.3: Average dose rate for different COSE extraction speeds.

The typical dose at the detector for these measurements has been in the order of 3 Gy. While this is not sufficient to trigger the FLASH effect (typically requiring fractions larger than 8 Gy), the dose at the position of the Bragg peak will be higher, measured to be around 9 Gy using a solid water phantom, just large enough for the FLASH effect. However, for lower proton beam energies, the FWHM of the beam width will change, spreading out the dose over a larger area. Additionally, if a passive scatterer is used to cover a three-dimensional tumor volume with a single proton energy, this will further reduce the dose arriving at the patient. Therefore, a larger number of particles per synchrotron spill is required. Currently, MedAustron injects a factor 4 fewer particles than what would be possible, in order to meet worst-case safety limits (for example, if a quadrupole magnet breaks down) [333]. If these safety considerations could be addressed, then a higher synchrotron filling could provide a sufficient number of particles for FLASH therapy in a single synchrotron spill.

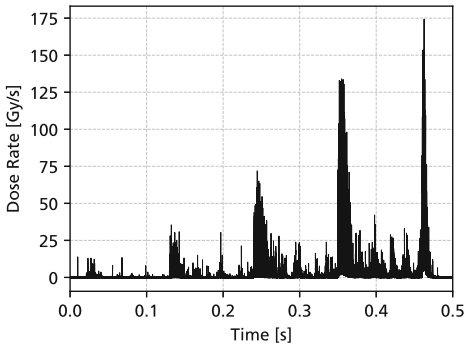

Figure 8.4.4: Pulsed COSE extraction with five pulses.

With the possibility of reaching the FLASH dose rate threshold demonstrated using single-pulse COSE extraction, pulsed extraction modalities have also been investigated, depicted in Figure 8.4.4. The ramping of the magnets was split up into five steps, with a duration of 10 ms and a spacing of 100 ms.

While again, dose rates in excess of the FLASH threshold can be obtained, a significant dose rate is also extracted in between the pulses. This is likely a result of a small overshoot in the magnet control loop, which can occur at such fast ramp rates. The non-zero dose rate in between pulses results in significant challenges in adapting COSE for clinical FLASH beams, as additional techniques (such as a beam chopper) would need to be employed to limit the dose between pulses. Additionally, the minimum pulse width in COSE is limited to around 10 ms by the ramping speed of the magnets. RF-based extraction methods, in contrast, can control the extraction at MHz time scales, allowing for a more fine-grained control of the dose rate and a fast shutoff time if the irradiation needs to be aborted.

8.5 Pulsed RF-Knockout (RF-KO)

The RF knockout (RF-KO) extraction technique uses an RF electric field to excite lateral oscillations of the particle in the accelerator ring. If this excitation is high enough, they can pass by an electromagnetic septum and be extracted. At MedAustron, this has been implemented for a coasting (unbunched) proton beam [32]. The RF signals are set to a multiple of the horizontal betatron tune (the frequency of the particles' oscillation around the reference orbit) of the accelerator, corresponding to 1.596 MHz for 252.7 MeV protons. Using a software-defined radio (SDR), different RF signals (and modulations thereof) are generated in a flexible way, before being amplified and applied to Schottky monitor plates serving as an RF cavity [32].

Figure 8.5.1 shows measurements of a typical pulsed RF-KO extraction using a fixed signal amplitude, a pulse length of 2 ms and a duty cycle of 50 %. Very high dose rates up to 1.2 kGy s^{-1} can be extracted, with an exponential decrease in time as the beam is extracted. For each pulse of the RF-KO signal (depicted in Figure 8.5.1b), a corresponding extraction can be observed, and when the RF-KO signal is turned off, the dose rate remains zero, which is a significant improvement over the results for COSE.

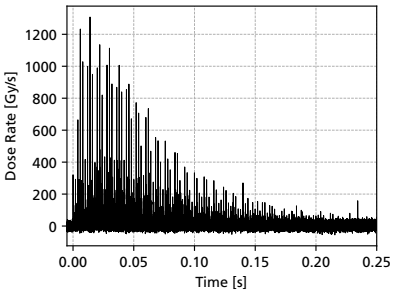

(a) Entire extraction

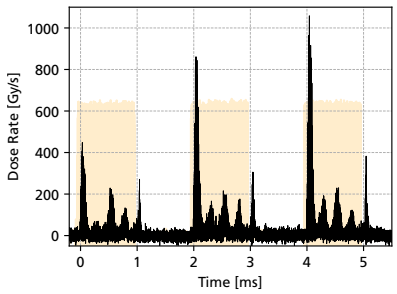

(b) Individual RF-KO pulses

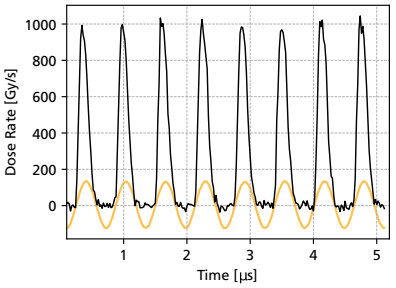

(c) Pulse substructure

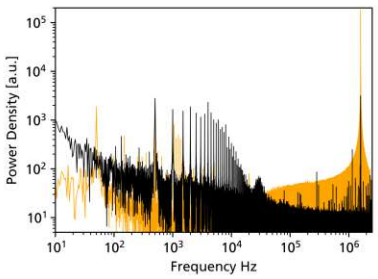

(d) Fourier spectrum

Figure 8.5.1: Typical measured extraction profiles for a pulsed RF-KO extraction with a repetition rate of 500 Hz and a duty cycle of 50 %. The sinusoidal RF-KO signal is indicated in orange.

At the beginning of each pulse, a spike in the dose rate can be observed, before the extraction settles to levels around $100\,\mathrm{Gy\,s^{-1}}$. This initial spike corresponds to all particles in the relevant phase space quickly being extracted, after which the extraction efficiency is limited by refilling of this phase space [34].

When zooming into the microsecond level, a substructure of the pulses can be observed, depicted in Figure 8.5.1c. This substructure is modulated by the oscillation frequency of the particles around the reference orbit (excited by the RF-KO signal), as the extraction occurs only in one direction of the oscillation. In the Fourier spectrum (Figure 8.5.1d), the effect of the RF-KO excitation is clearly visible around 1.6 MHz, together with the 500 Hz duty cycle of the extraction (and associated harmonics). The RF-KO signal was also frequency modulated with a sawtooth signal with an amplitude of $\Delta f = 800\,\mathrm{Hz}$, in order to cover the momentum spread of the beam [322].

In-depth studies have been undertaken on how to improve the RF-KO extraction by increasing the dose rate, changing the duty cycle, and adapting the substructure using different modulation techniques. Figure 8.5.2 shows two measurements of this investigation. The speed of the RF-KO extraction can be controlled by the amplitude of the RF-KO signal, tunable via a "gain" parameter of the SDR. The measured dose rate is shown for four different gain settings, and the number of extracted particles has been calibrated by using an EBT3 film (as the synchrotron is not always filled with the same exact amount of particles). While the extraction always has an exponential time profile, the extraction time can be scaled from 4 s seconds down to around 200 ms.

For gain parameters above 0.35, the dose rate saturates, as the limitations of the amplifiers are reached. Nevertheless, the total extracted dose, measured by the SiC beam monitor, remains constant, even for dose rates up to $1\,\mathrm{kGy\,s^{-1}}$.

Figure 8.5.2 (right) shows measurements with different frequency offsets relative to the betatron tune of the particles in the ring. For each RF-KO pulse, the extracted dose has been added together and normalized to the total extracted dose. If the RF-KO excitation frequency does not exactly match the betatron tune, then the number of particles that fall into the excited phase space is reduced, resulting in a slower excitation. This, therefore, presents another "knob" for modifying the extraction speed. Additionally, different frequency offsets have been shown to result in a different pulse substructure, with in-depth analysis and simulations currently ongoing.

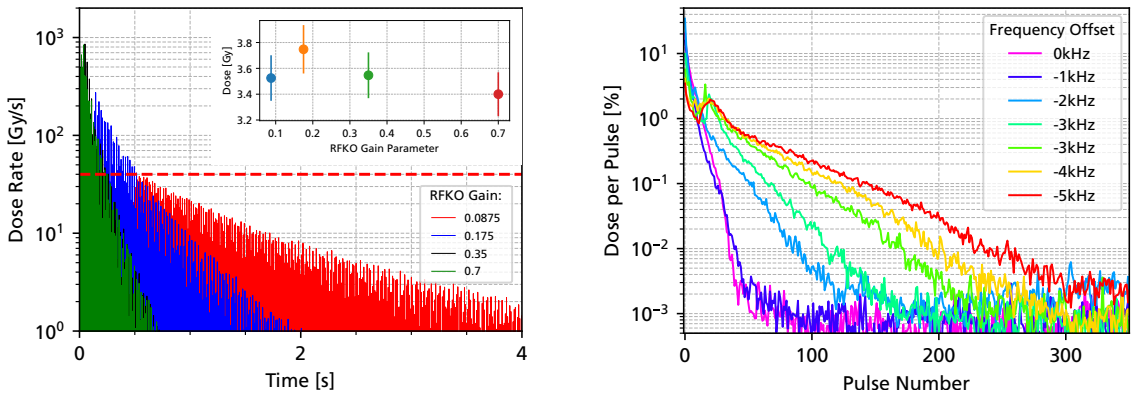

Figure 8.5.2: Pulsed RF-KO extractions for 252.7 MeV protons using a repetition rate of 500 Hz and a duty cycle of 50 % for different amplitudes of the RF-KO signal (left), and different frequency offsets relative to the horizontal betatron tune (right).

8.5.1 Amplitude Modulation

As described in Section 8.2.1, FLASH beams could be implemented safely in the clinic by using a pulsed extraction, where the dose for each pulse is kept below 0.25 Gy. However, the RF-KO extractions using a constant excitation amplitude (previously presented) have shown large variations in the dose per pulse, with the first 3 pulses extracting up to 20 % of the synchrotron. In order to obtain a more uniform pulse distribution, amplitude modulation of the RF-KO signal has been used. This was possible using the RF system of the accelerator, which is synchronized to the extraction and allows for for the frequency and amplitude of the RF-KO signal to be specified with a sample rate of 100 kSa/s.

Figure 8.5.3 shows the result of a manual tuning of the RF-KO amplitude to obtain a uniform extraction. Again 252.7 MeV protons have been used with a pulse repetition rate of 500 Hz and a duty cycle of 1 ms. The first 80 pulses show a very uniform dose distribution, around 1 % of the total dose for each pulse, reproducible from spill to spill. After around 90 pulses, however, the extracted dose starts to reduce, as the limit of the RF amplifier is reached. This extraction modality presents a very promising candidate for a FLASH-capable beam, with the beam being extracted in around 150 ms.

Assuming a dose of 9 Gy in the Bragg peak for a single synchrotron fill, the 80 RF-KO pulses will each contain a dose of around 0.1 Gy, respecting the safety limits of 0.25 Gy.

The impact of randomized pulse-to-pulse variations (between 0.1 ms and 10 ms) has also been studied, depicted in the right-hand side of Figure 8.5.3. The dose-per-pulse has been observed to change by a maximum 50 %, with the largest impact at the beginning of the extraction. However, for a dose per pulse of 0.1 Gy, this will be still in the safety limit of 0.25 Gy.

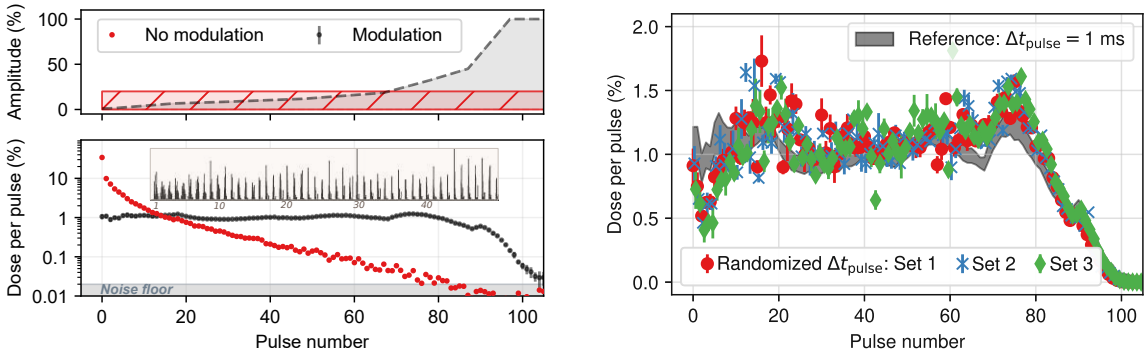

Figure 8.5.3: Left: Amplitude modulated RF-KO extraction, showing the amplitude of the RF-KO signal (top) and the extracted dose per pulse (bottom). Right: Amplitude-modulated RF-KO extraction for randomized pulse-to-pulse spacing between 1 ms and 10 ms. Taken from [33].

In summary, pulsed and amplitude-modulated RF-KO extraction has demonstrated its viability for providing FLASH-like beams that can be delivered in a clinically safe manner. Simulation studies are currently ongoing to develop a deeper understanding of the accelerator physics processes during extraction and the effect of different RF-KO signal frequencies and amplitudes on the time profile and pulse substructure. Additionally, FLASH dose rates have also been demonstrated using phase-displacement extraction [33], although these results are not reported here. These developments will continue in the upcoming "FLASH-BPM" FFG-funded project [334], which aims to build a 4H-SiC-based dose-delivery system that can be employed for pre-clinical FLASH radiotherapy studies in the future.

9 Discussion and Outlook

This thesis is dedicated to studying the performance of silicon carbide (SiC) detectors in high-energy physics and medical applications. Silicon carbide (and its polytype 4H) has been the recipient of renewed research interest in the community, as the investments by the power electronics industry have increased material quality and wafer sizes, while simultaneously decreasing cost. The work presented in this thesis has been performed as a part of the "HiBPM" (Hi-Precision Beam Position and Intensity Monitor for Accurate Cancer Treatment with Ions) FFG-funded project, which aims at employing SiC strip detectors at the MedAustron ion therapy center. Additionally, part of the measurements presented in this thesis were undertaken as part of the RD50 SiC-LGAD common project, where two runs of 4H-SiC detectors (without a gain layer) were produced by CNM (Barcelona) in 2024 and 2025.

As a first step, Monte-Carlo simulations of 4H-SiC detectors have been performed using the Allpix^2 framework in Section 5, with a special focus on the time resolution. Due to its high charge carrier drift velocities, 4H-SiC is often advertised as being capable of reaching a better time resolution than silicon [335]. However, Monte-Carlo simulations have shown that the time resolution of planar 4H-SiC sensors (without any internal gain) is limited by the signal-to-noise ratio, rather than the stochastic Landau fluctuations of the energy deposition by an ionizing particle. This is mainly a result of the ionization energy (energy required to create an electron-hole pair) in 4H-SiC being more than twice as large as for silicon. However, the situation is different for sensors with internal gain, such as Low-Gain Avalanche Diodes (LGADs). Here, the low charge yield in 4H-SiC can be overcome, and the performance can surpass that of silicon. For a thickness of 50 µm, simulations have obtained a Landau term of 22 ps for SiC-LGADs, which is a factor 1.4 better than the time resolution for Si-LGADs (30 ps). This is the first time that the time resolution limit of SiC-LGADs has been quantified in simulations and further substantiates the large community effort towards developing SiC-LGADs [20, 141, 336]. Up to now, however, the timing resolution that has been reached in experiments lags behind this simulated performance, likely due to experimental limitations and the large capacitance of the devices manufactured so far [19]. The geometry of the RD50-SiC-LGAD design (which is currently being manufactured) has been simulated in Allpix^2 as well, with a good agreement to TCAD simulations, opening the door for future simulation studies.

A large portion of the work performed in this thesis has been the laboratory characterization of 4H-SiC detectors. The wide bandgap of 4H-SiC results in very small leakage currents (on the order of pA), while simultaneously, high bias voltages need to be applied (due to epitaxial doping concentrations around $1 \times 10^{14}\,\mathrm{cm}^{-3}$), which makes electrical characterization challenging. Additionally, 4H-SiC detectors are typically limited to thicknesses below 100 µm (due to limitations in epitaxial growth), resulting in very short signals (<1 ns). As a part of this thesis, three experimental setups, a high-voltage (3 kV) probe station, an alpha spectroscopy vacuum setup, and a UV-laser-based TCT setup have been built or improved to characterize 4H-SiC detectors, detailed in Section 4.

Section 6 presents the electrical characterization of three runs of planar 4H-SiC detectors produced by CNM. Two of these runs have been performed as a part of the RD50-SiC-LGAD project (for the first time on six-inch wafers), discussed in Section 6.3. Wafer maps were performed, characterizing all 173 PiN diodes on the wafer, as well as various test structures. The first production (runs 16886 and 17407) encountered issues during manufacturing due to an error in the mask layout, where metal melted and flowed across the wafer, instead of forming a low-resistance ohmic contact with the silicon carbide. This reduced yields down to around 40 %, and prevented most of the complex structures (such

as strip detectors, or MOS devices) from being used. Nevertheless, simple diodes have successfully been produced and characterized. In the second production (run 17560), these issues have been addressed, and the yield was increased to approximately 75 %.

The characterization of 4H-SiC detectors conducted in this thesis also includes a study of the material parameters. For 4H-SiC, many material parameters are still not precisely known, or values typically used in the community date back to measurements conducted in the 60s (with the wrong SiC polytype) [61]. The ionization energy of 4H-SiC, where there have been significant disagreements in the literature, has been studied in Section 6.4 and a value of (7.83 ± 0.02) eV was found [46]. Additionally, studies of the energy resolution for 4H-SiC PiN diodes with and without metal covering the active area have been performed, reaching 30 keV (0.5 %) FWHM. This energy resolution is likely limited by non-uniformities of the passivation covering the detector, and studies are currently ongoing to remove the passivation by chemical etching.

In Section 6.5, the transient-current technique (TCT) has been applied to 50 µm thick 4H-SiC PiN diodes. Because of this very small detector thickness, the expected drift times are very short (< 500 ps), which required high-speed readout electronics to be employed. Different types of readout electronics, which are currently used in the community, are investigated in detail in Section 3. By performing sine sweeps and measuring the impulse response, the transfer functions of the readout electronics were obtained, serving as an input to simulations.
Additionally, a new high-frequency readout electronics prototype, based on a commercial microwave-integrated circuit (MMIC) low-noise amplifier, has been developed. This amplifier, together with a low capacitance (<0.1 pF) 4H-SiC diode, demonstrated a rise time as short as 60 ps, corresponding to a bandwidth of almost 6 GHz. With this, the transient current in 4H-SiC detectors has been measured experimentally for the first time. Clear differences in the transient current were observed for alpha particles, UV-TCT, and proton beams. Additionally, the UV-TCT measurements allowed for the drift of electrons and holes to be distinguished, and their drift velocities to be measured. The high-frequency readout electronics have been adapted to a custom PCB, which will serve as a very valuable tool in the future, allowing TCT techniques, such as ion-beam induced current (IBIC [225]) or two-photon-absorption TCT (TPA-TCT [277, 279]) to be applied to not just 4H-SiC detectors, but any other thin detectors with short drift times (such as Si-LGADs). Further characterization efforts of the readout electronics are also underway, using very thin (10 µm) diamond detectors that can max out the electronics bandwidth.

The results from neutron irradiation studies of 4H-SiC detectors up to 1 MeV neutron equivalent fluences of 1×10^{16} [16] and 1×10^{18} $n_{eq.}/cm^2$ [337] are presented in Section 7. The radiation hardness of 4H-SiC is of great interest to the high-energy physics community, as the ever-increasing detector requirements of collider experiments have prompted the community to look for alternatives to silicon [6]. According to the larger atomic displacement energy of the atoms in 4H-SiC than in silicon, 4H-SiC is often referred to as being more radiation hard [14]. Additionally, the wide bandgap of 4H-SiC results in very small leakage currents (<1 pA/mm^2), even after irradiation (see Section 7.2.1), which allows the detectors to be operated without any cooling [338]. This not only saves operating costs, but also results in a lighter detector design with an improved radiation length (reducing multiple scattering). In forward bias, the conduction after irradiation is severely limited by an electric field barrier of trap-induced space charge [267, 268], allowing the detectors to be operated with hundreds of volts of forward bias. The capacitance of the detectors after irradiation is independent of the bias voltage and corresponds to the thickness of the epitaxial layer. This can be attributed to the *n*-dopants being trapped in defects with energy levels sufficiently deep such that almost no trap emission takes place during the kHz time scales of capacitance measurements. These deep traps, however, can also introduce a fixed space charge, which will affect the electric field inside the detector.

Charge collection efficiency measurements after irradiation up to 1×10^{16} $n_{eq.}/cm^2$ have been carried out using alpha particles [254], UV-TCT [266], and proton beams [16]. For a fluence of 1×10^{15} $n_{eq.}/cm^2$, 62.4 MeV protons can still be detected, with a charge collection efficiency (CCE) of 50 %. At a fluence of

1×10^{16} $n_{eq.}/cm^2$, UV-TCT measurements have shown that the CCE decreases to approximately 10 %. Additionally, the CCE has been observed to follow a square-root law as a function of the bias voltages, which can be explained by deep donor-like traps (such as the carbon vacancy $EH_{6,7}$) introducing an effective doping (with a measured introduction rate of $\eta = 2.9\,cm^{-1}$), limiting the expansion of the electric field in the device [267]. Similar behavior has also been observed in TPA-TCT [252] and IBIC [275] studies by other groups. Only for a fluence of 1×10^{16} $n_{eq.}/cm^2$ can a significant decrease of the collected charge from the expected charge collection distance (given by the effective doping) be observed. These results illustrate why the charge collection efficiency of 50 µm thin 4H-SiC detectors rapidly decreases at fluences above 1×10^{15} $n_{eq.}/cm^2$, where 300 µm thick silicon detectors can still reach similar (or better) CCEs. Future studies should be performed on how this can be improved, either by carbon implantation (to fill the carbon vacancies introduced by radiation damage), or annealing [109, 116].

First systematic studies of the compensation of the epitaxial layer n-doping in 4H-SiC detectors, aiming at fluences below 1×10^{14} $n_{eq.}/cm^2$, have been performed very recently using proton beams at MedAustron. Although results from these studies are not reported in this thesis, donor removal coefficients in the range of $4.3\,cm^{-1}$ to $6.6\,cm^{-1}$ have been measured for 252.7 MeV protons [339]. This donor removal will have a significant impact on the gain layer of SiC-LGADs, and recent studies in the literature have shown that the gain of SiC-LGADs indeed decreases significantly for GeV proton irradiation to fluences around $5 \times 10^{14}\,cm^{-2}$ [340–342].

A set of 4H-SiC PiN diodes has been neutron-irradiated to extreme levels of 1×10^{18} $n_{eq.}/cm^2$, expected at future hadron colliders [4]. At this fluence, not only is the n-doping of the epitaxial layer compensated, but also the highly doped n^{++} buffer, which separates epitaxy from its substrate, is deactivated. This resulted in uncharacteristically high (for 4H-SiC) currents, around 10 nA at 1.5 kV, with a strong temperature dependency. By performing measurements between −40 °C and 25 °C, an activation energy of 0.24 eV was extracted, hypothesized to be related to charge carrier injection by the aluminum p^+ implant with a similar energy level.

Irradiated 4H-SiC detectors can also detect particles when operated in forward bias. Using UV-TCT and alpha particles, charge-collection efficiencies in excess of 100 % have been obtained, also by other groups using IBIC and TPA-TCT [225]. While this effect has been a significant point of discussion in the community [279], it has been shown in this thesis that the excess CCE only occurs for high charge densities, and not for 62.4 MeV proton beams. In forward-bias operated irradiated 4H-SiC detectors, trapped space charge at the anode and cathode prevents charge carriers from being injected into the device and limits the current [268]. If, however, a significant amount of charge is injected into the device, these charge carriers can screen the electric field at the cathode and anode while they drift past it, reducing the electric field barrier and resulting in a transient forward conduction, adding to the injected charge. Measurements demonstrating this effect are presented in Section 7.4. If the injected charge is either sufficiently small as not to disturb the electric field in the detector, or sufficiently spread out, a charge-collection efficiency below 100 % is obtained, in agreement with measurements obtained using proton beams. In the future, studies are planned to be performed using low-capacitance irradiated 4H-SiC diodes and the high-bandwidth readout electronics previously discussed, in order to provide a more detailed insight into this process.

Finally, 4H-SiC detectors have been applied in a medical context as a beam intensity monitor with a high temporal resolution at the ion therapy center MedAustron. Silicon carbide provides many advantages for dosimetry (such as its fast charge carrier velocity, insensitivity to visible light, and lower thermal variations) [26]. At MedAustron, studies are currently ongoing for a number of improved synchrotron extraction techniques, with the ultimate goal of delivering ultra-high dose rate beams that would allow for the FLASH effect to be studied in pre-clinical trials [32, 33]. The FLASH effect occurs when irradiation is performed at very high dose rates (>40 $\mathrm{Gy\,s^{-1}}$) and a sufficiently large dose, and has been shown to improve clinical outcomes [31, 297]. However, delivering beams capable of triggering the FLASH effect at synchrotrons is challenging, especially because clinical safety requirements have to be met [299], Additionally, conventional dosimetry (using ionization chambers) is no longer reliable at ultra-high dose rates and exhibits saturation effects [301], which requires novel approaches, for example, using solid-state detectors [290, 319, 320].

A 4H-SiC beam intensity monitor, based on a 20 MHz transimpedance amplifier, has been developed to provide relative dosimetry and to give insight into the temporal profiles of novel beam extraction techniques [34]. Different low-extraction modalities, including constant-optics slow-extraction (COSE), phase displacement extraction (PDE), and RF knockout (RF-KO), have been implemented at MedAustron and studied using the SiC beam intensity monitor. The RF-KO technique, specifically, has shown promise to deliver a pulsed beam with FLASH-compatible dose rates, as well as the ability to be modulated in different ways [34]. The high bandwidth of the beam intensity monitor, compared to the currently existing systems, such as ionization chambers or beam current transformers, has allowed these extraction methods to be studied in detail, resolving each turn of the particles in the synchrotron. No saturation or dose-rate dependencies have been observed, up to dose rates of 10 $\mathrm{kGy\,s^{-1}}$, where the response of the ionization-chamber-based dose-delivery system at MedAustron was already significantly saturated.

Funding Acknowledgments

This work was supported by the Austrian Research Promotion Agency (FFG) in the project «HiBPM» (883652).

Production and development of the 4H-SiC samples was supported by the Spanish Ministry of Science, Innovation and Universities (grant number CEX2023-001397-M), by the European Union's ERDF program (MCIN/AEI/10.13039/501100011033/) «A way of making Europe» under grant reference PID2021-124660OB-C22, and by the Spanish State Research Agency (AEI) and European Regional Development Fund (ERDF), ref. RTC-2017-6369-3.

The production of the planar 6″-SiC samples has been supported in part by the RD50 collaboration (RD50-SiC-LGAD common project)

The financial support of the Austrian Ministry of Education, Science and Research is gratefully acknowledged for providing beam time and research infrastructure at MedAustron.

This project has received funding from the European Union's Horizon Europe Research and Innovation programme under Grant Agreement No 101057511 (EURO-LABS)

Acknowledgments

First and foremost, I would like to thank Thomas Bergauer for making this PhD project possible and for his continuous support and guidance over the past three and a half years. I am grateful for the freedom I was given to pursue my own ideas and interests, and for the countless opportunities to present my work internationally.

Next, I would like to thank Albert Hirtl for his valuable supervision, support, and advice.

I am deeply grateful to my office mates over the past few years, Philipp Gaggl, Simon Waid, and Jürgen Burin, for their companionship and the countless in-depth discussions we have had, which have made the day-to-day research both productive and enjoyable. I would especially like to thank Philipp for his friendship and for the weekly pub quizzes.

I would also like to thank Matthias Knopf, Sebastian Onder and Daniel Radmanovac for their excellent collaboration during countless hours in the lab and beamtimes, as well as for their time at conferences and outside of work.

I benefited greatly from the guidance of Stefan Gundacker and Ioannis Kopsalis, and I am grateful for their mentorship and for the critical feedback they provided, as well as for introducing me to new ideas and concepts.

I would like to thank all the project, bachelor's, and master's thesis students that I had the pleasure of supervising and working with.

My sincere thanks go to Andreas Bauer for his exceptional wire bonding skills and to Klaus-Dieter Fischer for repeatedly reviving readout boards after I had stressed them a little too much. Your skill and patience were essential to the success of many measurements.

Furthermore, I would like to express my gratitude to Stefan Schultschick, Richard Thalmeier, Bernhard Arnold, Wolfgang Brander, Margit Oberegger, Florian Buchsteiner, Roland Stark, and Marco Kunisch for their help in building and maintaining new setups in the clean room.

Merci Nathalie de m'aider à redécouvrir le plaisir de la langue française.

I would like to express my gratitude to Elisabeth Renner, Claus Schmitzer, and Matthias Kausel for their close collaboration and for making it such a pleasure to work with them. In addition, I would like to thank the MedAustron operators for their support and troubleshooting during numerous beam times.

I would also like to thank Giulio Pellegrini and Joan-Marc Rafí for our close and fruitful collaboration on 4H-SiC detectors over the past three years, as well as for hosting me during visits to CNM.

Finally, I would like to express my gratitude to the RD50 and DRD3 communities. I immediately felt welcome in the community, and greatly appreciated the open exchange of knowledge, samples, and ideas.

I would also like to thank my family for their unwavering support over the past 25 years.

To Kris: Thank you for your friendship, inspiration, and encouragement
To Lars: Thank you for more than a decade of friendship and the countless adventures we have shared.

References

[1] Frank Hartmann. *Evolution of silicon sensor technology in particle physics*. en. 2nd ed. Springer Tracts in Modern Physics. Basel, Switzerland: Springer International Publishing, 2017.

[2] CERN. *CERN Yellow Reports: Monographs, Vol 4 (2017): High-Luminosity Large Hadron Collider (HL-LHC) Technical Design Report V. 0.1*. en. 2017. DOI: 10.23731/CYRM-2017-004.

[3] Georg Steinbrueck. *Radiation Hard Pixel Sensors for the Phase 2 Upgrade of the CMS Inner Tracker*. Tech. rep. Geneva: CERN, 2024.

[4] Micael Benedikt. *Future Circular Collider Feasibility Study Report Volume 1 : Physics and Experiments*. Version 2.0. 2025. DOI: 10.17181/CERN.9DKX.TDH9.

[5] *DRD3 - R&D on Semiconductor Detectors*. 2025. URL: https://drd3.web.cern.ch/.

[6] ECFA Detectors R&D Roadmap Process Group. *The 2021 ECFA detector research and developement roadmap*. CERN, 2021. DOI: 10.17181/CERN.XDPL.W2EX.

[7] Michael Moll. "Displacement Damage in Silicon Detectors for High Energy Physics". In: *IEEE Transactions on Nuclear Science* 65 (2018), pp. 1561–1582. DOI: 10.1109/TNS.2018.2819506.

[8] S.I. Parker, C.J. Kenney, and J. Segal. "3D - A proposed new architecture for solid-state radiation detectors". In: *Nuclear Instruments and Methods in Physics Research Section A: Accelerators, Spectrometers, Detectors and Associated Equipment* 395 (1997). Proceedings of the Third International Workshop on Semiconductor Pixel Detectors for Particles and X-rays, pp. 328–343. DOI: https://doi.org/10.1016/S0168-9002(97)00694-3.

[9] G. Pellegrini et al. "Technology developments and first measurements of Low Gain Avalanche Detectors (LGAD) for high energy physics applications". In: *Nuclear Instruments and Methods in Physics Research Section A: Accelerators, Spectrometers, Detectors and Associated Equipment* 765 (2014). HSTD-9 2013 - Proceedings of the 9th International "Hiroshima" Symposium on Development and Application of Semiconductor Tracking Detectors, pp. 12–16. DOI: https://doi.org/10.1016/j.nima.2014.06.008.

[10] M. Tornago et al. "Resistive AC-Coupled Silicon Detectors: Principles of operation and first results from a combined analysis of beam test and laser data". In: *Nuclear Instruments and Methods in Physics Research Section A: Accelerators, Spectrometers, Detectors and Associated Equipment* 1003 (2021), p. 165319. DOI: https://doi.org/10.1016/j.nima.2021.165319.

[11] M. Bruzzi et al. "Radiation-hard semiconductor detectors for SuperLHC". In: *Nuclear Instruments and Methods in Physics Research Section A: Accelerators, Spectrometers, Detectors and Associated Equipment* 541 (2005). Development and Application of Semiconductor Tracking Detectors, pp. 189–201. DOI: https://doi.org/10.1016/j.nima.2005.01.056.

[12] Eva Calvo Giraldo et al. "The Diamond Beam Loss Monitoring System at CERN LHC and SPS". en. In: *11th Int. Beam Instrum. Conf.* (2022). DOI: 10.18429/JACOW-IBIC2022-TU2C2.

[13] F. Moscatelli et al. "Radiation hardness after very high neutron irradiation of minimum ionizing particle detectors based on 4H-SiC p/sup +/n junctions". In: *IEEE Transactions on Nuclear Science* 53 (2006), pp. 1557–1563. DOI: 10.1109/TNS.2006.872202.

[14] Marzio De Napoli. "SiC detectors: A review on the use of silicon carbide as radiation detection material". In: *Frontiers in Physics* 10 (2022), p. 898833. DOI: 10.3389/fphy.2022.898833.

[15] Andreas Gsponer. *Update on the RD50-SiC-LGAD Project*. https://indico.cern.ch/event/1439336/contributions/6242447/. 2nd DRD3 week on Solid State Detectors R&D. CERN, Geneva, Switzerland, 2024.

[16] Andreas Gsponer et al. "Neutron radiation induced effects in 4H-SiC PiN diodes". In: *Journal of Instrumentation* 18 (2023), p. C11027. DOI: 10.1088/1748-0221/18/11/C11027.

[17] D. Carbone et al. “Characterization of newly developed large area SiC sensors for the NUMEN experiment”. In: *Nuclear Instruments and Methods in Physics Research Section A: Accelerators, Spectrometers, Detectors and Associated Equipment* 1069 (2024), p. 169960. DOI: https://doi.org/10.1016/j.nima.2024.169960.

[18] Sebastian Onder et al. “Design and simulation of a 4H-SiC low gain avalanche diode with trench-isolation”. In: *Nuclear Instruments and Methods in Physics Research Section A: Accelerators, Spectrometers, Detectors and Associated Equipment* 1080 (2025), p. 170740. DOI: https://doi.org/10.1016/j.nima.2025.170740.

[19] Radek Novotný et al. *First generation 4H-SiC LGAD production and its performance evaluation*. 2025. arXiv: 2503.07490 [physics.ins-det].

[20] P. Barletta et al. *Fast Timing With Silicon Carbide Low Gain Avalanche Detectors*. 2022. arXiv: 2203.08554 [physics.ins-det].

[21] Sebastian Onder et al. “Towards Silicon Carbide Monolithic Active Pixel Radiation Sensors”. In: *2024 Austrochip Workshop on Microelectronics (Austrochip)*. 2024 Austrochip Workshop on Microelectronics (Austrochip). Vienna, Austria: IEEE, 2024, pp. 1–4. DOI: 10.1109/Austrochip62761.2024.10716230.

[22] Andreas Gsponer. *Wide Bandgap Electronics and Detectors*. https://indico.cern.ch/event/1516157/contributions/6445370/. (Invited talk). Brookhaven National Laboratory, Upton, NY, USA, 2025.

[23] M.C. Jiménez-Ramos et al. “Spectrometric performance of SiC radiation detectors at high temperature”. In: *Radiation Physics and Chemistry* 214 (2024), p. 111283. DOI: https://doi.org/10.1016/j.radphyschem.2023.111283.

[24] Frank H. Ruddy et al. “Performance and Applications of Silicon Carbide Neutron Detectors in Harsh Nuclear Environments”. In: *EPJ Web of Conferences* 253 (2021). Ed. by A. Lyoussi et al., p. 11003. DOI: 10.1051/epjconf/202125311003.

[25] Celeste Fleta et al. “State-of-the-art silicon carbide diode dosimeters for ultra-high dose-per-pulse radiation at FLASH radiotherapy”. In: *Physics in Medicine & Biology* 69 (2024), p. 095013. DOI: 10.1088/1361-6560/ad37eb.

[26] Elisabetta Medina et al. “Radiation Hardness Study of Silicon Carbide Sensors under High-Temperature Proton Beam Irradiations”. In: *Micromachines* 14 (2023). DOI: 10.3390/mi14010166.

[27] Simon Waid et al. “SiC based beam monitoring system for particle rates from kHz to GHz”. In: *Journal of Instrumentation* 19 (2024). Publisher: IOP Publishing, p. C04055. DOI: 10.1088/1748-0221/19/04/C04055.

[28] L Badano et al. *Proton-Ion Medical Machine Study (PIMMS), 1*. CERN, 2000.

[29] Mauro Pivi et al. “Overview and Status of the MedAustron Ion Therapy Center Accelerator”. en. In: *Proceedings of the 8th Int. Particle Accelerator Conf.* (2017). DOI: 10.18429/JACOW-IPAC2017-THPVA076.

[30] Gambino, Nadia et al. “Status of helium ion beams commissioning at MedAustron ion therapy center”. en. In: *Proceedings of the 9th Int. Particle Accelerator Conf.* (2024). DOI: 10.18429/JACOW-IPAC2024-TUPS06.

[31] Anastasia Velalopoulou et al. “FLASH Proton Radiotherapy Spares Normal Epithelial and Mesenchymal Tissues While Preserving Sarcoma Response”. In: *Cancer Research* 81 (2021), pp. 4808–4821. DOI: 10.1158/0008-5472.CAN-21-1500.

[32] F. Kuehteubl et al. “Investigating alternative extraction methods at MedAustron”. English. In: *Proc. 14th International Particle Accelerator Conference* (Venice, Italy). IPAC’23 - 14th International Particle Accelerator Conference. 2023, pp. 2419–2422. DOI: 10.18429/JACoW-IPAC2023-TUPM091.

[33] E. Renner et al. “Investigating pulsed slow extraction schemes at the MedAustron synchrotron”. English. In: *Proc. IPAC’24* (Nashville, TN). IPAC’24 - 15th International Particle Accelerator Conference. 2024, pp. 3595–3598. DOI: 10.18429/JACoW-IPAC2024-THPR41.

[34] Simon Waid et al. “Pulsed RF knock-out extraction: a potential enabler for FLASH hadrontherapy in the Bragg peak”. In: *Physics in Medicine & Biology* 69 (2024), p. 125007. DOI: 10.1088/1361-6560/ad5072.

[35] Matthias Kausel et al. *A double multi-turn injection scheme for generating mixed helium and carbon ion beams at medical synchrotron facilities*. 2025.

[36] J J Berzelius. “Untersuchungen über die Flussspathsäure und deren merkwürdigsten Verbindungen”. en. In: *Ann. Phys.* 77 (1824), pp. 169–230.

[37] Edward.G. Acheson. “Production of artificial crystalline carbonaceous materials, carborundum”. U.S. pat. 1892.

[38] H. J. Round. “A Note on Carborundum”. In: *Electrical World* 49 (1907). Letter dated 9 February 1907, p. 309.

[39] Henri Moissan. “Nouvelles recherches sur la météorité de Cañon Diablo”. In: *Comptes Rendus Hebdomadaires des Séances de l’Académie des Sciences* 139 (1905), pp. 773–786.

[40] K. M. Pitman, A. M. Hofmeister, A. B. Corman, and A. K. Speck. “Optical properties of silicon carbide for astrophysical applications: I. New laboratory infrared reflectance spectra and optical constants”. In: *Astronomy&Astrophysics* 483 (2008), pp. 661–672. DOI: 10.1051/0004-6361:20078468.

[41] Giuseppe Iannaccone, Christian Sbrana, Iacopo Morelli, and Sebastiano Strangio. “Power Electronics Based on Wide-Bandgap Semiconductors: Opportunities and Challenges”. In: *IEEE Access* 9 (2021), pp. 139446–139456. DOI: 10.1109/ACCESS.2021.3118897.

[42] Gerald Rescher. “Behavior of SiC-MOSFETs under temperature and voltage stress”. en. PhD thesis. TU Wien, 2018. DOI: 10.34726/HSS.2018.60783.

[43] Richard Babcock. “Radiation Damage in SiC”. In: *IEEE Transactions on Nuclear Science* 12 (1965), pp. 43–47. DOI: 10.1109/TNS.1965.4323922.

[44] Tsunenobu Kimoto and James A Cooper. *Fundamentals of silicon carbide technology*. en. Wiley - IEEE. Nashville, TN: John Wiley & Sons, 2014. DOI: 10.1002/9781118313534.

[45] Navitas Semiconductor. “Efficient 400-800V Charging & Conversion with GaNFast Power ICs & GeneSiC Trench-Assisted Planar Gate MOSFETs,” in: *Advanced Automotive Tech Forum 2023*. 2023.

[46] Andreas Gsponer et al. “Measurement of the electron-hole pair creation energy in a 4H-SiC p-n diode”. In: *Nuclear Instruments and Methods in Physics Research Section A: Accelerators, Spectrometers, Detectors and Associated Equipment* 1064 (2024), p. 169412. DOI: 10.1016/j.nima.2024.169412.

[47] K. Park, M. A. Stroscio, and C. Bayram. “Investigation of electron mobility and saturation velocity limits in gallium nitride using uniaxial dielectric continuum model”. In: *Journal of Applied Physics* 121 (2017), p. 245109. DOI: 10.1063/1.4990424.

[48] S. Agostinelli et al. “Geant4-a simulation toolkit”. In: *Nuclear Instruments and Methods in Physics Research Section A: Accelerators, Spectrometers, Detectors and Associated Equipment* 506 (2003), pp. 250–303. DOI: 10.1016/s0168-9002(03)01368-8.

[49] Anthony Lely. *Darstellung von Einkristallen von Siliciumcarbid und Beherrschung von Art und Menge der eingebauten Verunreinigungen*. Laboratoria N.V. Philips' Gloeilampenfabrieken. N.V. Philips' Gloeilampenfabrieken, 1955.

[50] Oda Marie Ellefsen, Matthias Arzig, Johannes Steiner, Peter Wellmann, and Pål Runde. "Optimization of the SiC Powder Source Material for Improved Process Conditions During PVT Growth of SiC Boules". In: *Materials* 12 (2019). DOI: 10.3390/ma12193272.

[51] Korea IT News. *ESTech supplies first 8-inch SiC ingot growth furnace to Senic*. 2022. URL: https://english.etnews.com/20220613200001?SNS=00002.

[52] PVA Crystal Growing Systems GmbH. *SiCma System*. 2025. URL: https://www.pvatepla-cgs.com/en/machines/physical-vapor-transport-systems/.

[53] Akihiko Yoshikawa, Hiroyuki Matsunami, and Yasushi Nanishi. *Wide Bandgap Semiconductors*. Springer Berlin Heidelberg, 2007. DOI: 10.1007/978-3-540-47235-3.

[54] mi2-factory GmbH. *Energy-Filtered Ion Implantation*. 2025.

[55] Viktoria Hinger. "Silicon sensor process quality control for the CMS phase-2 upgrade". Thesis. Technische Universität Wien, 2021. DOI: 10.34726/hss.2021.47360.

[56] Glenn F Knoll. *Radiation Detection and Measurement*. en. 4th ed. Chichester, England: John Wiley & Sons, 2010.

[57] Hermann Kolanoski and Norbert Wermes. *Particle Detectors: Fundamentals and Applications*. Oxford: Oxford University Press USA - OSO, 2020. 1 p.

[58] G L Zhao and D Bagayoko. "Electronic structure and charge transfer in 3C- and 4H-SiC". In: *New Journal of Physics* 2 (2000), pp. 16–16. DOI: 10.1088/1367-2630/2/1/316.

[59] Helmuth Spieler. *Semiconductor Detector Systems*. Oxford University Press, 2005. DOI: 10.1093/acprof:oso/9780198527848.001.0001.

[60] W. Shockley. "The Theory of p-n Junctions in Semiconductors andp-nJunction Transistors". In: *Bell System Technical Journal* 28 (1949), pp. 435–489. DOI: 10.1002/j.1538-7305.1949.tb03645.x.

[61] Jürgen Burin, Philipp Gaggl, Simon Waid, Andreas Gsponer, and Thomas Bergauer. *TCAD Parameters for 4H-SiC: A Review*. 2025. arXiv: 2410.06798 [cond-mat.mtrl-sci].

[62] Dieter K. Schroder. *Semiconductor Material and Device Characterization*. Wiley, 2005. DOI: 10.1002/0471749095.

[63] R. N. Hall. "Electron-Hole Recombination in Germanium". In: *Phys. Rev.* 87 (2 1952), pp. 387–387. DOI: 10.1103/PhysRev.87.387.

[64] W. Shockley and W. T. Read. "Statistics of the Recombinations of Holes and Electrons". In: *Phys. Rev.* 87 (5 1952), pp. 835–842. DOI: 10.1103/PhysRev.87.835.

[65] Alexandra Junkes and DESY. "Influence of radiation induced defect clusters on silicon particle detectors; 1st edition". Universität Hamburg, Diss., 2011. Dr. Hamburg: Universität Hamburg, 2011. DOI: 10.3204/PHPPUBDB-17257.

[66] D M Caughey and R E Thomas. "Carrier mobilities in silicon empirically related to doping and field". In: *Proc. IEEE Inst. Electr. Electron. Eng.* 55 (1967), pp. 2192–2193. DOI: 10.1109/PROC.1967.6123.

[67] Ryoya Ishikawa, Hajime Tanaka, Mitsuaki Kaneko, and Tsunenobu Kimoto. "Experimental and Theoretical Study on Anisotropic Electron Mobility in 4H-SiC". In: *physica status solidi (b)* 260 (2023), p. 2300275. DOI: https://doi.org/10.1002/pssb.202300275.

[68] Ryoya Ishikawa, Hajime Tanaka, Mitsuaki Kaneko, and Tsunenobu Kimoto. “Origin of hole mobility anisotropy in 4H-SiC”. In: *Journal of Applied Physics* 135 (2024), p. 075704. DOI: 10.1063/5.0186307.

[69] G. Masetti, M. Severi, and S. Solmi. “Modeling of carrier mobility against carrier concentration in arsenic-, phosphorus-, and boron-doped silicon”. In: *IEEE Transactions on Electron Devices* 30 (1983), pp. 764–769. DOI: 10.1109/T-ED.1983.21207.

[70] Kent Bertilsson, C. Harris, and Hans-Erik Nilsson. “Calculation of lattice heating in SiC RF power devices”. In: *Solid-State Electronics* 48 (2004), pp. 2103–2107. DOI: https://doi.org/10.1016/j.sse.2004.08.001.

[71] C. Canali, G. Majni, R. Minder, and G. Ottaviani. “Electron and hole drift velocity measurements in silicon and their empirical relation to electric field and temperature”. In: *IEEE Transactions on Electron Devices* 22 (1975), pp. 1045–1047. DOI: 10.1109/T-ED.1975.18267.

[72] C A "Lee, R A Logan, R L Batdorf, J J Kleimack, and W" Wiegmann. “"Ionization rates of holes and electrons in silicon"”. In: *"Phys. Rev."* 134 (1964), "A761–A773". DOI: 10.1103/PhysRev.134.A761.

[73] Y. Okuto and C.R. Crowell. “Threshold energy effect on avalanche breakdown voltage in semiconductor junctions”. In: *Solid-State Electronics* 18 (1975), pp. 161–168. DOI: https://doi.org/10.1016/0038-1101(75)90099-4.

[74] W. S. Loh et al. “Impact Ionization Coefficients in 4H-SiC”. In: *IEEE Transactions on Electron Devices* 55 (2008), pp. 1984–1990. DOI: 10.1109/TED.2008.926679.

[75] Esteban Currás Rivera and Michael Moll. “Study of Impact Ionization Coefficients in Silicon With Low Gain Avalanche Diodes”. In: *IEEE Transactions on Electron Devices* 70 (2023), pp. 2919–2926. DOI: 10.1109/TED.2023.3267058.

[76] Keithley Instruments Inc. *Keithley Low Level Measurements Handbook - 7th Edition*. 2013. URL: https://www.tek.com/en/documents/product-article/keithley-low-level-measurements-handbook---7th-edition.

[77] Keysight Technologies. *The Parametric Measurement Handbook*. 2020. URL: https://www.keysight.com/us/en/assets/7018-05884/application-notes/5992-2508.pdf.

[78] Keysight Technologies. *Impedance Measurement Handbook*. 2019. URL: https://www.keysight.com/us/en/assets/7018-06840/application-notes/5950-3000.pdf.

[79] Texas Instruments. *LMP7721*. 2025. URL: https://www.ti.com/product/LMP7721.

[80] Tektronix Inc. *Keithley 2400 Standard Series SMU*. 2025. URL: https://www.tek.com/en/products/keithley/source-measure-units/2400-standard-series-sourcemeter.

[81] Tektronix Inc. *Keithley Electrometer Series 6500 & 6430*. 2025. URL: https://www.tek.com/de/products/keithley/low-level-sensitive-and-specialty-instruments/electrometers#.

[82] H. Bethe. “Zur Theorie des Durchgangs schneller Korpuskularstrahlen durch Materie”. In: *Annalen der Physik* 397 (1930), pp. 325–400. DOI: https://doi.org/10.1002/andp.19303970303.

[83] Particle Data Group. “Review of Particle Physics”. In: *Progress of Theoretical and Experimental Physics* 2022 (2022), p. 083C01. DOI: 10.1093/ptep/ptac097.

[84] R. M. Sternheimer and R. F. Peierls. “General Expression for the Density Effect for the Ionization Loss of Charged Particles”. In: *Phys. Rev. B* 3 (11 1971), pp. 3681–3692. DOI: 10.1103/PhysRevB.3.3681.

[85] Lev Davidovich Landau. “On the Energy Loss of Fast Particles by Ionisation”. In: *J. Phys. (USSR)* 8 (1944). DOI: 10.1016/b978-0-08-010586-4.50061-4.

[86] P. V. Vavilov. "Ionization losses of high-energy heavy particles". In: *Sov. Phys. JETP* 5 (1957), pp. 749–751.

[87] Hans Bichsel. "Straggling in thin silicon detectors". In: *Rev. Mod. Phys.* 60 (3 1988), pp. 663–699. DOI: 10.1103/RevModPhys.60.663.

[88] Felix Ulrich-Pur. "Advancing ion computed tomography by incorporating time-of-flight and 4D tracking". Thesis. Technische Universität Wien, 2022. DOI: 10.34726/hss.2022.62102.

[89] Beer. "Bestimmung der Absorption des rothen Lichts in farbigen Flüssigkeiten". In: *Annalen der Physik* 162 (1852), pp. 78–88. DOI: 10.1002/andp.18521620505.

[90] Jean-Henri Lambert. *Photometria sive de mensura et gradibus luminis, colorum et umbrae*. Sumptibus viduae Eberhardi Klett, typis Christophori Petri Detleffsen, 1760.

[91] J. Tauc. "Optical properties and electronic structure of amorphous Ge and Si". In: *Materials Research Bulletin* 3 (1968), pp. 37–46. DOI: https://doi.org/10.1016/0025-5408(68)90023-8.

[92] S. G. Sridhara, R. P. Devaty, and W. J. Choyke. "Absorption coefficient of 4H silicon carbide from 3900 to 3250 Å". In: *Journal of Applied Physics* 84 (1998), pp. 2963–2964. DOI: 10.1063/1.368403.

[93] Claude A. Klein. "Bandgap Dependence and Related Features of Radiation Ionization Energies in Semiconductors". In: *Journal of Applied Physics* 39 (1968), pp. 2029–2038. DOI: 10.1063/1.1656484.

[94] William Shockley. "Problems related to p-n junctions in silicon". In: *Solid-State Electronics* 2 (1961), pp. 35–67. DOI: https://doi.org/10.1016/0038-1101(61)90054-5.

[95] G. Lioliou and A.M. Barnett. "Electron-hole pair creation and conversion efficiency in radioisotope microbatteries". In: *Applied Radiation and Isotopes* 180 (2022), p. 110042. DOI: https://doi.org/10.1016/j.apradiso.2021.110042.

[96] International Commission on Radiation Units and Measurements. *Average energy required to produce an ion pair. ICRU report 31*. 1979.

[97] Armin Lühr, Cläre von Neubeck, Mechthild Krause, and Esther G.C. Troost. "Relative biological effectiveness in proton beam therapy - Current knowledge and future challenges". In: *Clinical and Translational Radiation Oncology* 9 (2018), pp. 35–41. DOI: 10.1016/j.ctro.2018.01.006.

[98] Andrea Peeters et al. "How costly is particle therapy? Cost analysis of external beam radiotherapy with carbon-ions, protons and photons". In: *Radiotherapy and Oncology* 95 (2010), pp. 45–53. DOI: 10.1016/j.radonc.2009.12.002.

[99] Gunnar Lindstroem and Angela Vasilescu. *Displacement Damage in Silicon*. 2000. URL: https://rd50.web.cern.ch/NIEL/default.html.

[100] M. Huhtinen. "Simulation of non-ionising energy loss and defect formation in silicon". In: *Nuclear Instruments and Methods in Physics Research Section A: Accelerators, Spectrometers, Detectors and Associated Equipment* 491 (2002), pp. 194–215. DOI: https://doi.org/10.1016/S0168-9002(02)01227-5.

[101] Ivana Capan. "Electrically Active Defects in 3C, 4H, and 6H Silicon Carbide Polytypes: A Review". In: *Crystals* 15 (2025). DOI: 10.3390/cryst15030255.

[102] José Coutinho. "Theory of the Thermal Stability of Silicon Vacancies and Interstitials in 4H-SiC". In: *Crystals* 11 (2021). DOI: 10.3390/cryst11020167.

[103] F. Nava, A. Castaldini, A. Cavallini, P. Errani, and V. Cindro. "Radiation Detection Properties of 4H-SiC Schottky Diodes Irradiated Up to 10^{16} n/cm^2 by 1 MeV Neutrons". In: *IEEE Transactions on Nuclear Science* 53 (2006). Publisher: Institute of Electrical and Electronics Engineers (IEEE), pp. 2977–2982. DOI: 10.1109/tns.2006.882777.

[104] Frank H. Ruddy, Sandeep K. Chaudhuri, and Krishna C. Mandal. "A Review of the Effects of Fast-Neutron Irradiation on the Performance of 4H-SiC Schottky Barrier Detectors". In: *IEEE Transactions on Nuclear Science* (2024), pp. 1–1. DOI: 10.1109/TNS.2024.3355293.

[105] Simon Waid et al. "Detector development for particle physics". In: *e+i Elektrotechnik und Informationstechnik* (2024). DOI: 10.1007/s00502-023-01201-w.

[106] D. Pitzl et al. "Type inversion in silicon detectors". In: *Nuclear Instruments and Methods in Physics Research Section A: Accelerators, Spectrometers, Detectors and Associated Equipment* 311 (1992), pp. 98–104. DOI: https://doi.org/10.1016/0168-9002(92)90854-W.

[107] Aamenah Siddiqui, Anders Hallén, Arshad Hussain, and Muhammad Usman. "Carrier removal rates in 4H-SiC power diodes - A predictive analytical model". In: *Materials Science in Semiconductor Processing* 167 (2023), p. 107771. DOI: https://doi.org/10.1016/j.mssp.2023.107771.

[108] Alfio Samuele Mancuso et al. "Defects Induced by High-Temperature Neutron Irradiation in 250 µm-Thick 4H-SiC p-n Junction Detector". In: *Materials* 18 (2025), p. 2413. DOI: 10.3390/ma18112413.

[109] Pavel Hazdra and Jan Vobecký. "Radiation Defects Created in *n* -Type 4H-SiC by Electron Irradiation in the Energy Range of 1-10 MeV". In: *physica status solidi (a)* 216 (2019), p. 1900312. DOI: 10.1002/pssa.201900312.

[110] Karl Hecht. "Zum Mechanismus des lichtelektrischen Primärstromes in isolierenden Kristallen". In: *Zeitschrift für Physik* 77 (1932), pp. 235–245. DOI: 10.1007/bf01338917.

[111] Gian-Franco Dalla Betta and Marco Povoli. "Progress in 3D Silicon Radiation Detectors". In: *Frontiers in Physics* 10 (2022). DOI: 10.3389/fphy.2022.927690.

[112] G. Lucas and L. Pizzagalli. "Comparison of threshold displacement energies in β-SiC determined by classical potentials and ab initio calculations". In: *Nuclear Instruments and Methods in Physics Research Section B: Beam Interactions with Materials and Atoms* 229 (2005), pp. 359–366. DOI: https://doi.org/10.1016/j.nimb.2004.12.119.

[113] V. V. Kozlovski, A. E. Vasil'ev, and A. A. Lebedev. "Role of Low-Temperature Annealing in Modifying Silicon Carbide by Beams of Charged Particles". In: *Journal of Surface Investigation: X-ray, Synchrotron and Neutron Techniques* 15 (2021), pp. 341–344. DOI: 10.1134/s1027451021020257.

[114] Mitsuhiro Kushibe et al. "Carrier Lifetimes in 4H-SiC Epitaxial Layers on the C-Face Enhanced by Carbon Implantation". In: *Silicon Carbide and Related Materials 2017*. Vol. 924. Materials Science Forum. Trans Tech Publications Ltd, 2018, pp. 432–435. DOI: 10.4028/www.scientific.net/MSF.924.432.

[115] L. Storasta and Hidekazu Tsuchida. "Reduction of Traps and Improvement of Carrier Lifetime in SiC Epilayer by Ion Implantation". In: *Silicon Carbide and Related Materials 2006*. Vol. 556. Materials Science Forum. Trans Tech Publications Ltd, 2007, pp. 603–606. DOI: 10.4028/www.scientific.net/MSF.556-557.603.

[116] Joan Marc Rafí et al. "Low Temperature Annealing of Electron, Neutron and Proton Irradiation Effects on SiC Radiation Detectors". In: *IEEE Transactions on Nuclear Science* (2023), pp. 1–1. DOI: 10.1109/TNS.2023.3307932.

[117] Ekrem Almaz, Stephen Stone, Thomas E. Blue, and Joseph P. Heremans. "The effects of neutron irradiation and low temperature annealing on the electrical properties of highly doped 4H silicon carbide". In: *Nuclear Instruments and Methods in Physics Research Section A: Accelerators, Spectrometers, Detectors and Associated Equipment* 622 (2010), pp. 200–206. DOI: 10.1016/j.nima.2010.06.211.

[118] Vitalii V. Kozlovski, Oleg Korolkov, Alexander A. Lebedev, Jana Toompuu, and Natalja Sleptsuk. "Comparative Results of Low Temperature Annealing of Lightly Doped N-Layers of Silicon Carbide Irradiated by Protons and Electrons". In: *Silicon Carbide and Related Materials 2019*. Vol. 1004. Materials Science Forum. Trans Tech Publications Ltd, 2020, pp. 231–236. DOI: 10.4028/www.scientific.net/MSF.1004.231.

[119] S. Ramo. "Currents Induced by Electron Motion". In: *Proceedings of the IRE* 27 (1939), pp. 584–585. DOI: 10.1109/jrproc.1939.228757.

[120] W. Shockley. "Currents to Conductors Induced by a Moving Point Charge". In: *Journal of Applied Physics* 9 (1938), pp. 635–636. DOI: 10.1063/1.1710367.

[121] W. Riegler and G. Aglieri Rinella. "Time resolution of silicon pixel sensors". In: *Journal of Instrumentation* 12 (2017), P11017. DOI: 10.1088/1748-0221/12/11/P11017.

[122] Sebastian Pape, Esteban Currás, Marcos Fernández García, and Michael Moll. "Techniques for the Investigation of Segmented Sensors Using the Two Photon Absorption-Transient Current Technique". In: *Sensors* 23 (2023), p. 962. DOI: 10.3390/s23020962.

[123] E. Currás, M. Fernández, and M. Moll. "Gain reduction mechanism observed in Low Gain Avalanche Diodes". In: *Nuclear Instruments and Methods in Physics Research Section A: Accelerators, Spectrometers, Detectors and Associated Equipment* 1031 (2022), p. 166530. DOI: https://doi.org/10.1016/j.nima.2022.166530.

[124] M. De Napoli, F. Giacoppo, G. Raciti, and E. Rapisarda. "Study of charge collection efficiency in 4H-SiC Schottky diodes with 12C ions". In: *Nuclear Instruments and Methods in Physics Research Section A: Accelerators, Spectrometers, Detectors and Associated Equipment* 608 (2009), pp. 80–85. DOI: https://doi.org/10.1016/j.nima.2009.06.018.

[125] Felix Ulrich-Pur et al. "First experimental time-of-flight-based proton radiography using low gain avalanche diodes". In: *Physics in Medicine&Biology* 69 (2024), p. 075031. DOI: 10.1088/1361-6560/ad3326.

[126] Marco Ferrero, Roberta Arcidiacono, Marco Mandurrino, Valentina Sola, and Nicolo Cartiglia. *Ultra-fast silicon detectors: design, tests, and performances*. en. Ed. by Marco Ferrero. First edition. Series in sensors. Boca Raton: CRC Press, 2021. DOI: 10.1201/9781003131946.

[127] M. Ferrero et al. *Timing resolution of thin LGAD sensors for high radiation environments*. https://indico.cern.ch/event/1455346/contributions/6323206/. 20th Anniversary "Trento" Workshop on Advanced Silicon Radiation Detectors (TREDI 2025). 2025.

[128] Claudio Piemonte et al. "Performance of NUV-HD Silicon Photomultiplier Technology". In: *IEEE Transactions on Electron Devices* 63 (2016), pp. 1111–1116. DOI: 10.1109/TED.2016.2516641.

[129] Marion Missio and on behalf of the ATLAS HGTD collaboration. "Overview of the ATLAS High-Granularity Timing Detector: project status and results". In: *Journal of Instrumentation* 19 (2024), p. C04008. DOI: 10.1088/1748-0221/19/04/C04008.

[130] H. F. -W. Sadrozinski et al. "Sensors for ultra-fast silicon detectors". In: *Nucl. Instrum. Meth. A* 765 (2014). Ed. by Yoshinobu Unno, Yasushi Fukazawa, Suen Hou, Takashi Ohsugi, and Hartmut F. -W. Sadrozinski, pp. 7–11. DOI: 10.1016/j.nima.2014.05.006.

[131] Nicolo Cartiglia. *Weightfield2*. https://www.to.infn.it/~cartigli/Weightfield2/index.html. 2025.

[132] Jairo Villegas, Neil Moffat, Giulio Pellegrini, and Salvador Hidalgo. "nLGAD Detectors for Low Penetrating Particles: Concept and First Results". In: *2023 14th Spanish Conference on Electron Devices (CDE)*. 2023, pp. 1–4. DOI: 10.1109/CDE58627.2023.10339519.

[133] K. Okabe et al. “Performance review of the prototype SiC muon beam monitor for COMET experiment”. In: *Nuclear Instruments and Methods in Physics Research Section A: Accelerators, Spectrometers, Detectors and Associated Equipment* 1080 (2025), p. 170798. DOI: https://doi.org/10.1016/j.nima.2025.170798.

[134] V Lauer et al. “Electrical and optical characterisation of vanadium in 4H and 6H-SiC”. In: *Materials Science and Engineering: B* (1999), pp. 248–252. DOI: https://doi.org/10.1016/S0921-5107(98)00512-1.

[135] Kazutoshi Kojima, Shin-ichiro Sato, Takeshi Ohshima, and Shin-Ichiro Kuroki. “Growth of vanadium doped semi-insulating 4H-SiC epilayer with ultrahigh-resistivity”. In: *Journal of Applied Physics* 131 (2022), p. 245107. DOI: 10.1063/5.0095457.

[136] Ivana Capan. “4H-SiC Schottky Barrier Diodes as Radiation Detectors: A Review”. In: *Electronics* 11 (2022). DOI: 10.3390/electronics11040532.

[137] Krishna C. Mandal, Sandeep K. Chaudhuri, and Frank H. Ruddy. “High-Resolution Alpha Spectrometry Using 4H-SiC Detectors: A Review of the State-of-the-Art”. In: *IEEE Transactions on Nuclear Science* 70 (2023), pp. 823–830. DOI: 10.1109/TNS.2023.3267996.

[138] J.M. Rafí et al. “Four-quadrant silicon and silicon carbide photodiodes for beam position monitor applications: electrical characterization and electron irradiation effects”. In: *Journal of Instrumentation* 13 (2018), pp. C01045–C01045. DOI: 10.1088/1748-0221/13/01/C01045.

[139] T. Slavicek, S. Petersson, S. Pospisil, G. Thungstrom, and M. Slavickova. “SiC based charged particle strip sensor spectrometer with neutron detection capability”. In: *Journal of Instrumentation* 15 (2020), p. C01036. DOI: 10.1088/1748-0221/15/01/C01036.

[140] Tetsuichi Kishishita et al. “Hybrid SiC Pixel Detector for Charged-Particle Beam Monitor”. In: *IEEE Transactions on Nuclear Science* 70 (2023), pp. 1210–1214. DOI: 10.1109/TNS.2023.3265318.

[141] Tao Yang et al. “Ultra-Fast 4H-SiC LGAD With Etched Termination and Field Plate”. In: *IEEE Electron Device Letters* 46 (2025), pp. 845–847. DOI: 10.1109/LED.2025.3548509.

[142] Joost Romijn et al. “Integrated 64 pixel UV image sensor and readout in a silicon carbide CMOS technology”. In: *Microsystems&Nanoengineering* 8 (2022). DOI: 10.1038/s41378-022-00446-3.

[143] Alexander May et al. “A 4H-SiC CMOS Technology enabling Smart Sensor Integration and Circuit Operation above 500 °C”. In: *2024 Smart Systems Integration Conference and Exhibition (SSI)*. 2024, pp. 1–5. DOI: 10.1109/SSI63222.2024.10740550.

[144] J.S. Weiner et al. “SiGe differential transimpedance amplifier with 50-GHz bandwidth”. In: *IEEE Journal of Solid-State Circuits* 38 (2003), pp. 1512–1517. DOI: 10.1109/JSSC.2003.815969.

[145] Simon Waid. *Silicon carbide diode on UCSC LGAD board*. https://www.oeaw.ac.at/en/hephy/research/detector-development. 2025.

[146] Lavakumar Navilipuri. *Design and Layout of a Transimpedance Amplifier (tia) at 50 GHz for Optical Receivers in ihp 130nm SiGe BiCMOS Technology*. en. 2022. DOI: 10.24406/PUBLICA-738.

[147] K C Gupta, Ramesh Garg, and Rakesh Chadha. *Computer-aided design of microwave circuits*. Norwood, MA: Artech House, 1981.

[148] Inyong Kwon, Taehoon Kang, Byron T. Wells, Lawrence J. D’Aries, and Mark D. Hammig. “A High-Gain 1.75-GHz Dual-Inductor Transimpedance Amplifier With Gate Noise Suppression for Fast Radiation Detection”. In: *IEEE Transactions on Circuits and Systems II: Express Briefs* 63 (2016), pp. 356–360. DOI: 10.1109/TCSII.2015.2503583.

[149] Andreas Gsponer. *sma100b-transfer-function*. https://gitlab.com/dd-hephy/HiBPM/sma100b-transfer-function. 2025.

[150] Rohde&Schwarz. *R&S RTP HIGH-PERFORMANCE OSCILLOSCOPE Specifications*. https://www.rohde-schwarz.com/au/products/test-and-measurement/oscilloscopes/rs-rtp-oscilloscope_63493-469056.html. 2025.

[151] Rohde&Schwarz. *R&S SMA100B RF AND MICROWAVE SIGNAL GENERATOR Specifications*. https://www.rohde-schwarz.com/products/test-and-measurement/analog-signal-generators/rs-sma100b-rf-and-microwave-signal-generator_63493-427776.html. 2025.

[152] CIVIDEC Instrumentation. *C2-HV Broadband Amplifier, 2 GHz, 40 dB*. https://cividec.at/index.php?module=public.product&idProduct=34&scr=0. 2025.

[153] M. Ferrero et al. "Compensated LGAD - an innovative design of thin silicon sensors for very high fluences". In: *Journal of Instrumentation* 20 (2025), p. C07023. DOI: 10.1088/1748-0221/20/07/C07023.

[154] Particulars Advanced Measurement Systems. *Amplifiers*. 2025. URL: https://particulars.si/products.php?prod=amplifiers.html.

[155] Mouser Electronics. *TB-PMA3-14LN+*. hhttps://mou.sr/4e6p82Y. 2025.

[156] Mini-Circuits. *ZX60-14LN-S+*. https://www.minicircuits.com/WebStore/dashboard.html?model=ZX60-14LN-S%2B. 2025.

[157] C. Allaire et al. "Beam test measurements of Low Gain Avalanche Detector single pads and arrays for the ATLAS High Granularity Timing Detector". In: *Journal of Instrumentation* 13 (2018), P06017. DOI: 10.1088/1748-0221/13/06/P06017.

[158] Matias Senger. *Chubut board*. https://github.com/SengerM/ChubutBoard. 2022.

[159] Dennis Sperlich. *Freiburg Timing Board*. 2023. URL: https://gitlab.cern.ch/dsperlic/FreiburgTimingBoard.

[160] Vagelis Gkougkousis. *UcscSingleChannel*. https://twiki.cern.ch/twiki/bin/view/Main/UcscSingleChannel. 2020.

[161] Wilhelm Krüger. *Performance of the LGAD-based in-beam detector at HADES*. Presented at Vertex 2022. 2022. URL: https://indico.cern.ch/event/1140707/contributions/5006224/.

[162] R. Heller et al. "Combined analysis of HPK 3.1 LGADs using a proton beam, beta source, and probe station towards establishing high volume quality control". In: *Nuclear Instruments and Methods in Physics Research Section A: Accelerators, Spectrometers, Detectors and Associated Equipment* 1018 (2021), p. 165828. DOI: https://doi.org/10.1016/j.nima.2021.165828.

[163] Bernhard Arnold. *Diode Measurement: IV/CV measurements for silicon sensors*. 2025. URL: github.com/hephy-dd/diode-measurement.

[164] Keithley Instruments. *Model 2657A-PM-200 Protection Module User's Guide*. 2017. URL: https://download.tek.com/datasheet/PA-1055B_Mar_2017_2657A-PM-200.pdf.

[165] Keithley Instruments. *CVU-3K-KIT 3 kV Bias Tee Kit*. 2014. URL: https://download.tek.com/manual/071321100(Oct2014)(CVU-3K-KIT).pdf.

[166] H. Jungclaussen. "Analyse der impulsform von Silizium-Detektoren". In: *Nuclear Instruments and Methods* 51 (1967), pp. 210–212. DOI: 10.1016/0029-554X(67)90003-1.

[167] H.R. Zulliger, C.B. Norris, T.W. Sigmon, and R.H. Pehl. "Electric field profile and electron drift velocities in lithium drifted silicon". In: *Nuclear Instruments and Methods* 70 (1969), pp. 125–133. DOI: 10.1016/0029-554X(69)90370-X.

[168] V. Eremin, N. Strokan, E. Verbitskaya, and Z. Li. "Development of transient current and charge techniques for the measurement of effective net concentration of ionized charges (Neff) in the space charge region of p-n junction detectors". In: *Nuclear Instruments and Methods in Physics Research Section A: Accelerators, Spectrometers, Detectors and Associated Equipment* 372 (1996), pp. 388–398. DOI: 10.1016/0168-9002(95)01295-8.

[169] Gregor Kramberger. "Signal development in irradiated silicon detectors". PhD thesis. Ljubljana: University of Ljubljana, 2001.

[170] G. Kramberger et al. "Investigation of Irradiated Silicon Detectors by Edge-TCT". In: *IEEE Transactions on Nuclear Science* 57 (2010), pp. 2294–2302. DOI: 10.1109/TNS.2010.2051957.

[171] Moritz Oliver Wiehe. "Development of a two-photon absorption - TCT system and study of radiation damage in silicon detectors". PhD thesis. Freiburg U., Freiburg U., 2021. DOI: 10.6094/UNIFR/223092.

[172] Patrick Kraus. "Measurement of Time-Resolution of Silicon LGADs". Project Thesis. Technische Universität Wien, 2023.

[173] Ivan Paz et al. "Position-resolved charge collection of silicon carbide detectors with an epitaxially-grown graphene layer". In: *Scientific Reports* 14 (2024). DOI: 10.1038/s41598-024-60535-3.

[174] Marcos A. de Araújo, Rubens Silva, Emerson de Lima, Daniel P. Pereira, and Paulo C. de Oliveira. "Measurement of Gaussian laser beam radius using the knife-edge technique: improvement on data analysis". In: *Applied Optics* 48 (2009), p. 393. DOI: 10.1364/AO.48.000393.

[175] L. A. Zenteno, E. Snitzer, H. Po, R. Tumminelli, and F. Hakimi. "Gain switching of a Nd+3-doped fiber laser". In: *Opt. Lett.* 14 (1989), pp. 671–673. DOI: 10.1364/OL.14.000671.

[176] A.L.S. GmbH. *PiLas DX Test Report*. 2021.

[177] Matthias Knopf. "Response of Si, SiC and LGAD semiconductor detector systems to alpha radiation". Master's Thesis. Technische Universität Wien, 2023. DOI: 10.34726/hss.2023.106885.

[178] Eckert & Ziegler Nuclitec GmbH. *Calibration Standards and Instruments. Product Information*. https://cesio.cz/wp-content/uploads/2022/12/EZN_Isotrak.pdf. 2009.

[179] CIVIDEC Instrumentation. *Cx-L Spectroscopic Amplifier*. https://cividec.at/index.php?module=public.product&idProduct=40&scr=0. 2025.

[180] Amptek. *A250CF CoolFET Charge Sensitive Preamplifier*. 2025. URL: https://www.amptek.com/internal-products/obsolete-products/a250cf-coolfet-charge-sensitive-preamplifier.

[181] Wolfram Westmeier. *Practical Notes on Alpha Spectrometry*. Dr. Westmeier GmbH, 2013.

[182] Friedrich Paschen. "Ueber die zum Funkenübergang in Luft, Wasserstoff und Kohlensäure bei verschiedenen Drucken erforderliche Potentialdifferenz". In: *Annalen der Physik* 273 (1889), pp. 69–96. DOI: 10.1002/andp.18892730505.

[183] E. Griesmayer, T. Schreiner, and M. Pavlovič. "The MedAustron project". In: *Nuclear Instruments and Methods in Physics Research Section B: Beam Interactions with Materials and Atoms* 258 (2007). Inelastic Ion-Surface Collisions, pp. 134–138. DOI: https://doi.org/10.1016/j.nimb.2006.12.082.

[184] M. Benedikt and A. Wrulich. "MedAustron-Project overview and status". In: *The European Physical Journal Plus* 126 (2011). DOI: 10.1140/epjp/i2011-11069-9.

[185] Christoph Kurfürst et al. "Status of the MedAustron Beam Commissioning with Protons and Carbon Ions". In: *Proceedings of the 9th Int. Particle Accelerator Conf.* (2018). DOI: 10.18429/JACOW-IPAC2018-TUPAF004.

[186] Marcus Palm. "Performance requirements of the MedAustron beam delivery system". http://hdl.handle.net/20.500.12708/160047. PhD thesis. Technische Universität Wien, 2016.

[187] Antonio G. Amico et al. *Commissioning of pencil beam dose calculation algorithm of RayStation v8BSP1 for the MedAustron scanned carbon ion beam delivery system*. 2022. DOI: 10.13140/RG.2.2.22687.84649.

[188] EBG MedAustron. *IR1 Instructions for Use*. Version 11. 2024.

[189] M.J Berger, J.S Coursey, M.A Zucker, and J. Chang. *ESTAR, PSTAR, and ASTAR: Computer Programs for Calculating Stopping-Power and Range Tables for Electrons, Protons, and Helium Ions (version 1.2.3)*. 2025. URL: http://physics.nist.gov/Star.

[190] M. Christanell, M. Tomaschek, and T. Bergauer. "4H-silicon carbide as particle detector for high-intensity ion beams". In: *Journal of Instrumentation* 17 (2022), p. C01060. DOI: 10.1088/1748-0221/17/01/C01060.

[191] Felix Ulrich-Pur et al. "Commissioning of low particle flux for proton beams at MedAustron". In: *Nuclear Instruments and Methods in Physics Research Section A: Accelerators, Spectrometers, Detectors and Associated Equipment* 1010 (2021), p. 165570. DOI: https://doi.org/10.1016/j.nima.2021.165570.

[192] S. Spannagel et al. "Allpix2: A modular simulation framework for silicon detectors". In: *Nuclear Instruments and Methods in Physics Research Section A: Accelerators, Spectrometers, Detectors and Associated Equipment* 901 (2018), pp. 164–172. DOI: 10.1016/j.nima.2018.06.020.

[193] S. Spannagel and P. Schütze. "Allpix2 - silicon detector Monte Carlo simulations for particle physics and beyond". In: *Journal of Instrumentation* 17 (2022), p. C09024. DOI: 10.1088/1748-0221/17/09/c09024.

[194] D. Dannheim et al. "Combining TCAD and Monte Carlo methods to simulate CMOS pixel sensors with a small collection electrode using the Allpix2 framework". In: *Nuclear Instruments and Methods in Physics Research Section A: Accelerators, Spectrometers, Detectors and Associated Equipment* 964 (2020), p. 163784. DOI: https://doi.org/10.1016/j.nima.2020.163784.

[195] R. Ballabriga et al. "Transient Monte Carlo simulations for the optimisation and characterisation of monolithic silicon sensors". In: *Nuclear Instruments and Methods in Physics Research Section A: Accelerators, Spectrometers, Detectors and Associated Equipment* 1031 (2022), p. 166491. DOI: https://doi.org/10.1016/j.nima.2022.166491.

[196] Jixing Ye, Angelo Loi, Adriano Lai, and Gian-Franco Dalla Betta. "Design and simulation of modified 3D-trench electrode sensors". In: *JINST* 18 (2023), p. C11021. DOI: 10.1088/1748-0221/18/11/C11021.

[197] Andrea Visibile. *Impact ionisation models and LGAD sensors in the context of the High Granularity Timing Detector simulation in ATLAS*. https://indico.cern.ch/event/1346382/contributions/5959182/. 5th Allpix Squared User Workshop. University of Oxford, 2024.

[198] Faiz Ishaqzai. *TCT simulations of synthetic diamonds using Allpix squared*. https://indico.cern.ch/event/1346382/contributions/5938012/. 5th Allpix Squared User Workshop. University of Oxford, 2024.

[199] Pietro Grutta. *Simulation of sapphire micro-strip detectors with Allpix Squared for the LUXE's Gamma Beam Profiler detector*. https://indico.cern.ch/event/1252505/contributions/5361730/. 4th Allpix Squared User Workshop. DESY, Hamburg, Germany, 2023.

[200] Andreas Gsponer. *Time Resolution Simulations of 4H-SiC PiN Detectors*. https://indico.cern.ch/event/1252505/contributions/5344630/. 4th Allpix Squared User Workshop. DESY, Hamburg, Germany, 2023.

[201] J. Allison et al. “Recent developments in Geant4”. In: *Nuclear Instruments and Methods in Physics Research Section A: Accelerators, Spectrometers, Detectors and Associated Equipment* 835 (2016), pp. 186–225. DOI: 10.1016/j.nima.2016.06.125.

[202] J. Allison et al. “Geant4 developments and applications”. In: *IEEE Transactions on Nuclear Science* 53 (2006), pp. 270–278. DOI: 10.1109/tns.2006.869826.

[203] Simon Spannagel. *Allpix Squared - Version 2.0 and Onwards*. https://indico.cern.ch/event/1058977/contributions/4632035/. 10th Beam Telescopes and Test Beams Workshop. Lecce, Italy, 2022.

[204] Esteban Currás, Marcos Fernández, and Michael Moll. “Gain suppression mechanism observed in Low Gain Avalanche Detectors”. In: *Nucl. Instrum. Methods Phys. Res., A* 1031 (2022). 14 pages, 10 figures, p. 166530. DOI: 10.1016/j.nima.2022.166530. arXiv: 2107.10022.

[205] W. Riegler. “An application of extensions of the Ramo-Shockley theorem to signals in silicon sensors”. In: *Nuclear Instruments and Methods in Physics Research Section A: Accelerators, Spectrometers, Detectors and Associated Equipment* 940 (2019), pp. 453–461. DOI: https://doi.org/10.1016/j.nima.2019.06.056.

[206] Larissa Mendes et al. “Transient simulations of MAPS using TCAD, Allpix squared & SPICE”. In: *Nuclear Instruments and Methods in Physics Research Section A: Accelerators, Spectrometers, Detectors and Associated Equipment* 1080 (2025), p. 170749. DOI: https://doi.org/10.1016/j.nima.2025.170749.

[207] Giuseppe Bertuccio, Stefano Caccia, Donatella Puglisi, and Daniele Macera. “Advances in silicon carbide X-ray detectors”. In: *Nuclear Instruments and Methods in Physics Research Section A: Accelerators, Spectrometers, Detectors and Associated Equipment* 652 (2011), pp. 193–196. DOI: 10.1016/j.nima.2010.08.046.

[208] I.B. Smirnov. “Modeling of ionization produced by fast charged particles in gases”. In: *Nuclear Instruments and Methods in Physics Research Section A: Accelerators, Spectrometers, Detectors and Associated Equipment* 554 (2005), pp. 474–493. DOI: https://doi.org/10.1016/j.nima.2005.08.064.

[209] Paul Sommerer. “Validation of the AllPix2 simulation framework for the development of SiC particle detectors”. Master’s Thesis. Technische Universität Wien, 2024. DOI: 10.34726/hss.2024.118301.

[210] W. H. Furry. “On Fluctuation Phenomena in the Passage of High Energy Electrons through Lead”. In: *Phys. Rev.* 52 (6 1937), pp. 569–581. DOI: 10.1103/PhysRev.52.569.

[211] G. Udny Yule. “A Mathematical Theory of Evolution, Based on the Conclusions of Dr. J. C. Willis, F.R.S.” In: *Philosophical Transactions of the Royal Society of London. Series B, Containing Papers of a Biological Character* 213 (1925), pp. 21–87.

[212] *Garfield++*. 2025. URL: https://garfieldpp.docs.cern.ch/.

[213] P.K. Rout et al. “Fast simulation of avalanche and streamer in GEM detector using hydrodynamic approach”. In: *Journal of Instrumentation* 16 (2021), P02018. DOI: 10.1088/1748-0221/16/02/P02018.

[214] Daniel Hynds. *Monte Carlo Simulations - Allpix squared 2*. Advanced UK Instrumentation Training 2024. 2024. URL: https://indico.global/event/1776/contributions/30952/.

[215] Andreas Gsponer. “Measurements and Simulations of High Rate 4H-SiC Particle Detectors”. https://indico.cern.ch/event/1157463/contributions/4922796/. 40th. RD50 Workshop. CERN, Geneva, Switzerland, 2022.

[216] Yuhang Tan et al. “Timing Performance Simulation for 3D 4H-SiC Detector”. In: *Micromachines* 13 (2021), p. 46. DOI: 10.3390/mi13010046.

[217] Edoardo Bossini and Nicola Minafra. “Diamond Detectors for Timing Measurements in High Energy Physics”. In: *Frontiers in Physics* 8 (2020). DOI: 10.3389/fphy.2020.00248.

[218] Werner Riegler. *Time resolution limits in silicon sensors from Landau fluctuations and electronics noise*. 2025. arXiv: 2504.02570 [hep-ex].

[219] Yuanbo Cheng, Johan Karlsson, and Jian Li. “Cramér-Rao Bound for Signal Parameter Estimation From Modulo ADC Generated Data”. In: *IEEE Transactions on Signal Processing* 72 (2024), pp. 4268–4285. DOI: 10.1109/TSP.2024.3453346.

[220] Dong Ji, Burcu Ercan, and Srabanti Chowdhury. “Experimental Determination of Velocity-Field Characteristic of Holes in GaN”. In: *IEEE Electron Device Letters* 41 (2020), pp. 23–25. DOI: 10.1109/LED.2019.2953873.

[221] Evangelos-Leonidas Gkougkousis, Edgar Lemos Cid, and Viktor Coco. “Considerations on time resolution of neutron irradited single pixel 3D structures at fuences up to 1017 neq/cm2 using 120 GeV SPS pion beams”. In: *Nuclear Instruments and Methods in Physics Research Section A: Accelerators, Spectrometers, Detectors and Associated Equipment* 1070 (2025), p. 170012. DOI: https://doi.org/10.1016/j.nima.2024.170012.

[222] Thomas Bergauer. *Silicon Carbide LGAD RD50 common project*. https://indico.cern.ch/event/1132520/contributions/5146528/. 41st RD50 Workshop on Radiation Hard Semiconductor Devices for Very High Luminosity Colliders. Seville, Spain, 2022.

[223] Philippe Raymond M. Godignon, Maria Celeste Fleta Corral, Giulio Pellegrini, and Consuelo Guardiola Salmeron. *Silicon carbide dosimeter for high dose pulsed radiation*. European patent application EP 4379427 A1. 2024. URL: https://data.epo.org/publication-server/rest/v1.2/publication-dates/2024-06-05/patents/EP4379427NWA1/document.pdf.

[224] Joan Marc Rafí et al. “Electron, Neutron, and Proton Irradiation Effects on SiC Radiation Detectors”. In: *IEEE Transactions on Nuclear Science* 67 (2020), pp. 2481–2489. DOI: 10.1109/TNS.2020.3029730.

[225] M.C. Jiménez-Ramos et al. “IBIC analysis of SiC detectors developed for fusion applications”. In: *Radiation Physics and Chemistry* 177 (2020), p. 109100. DOI: https://doi.org/10.1016/j.radphyschem.2020.109100.

[226] Raúl Pérez Rodríguez. “Planar Edge Terminations and Related Manufacturing Process Technology for High Power 4H-SiC Diodes”. http://hdl.handle.net/10803/3370. PhD thesis. Universitat Autònoma de Barcelona, 2005.

[227] Philippe Godignon et al. “SiC Schottky diodes for harsh environment space applications”. In: *IEEE Transactions on Industrial Electronics* 58 (2011), pp. 2582–2590. DOI: 10.1109/TIE.2010.2080252.

[228] Manuel Christanell. “4H-Silicon carbide as real time monitor for high-intensity ion beams”. MA thesis. Technische Unversität Wien, 2021. DOI: 10.34726/HSS.2021.81480.

[229] Maximilian Tomaschek. “Material study on the use of silicon carbide in position-sensitive particle detectors”. MA thesis. Technische Unversität Wien, 2021. DOI: 10.34726/HSS.2021.92532.

[230] Markus Göbel. “Studies on irradiated 4H-SiC diodes as semiconductor particle detectors”. Thesis. Technische Universität Wien, 2022. DOI: 10.34726/hss.2022.103471.

[231] Philipp Gaggl. *Improving TCAD simulation of 4H-SiC particle detectors*. https://indico.cern.ch/event/1270076/contributions/5450202. 42nd RD50 Workshop on Radiation Hard Semiconductor Devices for Very High Luminosity Colliders. Tivat, Montenegro, 2023.

[232] Philips'Gloeilampenfabrieken. "A method of measuring specific resistivity and Hall effect of discs of arbitrary shape". In: *Philips Research Reports* 13 (1958), pp. 1–9.

[233] Keithley Instruments. *Making van der Pauw Resistivity and Hall Voltage Measurements Using the 4200A-SCS Parameter Analyzer*. Application Note. 2025. URL: https://www.tek.com/en/documents/application-note/van-der-pauw-and-hall-voltage-measurements-4200a-scs-parameter-analyzer.

[234] Giulio Pellegrini. *Development of innovative SiC detectors for harsh environments*. https://indico.cern.ch/event/1507215/contributions/6540435/. 3rd DRD3 week on Solid State Detectors R&D. Amsterdam, Netherlands, 2025.

[235] F. Moscatelli et al. "Measurements and TCAD simulations of innovative RSD and DC-RSD LGAD devices for future 4D tracking". In: *Nuclear Instruments and Methods in Physics Research Section A: Accelerators, Spectrometers, Detectors and Associated Equipment* 1064 (2024), p. 169380. DOI: https://doi.org/10.1016/j.nima.2024.169380.

[236] Norbert Gál et al. "High-resolution alpha-particle detector based on Schottky barrier 4H-SiC detector operated at elevated temperatures up to 500C". In: *Applied Surface Science* 635 (2023), p. 157708. DOI: https://doi.org/10.1016/j.apsusc.2023.157708.

[237] Timothy R. Garcia, Ashutosh Kumar, Benjamin Reinke, Thomas E. Blue, and Wolfgang Windl. "Electron-hole pair generation in SiC high-temperature alpha particle detectors". In: *Applied Physics Letters* 103 (2013), p. 152108. DOI: 10.1063/1.4824774.

[238] Sandeep K. Chaudhuri, Kelvin J. Zavalla, and Krishna C. Mandal. "Experimental determination of electron-hole pair creation energy in 4H-SiC epitaxial layer: An absolute calibration approach". In: *Applied Physics Letters* 102 (2013), p. 031109. DOI: 10.1063/1.4776703.

[239] M. V. S. Chandrashekhar, Christopher I. Thomas, and Michael G. Spencer. "Measurement of the mean electron-hole pair ionization energy in 4H SiC". In: *Applied Physics Letters* 89 (2006), p. 042113. DOI: 10.1063/1.2243799.

[240] Alessandro Lo Giudice, Franco Fizzotti, Claudio Manfredotti, Ettore Vittone, and Filippo Nava. "Average energy dissipated by mega-electron-volt hydrogen and helium ions per electron-hole pair generation in 4H-SiC". In: *Applied Physics Letters* 87 (2005), p. 222105. DOI: 10.1063/1.2135507.

[241] B.F. Phlips et al. "Silicon carbide pin diodes as radiation detectors". In: *IEEE Nuclear Science Symposium Conference Record, 2005*. Vol. 3. 2005, pp. 1236–1239. DOI: 10.1109/NSSMIC.2005.1596542.

[242] A.A. Lebedev, A.M. Ivanov, and N.B. Strokan. "Radiation resistance of SiC and nuclear-radiation detectors based on SiC films". In: *Semiconductors* 38 (2004), pp. 125–147.

[243] A.M. Ivanov et al. "High-resolution short range ion detectors based on 4H-SiC films". In: *Technical Physics Letters* 30 (7 2004), pp. 575–577. DOI: 10.1134/1.1783406.

[244] G. Bertuccio and R. Casiraghi. "Study of silicon carbide for X-ray detection and spectroscopy". In: *IEEE Transactions on Nuclear Science* 50 (2003), pp. 175–185. DOI: 10.1109/TNS.2003.807855.

[245] J.-L Agram et al. "The silicon sensors for the Compact Muon Solenoid tracker—design and qualification procedure". In: *Nuclear Instruments and Methods in Physics Research Section A: Accelerators, Spectrometers, Detectors and Associated Equipment* 517 (2004), pp. 77–93. DOI: 10.1016/j.nima.2003.08.175.

[246] S Jan et al. "GATE: a simulation toolkit for PET and SPECT". In: *Physics in Medicine and Biology* 49 (2004), pp. 4543–4561. DOI: 10.1088/0031-9155/49/19/007.

[247] M.N. Mazziotta. "Electron-hole pair creation energy and Fano factor temperature dependence in silicon". In: *Nuclear Instruments and Methods in Physics Research Section A: Accelerators, Spectrometers, Detectors and Associated Equipment* 584 (2008), pp. 436–439. DOI: https://doi.org/10.1016/j.nima.2007.10.043.

[248] Giuseppe Bertuccio, Stefano Caccia, Donatella Puglisi, and Daniele Macera. "Advances in silicon carbide X-ray detectors". In: *Nuclear Instruments and Methods in Physics Research Section A: Accelerators, Spectrometers, Detectors and Associated Equipment* 652 (2011). Symposium on Radiation Measurements and Applications (SORMA) XII 2010, pp. 193–196. DOI: 10.1016/j.nima.2010.08.046.

[249] Eduardo García-Toraño. "Current status of alpha-particle spectrometry". In: *Applied Radiation and Isotopes* 64 (2006). Proceedings of the 15th International Conference on Radionuclide Metrology and its Applications, pp. 1273–1280. DOI: https://doi.org/10.1016/j.apradiso.2006.02.034.

[250] Murray A. Lampert and Ronald B. Schilling. "Chapter 1 Current Injection in Solids: The Regional Approximation Method". In: *Semiconductors and Semimetals*. Vol. 6. 1970, pp. 1–96. DOI: 10.1016/S0080-8784(08)62630-7.

[251] Z Li, C. J Li, V Eremin, and E Verbitskaya. "Direct observation and measurements of neutron-induced deep levels responsible for Neff changes in high-resistivity silicon detectors using TCT". In: *Nuclear Instruments and Methods in Physics Research Section A: Accelerators, Spectrometers, Detectors and Associated Equipment*. Radiation Effects on Semiconductor Materials, Detectors and Devices 388 (1997), pp. 297–307. DOI: 10.1016/S0168-9002(96)01252-1.

[252] Christian Dorfer et al. "Mapping the impact of defect distributions in silicon carbide devices using the edge transient-current technique". In: *Applied Physics Letters* 122 (2023), p. 183503. DOI: 10.1063/5.0142217.

[253] Marcos Fernández García et al. "High resolution 3D characterization of silicon detectors using a Two Photon Absorption Transient Current Technique". In: *Nuclear Instruments and Methods in Physics Research Section A: Accelerators, Spectrometers, Detectors and Associated Equipment* 958 (2020). Proceedings of the Vienna Conference on Instrumentation 2019, p. 162865. DOI: https://doi.org/10.1016/j.nima.2019.162865.

[254] P. Gaggl et al. "Charge collection efficiency study on neutron-irradiated planar silicon carbide diodes via UV-TCT". In: *Nuclear Instruments and Methods in Physics Research Section A: Accelerators, Spectrometers, Detectors and Associated Equipment* 1040 (2022), p. 167218. DOI: 10.1016/j.nima.2022.167218.

[255] P. Praus et al. "Charge transport in semi insulating bulk 4H-Silicon carbide: Effect of metallization and wafer homogeneity". In: *Results in Physics* 43 (2022), p. 106110. DOI: https://doi.org/10.1016/j.rinp.2022.106110.

[256] Iván Vila. "Radiation tolerance study of neutron-irradiated sic pn planar diodes". In: *18th Trento Workshop on Advanced Silicon Radiation Detectors, Trento*. 2023.

[257] Andreas Gsponer, Philipp Gaggl, Jürgen Burin, Simon Waid, and Thomas Bergauer. "Observation of Charge Enhancement in forward-biased neutron-irradiated 4H-SiC PiN Detectors in UV-TCT Measurements". In: *Proceedings of Technology & Instrumentation in Particle Physics - PoS(TIPP2023)*. Technology & Instrumentation in Particle Physics. Cape Town, Western Cape, South Africa: Sissa Medialab, 2025, p. 103. DOI: 10.22323/1.468.0103.

[258] G. Kramberger et al. "Investigation of Irradiated Silicon Detectors by Edge-TCT". In: *IEEE Transactions on Nuclear Science* 57 (2010), pp. 2294–2302. DOI: 10.1109/TNS.2010.2051957.

[259] Finn Feindt. "Edge-TCT for the Investigation of Radiation Damaged Silicon Strip Sensors". Universität Hamburg, Masterarbeit, 2016. MS. Hamburg: Universität Hamburg, 2017, p. 95. DOI: 10.3204/PUBDB-2017-00850.

[260] C. Canali, G. Ottaviani, and A. Alberigi Quaranta. "Drift velocity of electrons and holes and associated anisotropic effects in silicon". In: *Journal of Physics and Chemistry of Solids* 32 (1971), pp. 1707–1720. DOI: 10.1016/S0022-3697(71)80137-3.

[261] C. Gallrapp et al. "Study of gain homogeneity and radiation effects of Low Gain Avalanche Pad Detectors". In: *Nuclear Instruments and Methods in Physics Research Section A: Accelerators, Spectrometers, Detectors and Associated Equipment* 875 (2017), pp. 27–34. DOI: https://doi.org/10.1016/j.nima.2017.07.038.

[262] Julian Becker, Eckhart Fretwurst, and Robert Klanner. "Measurements of charge carrier mobilities and drift velocity saturation in bulk silicon of <111> and <100> crystal orientation at high electric fields". In: *Solid-State Electronics* 56 (2011), pp. 104–110. DOI: https://doi.org/10.1016/j.sse.2010.10.009.

[263] M. MARTINI, J.W. MAYER, and K.R. ZANIO. "Drift Velocity and Trapping in Semiconductors-Transient Charge Technique". In: *Applied Solid State Science*. Ed. by Raymond Wolfe. Vol. 3. Applied Solid State Science. Elsevier, 1972, pp. 181–261. DOI: https://doi.org/10.1016/B978-0-12-002903-7.50010-2.

[264] *SINGULAR LASER FACILITY LABORATORY OF THE UPV/EHU*. 2025. URL: https://www.ehu.eus/en/web/sgiker/laser-tresna-aurkezpena.

[265] Ashish Bisht et al. "Characterization of novel trench-isolated LGADs for 4D tracking". In: *Nuclear Instruments and Methods in Physics Research Section A: Accelerators, Spectrometers, Detectors and Associated Equipment* 1048 (2023), p. 167929. DOI: https://doi.org/10.1016/j.nima.2022.167929.

[266] P. Gaggl et al. "Performance of neutron-irradiated 4H-silicon carbide diodes subjected to alpha radiation". In: *Journal of Instrumentation* 18 (2023). Publisher: IOP Publishing, p. C01042. DOI: 10.1088/1748-0221/18/01/C01042.

[267] Philipp Gaggl et al. "TCAD modeling of radiation-induced defects in 4H-SiC diodes". In: *Nuclear Instruments and Methods in Physics Research Section A: Accelerators, Spectrometers, Detectors and Associated Equipment* 1070 (2025), p. 170015. DOI: 10.1016/j.nima.2024.170015.

[268] Jürgen Burin et al. "TCAD Simulations of Radiation Damage in 4H-SiC". In: *2024 Austrochip Workshop on Microelectronics (Austrochip)*. 2024 Austrochip Workshop on Microelectronics (Austrochip). Vienna, Austria: IEEE, 2024, pp. 1–4. DOI: 10.1109/Austrochip62761.2024.10716221.

[269] Igor Mandić. *Irradiation to extreme neutron fluences*. https://indico.cern.ch/event/1370378/contributions/5984977/. EURO-LABS 3rd Annual Meeting. CERN, 2024.

[270] KM Bartholomew et al. *History, Development and Future of TRIGA Research Reactors*. Technical Reports Series. Vienna: INTERNATIONAL ATOMIC ENERGY AGENCY, 2016.

[271] Dejan Žontar. "Study of radiation damage in silicon detectors for high luminosity experiments at LHC". PhD thesis. Ljubljana U., 1998.

[272] Peter Salajka. "Irradiation of silicon detectors for HEP experiments in the Triga Mark II reactor of ATI". Diploma Thesis. Technische Universität Wien, 2021. DOI: 10.34726/hss.2021.92420.

[273] Marcella Cagnazzo. "Neutronic modelling of the new TRIGA core and experimental validation". Thesis. Technische Universität Wien, 2018. DOI: 10.34726/hss.2018.35408.

[274] Sven Mägdefessel, Riccardo Mori, Niels Sorgenfrei, and Ulrich Parzefall. *Understanding the Frequency Dependence of Capacitance Measurements of Irradiated Silicon Detectors*. 2023. arXiv: 2301.09371 [physics.ins-det].

[275] Ettore Vittone, Paolo Olivero, Milko Jakšic, and Željko Pastuović. "4H-SiC Schottky diode radiation hardness assessment by IBIC microscopy". In: *Nuclear Instruments and Methods in Physics Research Section B: Beam Interactions with Materials and Atoms* 537 (2023), pp. 14–22. DOI: https://doi.org/10.1016/j.nimb.2023.01.009.

[276] S. Sciortino et al. "Effect of heavy proton and neutron irradiations on epitaxial 4H-SiC Schottky diodes". In: *Nuclear Instruments and Methods in Physics Research Section A: Accelerators, Spectrometers, Detectors and Associated Equipment* 552 (2005). Proceedings of the 5th International Conference on Radiation Effects on Semiconductor Materials, Detectors and Devices, pp. 138–145. DOI: https://doi.org/10.1016/j.nima.2005.06.017.

[277] Carmen Torres Muñoz. *Characterization by IBIC of neutron irradiated SiC detectors at CNA*. https://indico.cern.ch/event/1439336/contributions/6242448/. 3rd DRD3 week on Solid State Detectors R&D. Amsterdam, Netherlands, 2025.

[278] Pavel Hazdra and Stanislav Popelka. "Displacement damage and total ionisation dose effects on 4H-SiC power devices". In: *IET Power Electronics* 12 (2019), pp. 3910–3918. DOI: https://doi.org/10.1049/iet-pel.2019.0049.

[279] Ivan Vila Alvarez. *Observation of signal multiplication in neutron irradiated SiC detectors characterized using TPA-TCT*. https://indico.cern.ch/event/1439336/contributions/6242449/. 3rd DRD3 week on Solid State Detectors R&D. Amsterdam, Netherlands, 2025.

[280] I. Mandić et al. "Measurements with silicon detectors at extreme neutron fluences1". In: *Journal of Instrumentation* 15 (2020), P11018. DOI: 10.1088/1748-0221/15/11/P11018.

[281] A. Lampis et al. "Could we efficiently operate 3D silicon pixel-based tracking detectors irradiated with neutron fluences up to $1 \cdot 10^{18}$ n_{eq}/cm^2?" In: *Nuclear Instruments and Methods in Physics Research Section A: Accelerators, Spectrometers, Detectors and Associated Equipment* 1080 (2025), p. 170761. DOI: https://doi.org/10.1016/j.nima.2025.170761.

[282] Svante Arrhenius. "Über die Reaktionsgeschwindigkeit bei der Inversion von Rohrzucker durch Säuren". In: *Zeitschrift für Physikalische Chemie* 4 (1889), pp. 226–248. DOI: doi:10.1515/zpch-1889-0416.

[283] Koutarou Kawahara, Hiroshi Watanabe, Naruhisa Miura, Shuhei Nakata, and Satoshi Yamakawa. "Shallow and Deep Levels in Al-Implanted p-Type 4H-SiC Measured by Thermal Admittance Spectroscopy". In: *Materials Science Forum* (2015), pp. 403–406. DOI: 10.4028/www.scientific.net/msf.821-823.403.

[284] Atsushi Koizumi, Jun Suda, and Tsunenobu Kimoto. "Temperature and doping dependencies of electrical properties in Al-doped 4H-SiC epitaxial layers". In: *Journal of Applied Physics* 106 (2009), p. 013716. DOI: 10.1063/1.3158565.

[285] Hideharu Matsuura et al. "Dependence of acceptor levels and hole mobility on acceptor density and temperature in Al-doped p-type 4H-SiC epilayers". In: *Journal of Applied Physics* 96 (2004), pp. 2708–2715. DOI: 10.1063/1.1775298.

[286] Liutauras Storasta, Hidekazu Tsuchida, Tetsuya Miyazawa, and Takeshi Ohshima. "Enhanced annealing of the Z12 defect in 4H-SiC epilayers". In: *Journal of Applied Physics* 103 (2008). DOI: 10.1063/1.2829776.

[287] Antonio Castaldini, Anna Cavallini, Lorenzo Rigutti, and Filippo Nava. "Low temperature annealing of electron irradiation induced defects in 4H-SiC". In: *Applied Physics Letters* 85 (2004), pp. 3780–3782. DOI: 10.1063/1.1810627.

[288] Simon Waid et al. “From single particles to clinical beam rates: A wide dynamic range beam monitor”. In: *Nuclear Instruments and Methods in Physics Research Section A: Accelerators, Spectrometers, Detectors and Associated Equipment* 1080 (2025), p. 170674. DOI: https://doi.org/10.1016/j.nima.2025.170674.

[289] Selamnesh Nida et al. “Silicon carbide X-ray beam position monitors for synchrotron applications”. In: *Journal of Synchrotron Radiation* 26 (2019), pp. 28–35. DOI: 10.1107/S1600577518014248.

[290] Giuliana Milluzzo et al. “Comprehensive dosimetric characterization of novel silicon carbide detectors with UHDR electron beams for FLASH radiotherapy”. In: *Medical Physics* 51 (2024), pp. 6390–6401. DOI: https://doi.org/10.1002/mp.17172.

[291] C. Okpuwe et al. “Silicon carbide detectors for dosimetry and monitoring of ultra-high dose rate beams”. In: *Journal of Instrumentation* 19 (2024), p. C03064. DOI: 10.1088/1748-0221/19/03/C03064.

[292] *Hi-Precision Beam Position and Intensity Monitor for Accurate Cancer Treatment with Ions*. 2021. URL: https://projekte.ffg.at/projekt/3968838.

[293] F Osmic et al. “Overview of the Beam diagnostics in the Medaustron Accelerator:Design choices and test Beam commissioning”. In: *Conf. Proc.* (2012), MOPPR002.

[294] Andrea De Franco et al. “Slow Extraction Optimization at the MedAustron Ion Therapy Center: Implementation of Front End Acceleration and RF Knock Out”. In: *9th International Particle Accelerator Conference*. 2018. DOI: 10.18429/JACoW-IPAC2018-MOPML025.

[295] Andrea De Franco et al. “Upgrade Study of the MedAustron Ion Beam Center”. In: *8th International Particle Accelerator Conference*. 2017. DOI: 10.18429/JACoW-IPAC2017-THPVA074.

[296] Pauline Gut, Miriam Krieger, Tony Lomax, Damien C. Weber, and Jan Hrbacek. “Combining rescanning and gating for a time-efficient treatment of mobile tumors using pencil beam scanning proton therapy”. In: *Radiotherapy and Oncology* 160 (2021), pp. 82–89. DOI: 10.1016/j.radonc.2021.03.041.

[297] Marie-Catherine Vozenin et al. “The Advantage of FLASH Radiotherapy Confirmed in Mini-pig and Cat-cancer Patients”. In: *Clinical Cancer Research* 25 (2019), pp. 35–42. DOI: 10.1158/1078-0432.CCR-17-3375.

[298] Vincent Favaudon et al. “Ultrahigh dose-rate FLASH irradiation increases the differential response between normal and tumor tissue in mice”. In: *Science Translational Medicine* 6 (2014), 245ra93–245ra93. DOI: 10.1126/scitranslmed.3008973.

[299] Simon Jolly, Hywel Owen, Marco Schippers, and Carsten Welsch. “Technical challenges for FLASH proton therapy”. In: *Physica Medica* 78 (2020), pp. 71–82. DOI: https://doi.org/10.1016/j.ejmp.2020.08.005.

[300] Koji Tsuboi, Takeji Sakae, and Ariungerel Gerelchuluun. *Proton Beam Radiotherapy: Physics and Biology*. Springer Singapore, 2020. DOI: 10.1007/978-981-13-7454-8.

[301] Andreas Schüller et al. “The European Joint Research Project UHDpulse - Metrology for advanced radiotherapy using particle beams with ultra-high pulse dose rates”. In: *Physica Medica* 80 (2020), pp. 134–150. DOI: https://doi.org/10.1016/j.ejmp.2020.09.020.

[302] D. L. DEWEY and J. W. BOAG. “Modification of the Oxygen Effect when Bacteria are given Large Pulses of Radiation”. In: *Nature* 183 (1959), pp. 1450–1451. DOI: 10.1038/1831450a0.

[303] C. D. TOWN. “Effect of High Dose Rates on Survival of Mammalian Cells”. In: *Nature* 215 (1967), pp. 847–848. DOI: 10.1038/215847a0.

[304] Binwei Lin et al. “FLASH Radiotherapy: History and Future”. In: *Frontiers in Oncology* 11 (2021). DOI: 10.3389/fonc.2021.644400.

[305] Giulia Rosini, Esther Ciarrocchi, and Beatrice D'Orsi. "Mechanisms of the FLASH effect: current insights and advances". In: *Frontiers in Cell and Developmental Biology* (2025). DOI: 10.3389/fcell.2025.1575678.

[306] H. Weiss, E.R. Epp, J.M. Heslin, C.C. Ling, and A. Santomasso. "Oxygen Depletion in Cells Irradiated at Ultra-high Dose-rates and at Conventional Dose-rates". In: *International Journal of Radiation Biology and Related Studies in Physics, Chemistry and Medicine* 26 (1974), pp. 17–29. DOI: 10.1080/09553007414550901.

[307] H. A. S. van den Brenk, R. C. Kerr, Wendy Richter, and M. P. Papworth. "Enhancement of Radiosensitivity of Skin of Patients by High Pressure Oxygen". In: *The British Journal of Radiology* 38 (1965), pp. 857–864. DOI: 10.1259/0007-1285-38-455-857.

[308] Jeannette Jansen et al. "Does FLASH deplete oxygen? Experimental evaluation for photons, protons, and carbon ions". In: *Medical Physics* 48 (2021), pp. 3982–3990. DOI: https://doi.org/10.1002/mp.14917.

[309] Frank Schneider et al. "Rapid and reversible adaptation of a clinical linear accelerator for electron FLASH radiotherapy". In: *Physica Medica* 136 (2025), p. 105032. DOI: 10.1016/j.ejmp.2025.105032.

[310] Muhammad Ramish Ashraf et al. "Dosimetry for FLASH Radiotherapy: A Review of Tools and the Role of Radioluminescence and Cherenkov Emission". In: *Frontiers in Physics* 8 (2020). DOI: 10.3389/fphy.2020.00328.

[311] Eric S. Diffenderfer, Brita S. Sørensen, Alejandro Mazal, and David J. Carlson. "The current status of preclinical proton FLASH radiation and future directions". In: *Medical Physics* 49 (2022), pp. 2039–2054. DOI: https://doi.org/10.1002/mp.15276.

[312] Shouyi Wei et al. "FLASH Radiotherapy Using Single-Energy Proton PBS Transmission Beams for Hypofractionation Liver Cancer: Dose and Dose Rate Quantification". In: *Frontiers in Oncology* 11 (2022). DOI: 10.3389/fonc.2021.813063.

[313] Shouyi Wei et al. "Advanced pencil beam scanning Bragg peak FLASH-RT delivery technique can enhance lung cancer planning treatment outcomes compared to conventional multiple-energy proton PBS techniques". In: *Radiotherapy and Oncology* 175 (2022), pp. 238–247. DOI: 10.1016/j.radonc.2022.08.005.

[314] Shouyi Wei, Haibo Lin, J. Isabelle Choi, Charles B. Simone, and Minglei Kang. "A Novel Proton Pencil Beam Scanning FLASH RT Delivery Method Enables Optimal OAR Sparing and Ultra-High Dose Rate Delivery: A Comprehensive Dosimetry Study for Lung Tumors". In: *Cancers* 13 (2021). DOI: 10.3390/cancers13225790.

[315] J W Boag, E Hochhäuser, and O A Balk. "The effect of free-electron collection on the recombination correction to ionization measurements of pulsed radiation". In: *Physics in Medicine & Biology* 41 (1996), p. 885. DOI: 10.1088/0031-9155/41/5/005.

[316] F. Di Martino, M. Giannelli, A. C. Traino, and M. Lazzeri. "Ion recombination correction for very high dose-per-pulse high-energy electron beams: ksat evaluation for very high dose-per-pulse electron-beams". In: *Medical Physics* 32 (2005), pp. 2204–2210. DOI: 10.1118/1.1940167.

[317] Kristoffer Petersson et al. "High dose-per-pulse electron beam dosimetry - A model to correct for the ion recombination in the Advanced Markus ionization chamber". In: *Medical Physics* 44 (2017), pp. 1157–1167. DOI: https://doi.org/10.1002/mp.12111.

[318] Francesco Romano, Claude Bailat, Patrik Gonçalves Jorge, Michael Lloyd Franz Lerch, and Arash Darafsheh. "Ultra-high dose rate dosimetry: Challenges and opportunities for FLASH radiation therapy". In: *Medical Physics* 49 (2022), pp. 4912–4932. DOI: 10.1002/mp.15649.

[319] Elisabetta Medina et al. “First experimental validation of silicon-based sensors for monitoring ultra-high dose rate electron beams”. In: *Frontiers in Physics* (2024). DOI: 10.3389/fphy.2024.1258832.

[320] Marco Marinelli et al. “A diamond detector based dosimetric system for instantaneous dose rate measurements in FLASH electron beams”. en. In: *Phys. Med. Biol.* 68 (2023), p. 175011. DOI: 10.1088/1361-6560/acead0.

[321] Yasuyuki Futami et al. “Broad-beam three-dimensional irradiation system for heavy-ion radiotherapy at HIMAC”. In: *Nuclear Instruments and Methods in Physics Research Section A: Accelerators, Spectrometers, Detectors and Associated Equipment* 430 (1999), pp. 143–153.

[322] Florian Kühteubl. “Slow Extraction Optimisation for the MedAustron Synchrotron”. en. PhD thesis. TU Wien, 2024. DOI: 10.34726/HSS.2024.88260.

[323] G Feldbauer, M Benedikt, and U Dorda. “Simulations of Various Driving Mechanisms for the 3rd Order Resonant Extraction from the MedAustron Medical Synchrotron”. In: *2nd International Particle Accelerator Conference* (2011).

[324] L Badano and S Rossi. *Characteristics of a betatron core for extraction in a proton-ion medical synchrotron*. Tech. rep. Geneva: CERN, 1997.

[325] Edmond Ciapala. *Stacking and phase displacement acceleration*. CERN Accelerator School. 1985. DOI: 10.5170/CERN-1985-019-V-1.195.

[326] V. Kain et al. “Resonant slow extraction with constant optics for improved separatrix control at the extraction septum”. In: *Phys. Rev. Accel. Beams* 22 (10 2019), p. 101001. DOI: 10.1103/PhysRevAccelBeams.22.101001.

[327] S van der Meer. *Stochastic extraction, a low-ripple version of resonant extraction*. Tech. rep. Geneva: CERN, 1978.

[328] M. G. Pullia et al. “Betatron Core Driven Slow Extraction at CNAO and MedAustron”. In: *Proc. of International Particle Accelerator Conference (IPAC'16), Busan, Korea, May 8-13, 2016* (Busan, Korea). International Particle Accelerator Conference. doi:10.18429/JACoW-IPAC2016-TUPMR037. Geneva, Switzerland, 2016, pp. 1330–1333. DOI: doi:10.18429/JACoW-IPAC2016-TUPMR037.

[329] International Electrotechnical Commission. *Medical electrical equipment. Part 2-64, Particular requirements for the basic safety and essential performance of light ion beam medical electrical equipment*. International Electrotechnical Commission, 2014.

[330] Daphnée Villoing et al. “Technical note: Proton beam dosimetry at ultra-high dose rates (FLASH): Evaluation of GAFchromic™ (EBT3, EBT-XD) and OrthoChromic (OC-1) film performances”. In: *Medical Physics* 49 (2022), pp. 2732–2745. DOI: 10.1002/mp.15526.

[331] Suphalak Khachonkham et al. “Characteristic of EBT-XD and EBT3 radiochromic film dosimetry for photon and proton beams”. In: *Physics in Medicine & Biology* 63 (2018), p. 065007. DOI: 10.1088/1361-6560/aab1ee.

[332] Matthias Knopf et al. *Characterizing the Delivered Spill Structure of Medical Proton and Carbon-Ion Beams at MedAustron using a High Frequency Silicon Carbide Readout*. 2025. arXiv: 2507.11593 [physics.ins-det].

[333] Andrea De Franco et al. “Optimization of synchrotron based ion beam therapy facilities for treatment time reduction, options and the MedAustron development roadmap”. In: *Physica Medica* 81 (2021), pp. 264–272. DOI: 10.1016/j.ejmp.2020.11.029.

[334] *Flash-BPM: Online Dosimetry for FLASH Radiotherapy*. 2021. URL: https://projekte.ffg.at/projekt/5136817.

[335] Tao Yang et al. “Time Resolution of the 4H-SiC PIN Detector”. In: *Frontiers in Physics* 10 (2022). DOI: 10.3389/fphy.2022.718071.

[336] Xin Shi et al. *SiC LGAD Detector*. CERN-DRD3-PROJECT-2024-002. 2024.

[337] Andreas Gsponer. *Silicon Carbide Detector Development for HEP and Medical Applications*. https://indico.cern.ch/event/1455346/contributions/6323070/. 20th Anniversary "Trento" Workshop on Advanced Silicon Radiation Detectors (TREDI 2025). 2025.

[338] Simon Waid et al. “Detector Development for Particle Physics”. In: *2023 Austrochip Workshop on Microelectronics (Austrochip)*. 2023 Austrochip Workshop on Microelectronics (Austrochip). Graz, Austria: IEEE, 2023, pp. 40–43. DOI: 10.1109/Austrochip61217.2023.10285161.

[339] Daniel Radmanovac. *In-situ Radiation Damage Study of Silicon Carbide Detectors subjected to Clinical Proton Beams*. https://indico.cern.ch/event/1507215/contributions/6540487/. 3rd DRD3 week on Solid State Detectors R&D. Amsterdam, Netherlands, 2025.

[340] Jiri Kroll and Radek Novotny. *Radiation effects in 4H-SiC PN diodes, LGAD sensors, and MOSFET transistors*. https://indico.cern.ch/event/1507215/contributions/6540481/. 3rd DRD3 week on Solid State Detectors R&D. Amsterdam, Netherlands, 2025.

[341] Yashas Satapathy et al. *Impact of Proton Irradiation on 4H-SiC Low Gain Avalanche Detectors (LGADs)*. 2025. arXiv: 2507.23062 [physics.ins-det].

[342] Sen Zhao et al. *The study of 4H-SiC LGAD after proton radiation*. https://arxiv.org/abs/2507.12238. 2025.